Heating and Thermalization of Minor Ions in the Solar Wind

by

Janelle A. Holmes

A dissertation submitted in partial fulfillment
of the requirements for the degree of
Doctor of Philosophy
(Applied Physics)
in the University of Michigan
2024

Doctoral Committee:

Professor Susan T. Lepri, Co-Chair
Associate Professor Jim Raines, Co-Chair
Professor Justin C. Kasper
Associate Research Professor Ward Manchester IV
Professor Mark B. Moldwin

Janelle A. Holmes
hjanelle@umich.edu
ORCID iD: 0009-0003-1900-6963
©Janelle A. Holmes
2024

ACKNOWLEDGMENTS

I'd like to thank my family, particularly my mother and sister. They are everything to me. Life in Ann Arbor have been a lot less fun without the companionship I gained at my martial arts gym, as well as with my tennis and racquetball partners. I'd like to thank them for all the hours of on the court and on the mats.

Thank you to my first advisor, Justin Kasper, as well as Sue Lepri and Jim Raines, who stepped in halfway through, for all the time and effort you've dedicated to me. Thanks also to my Applied Physics cohort, classmates, and research group members. Ben Alterman acted as a peer mentor from the day I stepped foot on campus to the day he left. Thank you, Chris Bert, for being a helpful classmate, groupmate, and friend.

Thanks also to the Solar Wind Ion Composition Spectrometer and Heavy Ion Sensor instrument teams for the data that was used heavily in this thesis. Thanks also to NESS SSERVI and NASA grant No. 80NSSC18K0986 for funding this work.

TABLE OF CONTENTS

Acknowledgments . . . . . **ii**

List of Figures . . . . . **v**

List of Tables . . . . . **x**

List of Appendices . . . . . **xi**

Abstract . . . . . **xii**

Chapter

1 Introduction **1**

1.1 Significance of Composition 1
1.2 Sources of the Fast and Slow Wind 3
1.2.1 Coronal Holes 3
1.2.2 Slow Sources 4
1.3 Solar Cycle 5
1.4 Minor Ions Kinetics out of Thermodynamic Equilibrium 7
1.5 Minor Ions and the Alfvénic Slow Wind 12
1.6 Radial Evolution of Ion Kinetics 14
1.7 Solar Wind Heating and Acceleration 16
1.8 Brief Description of HIS and SWICS 18
1.9 Science Questions 20
1.10 Chapter Overview 21

2 Preferential Heating Zone of Minor Ions **22**

2.1 Introduction 22
2.2 Methodology 25
2.2.1 SWICS and SWEPAM Datasets 25
2.2.2 Implementation of the Radial Boundary Model 26
2.2.3 Data Selection 27
2.3 Minor Ion Temperature Profiles 28
2.4 Discussion 36
2.5 Conclusions 38

3 Heating of Minor Ions in the Slow Alfvénic Wind **41**

3.1 Introduction 41

3.2 Methodology . . . 44
3.2.1 ACE/SWICS Data . . . 44
3.2.2 Selection and Description of Alfvénic Intervals . . . 45
3.2.3 Non-Alfvénic Wind . . . 49
3.2.4 Fast Wind . . . 49
3.3 Collisionality of the Slow Alfvénic Wind . . . 50
3.4 Preferential Heating of Minor Ions in the Slow Alfvénic Wind . . . 53
3.4.1 Direct σ_c Comparison . . . 61
3.5 Solar Cycle Variation . . . 65
3.6 Discussion . . . 70
3.6.1 Thermalization Curves . . . 70
3.6.2 Ion Dependencies . . . 71
3.6.3 Solar Cycle and σ_c . . . 73
3.7 Conclusions . . . 75

4 Heavy Ion Kinetics from 0.28-1 AU . . . 77

4.1 Introduction . . . 77
4.2 HIS Data (SWA-MAG) . . . 80
4.2.1 SWA . . . 80
4.2.2 HIS Densities . . . 80
4.3 Thermalization of Solar wind with Radial Considerations . . . 82
4.3.1 Radial Trends in Kinetic Moments . . . 82
4.3.2 Coulomb Thermalization . . . 88
4.4 Preferential Heating Zone Model Results . . . 99
4.4.1 Excess Temperature Decay Profiles . . . 99
4.4.2 Dependence on Ion Properties . . . 102
4.5 Preferential Heating Zone Model Predictions with Radial Considerations . 105
4.6 Discussion and Conclusions . . . 109
4.6.1 Radial Trends in Thermalization . . . 109
4.6.2 Comparison to Previous Work . . . 111
4.6.3 Conclusion/Future Work . . . 112

5 Conclusion . . . 114

5.1 Summary . . . 114
5.2 Limitations of this Work . . . 115
5.2.1 PHZ for Minor Ions . . . 115
5.2.2 Minor Ions in the Slow Alfvénic Wind . . . 115
5.2.3 Heavy Ion Sensor . . . 116
5.3 Future Work . . . 117

Appendices . . . 119

Bibliography . . . 142

LIST OF FIGURES

1.1 From McComas et al., 2008. SWOOPS images of solar corona during first three Ulysses orbit, showing the migration of the polar coronal holes. SSN plotted below. 6
1.2 From Kasper 2017, Figure 3. Schematic of collisional, preferential heating, and Coulomb relaxation zones. 9
1.3 Alpha VDFs from Marsch et al., 1982a 10
1.4 Proton VDFs from Marsch et al., 1982b 11
1.5 Example of Slow Alfvénic stream, as well as non-Alfvénic and fast, from D'Amicis et al., 2019. 13
1.6 Power spectra from Messenger and ACE, from Gershman et al., 2012 17

2.1 Excess temperature vs. collisional age for six selected ions at all solar wind speeds. Black diamonds are observed excess temperature, while red lines are model fits. Faint grey lines signify error based on variance within each bin. . . 29
2.2 Excess temperature vs. collisional age for six selected ions for solar wind speeds below 500 km s^{-1}. 30
2.3 The top left panel shows R_b dependence on charge to mass ratio . The top right shows the R_b-charge squared to mass dependence, and the bottom panel is mass ratio (m_i/m_p) . All panels in this figure refer only to $v < 500$ km s^{-1}. The pink dashed lines represent the R_b range predicted by [1] and [2] at the charge to mass ratio of alphas (0.5) 32
2.4 Excess temperature vs. charge to mass ratio at the radial PHZ boundary and at ACE. Grey lines denote the Chandran et al. [3] prediction for each mass. The bottom curve is for 4 amu, then 12 amu, 14 amu, etc. 33
2.5 Excess temperature vs. mass ratio calculated at preferential heating boundary and 1 AU. 33
2.6 Panel (a) is a visualization of the full range in energy-per-charge associated with typical solar wind velocities for high q/m alphas and low q/m Fe^{8}+ ions. Panel (b) is the ratio of recovered vs. input thermal speeds from idealized, continuous sampling vs. logarithmically spaced energy windows. 39

3.1 Example of one SA interval, preceded and followed by typical slow intervals. The same interval on the left and right is shown for alphas and O^{6+}, respectively. 46
3.2 Example of another SA interval. The same interval on the left and right is shown for alphas and O^{6+}, respectively. 47

3.3 Example of one SA interval, preceded and followed by what appear to be fast streams. The same interval on the left and right is shown for alphas and O^{6+}, respectively. 48
3.4 Histograms of temperature ratio in four different collisional age regimes: $A_c < 0.1$, $0.1 < A_c < 1.0$, $1.0 < A_c < 10.0$, and $A_c > 10.0$ 51
3.5 Preferential Heating Zone boundary model on the following subsets of data, from left to right column: all solar wind speeds, all speeds below 500 km/s, and speeds below 500 km/s with identified slow Alfvénic intervals removed. . 54
3.6 Ion trends from PHZ model. Left to right: SA wind, SNA wind, and typical slow wind from 1998-2002. Top to bottom: R_b vs. m_{ion}, R_b vs. q/m, R_b vs. q^2/m, ε_b vs. m_{ion}, and ε_b vs. q/m are listed. Rainbow color scheme for q/m plots. Two-toned for mass. 55
3.7 Direct comparisons of observed boundary excess temperature for SA wind vs. SNA, general slow, and all wind speeds. 60
3.8 Direct comparisons of radial boundary prediction for SA wind vs. SNA, general slow, and all wind speeds. 60
3.9 Top panels depict PHZ model results where $\sigma_c < 0.8, 0.7$, and 0.5, left to right. Bottom panels depict PHZ model results where $\sigma_c >$ 0.5, 0.3, and 0.2, left to right. 62
3.10 Direct comparison of predicted R_b between $\sigma_c > 0.8$ and $\sigma_c < 0.2$ 63
3.11 Direct comparison of observed ε_b between $\sigma_c > 0.8$ and $\sigma_c < 0.2$ 64
3.12 Each of these panels depicts a timeseries of an ion parameter overplotted with the monthly averaged SSN. Moving clockwise starting with the top left: He^{2+} R_b, He^{2+} ε_b, O^{6+} ε_b, O^{6+} R_b, ... 66
3.13 Each of these panels depicts an ion parameter plotted against the monthly averaged SSN. From top to bottom: predicted R_b for three abundant ions, ε_b for the same three ions, correlation coefficient of R_b and q/m calculated from model output from all ions, and slope of the linearization of ε_b and ion mass calculated from observed boundary excess temperature of all ions. 67
3.14 Same as above, but panel b shows high normalized cross-helicty wind, while panel c shows low cross-helicity. 68

4.1 Radial evolution of solar wind density and temperature for protons. Fast densities are shown in panel (a), fast temperatures in panel (b), slow densities in panel (c), and slow temperatures in panel (d). Fit is overplotted in black. Previous observations by Hellinger et al., 2011 , 2013, and Perrone et al., 2018 are overplotted in green, blue, and magenta, respectively. The top row shows the trends in fast wind and slow wind in the bottom. 83
4.2 Radial evolution of slow solar wind density and temperature for protons using 400 km/s as the upper limit. 84

4.3 Radial evolution of solar wind temperature for He^{2+}. Fast densities are shown in panel (a), fast temperatures in panel (b), slow densities in panel (c), and slow temperatures in panel (d). Fit is overplotted in black. Previous observations by Hellinger et al., 2011, 2013, and Perrone et al., are overplotted in green, blue, and magenta, respectively. The top row shows the trends in fast wind and the bottom slow speeds. 86
4.4 Radial evolution of solar wind density and temperature for O^{6+}. Fast densities are shown in panel (a), fast temperatures in panel (b), slow densities in panel (c), and slow temperatures in panel (d). Fit is overplotted in black. Previous observations by Hellinger et al., 2011, 2013, and Perrone et al., 2018 are overplotted in green, blue, and magenta, respectively. The top row shows the trends in fast wind and the bottom slow speeds. 87
4.5 Alpha temperature ratios vs. collisional age in the top row and radial distance in the middle. Fast wind is plotted to the right, slow wind to the left, and the full range in A_c for all speeds is shown in the middle on the bottom. 89
4.6 C^{5+} temperature ratios vs. collisional age in the top row and radial distance in the middle. Fast wind is plotted to the right, slow wind to the left, and the full range in A_c for all speeds is shown in the middle on the bottom. 90
4.7 O^{6+} temperature ratios vs. collisional age in the top row and radial distance in the middle. Fast wind is plotted to the right, slow wind to the left, and the full range in A_c for all speeds is shown in the middle on the bottom. 91
4.8 Fe^{10+} temperature ratios vs. collisional age in the top row and radial distance in the middle. Fast wind is plotted to the right, slow wind to the left, and the full range in A_c for all speeds is shown in the middle on the bottom. 92
4.9 Alpha differential velocities vs. collisional age in the top row and radial distance in the middle. Fast wind is plotted to the right, slow wind to the left, and the full range in A_c for all speeds is shown in the middle on the bottom. 94
4.10 C^{5+} differential velocities vs. collisional age in the top row and radial distance in the middle. Fast wind is plotted to the right, slow wind to the left, and the full range in A_c for all speeds is shown in the middle on the bottom. 95
4.11 O^{6+} differential velocities vs. collisional age in the top row and radial distance in the middle. Fast wind is plotted to the right, slow wind to the left, and the full range in A_c for all speeds is shown in the middle on the bottom. 96
4.12 Fe^{10+} differential velocities vs. collisional age in the top row and radial distance in the middle. Fast wind is plotted to the right, slow wind to the left, and the full range in A_c for all speeds is shown in the middle on the bottom. 97
4.13 Decay in ε with A_c for He^{2+} and C^{5+}, O^{6+}, and Fe^{10+}. Speeds less than 500 km/s. 100
4.14 Decay in ε with A_c for He^{2+} and C^{5+}, O^{6+}, and Fe^{10+}.All wind speeds. 101
4.15 R_b scaling with ion (a) mass, (b) q/m, and (c) q^2/m. Slow speeds only are on the left side. All speeds are on the right. 103
4.16 ε_b scaling with ion (a) mass and (b) q/m. Slow speeds only are depicted on the left, while all speeds are on the right. 104
4.17 The R_b vs. q/m plot for the dataset when less abundant/reliable ions are excluded. 105

4.18 He^{2+} R_b prediction vs. maximum radial distance. Minimum radial distances are represented in the legend to the right of the plot. 106
4.19 C^{5+} R_b prediction vs. maximum radial distance. Minimum radial distances are represented in the legend to the right of the plot. 107
4.20 O^{6+} R_b prediction vs. maximum radial distance. Minimum radial distances are represented in the legend to the right of the plot. 107
4.21 Fe^{10+} R_b prediction vs. maximum radial distance. Minimum radial distances are represented in the legend to the right of the plot. 108
4.22 Differential velocities vs. temperature ratio over all speeds for (clockwise) He^{2+}, C^{5+}, O^{6+}, and Fe^{10+} 110

A.1 Velocities and fits for all ion pairings between He^{2+}, C^{5+}, O^{6+}, and Fe^{10+} 120
A.2 From Hefti 1998 121
A.3 Temperatures and fits for all ion pairings between He^{2+},Fe^{10+}, O^{6+}, and C^{5+} . . 122
A.4 From Hefti 1998 123
A.5 Radial evolution of solar wind density and temperature for O^{6+}. Fit is overplotted in black. Previous observations by Hellinger et al., 2011, 2013, and Perrone et al., 2018 are overplotted in green, blue, and magenta, respectively. The top row shows the trends in fast wind, the middle slow wind, and the bottom all speeds. 125
A.6 Radial evolution of solar wind density and temperature for Fe^{10+}. Fit is overplotted in black. Previous observations by Hellinger et al., 2011, 2013, and Perrone et al., 2018 are overplotted in green, blue, and magenta, respectively. The top row shows the trends in fast wind, the middle slow wind, and the bottom all speeds. 126

B.1 The image on the left shows an unaltered dataset. The image on the right shows the results of multiplying proton density by two, which produces an R_b nearly 50 % larger than the unaltered dataset. WIND/SWE and ACE/SWICS are known to measure different densities during the same time periods, and the R_b produced by this model is heavily influenced by proton density. This would be a major contributing factor to the difference in results produced from the SWICS and SWE datasets. 128
B.2 The figure on the left shows the unaltered 90-second resolution WIND dataset. The figure on the right shows the dataset averaged down to two-hour resolution. Time averaging does result in an increased R_b value, in this case almost 50 % larger than the unaltered prediction. The results produced by the SWICS dataset at 2-hour place an upper limit on the radial PHZ boundary. 128

B.3 The figure on the left shows the original 90-second WIND data set from 1994-2021. The figure on the right shows the WIND dataset when limited to the pre-anomaly ACE/SWICS years of operation, 1998-2011. The WIND dataset used in K17 covers the end of Solar Cycle 22 up to the beginning of SC 25, which includes SC 22 solar minimum, all of SC 23, and SC 24 solar and descending phase. The SWICS dataset spans (portions of) SC 23 and 24. Kasper 2019 showed a correlation between predicted R_b and sunspot number, so it would follow that the variation over a solar cycle and between different cycles would lead to R_b variation. 129

C.1 Effects of varying error thresholds on the ion mass vs. R_b relationship. From top to bottom, $\sigma_n/n \leq 0.16$, $\sigma_n/n \leq 0.40$, and $\sigma_n/n \leq 0.58$. Full dataset is on the left, restricted to the most abundant ions is on the right. 134

C.2 Effects of varying error thresholds on the q/m vs. R_b relationship. From top to bottom, $\sigma_n/n \leq 0.16$, $\sigma_n/n \leq 0.40$, and $\sigma_n/n \leq 0.58$. Full dataset is on the left, restricted to the most abundant ions is on the right. 135

C.3 Effects of varying error thresholds on the q^2/m vs. R_b relationship. From top to bottom, $\sigma_n/n \leq 0.16$, $\sigma_n/n \leq 0.40$, and $\sigma_n/n \leq 0.58$. Full dataset is on the left, restricted to the most abundant ions is on the right. 136

C.4 Effects of varying error thresholds on the decay curves. From left to right, $\sigma_n/n \leq 0.16$, $\sigma_n/n \leq 0.40$, and $\sigma_n/n \leq 0.58$. Top row shows He^{2+}, followed by C^{5+}, O^{6+}, and Fe^{10+}. 137

C.5 Proton density distributions for SA, SNA, and Fast wind. 137

C.6 Proton Temperature distributions for SA, SNA, and Fast wind. Note that SA wind has a slightly higher peak than SNA wind, but SNA wind has a high population overall of temperatures comparable to and higher than the SA peak. 138

C.7 Derivative of A_c w/r/to proton density. 138

C.8 Derivative of A_c w/r/to proton temperature. 139

C.9 Proton density distributions in 3 solar wind types in different density regimes. From top to bottom, fast, SA, and SNA wind. From left to right, low density regime, high density, and the full distribution of densities. 140

C.10 Proton temperature in 3 solar wind types in different temperature regimes. From top to bottom: fast wind, SA wind, SNA wind. From left to right, low temperature, temperature covering SA peak T_p, high temperature, and the full distribution. Note that the second column overlaps with columns one and three. 141

LIST OF TABLES

2.1 For all solar wind speeds, r^2 values and correlation coefficients for all species are depicted in the top row. Charge states of C, N, O, Ne, Mg, Si, S, and Fe are calculated separately for q/m and q^2/m dependencies. 32

3.1 Collisional frequencies for varying solar wind regimes for most ions included in the SWICS 12-minute dataset. 52

4.1 Density fit coefficients. Fits are to the function: $n = a_0 * (R/R_0)^{a_1}\ cm^{-3}$ . . . 88

4.2 Temperature fit coefficients. Fits are to the function: $T = a_0 * (R/R_0)^{a_1}\ K$ . . 88

LIST OF APPENDICES

A HIS Validation - Heavy Ion Kinetics (Temperature ratios, velocity ratios) . . . 119

B PHZ Model Sensitivity 127

C Collisional Age, Density and Temperature in 3 Solar Wind Types 130

ABSTRACT

In this thesis, the preferential heating of heavy ions in the solar wind has been explored in different solar wind types, throughout the solar cycle, and with radial distance from the Sun. The ambient solar wind is often observed to be out of local thermodynamic equilibrium. The mechanisms of thermalization, the time and spatial scales on which it occurs, and the extent of it in solar wind streams all provide insight into local energy transfer. Nonthermal features of the solar wind are well-ordered by collisional age and thus can be used to provide information about the origin of the nonthermal state. The varying charge states and masses of minor ions provide further information about the mechanisms driving the solar wind's state closer to the sun and its evolution toward thermodynamic equilibrium.

In Chapter 2, which predicts the outer boundary of preferential heating for minor ions, collisional age is used to model the thermalization of minor ion species, predicting the radial distance at which preferential heating becomes less significant than thermalization due to Coulomb collisions. The results were compared to those found for alpha particles using WIND data, as well as a model of mass-dependent heating. Though the predictions of the preferential heating zone boundary were quite high, they did exhibit a clear mass and charge-to-mass dependence.

In Chapter 3, which concerns the heating of minor ions in the slow Alfvénic wind, slow-Alfvénic (SA) intervals from SC 23 solar maximum were selected, as well as fast and non-Alfvénic intervals. SWICS 12-minute data was used to analyze the collisionality of these wind types, with the overall goal of determining whether or not the SA intervals were collisional enough to be used in the preferential heating zone boundary model. It was found that the distinct collisionality of the three wind types is not fully dependent on density and temperature, which are the driving factors of collisional frequency. The Preferential Heating Zone model was run on SA and slow non-Alfvénic (SNA) wind, finding that the model predicts a lower boundary for SA wind than for SNA. It was also found that the radial boundary height and normalized cross-helicity are anticorrelated, while excess temperature at the boundary, tended to be higher in the SNA wind. The variation in excess heating and boundary height with solar cycle is explored as a possible cause for the results, and other explanations, such as the variation of ion abundances in the different solar wind types are discussed as well. Overall, radial boundary, excess temperature, and their dependence on

ion mass and charge-to mass in the slow wind with high Alfvénicity do not exhibit as much variability as the slow wind with low Alfvénicity.

Chapter 4, which tracks heavy ion kinetics from the inner heliosphere to 1 AU, applies the preferential heating zone model to Heavy Ion Sensor (HIS) observations, allowing for the direct input of varying distances from the Sun. Direct observations of the relaxation of T_{ion}/T_{proton} and Δv_{ip} with radial distance and A_c are compared to each other, as well as modeled and observed trends in ion parameters. This is done for slow, fast, and combined wind. The transition from heating to thermalization is observed at low collisional ages. Preferential heating zone model predictions in varying ranges of radial distance are compared, finding that when including data beyond about 150 R_s, model predictions become well-ordered, providing a range of expected radial boundary predictions at varying spacecraft distances. The presence of mass and mass to charge dependent radial scaling in Chapters 2 and 4 and the absence of these dependencies in Chapter 3, which is limited to solar maximum and ascending maximum, indicate that the ordering of the boundary location is more strongly tied to the solar cycle than the extent of the heating.

CHAPTER 1

Introduction

The solar wind is a high-speed, hot, weakly collisional plasma, subject to processes on length scales of thousands of kilometers (photospheric granules/supergranules) down to dissipation scales, and timescales from years (solar cycle) to months (Carrington rotation), minutes (solar flare travel time) down to seconds (plasma frequencies) [4]. It is comprised of about 95% hydrogen and about 4% helium, with the remaining percentage consisting of minor ions, though these percentages can vary under different conditions. The study of these minor ions, which, due to their low number density, are too sparse to significantly interact with the solar wind's bulk constituents, provides insight into the processes heating and accelerating the plasma as it transitions from photosphere to corona, and expands outward as the solar wind.

1.1 Significance of Composition

The composition of the solar wind is determined by its coronal source. Coronal hole and non-coronal hole wind carry with it signatures in composition that reflect source conditions. Spectroscopic evidence shows that photospheric abundances of minor ions do not exhibit significant spatial variation. Throughout the chromosphere and corona, processes such as thermal diffusion, Coulomb drag, and gravitational settling have varying impacts over different regions on minor ion charge states and abundances. This results in variations in these parameters that are heavily dependent on the source region (coronal holes, active regions, streamer belt), and that vary greatly from their typical values in the photosphere [5]. This evolution ceases low in the corona, though at varying heights based on the species, where electron density has dropped enough to that ionization recombination processes are no longer significant [6]. The source region-dependent elemental fractionation in the chromosphere and low corona and its cease close to the surface make minor ions suitable tracers for processes close to the Sun.

Using observations from Ulysses, Geiss et al., [7] showed that the solar wind has three main sources: high speed streams originating from polar coronal holes, slow streams originating from the regions surrounding coronal holes, and slow streams originating from current sheets. They also show that elemental abundances are ordered by first ionization time, more than ionization potential. The Ulysses data also confirms that high charge states in the slow solar wind can be attributed to high electron temperatures in the slow wind source regions. The combination of low- first ionization potential (FIP) with high-FIP, namely the Mg/O ratio, closely follows coronal temperatures and the O^{7+}/O^{6+} ratio. They, as well as Von Steiger et al., 1997, 2000 ([8];[9]) draw distinctions in the composition of slow wind associated with coronal holes and slow wind as an extension of helmet streamers. FIP bias refers to the increased abundance of ions with FIP below 10 eV, such as Fe, Mg, and Si in the upper solar atmosphere and slow solar wind. High FIP ions, such as O, Ne, and He, are found in reduced abundance in this region, but are enhanced in coronal loops and the slow wind when compared to photospheric abundances ([9];[10];[11]). The interplay between gravitational settling leads to the enhancement of heavier ion abundances in the low corona, and Coulomb drag, which can accelerate ions with a high q^2/m, leading to the enhancement of these ion abundances high in the corona, relative to photospheric abundances. These two effects do not have as large an impact in coronal hole regions, and consequently fast wind, as they do on the slow wind ([12];[5];[13]).

Kinetic features and the composition of the slow and fast wind are determined by their source on the solar surface and the processes that heat and accelerate the wind emerging from these regions, with slow wind presumably originating from the quiet sun streamer belt or the edges of coronal holes and active regions, and fast wind originating from the interiors of coronal holes ([14];[15]). There are deviations from the commonly held sources of the fast and slow wind that result in characteristics that deviate from the canonical bimodal picture, such as wind streaming at intermediate speeds with a blend of fast wind-like composition and slow wind-like charge states, and presumably emerging from the boundaries of coronal holes ([16];[17]). Similarly, wind streaming at slow speeds with fast wind-like composition and high Alfvénicity has been identified [18]. To term these other wind types as 'deviations' is not fully accurate, as they are neither singular, nor uncommon phenomena.

Due to oxygen being the most abundant heavy ion besides helium, the O^{7+}/O^{6+} is an excellent tracer of coronal source regions because the elemental abundances and ionization do not evolve with distance beyond about 5 solar radii (R_s). Additionally, Landi et al., [6] showed that the C^{6+}/C^{4+} ratio is even more sensitive than O^{7+}/O^{6+} to source region, and due to the more even distribution of carbon charge states ($C^{4\text{-}6+}$) compared to oxygen ($O^{5\text{-}8+}$),

temperature estimates based on these ratios are more statistically sound. The abundance ratios of other ions, such as Fe/O and Mg/O are also good tracers, as they demonstrate the relative abundance of high-FIP elements to a mid-FIP element, and tend to be lower and less variable in the fast wind than the slow.

1.2 Sources of the Fast and Slow Wind

1.2.1 Coronal Holes

Coronal holes are regions of rapidly expanding, open magnetic field lines. Due to the diverging field, density and temperature are lower, resembling photospheric conditions. Abundances also mirror photospheric levels. Coronal holes appear as dark regions in UV and X-ray spectroscopy due to their low density and temperature. While the interiors of coronal holes are far less structured than helmet streamers (i.e., less density and temperature variation, open magnetic field without current sheet, arcade, and potential for reconnection) they are not entirely steady state. Borovsky et al., 2016 [19] showed that coronal holes are not necessarily homogeneous. In fact, they found structures with amplitudes of a factor of two in magnetic field, composition and kinetic observations, and measures of Alfvénicity in WIND/SWE, ACE/SWEPAM, and Helios 1 and 2 data in unperturbed coronal hole plasma. This was identified by "flattop" velocity time series, wherein the velocity is high and has minimal variation [20].

Though the fast wind is taken to be collisionless due to its low density, acceleration of the slow wind as well as deceleration due to stream interactions may result in a continuum of wind speeds with varying collisional rates. Matteini et al., 2011 [21] gives a review of ion kinetic evolution as a result of Coulomb collisional coupling and instabilities driven by wave-particle interactions and wave-wave interactions. Coulomb coupling refers to the deflection in the of plasma species (test particle) drift due to elastic collisions with field particle species, wherein the deflection is a result of the interaction of the charged particle with the electric field generated by the field particle. Wave-particle interactions are the transfer of energy between plasma and plasma waves, which may occur when waves (e.g., Alfvén, slow/fast magnetosonic, ion-cyclotron, Langmuir), possess frequencies on the scale of plasma particle motions, allowing the wave to either gain energy from the particles, thus slowing and/or cooling them or lose energy to the particles, resulting in their heating and acceleration. Wave-wave interactions are the instabilities and subsequent wave growth that may arise due to the nonlinear couplings between waves. Refer to Verscharen et al., 2019 [4] and the references therein for a more complete discussion of these topics.

It is known that the double-adiabatic, or Chew, Goldberger, and Low (CGL) prediction [22] of solar wind expansion does not fully capture the evolution of kinetic properties due to the presence of processes such as collisional coupling, as well as departures of particle velocity distribution functions (VDFs) from thermodynamic equilibrium. The Hybrid Expanding Box Model has been used to study the resonance of Alfvén cyclotron waves in protons, alphas, and heavy ions ([23];[24]). They show that between protons, alphas, and O^{5+}, O^{5+} is heated most efficiently [23].

1.2.2 Slow Sources

Helmet streamers can be identified by their brightness when viewed in X-ray wavelengths. The streamer belt, the band of helmet streamers that traverses the Sun's lower latitudes, is thought to be the source of the slow wind. Unlike the relatively steady-state coronal holes and fast solar wind, the streamer belt is associated with a large amount of structure/variability in density and temperature [25].

Slow wind generation theories fall into three categories: open field acceleration via resonant wave heating, interchange reconnection between open field lines and closed loops formed around helmet streamers, pseudo-streamers, or complex structures with quasi-separatrix layers, and the release of plasma "blobs" due to weak magnetic fields above helmet streamer cusps. Remote sensing evidence supports a number of these theories. Hinode XRT (X-ray telescope) and EIS (EUV Imaging Spectrometer) observations have shown blue-shifted upflows from the edges of active regions reaching speeds of 100 km/s [26], with composition matching that measured by the Solar Wind Ion Composition Spectrometer (SWICS) aboard the Advanced Composition Explorer (ACE)in the slow solar wind [27].

White Light observations have shown that small-scale "blobs" rise above the cusps of coronal streamers, accelerating to 100 km/s in the vicinity of the cusps, and up to 400 km/s within 30 R_s of the surface. These blobs are actually very small flux ropes originating from streamers that form between coronal holes of opposite polarity, and traveling along the heliospheric plasma sheet. Above the cusp, the magnitude of the magnetic field goes to zero and polarity reverses. This reduction in magnetic field drives the plasma radially outward, and could lead to a pinching off, which produces the blob.

White light observations have also revealed that pseudostreamers form above bipolar regions embedded in open-field regions of the same polarity, and thus have no current sheet between them. Pseudostreamer cusps tend to extend to much lower heights than helmet streamers and do not typically emit "blobs". Pseudostreamer magnetic field remains

constant, so there is no strong driver pushing the plasma out. However, energy and flux may be released at the boundary of closed and open field lines of pseudostreamers via interchange reconnection.

The plasma sheet surrounding the current sheet is another potential candidate. Antonucci et al. [28] showed that in coronal holes, hydrogen kinetic temperatures are two orders of magnitude below oxygen while in equatorial streamers, hydrogen kinetic temperatures are one order of magnitude below oxygen. Bavassano et al. [29] show that the heliospheric plasma sheet is much thicker than the current sheet, and provide evidence combined with (much later) radio occultation data that the source of the plasma sheet are coronal streamers, and that the increased density surrounding the sheet can be traced back to the streamer boundaries prior to narrowing. Relative helium abundance is lower within the plasma sheet than outside it ([29]; [30]; [31]).

1.3 Solar Cycle

Solar magnetic activity follows an $\sim$11 year cycle, characterized by the presence and position of sunspots and the polar coronal holes, as well as the polarity reversal of the magnetic field. Sunspots are areas of increased magnetic flux on the solar surface, with distinct polarization. As such, sunspot number is an important indicator of the solar cycle. During solar minimum, the polar coronal holes are large and oriented at the Sun's magnetic North and South poles. Sunspots are rare, if present at all. Equatorial fast wind is prevalent, proton densities and temperatures in both the slow and fast regimes are lower, and charge state ratios such as O^{7+}/O^{6+} and C^{6+}/C^{4+} tend to be lower. Abundance ratios are low. During the ascending phase, sunspots begin to appear in mid-high latitudes on the solar surface and travel closer to the equatorial regions, leading to a deformation of the streamer belt.

During solar maximum, the polar coronal holes have traveled toward the equator and are much smaller. Sunspot-associated low latitude coronal holes are present throughout, resulting in a complex magnetic field structure, as observed by the Ulysses spacecraft during its first three orbits (1998 - 2006) [32]. See Figure 1.1. Fast wind is not as prominent, proton densities and temperatures are higher, and charge state ratios are higher due to the predominance of slow wind and transients. During this time, the polarity of the Sun reverses and sunspots with the opposite orientation begin to appear. Earth-facing sunspots, coronal holes, solar flares, and coronal mass ejections (CMEs) can cause interplanetary, transient events, such as interplanetary coronal mass ejections (ICMEs), solar energetic particle (SEP) events, shocks at stream interaction interfaces. This can lead to an increase in geomagnetic storms that impact satellites, increase radiation at high altitudes close to the

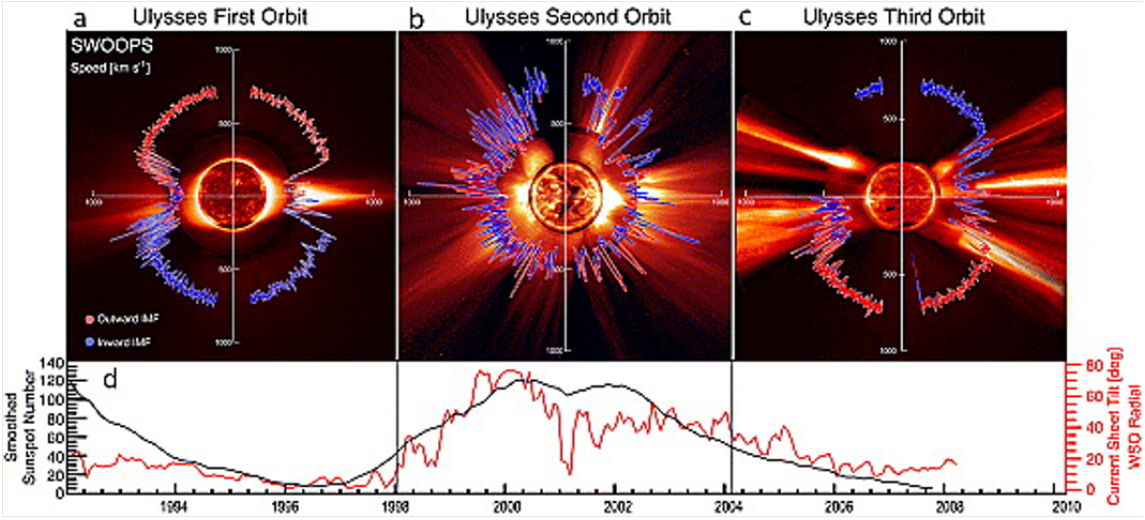

Figure 1.1 From McComas et al., 2008. SWOOPS images of solar corona during first three Ulysses orbit, showing the migration of the polar coronal holes. SSN plotted below.

poles, and produce brighter, more frequent aurora during solar maximum.

During the descending phase, the size and number of sunspots, now with the reversed polarity, begins to decrease and the polar coronal holes travel back to the now opposite poles. Eventually, the minimum sunspot number is achieved for the cycle and the solar magnetic field is once again dominated by the presence of the polar coronal holes, indicating solar minimum and the start of a new cycle. Technically, this 11-year cycle is half of a full $\sim$22-year cycle, which encompasses both polarities.

Minor ion kinetics, charge state ratios, and abundance ratios are strongly tied to their source on the solar surface and are heavily influenced by changes in said sources driven by the solar cycle. This in turn makes the above parameters highly sensitive to variations within the solar cycle, and differences between solar cycles. The solar wind helium abundance precedes the solar cycle with a velocity-dependent shift ([33];[34];[35]). Ion abundances and charge states are typically lower during solar minimum and higher during solar max. Slow wind is more subject to solar cycle variations than fast [36].

Likewise, the Alfvénic nature of the solar wind is also driven by the solar cycle. D'Amicis et al., [37] found that maximum of SC 23 was dominated by slow wind with high degrees of Alfvénicity, comparable to that found in the fast wind during solar minimum of the same cycle. This means that, at 1 AU, Alfvénic wind is observed throughout the solar cycle, but the predominant source, be it fast wind originating from polar coronal holes during solar minimum or SA wind from the edges of lower latitude coronal holes during solar maximum, shifts.

1.4 Minor Ions Kinetics out of Thermodynamic Equilibrium

A plasma in thermodynamic equilibrium is expected to have equal temperatures and velocities across all its constituent species. Remote imaging of the solar atmosphere and inner corona as well as measurements at 1 AU reveal the highly nonthermal nature of the solar wind, with “thermal" in this context referring to the state of thermodynamic equilibrium, and thermalization, the processes driving the plasma toward thermodynamic equilibrium. Alpha particles and heavy ions (mass > 4 amu) that are hotter than protons and electrons and differential streaming proportional to the Alfvén speed are indicative of dissipation mechanisms that preferentially heat some species more than others. Minor ion properties may be key in tracing preferential heating in the solar wind, and could potentially help to identify the combination of mechanisms heating the corona. The launch of Parker Solar Probe (PSP) in 2018 and Solar Orbiter (SO) in 2020 have provided the opportunity to compare theory/models to in-situ measurements of solar wind densities, velocities, and temperatures at unprecedented solar distances. The in-situ plasma instruments aboard both spacecraft provide a combination of proton and alpha measurements, with Solar Orbiter providing additional minor ion measurements ([38];[39];[40];[41]). These missions have and will continue to provide direct insight into key signatures of coronal heating and expansion. Measurements made by spacecraft at 1 AU, however, are still needed in combination with theory to predict and add context to data from PSP and SO.

As temperatures within the transition region of the solar atmosphere rise to 10^3 times higher than photospheric levels, the plasma remains highly collisional. Equal kinetic temperatures are maintained for ions and electrons in the inner corona up to about 0.3 solar radii (R_S) above the surface due to the frequent collisions that serve to thermalize the plasma ([42];[7];[43];[44]). Above the low corona, the frequency of ion-ion Coulomb collisions drops due to expansion driven by rising temperatures; consequently, electron collisions begin to dominate at larger radii. Differences in kinetic temperature between electrons, protons, and heavy ions are seen to develop and grow with distance from the Sun in the presence of dissipative processes that preferentially heat some species over others ([45];[4]). These differences may be due to the dependence of the heating processes on mass, charge, or a combination of both, thus making the study of heavy ions, with their multiple charge states, critical to unraveling the heating mechanisms in the solar corona and solar wind.

Heavy ions make up only a small fraction of the plasma in the corona and solar wind (< 0.1 %). Their varying mass and charge make them useful test particles for tracing

physical processes in the plasma. Many of these heavy ions start off neutral in the photosphere. As they expand up into the chromosphere, increasing electron temperatures and densities create an environment where ionization (and recombination) can proceed to strip electrons from these atoms until their charge states reflect the conditions in the corona ([46];[47];[48]). As the plasma expands out of the corona, eventually the electron density is low enough that collisional ionization and recombination cease. Charge states of the heavy ions become frozen-in and remain unchanged on their outward journey into the heliosphere ([49];[6]). While collisions with electrons and recombination cease, the weakly collisional solar wind still undergoes infrequent Coulomb collisions which act to thermalize the plasma, driving the temperatures of ions and protons to approach each other ([50]; [51]). It is important to differentiate between the electron temperatures that can be derived from heavy ion charge states observed in the solar wind, which reflect temperatures in the corona where freeze-in occurs, and kinetic temperatures of ions and protons which reflect the thermal spread of their velocity distributions. In this work we explore the kinetic temperatures of preferentially heated heavy ions.

Observations of temperature ratio variation in relation to the prevalence of Coulomb collisions can be traced back to determine temperatures of minor ions close to the Sun. By tracing this evolution from 1 AU back to within few R_s of the solar surface, one can determine the radial distance at which the effect of Coulomb thermalization supersedes that of any preferential heating mechanism. For a schematic of this process, wherein the expanding solar wind is divided into three radial zones: collisional zone, preferential heating zone, and relaxation zone, see Figure 3 in Kasper et al., [1], shown here in Fig. 1.2.

In the absence of direct observations of the dissipation mechanism responsible for coronal heating, the nonthermal signatures in the solar wind plasma can provide information about the dominant processes heating the corona. The solar wind emerging from the inner corona is highly nonthermal, as evidenced in observations of unequal temperatures across species, proton beams in proton velocity distribution functions, and large temperature anisotropies in protons and alpha particles by the Helios 1 and 2 spacecraft ([52];[53];[54]; [55]; [56]). In Figures 1.4 and 1.3 the bi-Maxwellian VDFs of alphas and protons are depicted, as well as their tendency to increase with speed and decrease with distance from the Sun.

These nonthermal features are either generated locally or remnants of processes that occurred closer to the Sun. Statistical studies have shown that the intensity and occurrence rate of these nonthermal properties are a function of the Coulomb collisions that occur as the solar wind propagates to the observing spacecraft, suggesting that Coulomb collisions thermalize the solar wind when their effects exceed any remaining preferential heating

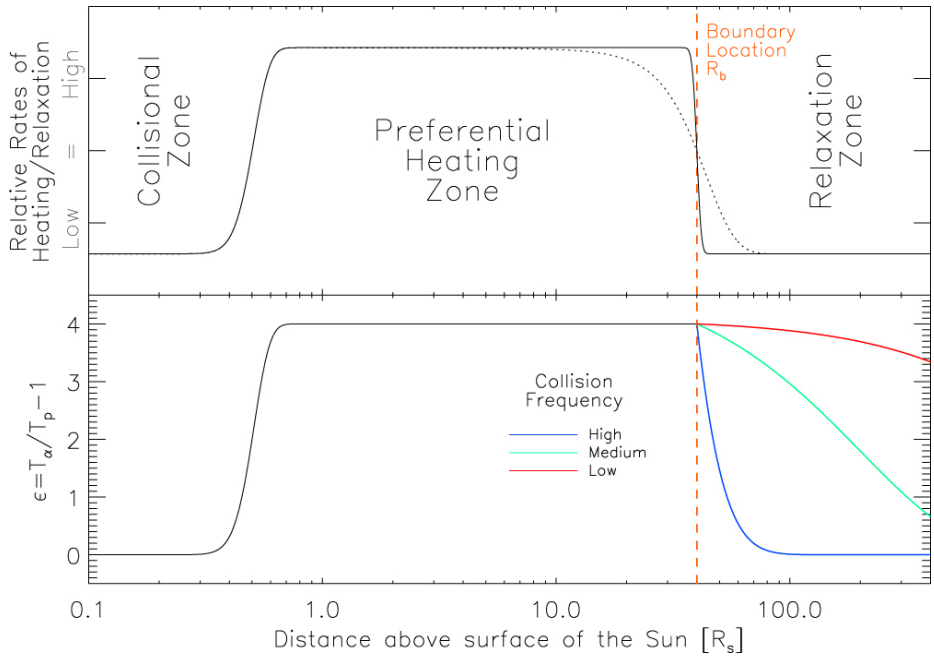

Figure 1.2 From Kasper 2017, Figure 3. Schematic of collisional, preferential heating, and Coulomb relaxation zones.

processes ([57];[58]).

Measurements of ion temperatures from the inner corona out to 1 AU reveal mass or supra-mass proportional temperatures across species. (e.g., [59];[60];[61]). Differential streaming between protons and minor ion species proportional to the Alfvén speed has been observed in the inner heliosphere ([33];[62]). At slow wind speeds and close to the Sun, differential streaming has a radial dependence, and alphas are decelerated relative to protons far from the Sun ([52];[63]). Such departures from local thermodynamic equilibrium are indicative of a preferential heating process potentially driven by differences in particle mass and charge. Verscharen et al. [64] demonstrated that the Alfvén and fast magnetosonic wave modes' instabilities are driven by differential alpha-proton speeds, as well as unequal temperatures and temperature anisotropies. Vetting out the actual relationship between temperature profiles and ion properties could aid in the identification of the predominant heating mechanism(s).

Given the collisional frequency between two species, Coulomb number, N_c is the estimated accumulation of Coulomb thermalization times as the plasma travels at the bulk speed from the Sun to the point of observation. A distinction must be made between calculations of Coulomb collisions using plasma conditions at 1 AU, referred to herein as N_c, and calculations taking into account the radial variation of the plasma kinetic properties, referred to as A_c. Using measurements from the Solar Wind Ion Composition Spectrometer

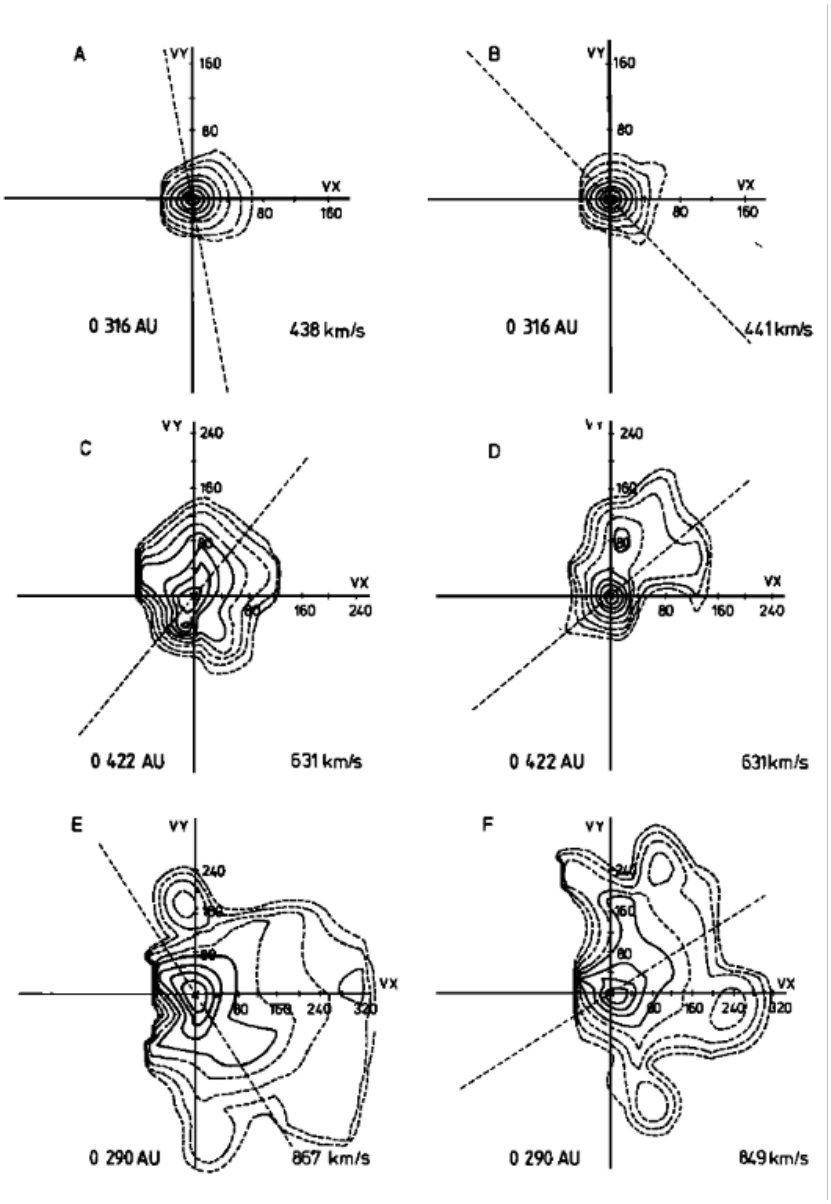

Figure 1.3 Alpha VDFs from Marsch et al., 1982a

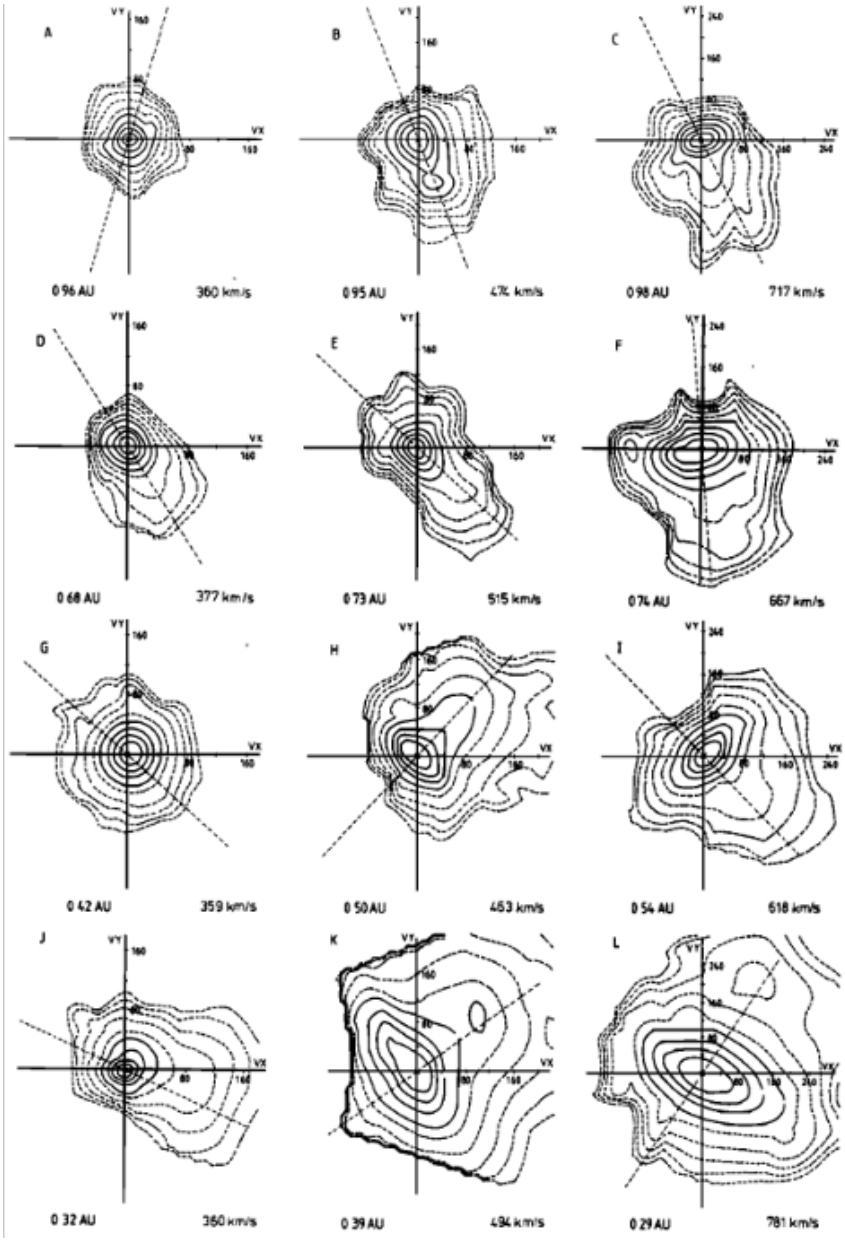

Figure 1.4 Proton VDFs from Marsch et al., 1982b

(SWICS) aboard the Advanced Composition Explorer (ACE), and following the aforementioned formalism, Tracy et al., [65] showed that the temperature ratios T_i/T_p of various species of minor ions to protons in the solar wind are well ordered by N_c, which can be expressed as follows,

$$N_c = \nu_{ip} * \frac{1(AU)}{U} \tag{1.1}$$

where ν_{ip} is the collisional frequency between some ion species i and protons p, and U is the solar wind bulk speed. Note here the use of the subscripts 'i' and 'p', which will be used throughout this thesis, and may differ from those used in referenced literature. Calculations of collisional frequencies of all possible species pairings detected by SWICS revealed that the most frequent and thus, most significant Coulomb interactions occur between ions and protons. Tracy et al. [60] extended their initial study to determine the mass dependency of the T_i/T_p for collisionally young solar wind, finding that $T_i/T_p \propto 4/3 * m_i/m_p$. Kasper et al. [1] developed and fit an analytical model of solar wind heating to Wind Solar Wind Experiment (SWE) measurements to determine the proposed radial boundary of the preferential heating zone (PHZ), determining that coronal heating is likely an ongoing process that extends to 20 - 40 R_s for He^{2+}. Kasper et al., [2] later compared the time evolution of their calculated radial boundary to yearly sunspot number averages that the preferential heating zone boundary varies with the solar cycle along with the Alfvén point with a correlation coefficient greater than 0.9.

1.5 Minor Ions and the Alfvénic Slow Wind

Work by D'amicis et al., ([37];[66]; [18]) have shown that speed alone does not give the full picture of the solar wind's origin at corona. Some slow speed wind exhibits features typical of fast wind, such as low, steady densities and O^{7+}/O^{6+}. Marsch et al., 1981 [67] identified a population of slow wind with qualities inconsistent with known of the slow wind. D'Amicis et al., 2015 and Antonucci et al., 2005 ([66];[28]) presented the first observational evidence of this secondary type of slow wind, originating from the edges of coronal holes, and bearing the same Alfvénic signatures, albeit reduced in amplitude, as fast wind.

Alfvénic slow wind possesses a strong v-B correlation despite slow streaming speeds. Alfvénic slow wind has high normalized cross-helicity, alignment between the magnetic and kinetic fluctuations resulting in a high normalized $\cos(\theta_{vB})$, and normalized residual energy (ratio of kinetic to magnetic energy fluctuations) close to one. This solar wind is

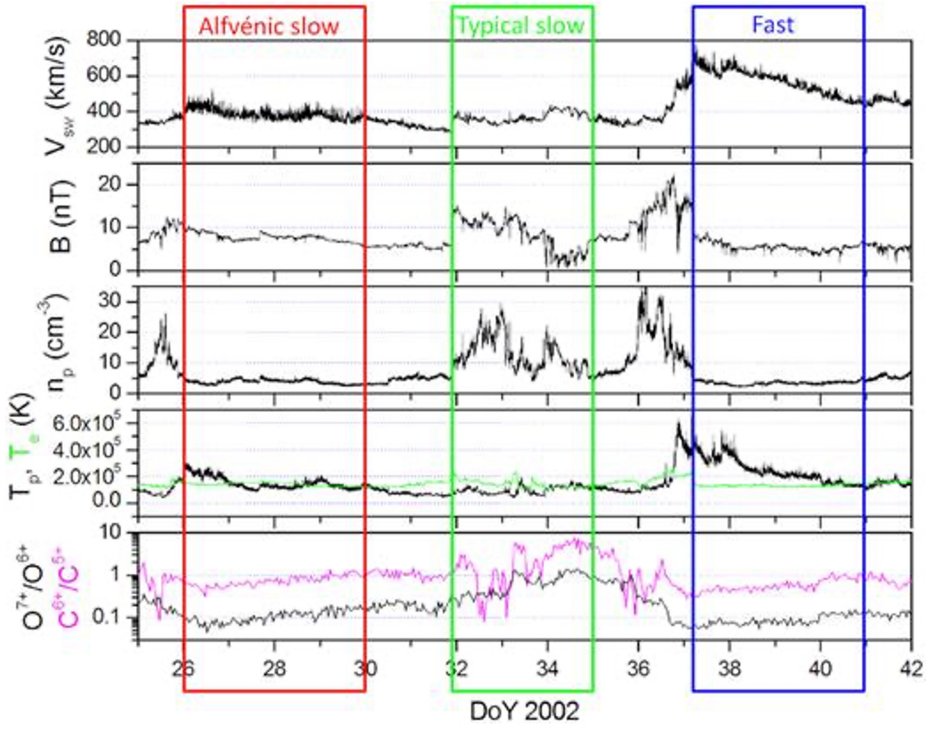

Figure 1.5 Example of Slow Alfvénic stream, as well as non-Alfvénic and fast, from D'Amicis et al., 2019.

more prevalent during solar maximum and can be observed out to 1 AU during this time ([68];[69];[70];[71]) An example of a slow-Alfvénic period from D'Amicis et al., 2019 is shown in Figure 1.5. Three time intervals are highlighted, depicting the differences between slow-Alfvénic, typical slow, and fast wind.

D'Amicis et al., [37] found that maximum of SC 23 was dominated by slow wind with high degrees of Alfvénicity, comparable to that found in the fast wind during solar minimum of the same cycle. Proton temperature is enhanced during slow Alfvénic periods, as well as minor ions. In a case study of Helios 2 data at different radial distances, they also show that Alfvénic correlations are degraded by fluctuations in density and magnetic field, rather than velocity.

Wind exhibiting Alfvénic characteristics tends to have low compressibility (constant density and velocity) ([72];[73]). Bruno and Bavassano, 1991 [74] define number density compressibility as the ratio of density fluctuations to the mean density, typically computed at 1-hour intervals. They define magnetic compressibility as ratio of the magnetic field magnitude fluctuations to the sum of the 1-hour averaged squared magnetic field components ([37];[74]). D'Amicis et al., 2011[37] find that cross-helicity and magnetic compressibility are anticorrelated, and no correlation between kinetic compressibility and Alfvénic

fluctuations.

Borovsky et al., 2019/2020 ([75];[76]) showed that there is a correlation between discontinuous jumps in ion composition (alpha to proton density ratios) and current sheet crossings, showing that the boundaries of magnetic flux tubes could also be boundaries for ion composition.

Fast and SA wind are characterized by higher power in magnetic and velocity field fluctuations, and a $1/f$ scaling at large scales, and either Kolmogrov (magnetic) or flat (velocity) scaling at higher frequencies, below the spectral break. Slow wind exhibits Kolmogrov scaling over entire scale range, typically ([77];[78]).

1.6 Radial Evolution of Ion Kinetics

As the solar wind expands into the heliosphere, it carries with it signatures from the solar surface, from within the ionization freeze-in point, and is subject to ongoing processes that both drive it out of and into thermodynamic equilibrium, with the latter tendency predominating as radial distance increases.

Overall, density and temperature decrease while velocity initially rapidly increases, then increases at a slower rate. Plasma beta increases as flow transitions from being driven by magnetic to dynamic pressure. Excess temperature between ions and differential streaming is reduced. Slow wind density and velocity are also subject to regions of compressibility. Transient events such as ICMEs, solar flares, and solar energetic particle events disrupt the "steady state" flow of the wind, injecting energy into the ambient flow and leading to composition and kinetics that vary from what is expected for ambient fast and slow wind.

Stream interactions occur when fast wind catches up to previously released slow wind. At this interface, slow wind temperatures rise and a compression region forms upstream from the interface (in the slow wind) while a rarefaction region forms downstream in the fast wind. This pressure gradient may steepen into a shock. If this interface persists for more than a Carrington rotation, the SIR is classified as a corotating interaction region, or CIR ([79];[80];[81]). As the SIR travels radially outward, the differences in temperature, pressure, and velocity grow [82].

Elliott et al., 2012 [83] examined the v-T profile at different radial distances, using data from various missions covering different time periods. They showed in previous work [84] that coronal hole-source wind may deviate from a simple linear relationship between temperature and velocity. Expounding on this, they show that deviations grow in the v-T profile with radial distance, and that, when separating compression and rarefaction regions, the distinction between the profiles of the respective regions begins to diverge at 0.5 AU,

and is largely distinct by 2.5 AU. This may mark the vicinity of half an AU as a distance at which solar wind flow transitions to being dynamically-dominated.

Perhaps the most well-known model of temperature evolution is that of adiabatic cooling, which describes the drop in temperature due to the spherical expansion of an ideal gas. In a collisionless plasma, the temperature anisotropies that arise due to the conservation of the magnetic moment in a weakening magnetic field must be taken into consideration. The slow solar wind has been observed to cool less rapidly than the adiabatic prediction in a collisional plasma. The fast wind deviates from the double adiabatic, decreasing slower than expected in the perpendicular direction, and more rapidly in the parallel direction ([52];[22]), with overall cooling (magnitude) slower than predictions. The double adiabatic prediction for temperature decay is:

$$T_\perp \propto \frac{B}{n^2}$$

in the fast wind, with $T_\parallel$ constant. The adiabatic prediction is:

$$T \propto r^{-4/3}$$

in the slow wind, due to isotropization from proton-proton Coulomb collisions [21].

Radial scaling laws have been estimated from observations of the solar wind kinetic moments from 0.3 to 1 AU. Using Helios data, Hellinger et al., 2011 [85] provided fits to fast wind densities, temperatures (parallel and perpendicular), magnetic field, and heat fluxes, from which they calculate parallel and perpendicular heating rates. Hellinger et al., 2013 [86] completes a similar analysis in the slow wind. Perrone et al., 2019 [87] compared the Hellinger fast wind result to reprocessed Helios observations of the core of the VDF for pure fast streams, finding slightly different scaling laws likely due to their method of selecting "unperturbed, coronal hole plasma", as well as determining the impact of proton-proton self-collisions. All of the aforementioned fits to Helios observations differ significantly from double adiabatic in the slow wind and adiabatic in the fast.

The radial evolution of density, temperature, and velocity will naturally give rise to changes in signatures of nonthermal behavior: temperature anisotropies, differential streaming, and excess heating of minor ions, as well as features not covered in this work, such as proton beams and the electron strahl. The preferential heating of ions, especially in the fast wind, in the direction perpendicular to the magnetic field is seen to be stronger close to the Sun, and diminish at larger distances. Instances of $T_\parallel > T_\perp$ increase in frequency as radial distance increases.

In 1970, Robbins et al. [88] first detected differential streaming when calculating al-

pha/proton density ratios, believing the 0.02 difference in streaming speeds to be a calculation error. Differential streaming in the slow wind has a radial dependence at low collisional ages and radial distances, as demonstrated in Neugebauer et al., 1998 and Mostafavi et al., 2022 ([89];[90];[63]). Comparisons of [63] with observations from Helios and Wind reveals that instances of protons streaming faster than alphas increases with radial distance. They actually show that WIND's 1 AU measurements exhibit a negative v_{ap} peak for slow solar wind, and a distinct double (positive and negative) peak in v $>$ 600 km/s. Johnson et al., 2024 [91] demonstrated that Coulomb collisional analysis can be used close to the sun to accurately predict differential streaming distributions at 1 AU.

Pre-SO, the Fast Imaging Plasma Spectrometer (FIPS) aboard MESSENGER had taken the closest solar wind composition measurements to the Sun [92]. These authors analyzed heavy ions up to 40 amu/e from March-December 2011, between 0.3 and 0.5 AU. They found that minor ion and proton velocities do not significantly differentiate until they reach speeds of about 450 km/s, above which differential streaming becomes significant. They also show alpha-to-proton temperature ratios of about 9. This is not in full agreement with latter work (i.e., [65];[60];[58];[1]), however FIPS took measurements much closer to the Sun, where temperature ratios could indeed be higher. They also show power law spectra spanning the inertial and dissipative ranges at different radial distances (ACE and MESSENGER locations). They observe (see Figure 1.6 from [92]) that the transition from inertial to the dissipative range evolves with radial distance, though the range of frequencies does not change significantly, due to their local gyrofrequencies, heavy ions receive more power through interactions with ion-cyclotron (IC) waves, enhanced compressibility near ion gyrofrequencies at 0.37 AU, and finally, no distinct jumps/discontinuities in the power spectra corresponding to the ion gyrofrequencies. Ions are interacting and receiving energy from magnetohydrodynamic (MHD) waves around 0.37 AU, and this interaction has diminished by 1 AU, establishing a clear mechanism through which minor ions could be preferentially heated through WPI with a q/m dependence. The authors posit that the lack of obvious jumps in the power spectra may be evidence that this heating could be a remnant of wave-particle interactions (WPI) that occurred closer to the Sun. This 0.37 location is not a hard barrier, but it demonstrates that the impacts of heating at or near the corona may still be significant at least to that distance.

1.7 Solar Wind Heating and Acceleration

Coronal heating theories must satisfy a number of observations, most of which expose the nonthermal nature of the solar wind in the inner heliosphere. Previously discussed

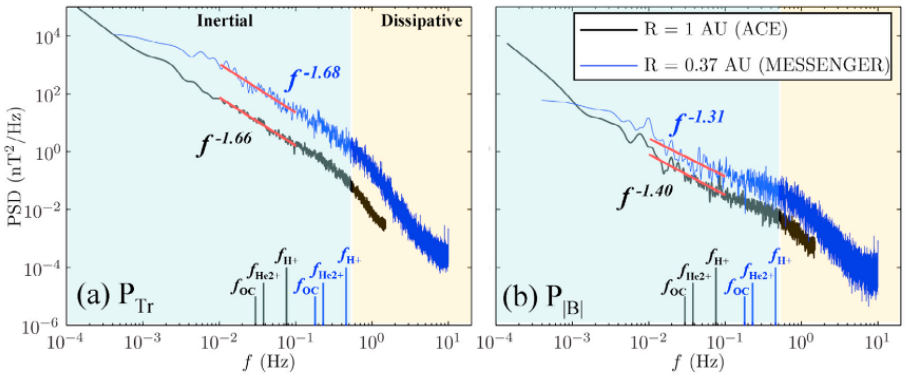

Figure 11. Representative high-resolution spectra for MESSENGER (in blue) and ACE (in black) during a time of coronal-hole-associated wind (ACE: 6 March 2011, 04:00:00–07:59:59 UTC; MESSENGER: 29 June 2011, 01:26:00–02:08:00 UTC). Power spectra are shown for (a) the trace of three-dimensional spectral density distributions of **B**, i.e. P_{Tr} and (b) fluctuations in the magnitude of **B**, i.e., $P_{|\mathbf{B}|}$. The local gyrofrequencies of key ions (H^+, He^{2+}, and $\langle OC \rangle$) are computed from average $|\mathbf{B}|$ values during this time period, ∼5 nT and ∼30 nT for ACE and MESSENGER, respectively.

Figure 1.6 Power spectra from Messenger and ACE, from Gershman et al., 2012

UVCS observations of emission lines in the corona reveal preferential heating of heavy ions [93] . The preferential heating is known to persist within 1 AU and even, though some thermalization has occurred, beyond 1 AU. Temperature anisotropies, with protons being preferentially heated in the direction perpendicular to the magnetic field, as well as ions under some conditions, must also be accounted for. Differential streaming is almost always bounded by the Alfvén velocity while temperature anisotropy is constrained by the mirror mode, ion-cyclotron, parallel-firehose, and oblique-firehose instabilities ([94]; [95];[96]). Magnetic switchbacks, which have been observed by spacecraft far from the Sun, but are frequently observed by PSP present another layer to the heat/energy generation mechanism(s) [97].

The two classes of heating theories that will briefly be discussed here are wave-particle interactions and reconnection-driven heating. In addition to these classes, other considerations, such as whether the heating source is local and ongoing or confined to the corona or inner heliosphere are necessary to the discussion. Finally, both classes of heating involve the transfer of energy to smaller and smaller scales. Thus, turbulent dissipation a key process in most heating theories, though they differ in the scale, or range of scales at which it becomes relevant.

Among the proposed heating theories is the generation of ion cyclotron waves by anisotropic dissipation of large-scale MHD waves perpendicular to the background magnetic field ([98];[99];[100]). Alfvén-Ion/cyclotron heating dependent on the 2nd-order Fermi process requires counter-propagating Alfvén waves, which to date have not been

detected by PSP, which has achieved perihelia as close as 10.4 solar radii. Perpendicular heating and proton-alpha drifts could also be driven by dissipation of high frequency Alfvén/ion cyclotron waves generated by plasma instabilities [101]. Stochastic heating, wherein fluctuations on the scale of ion gyroradii disturb ion orbits perpendicular to the magnetic field, leads to perpendicular kinetic energy diffusion ([102];[3]). While this list is not comprehensive (see [103];[15];[4] and the references listed therein for an overview of coronal heating models), the above theories identify signatures produced in plasma properties that are measurable and traceable.

Reconnection occurs in many processes/events throughout the heliosphere, such as solar flares, CMEs, CIRs, the heliospheric current sheet (HCS). The shuffling of magnetic field, open-coronal footpoints due to the Sun's differential rotation and tilt was proposed by ([104];[105]) as a means of transferring high-latitude magnetic field lines to low latitude, where they can reconnect with closed loops and generate the fast wind. Bale et al., [106] showed, using EUV observations from the Solar Dynamic Observatory (SDO), that reconnection generates the fast wind. Using PSP data, Raouafi et al., [107] showed that jets at the solar surface are generated by small-scale magnetic reconnection, releasing, heated, energized plasma, along with Alfvén waves into the corona. Their ubiquitous presence generates enough energy to heat and accelerate the fast solar wind, and the presence of the jets over closed loop regions indicates that they could possibly generate the slow wind.

1.8 Brief Description of HIS and SWICS

The primary instruments used in this work are the Solar Wind Ion Composition Spectrometer (SWICS) aboard the Advance Composition Explorer (ACE) and the Heavy Ion Sensor (HIS), part of the Solar Wind Analyzer (SWA) suite aboard Solar Orbiter (SO). Both are time-of-flight mass spectrometers that identify and characterize ions via triple coincidence measurements.

SWICS can only measure VDFs in the radial direction due to its limited field of view and the fact that it is a sun pointed spinner. Due to its wide field of view, HIS can measure full 3D minor ion VDFs, but only the radial direction is currently available. Please note that although SWICS and HIS are the same class of instrument and their general principle of operation is similar, they are not the same. The following is just a broad overview of the ion measurements.

For both HIS and SWICS, ions incident on the instrument's opening aperture pass through a selection voltage which only allows ions of a given E/q and are deflected through a specific angle. Prior to passing through the time-of-flight system, they are then acceler-

ated by 25 keV in order to have enough energy to be measured by the solid state detectors ([108];[109];[110];[9], [41];[111]). Please refer to Von Steiger et al., 2000 [9] for more detailed insight on how these measurements are made and converted to physical parameters.

The ion velocity vector is determined by angular information (HIS only) and the time it takes to pass through the time-of-flight system (triggering the start and stop). The selection of E/q, and measurements of time of flight and total energy allow quantification of an ions M, Q, and speed. [41] Refer to Shearer et al., 2014 [112] for a detailed description of the forward model and maximum likelihood method (MLM), which are used to identify and distinguish SWICS ions. This method is also used for HIS.

SWICS operates in two channels, the auxiliary and main channel. It passes through 64 logarithmically spaced energy windows with widths equal to 6.4% of the window center. The auxiliary channel, which measures protons and helium, ranges from 0.11 to 14 keV/e. The main channel, which measures ions with mass $\geq 4\ amu$, ranges from 0.45 to 60 keV/e, allowing for the detection of alphas with speeds ranging from 210 - 2400 km/s and low charge-state iron from 110 - 1280 km/s [113].

HIS measures minor ions within ranges from 0.5 keV/e to 78 keV/e, with E/q window widths of 8-9%, allowing for the detection of suprathermal ions as well as the solar wind's bulk composition. This energy range translates to speeds of 220 - 2700 km/s for alphas and 120 - 1460 km/s for low charge-state iron [41].

During a single timestep on each instrument, counts in each energy window are recorded for each identified ion. A full sweep of the energy windows builds a velocity distribution function for each detected ion, from which, the moments density, speed, temperature, and thermal velocity are calculated. This occurs at a 12-minute cadence for SWICS and a 30-second cadence for HIS (4 seconds in burst mode), though SWICS' published heavy ion data includes 1-hour and 2-hour averages of the twelve minute accumulations. SWICS proton data are available at the 12-minute cadence. HIS data is currently available at 10 minute time resolution.

Proton data are sourced from either the SWICS L2 proton or SWICS/SWEPAM Merged L3 proton data available online through the ACE Science Center. SWEPAM consists of two instruments, SWEPAM-I (for protons and alphas) and SWEPAM-E (for electrons). SWEPAM-I operates from 260 eV/q to 36 keV/q, with an energy resolution of 5% or 2.5%, and time resolution of 64 seconds [108]. These sources are available at 12-minute resolution and give similar results when run through Preferential Heating Zone boundary code.

Along with the composition data, magnetic field measurements are also needed to calculate measures of Alfvénicity in each solar wind regime. For this, the ACE Magnetometer (MAG) is used. ACE/MAG measures magnetic fields up to 6.5 x 10^{-4} nT at a rate of up to

24 samples/second [114]. The data provided via the ACE Science Center are at a 1-second cadence, averaged down for this work to either the 2-hour or 12-minute SWICS cadence.

Part of the SWA suite, the Proton and Alpha Sensor (PAS) is used in conjunction with the HIS composition data. PAS measures the full 3-D velocity distribution function of protons and alpha particles from 200 eV to 2 keV at up to a 4-second cadence in Normal Mode with an energy resolution of 5.5%. Data from the Solar Orbiter Archive are currently available at a 1-minute cadence. For this work, the PAS data are averaged down from its 1-minute cadence to match that of HIS [41].

Solar Orbiter Magnetometer (MAG) data are used alongside the HIS and PAS data. Magnetic field is measured at a much faster cadence than the composition data: up to 16 samples/second in Normal Mode and 128 samples/second in Burst Mode and measuring field strengths up to 5.8 x 10^{-4} nT. The data used in this work come from the Solar Orbiter Archive and are at a 1-second for SWA-MAG L2 data [115]., which is then averaged down to the 12-minute cadence.

1.9 Science Questions

In this thesis, we explore the heating of the solar wind through minor ion composition and plasma kinetics. Our main motivating questions are as follows:

1. What can minor ion measurements at 1 AU tell us about their heating and thermalization in the inner heliosphere?

   It has been shown that solar wind thermalization is well-ordered by collisional age, which can be used to determine conditions closer to the Sun. It is also known that minor ion composition is frozen-in close to the solar surface. There is evidence of both localized heating in the solar wind and heating that does not continue beyond the corona. Whether or not the location, or sphere of influence, of the heating source scales with ion properties (mass, q/m), is speed-dependent, or varies with the solar cycle can all provide insight into the dominant mechanisms. Does the location of the preferential heating zone depend on ion mass, q/m, or both? Does the distribution of minor ion excess temperatures at the boundary match or exceed non A_c-dependent observations? Do excess temperatures at the boundary agree with previous models based on stochastic heating?

2. How does the preferential heating and thermalization of slow Alfvénic ions differ from that of non-Alfvénic slow wind?

The slow Alfvénic wind is like the fast wind in composition and compressibility. PSP observations have shown that the solar wind is primarily Alfvénic close to the Sun. This would imply that there may be some processes, perhaps above the corona that differentiates non-Alfvénic wind from Alfvénic. Can comparisons of slow-Alfvénic and non-Alfvénic wind help to determine what processes generate the slow wind? Can differences in SA and SNA collisionality be attributed to differences in Alfvénicity rather than density? How do solar cycle variations differ between the two wind types?

3. How does heating and thermalization of heavy ions in the inner heliosphere vary with radial distance and connect to observations at 1 AU?

   How do Solar Orbiter measurements differ within/beyond the zone of preferential heating? How does model output differ? Do radial scaling laws match those found with previous spacecraft, and do minor ions obey the same scaling laws with the addition of mass proportionality?

1.10 Chapter Overview

The remainder of the dissertation will proceed as follows. Chapter 2 determines the radial extent of the preferential heating zone for heavy ions, as well as the radial dependence of that boundary and heating that occurs within. In chapter 3, the collisionality of Alfvénic and non-Alfvénic wind types are analyzed and compared. The preferential heating of the two types and radial dependencies of predicted R_b and observed excess temperature at the boundary are compared. Dependencies of preferential heating on solar cycle and Alfvénicity are also determined. Chapter 4 analyzes the radial evolution of heavy ion kinetics with Solar Orbiter Heavy Ion Sensor data and the relationship between spacecraft distance and PHZ boundary predictions. Findings are summarized and future work outlined in the concluding chapter (5).

CHAPTER 2

Preferential Heating Zone of Minor Ions

2.1 Introduction

The text of this Chapter is adapted from Holmes et al. [116], published in the Astrophysical Journal.

A plasma in thermodynamic equilibrium is expected to have equal temperatures and velocities across all its constituent species. Remote imaging of the solar atmosphere and inner corona as well as measurements at 1 AU reveal the highly nonthermal nature of the solar wind, with thermal in this context referring to the state of thermodynamic equilibrium, and thermalization, the processes driving the plasma toward thermodynamic equilibrium. Alpha particles and heavy ions (mass $>$ 4 amu) that are hotter than protons and electrons and differential streaming proportional to the Alfvén speed are indicative of dissipation mechanisms that preferentially heat some species more than others. Minor ion properties may be key in tracing preferential heating in the solar wind, and could potentially help to identify the combination of mechanisms heating the corona. The launch of Parker Solar Probe (PSP) in 2018 and Solar Orbiter (SO) in 2020 have provided the opportunity to compare theory/models to in-situ measurements of solar wind densities, velocities, and temperatures at unprecedented solar distances. The in-situ plasma instruments aboard both spacecraft provide a combination of proton and alpha measurements, with Solar Orbiter providing additional minor ion measurements ([38];[39];[40];[41]). These missions have and will continue to provide direct insight into key signatures of coronal heating and expansion. Measurements made by spacecraft at 1 AU, however, are still needed in combination with theory to predict and add context to data from PSP and SO.

As temperatures within the transition region of the solar atmosphere rise to 10^3 times higher than photospheric levels, the plasma remains highly collisional. Equal kinetic temperatures are maintained for ions and electrons in the inner corona up to about 0.3 solar radii (R_S) above the surface due to the frequent collisions that serve to thermalize the plasma

([42];[7];[43];[44]). Above the low corona, the frequency of ion-ion Coulomb collisions drops due to expansion driven by rising temperatures; consequently, electron collisions begin to dominate at larger radii. Differences in kinetic temperature between electrons, protons, and heavy ions are seen to develop and grow with distance from the Sun in the presence of some dissipative process that preferentially heats some species over others ([45];[4]). These differences may be due to the dependence of the heating processes on mass, charge, or a combination of both, thus making the study of heavy ions, with their multiple charge states, critical to unraveling the heating mechanisms in the solar corona and solar wind.

Heavy ions make up only a small fraction of the plasma in the corona and solar wind (< 0.1 %). Their varying mass and charge make them useful test particles for tracing physical processes in the plasma. Many of these heavy ions start off neutral in the photosphere. As they expand up into the chromosphere, increasing electron temperatures and densities create an environment where ionization (and recombination) can proceed to strip electrons from these atoms until their charge states reflect the conditions in the corona ([46];[47];[48]). As the plasma expands out of the corona, eventually the electron density is low enough that collisional ionization and recombination cease. Charge states of the heavy ions become frozen-in and remain unchanged on their outward journey into the heliosphere ([49];[6]). While ionization and recombination cease, the weakly collisional solar wind still undergoes infrequent Coulomb collisions which act to thermalize the plasma, driving the temperatures of ions and protons to approach each other ([50]; [51]). It is important to differentiate between the electron temperatures that can be derived from heavy ion charge states observed in the solar wind, which reflect temperatures in the corona where freeze-in occurs, and kinetic temperatures of ions and protons which reflect the thermal spread of their velocity distributions. In this work we explore the kinetic temperatures of preferentially heated heavy ions.

Observations of temperature ratio variation in relation to the prevalence of Coulomb collisions can be traced back to determine temperatures of minor ions close to the Sun. By tracing this evolution from 1 AU back to within few R_s of the solar surface, one can determine the radial distance at which the effect of Coulomb thermalization supersedes that of any preferential heating mechanism. For a schematic of this process, wherein the expanding solar wind is divided into three radial zones: collisional zone, preferential heating zone, and relaxation zone, see Figure 3 in Kasper et al. [1].

In the absence of direct observations of the dissipation mechanism responsible for coronal heating, the nonthermal signatures in the solar wind plasma can provide information about the dominant processes heating the corona. The solar wind emerging from the in-

ner corona is highly nonthermal, as evidenced in observations of unequal temperatures across species, proton beams in proton velocity distribution functions, and large temperature anisotropies in protons and alpha particles by the Helios 1 and 2 spacecraft ([53];[54]; [55]; [56]). These nonthermal features are either generated locally or remnants of processes that occurred closer to the Sun. Statistical studies have shown that the intensity and occurrence rate of these nonthermal properties are a function of the Coulomb collisions that occur as the solar wind propagates to the observing spacecraft, suggesting that Coulomb collisions thermalize the solar wind when their effects exceed any remaining preferential heating processes ([57];[58]).

Measurements of ion temperatures from the inner corona out to 1 AU reveal mass or supra-mass proportional temperatures across species. (e.g., [59];[60];[61]). Differential streaming between protons and minor ion species proportional to the Alfvén speed has been observed in the inner heliosphere ([33];[62]). Such departures from local thermodynamic equilibrium are indicative of a preferential heating process potentially driven by differences in particle mass and charge. Vetting out the actual relationship between temperature profiles and ion properties could aid in the identification of the predominant heating mechanism(s).

Among the proposed heating theories is the generation of ion cyclotron waves by anisotropic dissipation of large-scale MHD waves perpendicular to the background magnetic field ([98];[99];[100]). Perpendicular heating and proton-alpha drifts could also be driven by dissipation of high frequency Alfvén/ion cyclotron waves generated by plasma instabilities ([101]). Stochastic heating, wherein fluctuations on the scale of ion gyroradii disturb ion orbits perpendicular to the magnetic field, leads to perpendicular kinetic energy diffusion ([102];[3]). While this list is not comprehensive (see [103];[15];[4] and the references listed therein for an overview of coronal heating models), the above theories identify signatures produced in plasma properties that are measurable and traceable. This work is focused on evaluating wave-particle interaction driven heating mechanisms, which should impart dependencies on mass m or charge-to-mass ratio (q/m) in trends of unequal temperatures against kinetic properties and derived quantities.

Given the collisional frequency between two species, Coulomb number, N_c is the estimated accumulation of Coulomb thermalization times as the plasma travels at the bulk speed from the Sun to the point of observation. A distinction must be made between calculations of Coulomb collisions using plasma conditions at 1 AU, referred to herein as N_c, and calculations taking into account the radial variation of the plasma kinetic properties, referred to as A_c. Using measurements from the Solar Wind Ion Composition Spectrometer (SWICS) aboard the Advanced Composition Explorer (ACE), and following the aforementioned formalism, Tracy et al. [65] showed that the temperature ratios T_i/T_p of various

species of minor ions to protons in the solar wind are well ordered by N_c, which can be expressed as follows,

$$N_c = \nu_{ip} * \frac{1(AU)}{U} \tag{2.1}$$

where ν_{ip} is the collisional frequency between some ion species i and protons p, and U is the solar wind bulk speed. Note here the use of the subscripts 'i' and 'p', which will be used throughout this paper, and may differ from those used in referenced literature. Calculations of collisional frequencies of all possible species pairings detected by SWICS revealed that the most frequent and thus, most significant Coulomb interactions occur between ions and protons. Tracy et al. [60] extended their initial study to determine the mass dependency of the T_i/T_p for collisionally young solar wind, finding that $T_i/T_p \propto 4/3 m_i/m_p$. Kasper et al. [1] developed and fit an analytical model of solar wind heating to Wind Solar Wind Experiment (SWE) measurements to determine the proposed radial boundary of the preferential heating zone (PHZ), determining that coronal heating is likely an ongoing process that extends to 20 - 40 R_s for He^{2+} (α) ions . Kasper et al. [2] later compared the time evolution of their calculated radial boundary finding a correlation with average sunspot number and that the PHZ boundary varies with the solar cycle along with the Alfvén surface with a correlation coefficient greater than 0.9.

Here, the same procedure described in [1] is employed to find the outer boundary of the zone of preferential heating for minor ions. To gain insight on the heating sources that may be present, mass and charge per mass scaling relationships with various properties are explored. The remainder of the paper proceeds as follows: Section 2.2 gives a brief description of the dataset and adjustments made to the model, section 2.3 gives the radial boundary, and excess temperature decay profiles vs. collisional age for selected ions, and results, sources of error and next steps are discussed in sections 2.4 and 2.5, respectively.

2.2 Methodology

2.2.1 SWICS and SWEPAM Datasets

The Solar Wind Ion Composition Spectrometer (SWICS) aboard ACE uses a combination of time-of-flight, total energy, and energy-per-charge measurements to identify and characterize protons, alphas, and 102 heavy ions in the solar wind ([109];[110];[9]). This study uses the 2-hour averaged density, velocity, and thermal velocity derived from the velocity distribution functions of all heavy ions detected by the SWICS instrument. Proton measurements come from 12-minute SWICS/SWEPAM merged proton data product made

available through the ACE Science Center, and are averaged down to match the 2-hour resolution of the minor ion data. The datasets cover the period from August 1998 through January 2011 with interplanetary coronal mass ejections (ICMEs) removed.

2.2.2 Implementation of the Radial Boundary Model

The following is a brief summary of the theory behind and implementation of the radial boundary model for use with heavy ions. For an in-depth description, see [1]. The purpose of the derivation is to determine the evolution of excess temperature with collisional age. As such, the radial evolution of the equilibrium temperature excess, $\varepsilon = T_i/T_p - 1$ must be related to A_c, which, as previously stated, can be thought of as the radial accumulation of Coulomb collisional times. The model is based on several major assumptions about the preferential heating of ion species in the solar corona: that there is a zone of preferential heating in the corona, below which some unspecified heating processes dominate over thermalizing Coulomb collisions, resulting in nonthermal characteristics and preferential heating of heavy ion species relative to protons. This preferential ion heating brings each species to a particular value of ε. At the outer boundary, R_b, of this zone, where each species has a well defined temperature excess, ε_b, the cumulative effects of Coulomb collisions begin to surpass the contribution of the heating source, which may be localized or ongoing, resulting in a decay in excess temperature to some residual value, ε_r, observed at the spacecraft.

Beginning with the energy equation for each individual species, Kasper et al., [1] derives an expression for the radial evolution in excess temperature, assuming that while other heating processes may be ongoing, the preferential heating source cuts off at R_b, that the radial density of both species follows the same function, and that for all ion species the most significant Coulomb collisions occur between ions and protons, as determined by Tracy et al., [65]. These assumptions allow for cancellations and substitutions that allow $d\varepsilon/dr$ to be written in terms of Coulomb collisions, bulk speed, and ion to proton mass density ratio.

$$\frac{d\varepsilon}{dr} = -\varepsilon\Big[\frac{\nu_{ip}}{U} + \frac{\nu_{pi}}{U}(\varepsilon+1)\Big] = -\frac{\nu_{ip}}{U}\Big[\varepsilon(1+F) + \varepsilon^2 F\Big] \tag{2.2}$$

Here ν_{ip} is the ion to proton collisional frequency, ν_{pi} is the reversed interaction. Ions and protons are denoted by i and p, respectively. U is the solar wind bulk speed, and F the ion to proton mass density ratio. Coulomb collisions between two species are accounted for according to the expression derived in Hernandez et al., [117].

$$\nu_{ip} = 4\pi q_i^2 q_p^2 \frac{ln\Lambda n_p}{m_i \mu w_{ip}^3}, \tag{2.3}$$

defining a reduced mass ratio $\mu = m_i m_p/(m_i + m_p)$ and combined thermal speed $w_{ip}^3 = (2T_i/m_i + 2T_p/m_p)^{3/2}$. Using this frequency, a more rigorous expression for the accumulated effects of Coulomb thermalization compared to Eqn 1.1 accounting for the radial variation (A_c) in the plasma parameters can be derived. Note that [1] used $m_i = 4\ amu$ for alpha particle mass. This value is kept as a variable here to generalize to all minor ions. Aside from this, the equation shown below is identical to [1].

$$\int_{R_b}^{R_w} \frac{2}{m_i + 1} \frac{\left[1 + \frac{(\varepsilon+1)}{m_i}\right]^{3/2} d\varepsilon}{\varepsilon(1+F) + \varepsilon^2 F} = \frac{\tilde{\nu}_{ip}^w}{1 + 2\sigma - 1.5\delta} \frac{R_w}{U_w} \left[1 - \left(\frac{R_b}{R_w}\right)^{(-1-2\sigma+1.5\delta)}\right] \equiv -A_c, \tag{2.4}$$

where $\nu_{pi}/\nu_{ip} = n_i m_i / n_p m_p \equiv F$, and $\tilde{\nu}_{ip}^2$ is a reduced collisional frequency and all subscripts specific to α particles have been generalized to i. See [1] for the full expansion of the left side of the differential equation. Here δ and σ are fixed parameters accounting for the radial dependence of the ion temperature and velocity scaling, respectively. The scaling factors fall into a range reported by ([53];[85]). Kasper et al., [2] reports a linear relationship $\delta = 0.813 - 1.037\sigma$ between these values that minimizes RMS error between calculated values of the proposed boundary of preferential heating and the Alfvén point as well as $\delta = 2/3 - 4/3\sigma$ relation based on the collisional age equation. Variation of δ and σ within observed ranges and along these lines did not result in significantly different R_b or trends in mass ratio and q/m. Values of $\delta = 0.814$ and $\sigma = -.05$ are used here for consistency with previous work. Eqn 2.4 is fitted to the observed decay in ε with A_c to determine the best-fit values of R_b, ε_b, and ε_r.

2.2.3 Data Selection

Of the 103 ions characterized by SWICS, analysis for the following are included in this paper: He^{2+}, $C^{4\text{-}6+}$, $O^{5\text{-}8+}$, $Ne^{8\text{-}9+}$, $Mg^{6\text{-}12+}$, $Si^{6\text{-}12+}$, and $Fe^{9\text{-}13+}$. Density, speed, and thermal speed, calculated from moments of each ion's velocity distribution function, are used at each valid 2-hour timestep to determine excess temperature and collisional frequency. The number of valid data points at all solar wind bulk speeds varies between about 40,000 - 50,000 for the most abundant ions. This work was completed in two speed ranges: over all solar wind speeds and on $v < 500$ km s^{-1}. The exclusion of solar wind speeds above 500 km s^{-1} to focus on collisional slow wind yields a broader range of A_C values (c.f. Fig 2 in

[1]), but also reduces the dataset number by about 10,000 timesteps.

The binning routine employed here excludes bins in A_c that do not contain enough data points, or that those with an irregular distribution of data. This requirement only excludes the highest and lowest A_c bins for all ions, so though the curves might be truncated, there is no need for any interpolation within endpoints. Nearly all of the ions are skewed toward low A_c, leading to sparsely populated bins at high A_c and increasing uncertainty at the tail end of the decay curve. In some cases, this limits the model's ability to converge on a fit; these ions are considered nonviable and are not used in this study.

2.3 Minor Ion Temperature Profiles

The outer boundary of the PHZ for a given ion is determined by fitting the modeled temperature decay profile to the observed excess temperature when binned by collisional age via reduction of the χ^2/dof statistic. Excess temperature decay profiles and model fits calculated for selected ions from the SWICS dataset at all solar wind speeds are shown in Fig 2.1. The contents of Fig 2.2 are the same aside from the solar wind bulk speed, which is limited to all speeds below 500 km s^{-1}. In these figures, the black diamonds represent excess temperature calculated and binned from SWICS data, where temperatures were derived in the manner described by Shearer et al., [112]. The gray, vertical crosshairs represent the 1-σ uncertainty in ε for individual bins, while the horizontal are representative of the overall average of the uncertainties in A_c. The red curves depict the modeled decay, and the total number of binned data points is denoted by Npts. Free parameters R_b, boundary ε_b, and residual ε_r are printed on each plot, though in keeping with the convention introduced in [1], ε_1 denotes residual excess temperature (ε_r) and ε_0 denotes the difference between the boundary and residual excess ($\varepsilon_b - \varepsilon_r$).

The left sides of Figures 2.1a - 2.1f and 2.2a - 2.2f represent collisionally young solar wind, and the right sides, collisionally old wind. Limiting solar wind speeds to below 500 km s^{-1} causes the modeled and observed curves to shift to slightly higher A_c, as the observed data in each bin has a higher concentration of collisionally old wind. This is consistent with known properties of the slow and fast wind. Though profiles for only six ions are shown in this paper, the shift is present in all the curves analyzed. Nearly every ion also exhibits slightly lower ε values at low A_c under the slow wind limit, likely due to either preferential heating being more prevalent in the fast wind than the slow, or truncation the lowest A_c wind. Although these trends are consistent, for most ions, they are small enough to fall within the error margins for both ε and A_c.

A "bump" that occurs at low A_c in some ions, as reported by ([65];[60]), does not appear

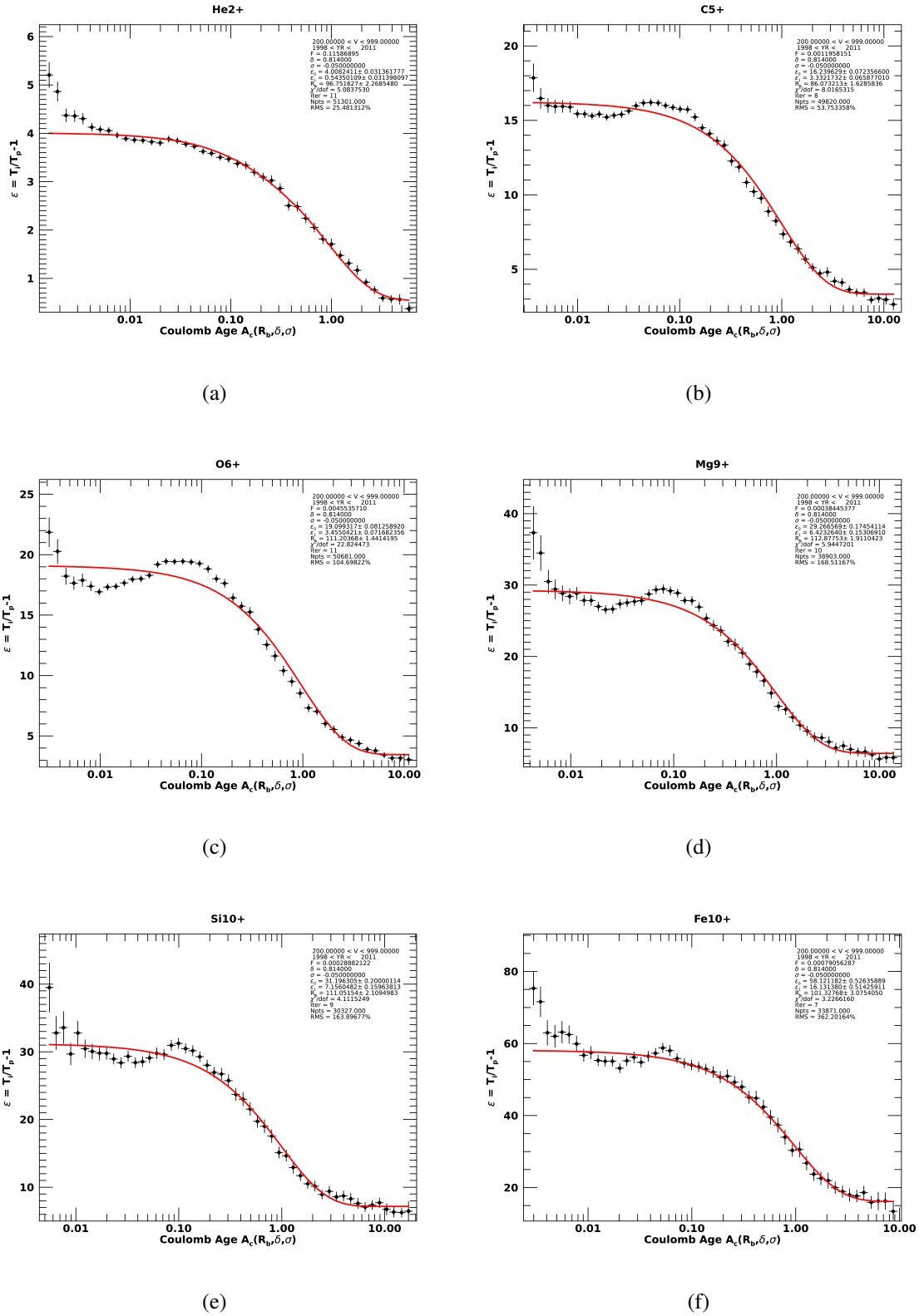

(a) (b)

(c) (d)

(e) (f)

Figure 2.1 Excess temperature vs. collisional age for six selected ions at all solar wind speeds. Black diamonds are observed excess temperature, while red lines are model fits. Faint grey lines signify error based on variance within each bin.

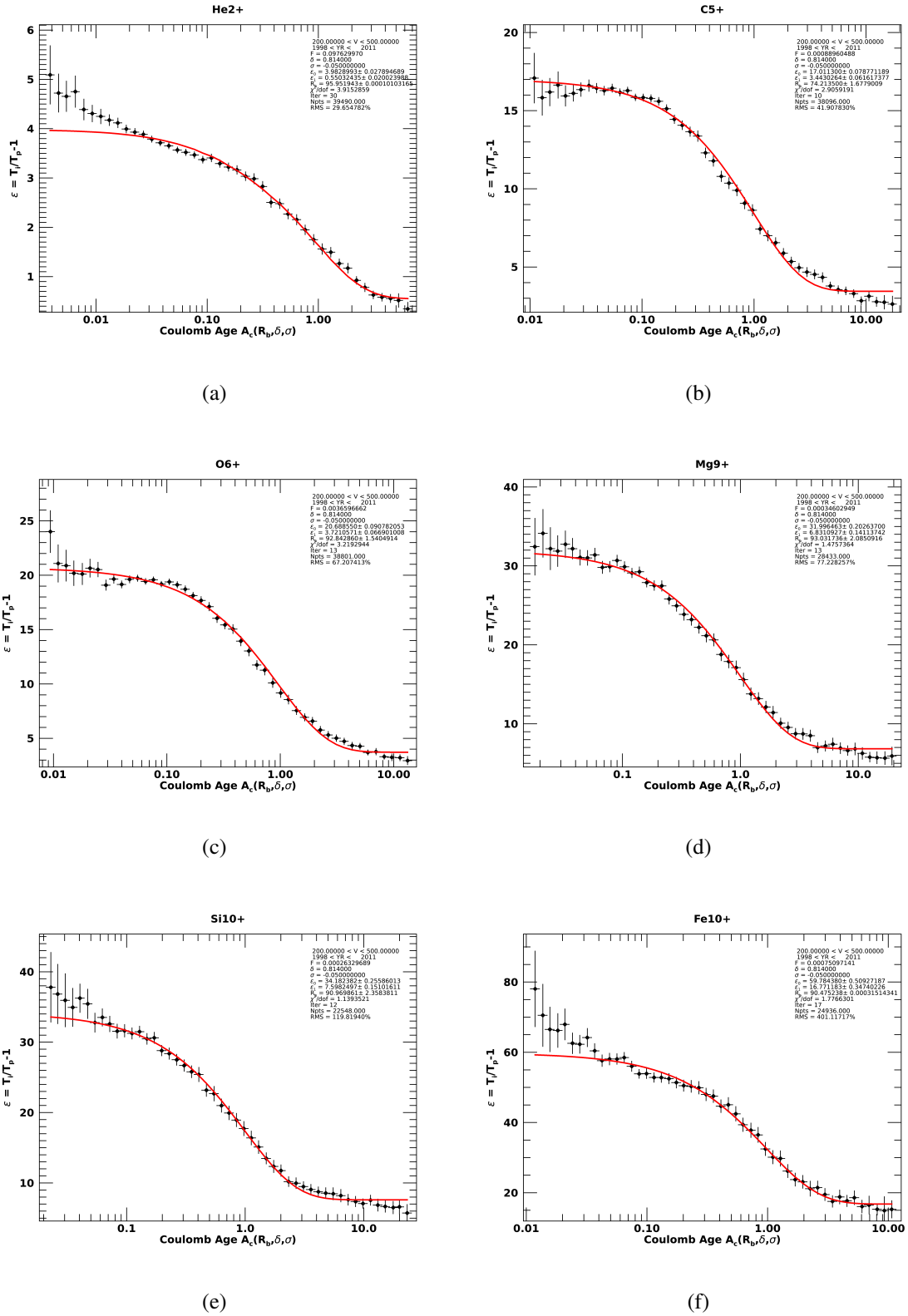

Figure 2.2 Excess temperature vs. collisional age for six selected ions for solar wind speeds below 500 km s^{-1}.

to be present when excluding solar wind speeds above 500 km s^{-1}. This is evident when comparing 2.1d with 2.2d, 2.1e with 2.2e, and 2.1f with 2.2f. The bump is a clear deviation from the expected exponential decay profile, and its occurrence in collisionally young wind may impact both predictions of the radial boundary and excess temperature at the boundary. For every analyzed ion, the bump begins around $A_c = .01$ and peaks at about $A_c = 0.1$. All or the majority of this range, $.01 \leq A_c \leq 0.1$, is present in the observed range for all ions in this study, regardless of the slow wind limit. This indicates that the flattening of the bump is not due to the truncation of collisionally young wind, but rather the removal of a subset of the wind with properties that may be independent of collisional age, the collisionless fast wind. Currently, the model does not account for this feature, but is still capable of reproducing observed boundary and residual excess temperature values (bins farthest to the left and right along the curve), and to an extent the shape of the relaxation curve at high Ac.

Ideally, fully thermalized, collisionally old solar wind would reach an asymptotic $\varepsilon \sim 0$. Previous work indicates the existence of a nonzero, residual excess temperature at high A_c corresponding to larger radial distances from the sun ([58];[1];[60]). For most cases in this work, the modeled relaxation curve appears to level out by $A_c \sim 10$, while the excess observed excess temperature bins still exhibit a marked decrease, albeit less shallow reduction than at intermediate A_c. Most minor ions in this study never achieve excess temperature values < 1, and that residual increases with increasing mass and charge per mass, as can be seen in the right panels of Fig 2.4 and 2.5.

Regardless of solar wind speed, the R_b predictions here extend to a much broader range than the results of [1]. χ^2/dof and rms values tend to be higher and more variable than what was found for alpha particles using WIND/SWE data. R_b for alpha particles lies at about $96\ R_s$ and heavier ions extend to even greater radial distance according to a weak charge-to-mass and mass-scaling. That the α-particle R_b reported here is above the upper limit may be explained by differences in implementation: velocity range, $sigma$ and $delta$ variables, and also by inherent differences between the SWICS and SWE datasets. This model is sensitive to time resolution of the data, SWICS and SWE are known to report different proton densities. The years included in these studies are different, comprised of varying proportions of solar cycles 22 (WIND only), 23, and 24. Accordingly, R_b values reported here for minor ions using the SWICS dataset can be taken as an upper limit on the preferential heating zone boundary, rather than an exact prediction.

R_b vs. charge-to-mass ratio, R_b vs. mass, and R_B vs. charge-squared-to-mass ratio appear in Figs. 2.3a, 2.3b and 2.3c, respectively. In Figs. 2.3a and 2.3b, the colors are associated with different elemental species, while in Fig. 2.3c, shades of blue correspond

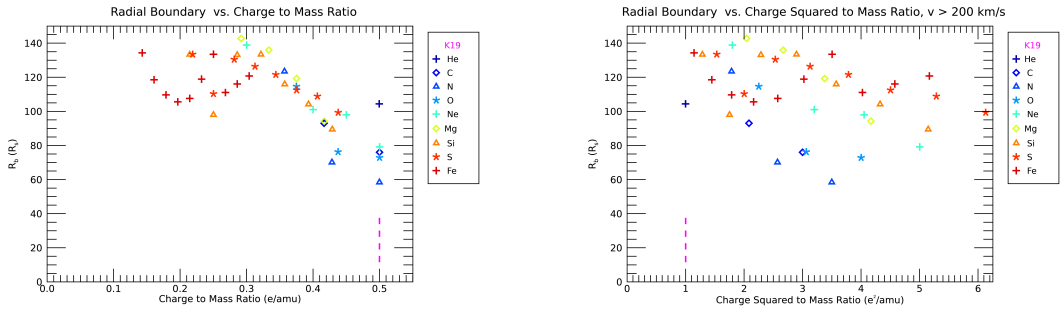

(a) (b)

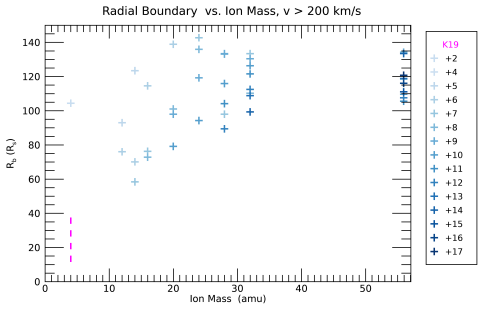

(c)

Figure 2.3 The top left panel shows R_b dependence on charge to mass ratio . The top right shows the R_b-charge squared to mass dependence, and the bottom panel is mass ratio (m_i/m_p) . All panels in this figure refer only to $v < 500$ km s^{-1}. The pink dashed lines represent the R_b range predicted by [1] and [2] at the charge to mass ratio of alphas (0.5)

Wind Type	r^2 (Rb vs. m)	r^2 (R_b vs. q/m)	r^2 (R_b vs. q^2/m)	cc (ε_b vs. m)	cc (ε_r vs. m)	cc (ε_b vs. q/m)	cc (ε_r vs. q/m)
All Speeds	0.27	0.45	0.07	0.92	0.86	-0.64	-0.80
v < 500 km/s	0.29	0.34	0.02	0.96	0.84	0.69	0.81

Table 2.1 For all solar wind speeds, r^2 values and correlation coefficients for all species are depicted in the top row. Charge states of C, N, O, Ne, Mg, Si, S, and Fe are calculated separately for q/m and q^2/m dependencies.

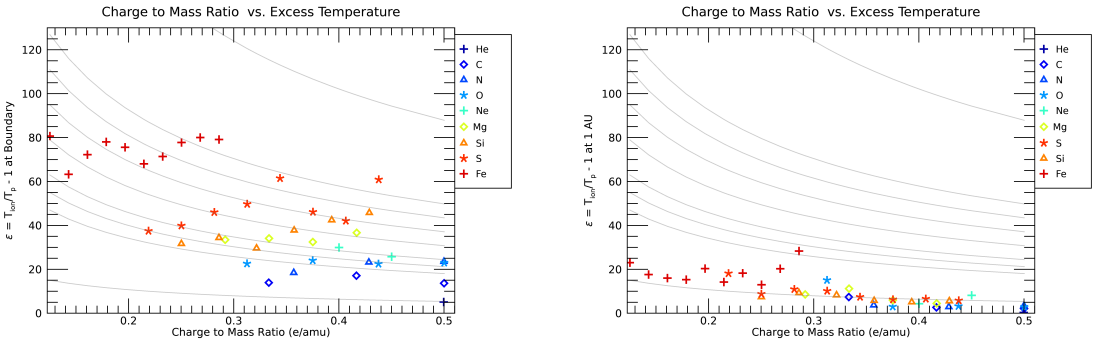

(a) (b)

Figure 2.4 Excess temperature vs. charge to mass ratio at the radial PHZ boundary and at ACE. Grey lines denote the Chandran et al. [3] prediction for each mass. The bottom curve is for 4 amu, then 12 amu, 14 amu, etc.

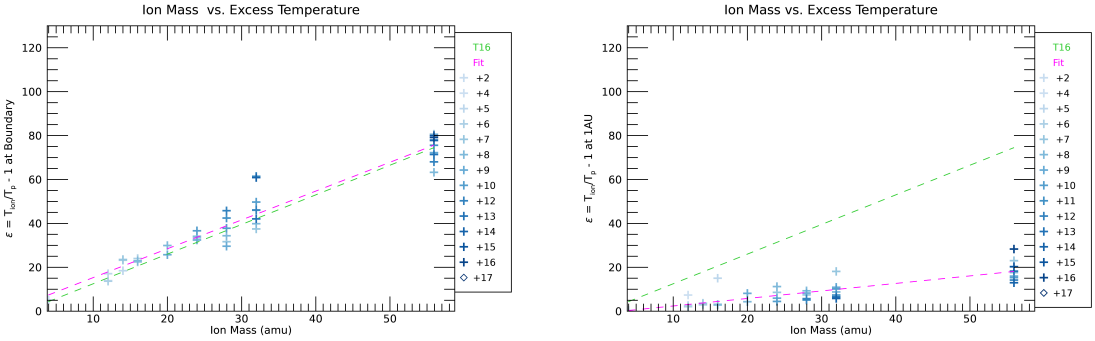

(a) (b)

Figure 2.5 Excess temperature vs. mass ratio calculated at preferential heating boundary and 1 AU.

to charge state. The pink dashed line indicates the range of R_b found in [1] and [2] for alpha particles. These plots show results for speeds below 500 km/s. Table 2.1 shows the r^2 correlations for all ions as well as correlation coefficients of the trends in observed boundary and residual excess temperature. The top row includes all speeds while the second row only shows wind speeds below 500 km s^{-1}. Though there is a visible relationship between ion mass and R_b, the r^2 correlation is only 0.27 for slow speeds, while correlation coefficient of ε_b and ion mass is high. Aside from R_b vs. q/m, correlation coefficients and r^2 are quite similar between the two wind types. Correlation coefficients of ε_b with ion mass and q/m are both higher in the slow wind. High charge-squared-to-mass ratio and high ion masses produce the highest radial boundary values. The strongest relationship is with mass, and Fig. 2.3c demonstrates that for a given element, R_b tends to increase with increasing charge state in the heaviest ions, and decrease with charge state in lower mass ions, such as N, C, O. The charge-to-mass and charge-squared-to-mass ratio plots show that, with some deviations, some species fall along lines with unique slopes. These relationships may be explored further in future work.

The scaling in excess temperature with mass is compared to a model of stochastic heating in the corona and inner heliosphere. When counter-propagating, low frequency, high amplitude Alfvén waves with wavelengths similar to ion gyroradii cause fluctuations in the electric and magnetic field randomized ion motions are incited in the plane perpendicular to the magnetic field. Diffusion of this kinetic energy leads to perpendicular heating ([102];[3]). Chandran et al., 2010 [118] models coronal perpendicular temperatures as

$$T_{\perp i} \propto A\left(\frac{A}{Z}\right)^{l} \tag{2.5}$$

where

$$l = \frac{2a}{1-a} \tag{2.6}$$

Here, a is a constant related to the velocity power spectrum of the turbulence and taken to be 1/4 in this case. Proportionality constants of 0.71 for protons and 1.0 for ions were used by Chandran et al., 2010 [118]. Ion mass and charge are A and Z, respectively. It must be noted that the Chandran 2010 model focuses on $r < 15\ R_s$, and the scaling factor found therein was chosen to match observed perpendicular temperature ratios in the corona. Here, .71 is not used and the scaling factor is left as a free parameter.

Fig 2.4 displays the excess temperature vs charge to mass ratio at ACE, along with predictions of the trend in temperature anisotropy for various masses made by the stochastic heating model presented in [118]. Figures 2.4a and 2.5a show the predictions at the boundary, and Figures 2.4b and 2.5b show conditions at 1 AU. The symbols in Figures 2.4a and

2.4b represent each ion in this study, with colors corresponding to ion mass and all charge states for a given mass shown in the same color. The faint gray lines are predictions of the ε curve with q/m at each of the masses used in this study, using the equations described above from the [118] model. Ions of the same species would be expected to fall along the gray line that corresponds to their mass. At the PHZ boundary (fig. 2.4a), only helium, carbon, and a few heavier ions with charge-to-mass approaching 0.5 fall near their mass lines (first from the bottom for alphas, second from bottom for Carbon, third from bottom for Nitrogen, etc). Ions of some other elements compare much less favorably with the predictions. In the extreme case, for Fe ions (red stars), the lowest charge states fall between the mass 20 and mass 24 line (rather than 56) but follow a similar trend with q/m. The higher charge states follow an opposite trend with q/m, crossing several mass lines. Because no directional distinction is made for the observed SWICS ion temperatures, their distribution and evolution are not due purely to a perpendicular heating source. It is known that alpha perpendicular temperatures decay more rapidly than parallel as radial distance from the Sun increases [52]. The flatter observed excess temperature curves for each species could be reflective of a reduced decay rate due to the presence of parallel temperatures. At 1 AU, none of the ions land very near to the curve corresponding to their mass, though a trend with q/m ratio does remain. Here, in both the PHZ boundary (2.4a) and the 1 AU (2.4b) cases, ε has a charge state dependence, though that dependence is less distinct for thermalized wind at 1 AU.

Fig 2.5 shows the relationship between ε values and ion-to-proton mass ratio (m_i/m_p) at the preferential heating boundary and at 1 AU. Here the symbols represent each ion, but the color gradient corresponds to different charge states, with lowest charge states marked in lightest blue and highest charge states darkest. Ions of the same element appear in columns. The excess temperatures shown here are in good agreement with the $T_i/T_p \sim 4/3 * m_i/m_p$ found in [60], depicted in Figures 2.5a and 2.5b with the green dashed line. The pink dashed line corresponds to the linear fit of the modeled ε values. The slight divergence in slopes at the highest ion masses are well within the uncertainty in ε_r and ε_b found by the model. The difference in slopes in figure 2.5b is expected, as the excess temperature values depicted by the symbols here are the model's prediction of residual excess temperature. When considering the evolution of ε for all ions with A_c, figure 2.5b is representative of a cross-cut of those ratios taken at high A_c and by extension, high radial distance. The model's ability to reproduce observed ε for minor ions at the low collisional ages associated with PHZ boundary may lend some credence to its predictions of the boundary itself. Direct observation of ε_b at the predicted R_b will help to verify the trends predicted in previous work and in this paper.

2.4 Discussion

Using the SWICS data set, it has been shown here that the heating model from [1] predicts a mass-dependent outer radial boundary of the preferential heating zone, though with significantly higher uncertainty than it does for alphas measured by Wind/SWE. There are a number of potential causes for this.

Observed excess temperature (ε) could decay with collisional age (A_c) in a manner that differs too greatly from the modeled exponential decay for some ions. Tracy et al., [65] and [60] found that many of the most abundant minor ions exhibit a bump in their temperature decay vs. collisional age profiles at low A_c. The low number density of the minor ions coupled with high ion mass lead to a lower collisional frequency and thus a higher concentration of data at low A_c and sparse data at high A_c when compared to what is observed for alpha particles in [1]. As such, the data fed into the model from 1 AU might not yield high enough A_c to capture the full decay curve or some ions. The values used for the residual excess temperature free parameter are between 0.5 for He^{2+} and 30 for Fe ions, much higher than the $.2 - .3$ detected by Wind/SWE. These high residuals could have a major impact on the predicted R_b values, which are calculated assuming full thermalization at 1 AU.

It could be that some minor ions are not fully thermalized by the time they have reached 1 AU, reflected in the remaining mass-dependence observed in residual excess temperatures. The ion heating model, which assumes full thermalization would then predict R_b using a truncated dataset. Additionally, this model assumes an unspecified preferential heating source that cuts off at the outer boundary. Such an assumption does not preclude the presence of some other, ongoing heating source. One must also consider how the results vary due to differing measurement techniques between HIS/SWICS and WIND/SWE.

Due to differences in the size of the SWICS and SWE datasets, this analysis could not be completed in 25 km s^{-1} windows as was done in Kasper 2017. Instead, the model was run on all solar wind speeds and again with 500 km s^{-1} as the upper limit. The exclusion of solar wind speeds higher than 500 km s^{-1} did reduce the overall available events to be binned by about 10,000. This reduced amount only impacted the quality of observed data for the least abundant ions. The exclusion of the fast wind, as expected, shifted the observed and model ε decay curves to higher collisional ages and higher temperature ratios. In most cases, calculated R_b were lowered by $1 - 30\ R_s$. The magnitude of this reduction had no apparent dependence on ion properties. The bump feature in the relaxation curve either became present or more prominent when wind speeds greater than 500 km s^{-1} were included, which significantly impacted reported χ^2/dof values.

Though the $\chi^2/dof < 2$ found by [1] was not achieved by all the ions included in this study, ε decay curves for alphas were fitted with $\chi^2/dof \sim 3.9$. in slow wind and $\chi^2/dof \sim 5.1$ in all speeds wind. χ^2/dof values of below about 5 were found for more abundant ions with a few exceptions, indicating that the model may not be capturing aspects of the temperature ratio decay for some heavy ions. The model either did not converge or resulted in poor fits with very high χ^2/dof values for less abundant ions, as is the case with C^{4+}. Among the abundant ions, there are still deviations from monotonic exponential decay, such as the bump feature seen at lower A_c in O^{6+} and Mg^{9+} in Fig 2.1c and 2.1d. The bump is either significantly reduced or not present when considering wind below 500 km s^{-1} , and though the inclusion of higher speeds does increase both predicted R_b and χ^2/dof, it does not significantly effect overall trends in R_b vs. ion mass and charge-to-mass. Note also slight steepening of the curve at the highest and lowest A_c values for some of the ions, such as C^{6+}. Less abundant ions such as C^{4+}, O^{5+}, Ne^{9+}, and Mg^{6+} all have ε curves that deviate significantly from expected exponential decay, likely driving the uncertainty. The standard deviation in each bin of observed ε is also much higher than what is found in the more abundant ions.

The right panels of Figs 2.4 and 2.5 reveal that at 1 AU none of the ions included in this study completely relax to the residual values found in [2]. In fact, there is a clear relationship between ε_r and charge to mass ratio as well as ε_r and m_i/m_p, which may partially be an instrumental effect. As SWICS steps through higher energy per charge, $(E/q)_{i+1} = (1+\rho_i)(E/q)_i$ deflection voltage windows on the entrance system (here ρ is a step-dependent growth factor and i signifies an E/q step), the gaps between the window centers grow ([109];[112]). Ions with higher m/q (or lower q/m for the sake of consistency with the rest of the paper) are measured in higher energy windows. Figure 2.6a depicts the range of energy windows that would be used to measure typical ion speeds, 200 - 800 km/s. The two ions shown, He^{2+} and Fe^{8+} represent the high and low end of the range of q/m detected by SWICS, respectively. Note that this is not the full range, as protons are detected in a different channel from the heavy ions, and lower charge states of iron are far less common than Fe^{8+}. Due to the logarithmic spacing of the E/q steps, the lower E/q values are closer together than the higher E/q values, which in turn implies that resolution of the VDF width varies across the energy per charge scan. This variation creates uncertainty in the widths of the distributions in both E/q and m/q, with the lower m/q (or higher q/m) ions having lower uncertainty. The thermal spread of the distributions in E/q, with wider thermal widths having less uncertainty than narrow, propagates through as temperature is determined from the second moment of each ion's VDF. It may be that this uncertainty is on order of ε_r, and calculations of excess temperature for fully or nearly thermalized minor

ions are not possible with the SWICS instrument.

In order to quantify the effects of the gaps between the logarithmically spaced energy windows sampled by the SWICS instrument, an idealized, continuous VDF was compared to one built from SWICS' energy window centers. The continuous VDFs were assigned varying ion speed peaks and thermal widths. The centers chosen for this were 400, 600, 800, and 1000 km s^{-1} and the thermal speeds were 60, 120, and 180, km s^{-1} . These parameters were then used to model a VDF from SWICS' noncontinuous sampling, and the recovered moments were calculated. The recovered thermal speeds were then compared to the input, shown in Fig 2.6b. This was completed for alphas and Fe^{8+} to look at the effects on a broad range in charge-to-mass ratios. The same was done for Fe^{8+} to show the full range in recovered v_{th}. Keep in mind that high q/m ions like alphas are measured in lower E/q windows, while low q/m ions like Fe^{8+} are measured in high. Alphas and Fe^{8+} traveling at the same speed would be measured in two very different E/q windows, and low q/m ions are measured over a much broader range of E/q. At low speeds, or in lower energy windows, the ratio between recovered v_{th} and input v_{th} remains close to one, but for higher energy windows, which would be used to sample lower q/m ions, this ratio increases, becoming higher at lower thermal speeds than it was for alphas. Of the thermal widths and ion speeds used here, the lowest $v_{th,rec}/v_{th}$ is about 1.005, and the highest is 1.11, with a clear energy dependence. The high estimates, however, are only achieved by using non-physical values in the solar wind (very fast and very cold). As such, the highest error likely to be introduced in real solar wind is about 5%. This is not enough to fully account for the highest residuals seen in the SWICS data.

2.5 Conclusions

The results shown here demonstrate that the PHZ boundary model from [1] can be applied SWICS 2-hour data to provide an upper limit on the boundary of preferential heating for minor ions. Although the R_b values are somewhat higher than expected, the more abundant ions have produced results qualitatively consistent with heating theories. Comparison with a model of stochastic heating highlights the charge-dependent stratification of temperatures within each species. The high R_b and high ε_r are likely tied to each other, and depending on their cause, could also be driving up χ^2/dof values. Recent work by Johnson et al. [119] has shown, using PSP and Wind data, that the preferential heating of alpha particles persists up to about 0.27 AU, beyond which Coulomb collisions provide the dominant thermalizing effect. While this is lower than the alpha particle result shown here with SWICS data, it is within the range of SWICS R_b predictions for ions with a q/m of about

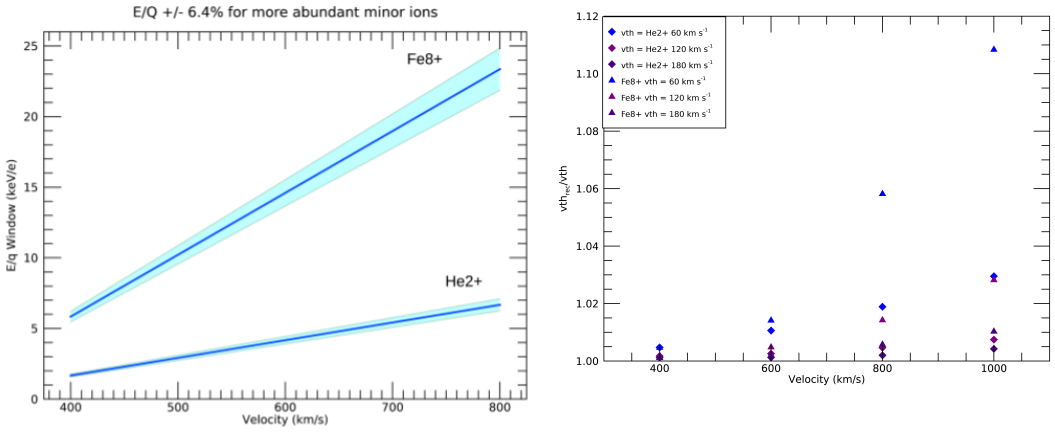

(a) (b)

Figure 2.6 Panel (a) is a visualization of the full range in energy-per-charge associated with typical solar wind velocities for high q/m alphas and low q/m Fe^{8}+ ions. Panel (b) is the ratio of recovered vs. input thermal speeds from idealized, continuous sampling vs. logarithmically spaced energy windows.

0.5. Further analysis is needed to determine the impact of the 2-hour vs. 12-minute cadence on the model predictions. Direct measurements of temperature ratios from the Heavy Ion Spectrometer aboard Solar Orbiter will be able to verify predictions for heavy ions with predicted $R_b > 60\ R_s$ [41].

This subset of the SWICS dataset does exhibit boundary dependencies on the associated ion properties, which could be an indication that the heating mechanism is indeed tied to ion gyrofrequencies and dependent on q/m. Again, verification of the higher R_b values predicted here will aid in discerning this.

We have quantified the effects of ACE/SWICS E/q stepping when compared to an idealized, continuously sampling instrument. The uncertainty introduced by this is only about 5%, not enough to fully account for the observed trends in ε_r vs. mass ratio and charge-to-mass ratio. Other explanations have been considered for this trend, but will be reserved for future work. The fact that the q/m dependence is still present, though diminished at 1 AU, could indicate that by 1 AU, minor ions have yet to be fully thermalized, and as such, traces of the preferential heating source are still present.

D'Amicis et al., [66] have demonstrated that solar wind behavior can be further categorized by distinguishing between Alfvénic, non-Alfvénic slow, and fast wind by identifying periods where magnetic field and bulk speed are well-correlated. Stansby et al. [120] show that the high variability in plasma parameters in the slow solar wind could be due to the presence of wind originating from the same sources as fast wind. This highly Alfvénic

slow wind, which aside from traveling at slower speeds, displays qualities more consistent with fast wind. Implementing such a distinction on the SWICS data set in conjunction with the [1] preferential heating model may lend greater insight into heating of minor ions. At closest approach, Parker Solar Probe (PSP) will fly within 10 R_s while its farthest perihelion was at 35 R_s. This range puts PSP at the perfect distance to investigate the solar wind's transition from the preferential ion heating zone to the relaxation zone. Solar Orbiter's orbit will reach perihelion around 60 R_s, placing it at a distance to see the edge of the preferential heating zone for the more non-thermal ions. This investigation, along with implementation of near-Sun PSP data and HIS data from Solar Probe will be reserved for future work.

CHAPTER 3

Heating of Minor Ions in the Slow Alfvénic Wind

3.1 Introduction

The kinetics and composition of minor ions in the solar wind serve as indicators of wind type/coronal sources, heating processes, and can also provide information about transient events throughout the solar wind's radial expansion. The solar wind is canonically divided into two categories based on bulk speed. The slow solar wind, with bulk speeds up to about 450 km/s, or 500 km/s in some cases [121], is characterized by high density, intermittency, high freeze-in temperatures, and higher concentrations of ions with low-first ionization potential (FIP) [122]. Fast solar wind, which typically peaks at around 700 - 750 km/s is characterized by low density, lower freeze-in temperatures, less variability in the kinetic moments, and photospheric elemental abundances ([123];[122]).

The differentiation of the wind types is reflective of their origin as well as the fractionation processes to which they are subject, and heavy ions play an important role in the identification and tracking of solar wind from different coronal sources. Fast solar wind, which originates from coronal holes does not undergo the same degree of fractionation as slow wind due to its low density and high speed [13]. The emphasis on coronal origin and the connection to the solar wind give rise to classifications lie outside the canonical slow/fast dichotomy (e.g., Stakhiv et al., 2015 [16]). This work focuses on the heating of slow Alfvénic wind, which streams at speeds comparable to the canonical slow wind, composition and Alfvénicity like that of the fast wind, and intermediate density and temperatures [18].

Spectroscopy, in-situ plasma and magnetic field measurements, and modeling and mapping of kinetic, composition, and magnetic field evolution can be employed to identify source regions of the solar wind in the corona and track the evolution of the wind at various distances. The complex coronal magnetic field topology must be modeled to determine the sources of the solar wind. One method is the Potential Field Source Surface Model,

developed by Altschuler and Newkir, 1969 and Wang and Sheeley, 1992 ([124], [125]).

Neugebauer et al., 2002 [126] used a PFSS model and Ulysses and ACE data to statistically categorize characteristics of varying active region and coronal hole solar wind. They found that the O^{7+}/O^{6+} ratio is generally lower in coronal hole wind, but not as low as that originating from polar coronal holes at solar minimum. They also showed that the characteristics of active region and coronal hole region wind during solar maximum are comparable to those produced during a Carrington rotation at solar minimum. Fu et al., 2015 [127] showed that the proportion of solar wind originating from active regions, quiet sun, and coronal holes has a solar cycle variation.

Parker Solar Probe observations have allowed for unprecedented mapping of solar wind back to source regions. Badman et al., 2020 and Panesenco et al., 2020 ([128];[129]) applied the PFSS model to map inner heliosphere wind to a coronal hole. Bale et al., 2019 [106] an extreme UV synoptic map to trace PSP-measured magnetic field lines back to a coronal hole, demonstrating that the solar wind measured had emerged from that source. PSP observations within .25 AU show that Alfvénic wind predominates in the inner heliosphere.

Plasma measurements, along with remote observations, have revealed that speed alone is not a fully sufficient qualifier for categorization, and that other characteristics determined by the solar wind's source region must be taken into account. Marsch et al., 1981 [67] first identified a slow stream with large differential speeds and temperature anisotropies in Helios 2 data. These nonthermal features were observed during solar minimum, in particular a period with high Alfvénic fluctuations, and are more often observed in fast wind. Since then, intervals of slow wind exhibiting a high v-B correlation have been identified in WIND, ACE, Helios, and PSP data. These periods, now known as the Alfvénic slow wind possess a strong v-B correlation despite slow streaming speeds.

Observations made by PSP have shown that the majority of solar wind in the inner heliosphere is highly Alfvénic, and it is now being postulated that the all solar wind starts out strongly Alfvénic but some processes cause some wind to lose Alfvénicity while other subsets of the wind retain it. The existence of slow Alfvénic wind demonstrates just how tied the different solar wind types are to their coronal origins. Understanding the slow Alfvénic wind, how it evolves over time and distance, and how it receives and dissipates energy provide further clues about how the solar wind evolves. Due to its similar origin to the fast wind and slower streaming velocity, it may serve as an intermediate tracer of heating and thermalization processes as the solar wind expands into the heliosphere. Here we study the preferential heating and Coulomb thermalization of minor ions in the slow Alfvénic wind. The following paragraphs are a brief overview of work done to characterize

the slow Alfvénic wind.

Various works ([37];[66];[18];[130]) have revealed much of the characteristics of Alfvénic slow wind, high normalized cross-helicity, high normalized $\cos(\theta_{vB})$, and. high residual energy. This wind type is more prevalent during solar maximum and can be observed out to 1 AU during this time. Normalized magnetic cross-helicity is the ratio of the alignment in velocity and magnetic field fluctuations to the total incompressible energy density ([68];[69];[70];[71]).

D'Amicis et al., 2011 [37] found that maximum of solar cycle 23 was dominated by slow wind with high degrees of Alfvénicity, comparable to that found in the fast wind during solar minimum of the same cycle. D'Amicis et al., 2015 and Antonucci et al., 2005 ([66];[28]) presented the first observational evidence of this secondary type of slow wind, thought to originate from active regions, and bearing the same Alfvénic signatures, albeit reduced in amplitude, as fast wind. Proton temperature is enhanced during slow Alfvénic periods, as well as heavy ion temperatures. In a case study of Helios 2 data at different radial distances, they also show that Alfvénic correlations are degraded by fluctuations in density and magnetic field, rather than velocity. Using Helios data from 0.3 to 1 AU [29] show that the heliospheric plasma sheet is much thicker than the current sheet. They provide observational evidence combined with (much later) radio occultation that the source of the plasma sheet are coronal streamers, and that the increased density surrounding the sheet can be traced back to the streamer boundaries prior to narrowing. Relative helium abundance is lower within the plasma sheet than outside it ([29];[30];[31]).

Bruno et al., 1991 [131] define number density compressibility and magnetic compressibility as the ratio of the standard deviation in the n and B to their respective 1-hour mean values ([37];[74]). D'Amicis et al., 2011 find that cross-helicity and magnetic compressibility are anticorrelated, and no correlation between kinetic compressibility and Alfvénic fluctuations. Wind exhibiting Alfvénic characteristics tends to have low compressibility (constant density and velocity) ([72];[73]). Fast and SA wind are characterized by higher power in magnetic and velocity field fluctuations, and a $1/f$ scaling at large scales, and either Kolmogorov (magnetic) or flat (velocity) scaling at higher frequencies, below the spectral break. Slow wind exhibits Kolmogorov scaling over entire scale range, typically ([77];[78]).

Fast and slow Alfvénic (SA) wind are less collisional than non-Alfvénic slow wind, and thus, could preserve characteristics of any preferential heating at the corona, or within the preferential heating zone ([51];[18]). Using Helios data, Stansby et al., 2019 [132] investigated a slow Alfvénic interval, determining that slow non-Alfvénic wind has the highest proton density flux, slow Alfvénic proton density flux is about half that of non-Alfvénic,

and fast wind is the lowest [132]. They also showed that slow non-Alfvénic electron temperatures exceed slow Alfvénic electron temperatures, and both are hotter than fast wind electron temperatures. Perrone et al., 2018 [87] showed, using re-processed HELIOS data that the rate of proton-proton self-collisions in fast solar wind streams decreases with radial distance between .3 and 1 AU, and is on order of 10^{-8} to 10^{-7} Hz. This decrease is faster than what would occur in an isotropic distribution. In the fast wind, wave-wave, wave-particle, and wave-turbulent interactions are the more dominant dissipative processes, rather than Coulomb collisions [133].

Due to their frozen-in temperatures and low relative abundance, minor ions are excellent tracers of coronal conditions. Mass and charge-dependent preferential heating within a certain distance of the corona result in nonthermal proton and heavy ion kinetic properties. Differentiating between SA, SNA, and fast wind can provide further context to observations further away from the sun. By examining the collisionality of minor ions during slow-Alfvénic intervals, this work aims to identify the differences in how minor ions are heated and subsequently thermalized in the different solar wind types. The chapter will proceed as follows: Section 3.2 outlines how slow-Alfvénic periods are selected. Section 3.3 explores the SA wind collisionality, while section 3.4 shows how the boundary of the preferential heating zone changes for different solar wind populations. Radial boundary variation with solar cycle is presented in section 3.5. Results and conclusions are discussed in sections 3.6 and 3.7, respectively.

3.2 Methodology

3.2.1 ACE/SWICS Data

The periods selected for this study were identified using data from the Solar Wind Ion Composition Spectrometer (SWICS) aboard the Advance Composition Explorer (ACE), as well as the magnetometer (MAG), and occur during the ascending phase of solar maximum of solar cycle 23, from late 1998 through most of 2002. The data are available at different cadences, 1-minute for MAG, 12-minute for SWEPAM proton density, velocity, and temperature/thermal speed, and 1-hour for minor ion kinetics and abundances. From top to bottom, the first five panels of figures 3.1, 3.2, and 3.3 show density, temperature, speed, ion to proton temperature ratio, and specific entropy. These quantities are shown at the 12-minute cadence. The sixth and seven panels, which contain ion and elemental abundance ratios, are shown at the 1-hour cadence. The magnetic field, displayed in the second to last panel, is averaged down to the 12-minute cadence and displayed here. Normalized cross-

helicity is shown in the last panel, with b- and v- fluctuations calculated over one-hour averages. Note that all calculations of collisional age, Alfvén speed, and cross-helicity are performed at the 12-minute cadence, with 12-minute averages of the magnetic field. Merged SWICS and SWEPAM data, provided by the Ace Science Center at a 12-minute cadence, are used for protons in both sections.

3.2.2 Selection and Description of Alfvénic Intervals

The reader is encouraged to refer to [66], [18] and [130] for a detailed overview of how slow Alfvénic periods are identified in the solar wind. Slow Alfvénic wind streams are characterized by initial drops in density and jumps in temperature, followed by a relatively steady period of density, temperature, and velocity. Magnetic field compressibility is low. These periods exhibit ion signatures in alignment with the fast wind, such as enhanced O^{7+}/O^{6+} , He/O, and Mg/O ratios. Additionally, magnetic cross-helicity as well as residual energy are enhanced during these intervals. Slow Alfvénic wind during these intervals is seen to peak as high as 600 km/s, though mean speeds are lower. As such, speeds of up to 600 km/s are included so as not to cut off any portion of the SA intervals. For this study, we focus on 42 intervals identified by R. D'Amicis and shared via private communication.

Figures 3.1 - 3.3 show examples of three of the forty-two Alfvénic periods used in this study. The orange lines denote the start and end of the slow Alfvénic interval.

While the plots in figures 3.1 - 3.3 are not representative of all Alfvén periods, they do contain some features that are typical. The intervals are often preceded by an increase in magnetic field magnitude and/or a change in field direction. This jump is followed by the characteristic steady field for the duration of the Alfvénic interval. The magnetic field and velocity become strongly correlated, resulting in a rather steady bulk velocity. Temperature ratios also become steady when compared to those seen in the preceding and subsequent non-Alfvénic winds. This is evident on the left hand side of the fourth panel of 2.1. Density is similarly steady, and is typically preceded and followed by either a small jump or drop. Note that when normalized to the mean, alpha density has greater variability than proton density, though that variability is still reduced within the Alfvénic periods. Due to its dependence on density and temperature, specific entropy S, another excellent distinguishing variable between wind types [19], is also less variable during these intervals.

The C^{6+}/C^{4+} and O^{7+}/O^{6+} ratios drop prior to nearly every Alfvénic period, during which they either remain steady or gradually rise. The intervals may also be followed by a jump in the ion abundance ratios. The lower temperature ratios seen during these intervals is well

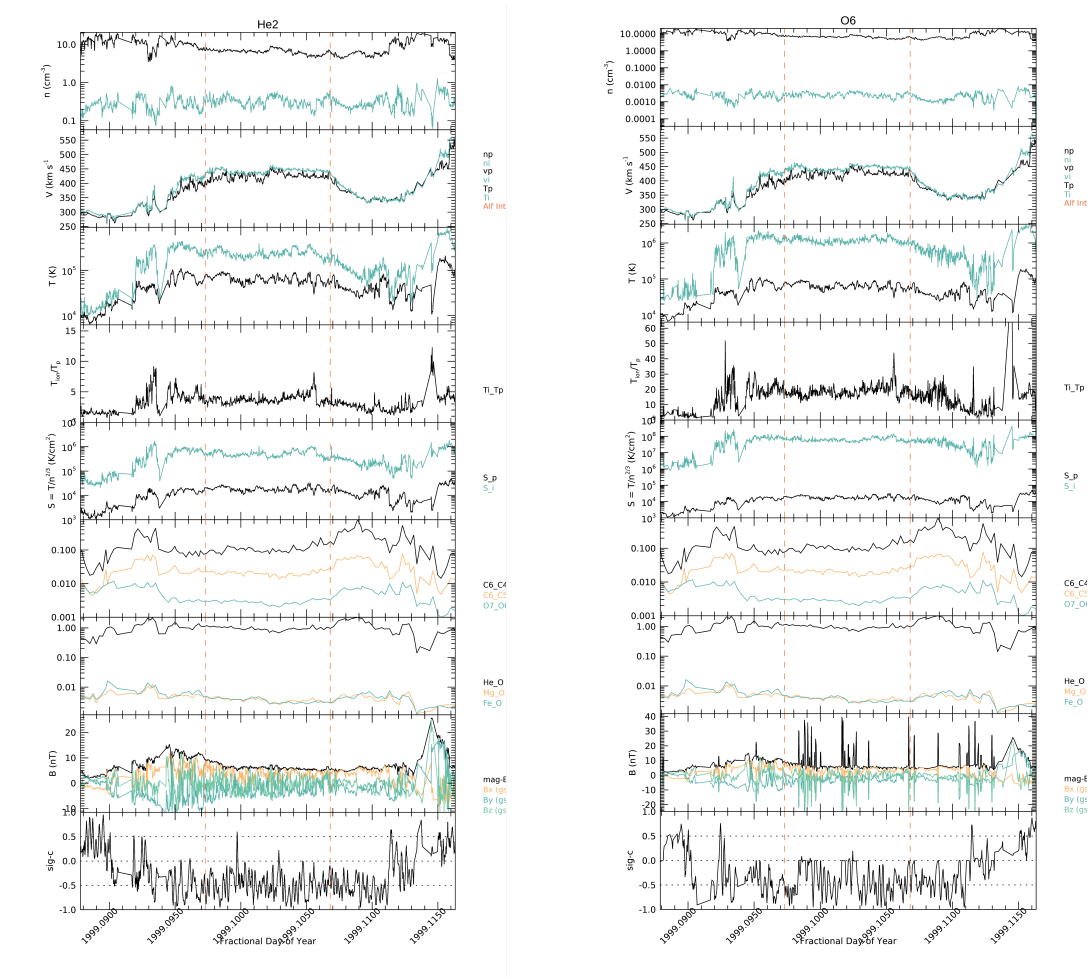

Figure 3.1 Example of one SA interval, preceded and followed by typical slow intervals. The same interval on the left and right is shown for alphas and O^{6+}, respectively.

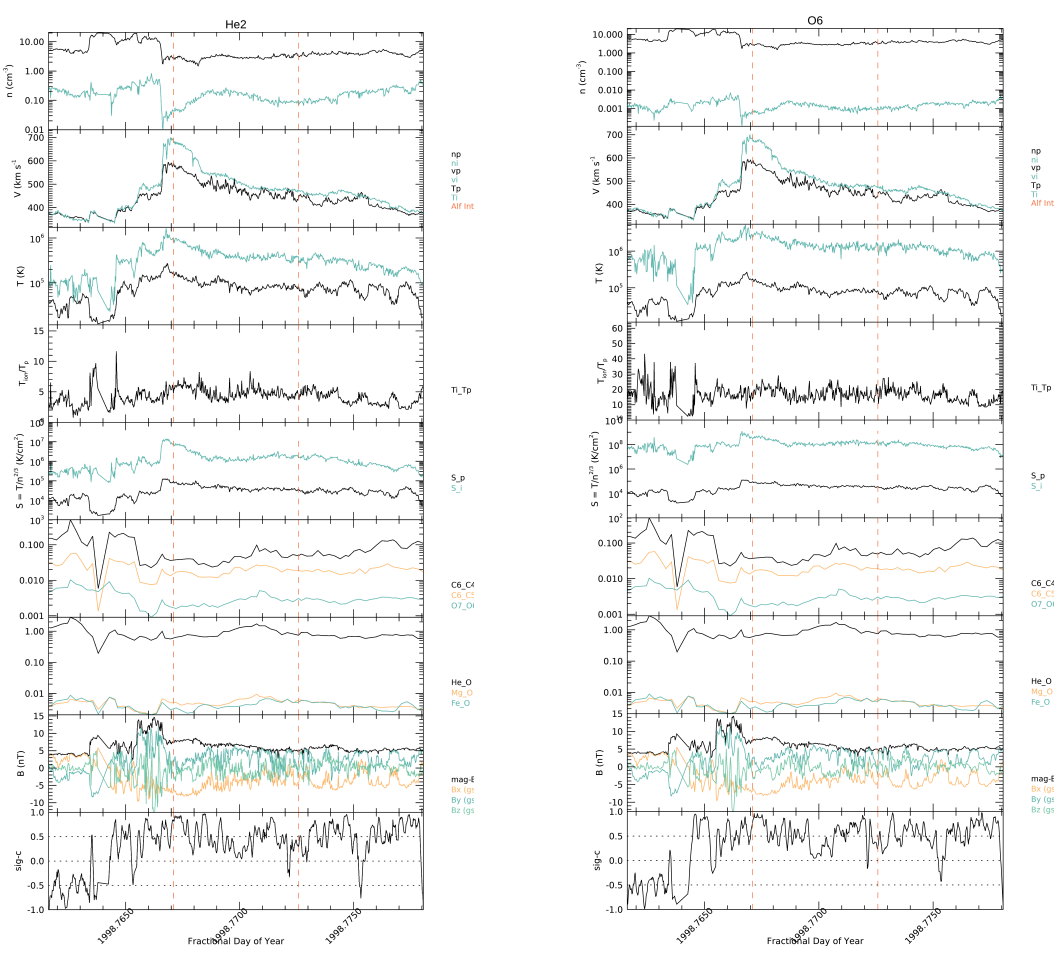

Figure 3.2 Example of another SA interval. The same interval on the left and right is shown for alphas and O^{6+}, respectively.

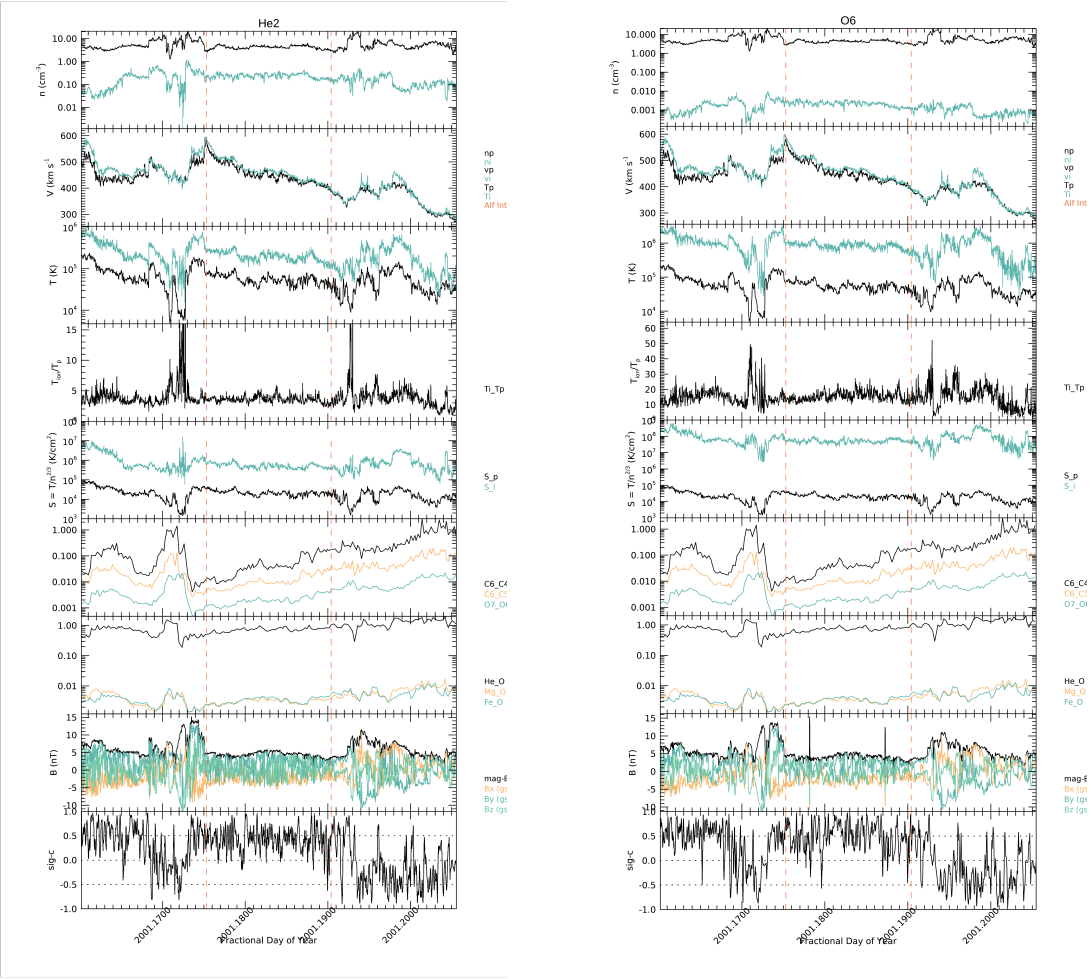

Figure 3.3 Example of one SA interval, preceded and followed by what appear to be fast streams. The same interval on the left and right is shown for alphas and O^{6+}, respectively.

in line with the favoring of lower charge states (caused by lower electron temperatures and lower freeze-in heights in the corona) observed in coronal hole source, and typically highly Alfvénic, wind.

Magnetic cross-helicity is commonly used to determine solar wind Alfvénicity, and describes the correlation between the velocity and magnetic field. It is calculated as:

$$\sigma_c = 2 * \frac{< v * b >}{< v^2 > + < b^2 >},$$

This relation is derived from the expression,

$$\sigma_c = \frac{< z_+^2 > - < z_-^2 >}{< z_+^2 > + < z_-^2 >},$$

which utilizes the Elsässer variables [134]. The Elsässer variables, $z^+ = u + b$ and $z^- = u - b$, describe the fluctuations in the velocity and magnetic field via the fluctuations in velocity about the mean Alfvén speed, taken over some time average. Here **b** is in Alfvén speed units: $b = \frac{B}{\sqrt{\mu_0 \rho}}$ ([135];[136]) Normalized cross-helicity of ±1 corresponds to pure Alfvénic streams, where the magnetic field and velocity vector are perfectly correlated (anti-correlated). In highly Alfvénic wind, the magnitude σ_c is often elevated, yet steady with comparison to non-Alfvénic periods.

3.2.3 Non-Alfvénic Wind

In addition to the SA intervals, periods of non-Alfvénic slow wind (SNA) are also utilized. Since SA and SNA wind are thought to have different origins, their heating mechanisms may also be different. They will certainly experience Coulomb thermalization at different rates. This would lead to differing heating and thermalization profiles for the two wind types, ordered in collisional age and distance. Distinguishing between the two will give insight into both of their heating and acceleration mechanisms. SNA wind is required to have velocity below 500 km/s, normalized cross-helicity below 0.4, must not occur during the identified SA intervals, and must have been measured during the same 1998-2002 period. Cumulatively, the forty-two SA intervals correspond to about 13,000 data points. Likewise, about 13,000 SNA data points are selected so that each wind type has comparable statistics.

3.2.4 Fast Wind

The last subset of solar wind used in this study is any time interval with velocity > 500 km/s that lies outside of the aforementioned SA intervals, but within the 1998-2002 ascending

maximum phase and maximum of the solar cycle. As with SNA wind, fast wind is limited to about 13,000 data points.

3.3 Collisionality of the Slow Alfvénic Wind

Fast solar wind originates from coronal holes, which contain open magnetic field lines. The origin of slow wind is less clear, but it is thought to originate from a number of sources. Theories include, but are not limited to, plasma 'blobs' emitted by pinched off helmet streamers (closed loop/closed field lines), and interchange reconnection between open and closed field lines over coronal streamers. The slow Alfvénic wind is thought to originate from active regions, often located at boundaries of coronal holes wherein it may be heated and accelerated primarily by Alfvén waves [66]. Due to the photospheric composition and low density of coronal holes and the fast wind emerging from them, it would follow that slow Alfvénic wind, with its theorized similar origin, would be similarly collisionless, or at least significantly less collisional than non-Alfvénic wind (See reviews by Feldman et al., 2005 [122] and Cranmer and Wineberger, 2019 [15] for more background on this).

The [1] PHZ boundary model relies on Coulomb collisions as the sole thermalizing process acting on the solar wind beyond the PHZ boundary. This assumption cannot be applied to the nearly collisionless fast wind, and its applicability to slow-Alfvénic populations is explored here. Fig. 3.4 shows histograms of collisional age for SA, SNA, and fast solar wind for alphas. Collisional age is divided into four regimes: $A_c < 0.1$, $0.1 < A_c < 1.0$, $1.0 < A_c < 10.0$, and $A_c > 10.0$. The histograms are of temperature ratio in each A_c regime, where each solar wind type is self-normalized. It is clear here that in terms of collisions, SA wind has characteristics of both slow and fast wind. Fast wind temperature ratios peak in the lowest collisional age regime, while a slightly higher proportion of SA wind than SNA wind is present. The highest proportion of SA wind is in the mid-low A_c regime, and it is absent in the highest regime. SNA wind remains high in the middle two regimes, and a very small proportion is still present at very $A_c < 10$. The depletion of fast wind across higher collisional age regimes is more gradual in higher charge state minor ions due to the dependence of collisional frequencies on ion charge state, though only helium is shown here.

Table 3.1 lists the median Coulomb collisional frequencies for some SWICS heavy ions with protons, calculated in the same manner as in [65]. The "all types" column does not distinguish between solar wind types, while "SA" calculates the collisional frequency for slow-Alfvénic intervals only. Fast is limited to speeds above 500 km/s, and SNA refers to the non-Alfvénic slow wind. The SA collisional frequency tends to be about 2.5-3 times

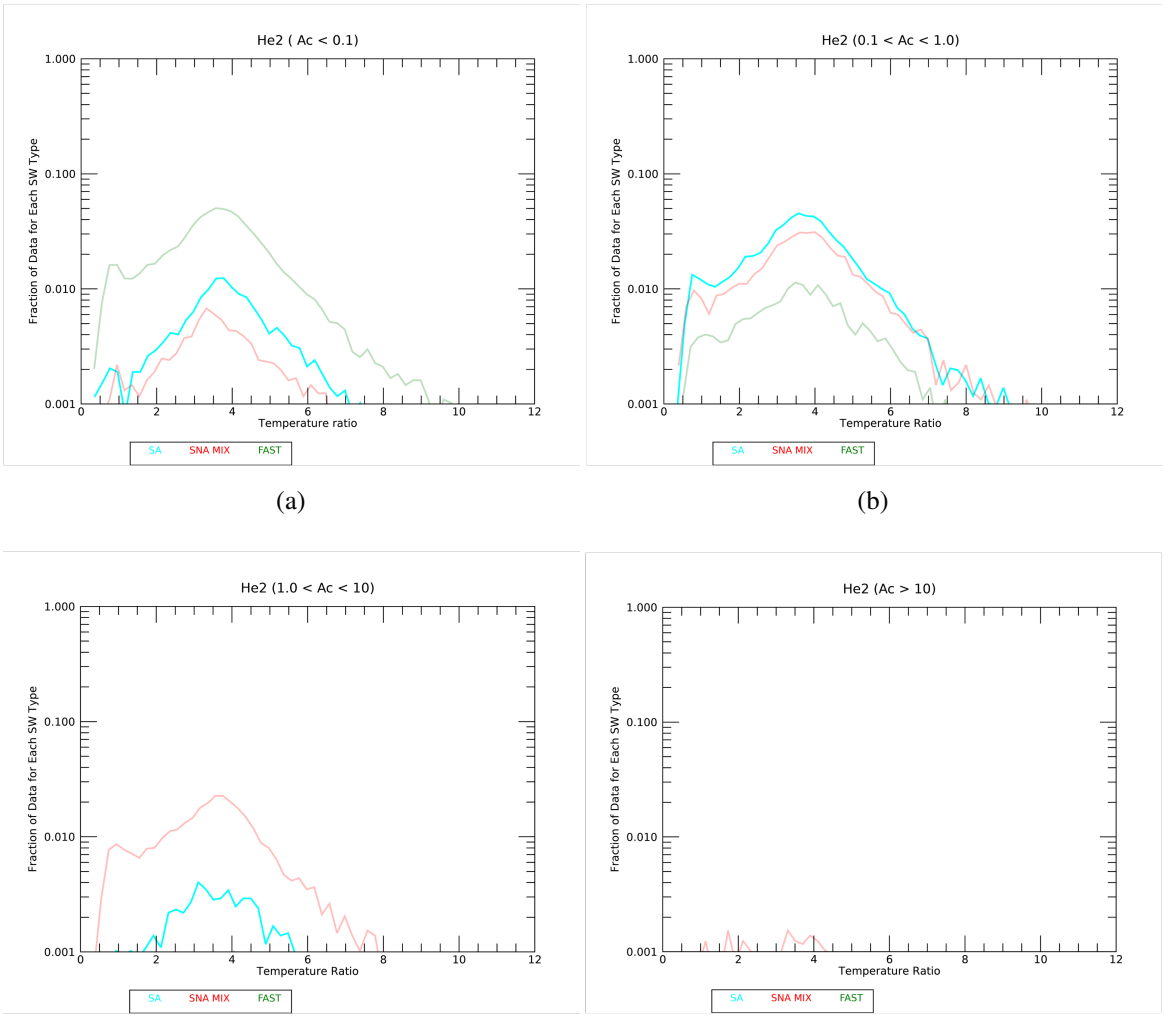

Figure 3.4 Histograms of temperature ratio in four different collisional age regimes: $A_c < 0.1$, $0.1 < A_c < 1.0$, $1.0 < A_c < 10.0$, and $A_c > 10.0$

Ion	All Types	SA	Fast	SNA
He2	1.87e-7	1.450e-7	5.14e-8	2.78e-7
C4	1.34e-7	2.00e-7	7.34e-8	2.94e-7
C5	2.88e-7	2.55e-7	9.67e-8	4.81e-7
C6	6.03e-7	5.09e-7	1.64e-7	9.14e-7
O5	1.41e-7	2.52e-7	1.00e-7	3.68e-7
O6	3.68e-7	2.99e-7	1.15e-7	5.68e-7
O7	6.58e-7	4.79e-7	1.68e-7	9.25e7
O8	1.61e-6	2.55e-6	4.21e-7	2.31e-6
Mg8	2.71e-7	4.26e-7	1.53e-7	7.60e-7
Mg9	4.78e-7	5.43e-7	1.96e-7	9.40e-7
Mg10	8.95e-7	7.60e-7	2.62e-7	1.37e-6
Si9	4.48e-7	5.58e-7	1.86e-7	8.64e-7
Si10	7.75e-7	7.96e-7	2.63e-7	1.56e-6
Si11	1.36e-6	1.02e-6	3.22e-7	2.16e-6
Si12	2.88e-6	2.59e-6	6.43e-7	3.10e-6
S10	5.76e-7	8.15e-7	2.41e-7	1.41e-6
S11	1.22e-6	2.06e-6	3.71e-7	3.44e-6
S12	2.45e-6	5.64e-6	7.42e-7	3.65e-6
S13	3.53e-6	5.15e-6	8.34e-7	3.46e-6
Fe8	2.17e-7	2.00e-7	7.20e8	3.85e-7
Fe9	2.62e-7	2.94e-7	9.13e-8	4.60e-7
Fe10	3.54e-7	4.20e-7	1.19e-7	6.55e-7
Fe11	4.38e-7	4.93e-7	1.57e-7	8.41e-7
Fe12	7.27e-7	6.96e-7	2.15e-7	1.65e-6
Fe13	1.28e-6	1.39e-6	3.21e-7	2.21e-6

Table 3.1 Collisional frequencies for varying solar wind regimes for most ions included in the SWICS 12-minute dataset.

higher than fast, and $50-70\%$ of that of SNA . The few exceptions to this are the less abundant, high charge state ions of a given species, such as O^{8+}. Due to these low abundances, the calculation of collisional frequency is not as reliable. Based on these collisional frequencies, the slow-Alfvénic wind may serve as an intermediate tracer, retaining signatures of its original heating and acceleration source to a greater extent than the non-Alfvénic slow wind.

The collisional frequency of heavy ion species with protons is driven by the proton density, proton and ion thermal velocities, and the heavy ion charge. The attribution of collisionality to a solar wind type must correlate A_c to its Alfvénicity while controlling for density and temperature. The distributions of proton density for SA has similarities and differences with both SNA and fast wind. This is not shown here, but can be found

in Appendix C. Qualitatively, SA wind and fast wind have similar density distributions, while the SA peak is shifted to higher densities. SNA wind peaks near at nearly the same density as SA wind, but the distribution is spread over a larger range, with a much higher population of high densities than the SA and fast wind types. The temperature of SA wind peaks between the SA and fast distributions. The full-width-half-maximum and skew of the SA distribution is closer to that of fast wind than SNA, which is more spread. Once again, fast and SA wind are qualitatively similar, with SA shifted to cooler, slower conditions. Refer to Appendix C for a more complete analysis of the dependence of collisionality on wind type vs. ion kinetics. Overall, we find that while proton density is the strongest driver of collisional frequency and thus, collisional age, the collisional behavior of the different wind types is still distinct in narrow bands of both proton density and temperature. The ordering of ion drifts by the magnetic field may be enough to prevent the randomized motion that leads to Coulomb collisions, regardless of density and temperature. Knowing that SA wind collisional frequencies are on the same order as SNA collisions, though still consistently lower, we proceed with the PHZ analysis on both slow wind types.

3.4 Preferential Heating of Minor Ions in the Slow Alfvénic Wind

The same analysis performed in the previous chapter is done here, using A_c to track excess temperature and thus, determine the location of the outer boundary of the zone of preferential heating. The two slow wind types, SA and SNA , are compared, as well as general slow wind. Figures 3.5 and 3.6 show the ε vs. A_c decay curves and ion trends, respectively, with SA in the leftmost column, SNA in the middle, and slow wind on the right. SNA wind limited to a number of data points comparable to that of the SA wind, while slow wind is not, partially to give insight into the effects of binning statistics on the results.

He^{2+}, which does not have a “bump" in its decay curve in the 2-hour data, has a bump at $A_c \sim 1$ in the 12-minute data, run on the years 1998-2002. This can be seen in Figs. 3.5a, 3.5b, and 3.5c. This feature is apparent in the SNA and general slow wind. The SA decay curve is not as smooth, and the feature is not discernible. He^{2+} has poor binning statistics (in epsilon) at the high and low end of the collisional age range, and which improve between $A_c \sim 0.02 - 0.2$. Conversely, SNA bins have higher uncertainty in excess temperature at low A_c, and moderately good statistics throughout the remainder of the decay curve. SA, SNA, and general slow wind cover a similar range in A_c, but slow wind actually achieves higher excess temperatures at the PHZ boundary, while SA wind achieves the lowest. These

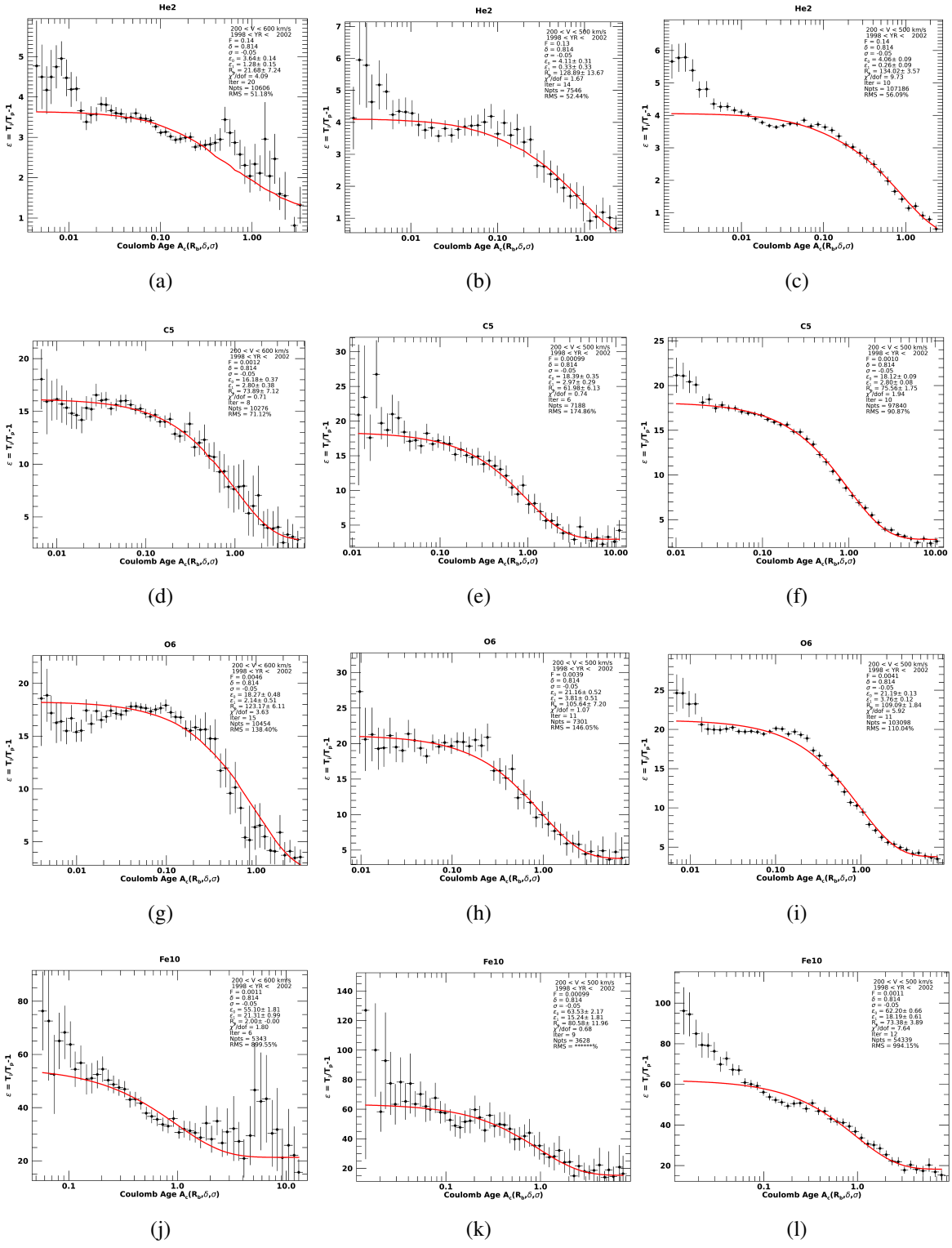

Figure 3.5 Preferential Heating Zone boundary model on the following subsets of data, from left to right column: all solar wind speeds, all speeds below 500 km/s, and speeds below 500 km/s with identified slow Alfvénic intervals removed.

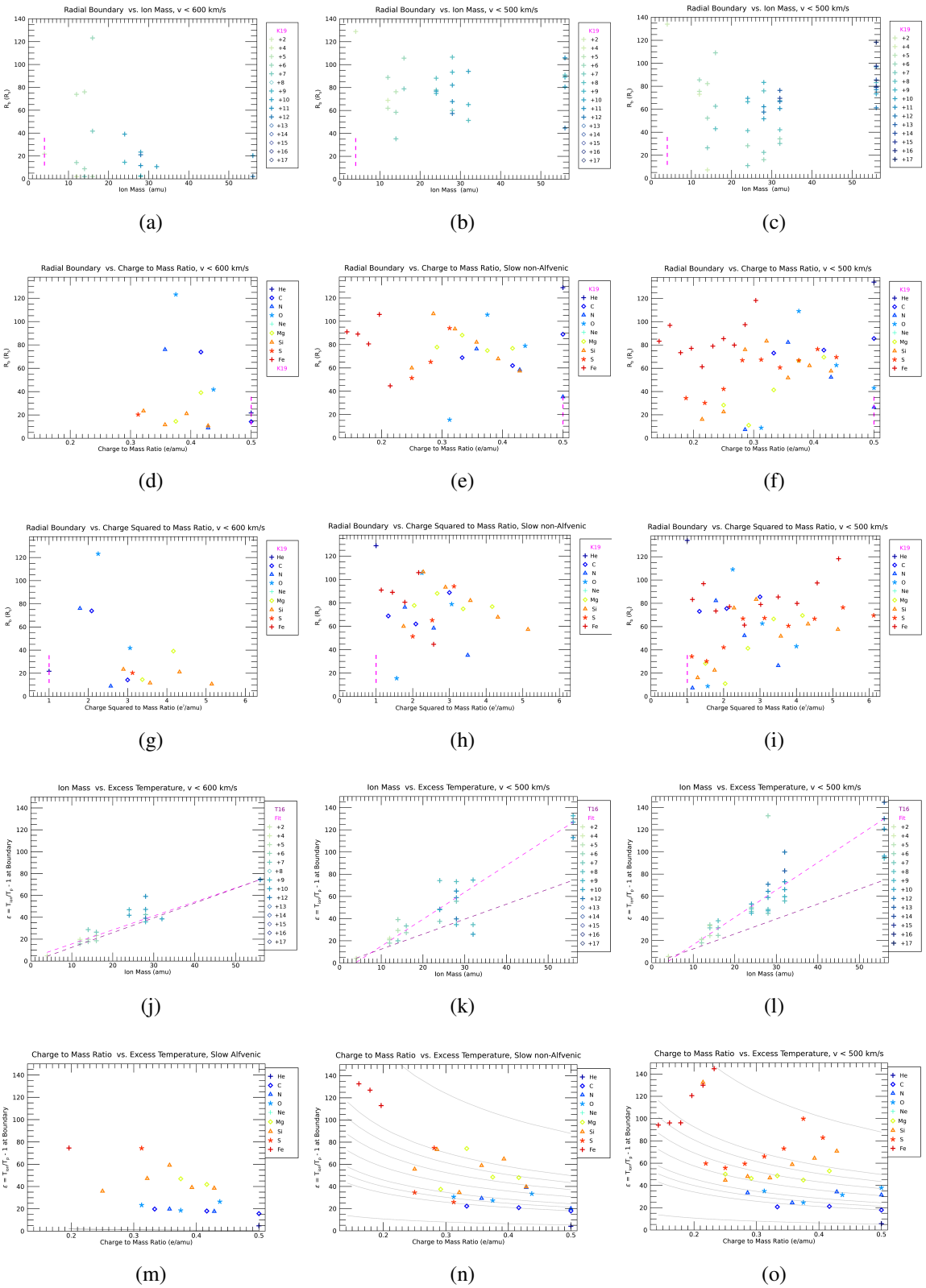

Figure 3.6 Ion trends from PHZ model. Left to right: SA wind, SNA wind, and typical slow wind from 1998-2002. Top to bottom: R_b vs. m_{ion}, R_b vs. q/m, R_b vs. q^2/m, ε_b vs. m_{ion}, and ε_b vs. q/m are listed. Rainbow color scheme for q/m plots. Two-toned for mass.

results are counterintuitive, knowing that minor ions are heated more and stream faster than protons to a greater extent in the fast wind than in the slow wind. By extension, SA wind should exhibit similar nonthermal features in response to preferential heating sources which are tied to the solar wind's Alfvénic nature, or Alfvénicity. However, this result is consistent for all of the utilized SWICS ions and for an alternate method of selecting "SA" wind. This will be explored further in the discussion. "All speeds" wind is not shown here, but the curve remains flat until $A_c \sim 1$, and the R_b prediction is higher than the other three categories.

It may be counter-intuitive that the slow wind in the column farthest to the right has the lowest levels of uncertainty (smallest error bars) yet the highest reduced χ^2. This is because the standard deviation in each "general slow" wind bin is much lower due to the category's higher population. The modeled decay curve is fitted based on the minimization of the χ^2/dof statistic, which can be thought of as an aggregation of deviations from the expected value divided by an already very small standard deviation. So, without adjusting weighting from wind type to wind type, χ^2/dof is more sensitive to any deviations from the expected value in the more robust bins than in the SA and SNA bins.

C^{5+} is shown in Figs. 3.5d, 3.5e, 3.5f. The binning statistics are similar here to that of He^{2+}. There is no easily apparent bump, though SA wind does have a slight increase in excess temperature at $A_c \sim 0.02$. Though it is not shown here, all speeds wind has a slight bump at $A_c \sim 0.1$. This is consistent with the results in the previous chapter using the 2-hour data across the entire dataset. SA wind is shifted to lower A_c than SNA and general slow wind. The latter two types have almost identical ranges. Again, SA excess temperature is the lowest of the three types, and SNA is the highest. SA and general slow R_b are similar, but both higher than the R_b prediction for SNA wind.

O^{6+} is shown in Figs. 3.5g, 3.5h, 3.5i. The binning statistics are consistent with other ions, with SA having less uncertainty at mid-range A_c and high uncertainty at low and high. SNA uncertainty is fairly consistent across collisional ages. The bump is present in all wind types, but less pronounced in SNA and general slow wind. The presence of the bump in slow wind is a bit more pronounced than in the 2-hour averaged data. Though it is not shown, the bump is very pronounced in all speeds wind as in the 2-hour dataset. SA ε_b is lower and is shifted to lower A_c than the other types. For O^{6+}, the R_b prediction is highest for SA wind and lowest for SNA.

Fe^{10+} is shown in Figs. 3.5j, 3.5k, 3.5l. Binning statistics are consistent with other ions, though overall uncertainty, and the number of data points is lower for Fe^{10+}. The model did not converge for SA wind, and produced a minimum R_b. The SNA R_b prediction is higher than that of the general prediction. There is no bump in any of the Fe^{10+} plots. In all speeds

wind, not shown here, a slight bump is present, though less pronounced than in the 2-hour SWICS results. Boundary excess temperature is lowest in SA wind and highest in SNA.

These ions, which are the some of the most abundant/reliable in the SWICS dataset, are representative of the other ions in some aspects, but differ from overall trends in others. For every ion considered, if a bump is present in the "all speeds" wind, it is diminished or not present in the slow and SNA wind types. It appears to be somewhat more present in some SA ions, but the decay curve is often too scattered for it to be easily discernible as the "bump." The feature is more apparent in lower mass ions: C, N, O, but much smaller in Mg and heavier ions.

For $C^{5,}$ O^{6+}, and Fe, there is good agreement in the R_b prediction across all wind types. For all other ions, the R_b prediction is consistently lower. The disagreement with heavier ions could be explained by a combination of SA wind collisionality and lower bin statistics, but the case of He^{2+} is more puzzling. This will be further addressed in the next few figures, as well as in the discussion.

The A_c shift for each of the wind types is as expected. SA decay curves are shifted to lower A_c for all ions, and often don't reach ε_r as low as the other wind types. This is consistent with the difference in collisional frequency between SA and SNA wind. Conversely, ε_b is higher in the SNA wind than for all other wind types for every ion. Again, this will be discussed further.

It was already mentioned that SA wind has higher uncertainty (in ε at the high- and low-A_c ends of the decay curve than SNA wind. The uncertainty in SNA bins is fairly constant throughout, causing it to have, in many ions, higher uncertainty than SA wind in the middle of the decay curve. One can tell visually that overall, SNA error/uncertainty tends to be lower than SA. In most cases, χ^2/dof is anywhere from 2-3 times higher in the SA wind than in the SNA. This combined with the increased uncertainty in the SA ε decay curves demonstrates that the PHZ model is in greater agreement with SNA wind observations, and that its output in the SNA wind is at least more reliable than the SA output.

Figure 3.6 shows the trends in R_b prediction and observed ε_b with ion characteristics. From top to bottom, the rows correspond to R_b vs. m_{ion}, R_b vs. q/m, R_b vs. q^2/m, ε_b vs. m_{ion}, and ε_b vs. q/m. The columns, from left to right, are SA, SNA, and general slow wind.

The R_b vs. m_{ion} in Figs. 3.6a, 3.6b, and 3.6c do not have the same trends as are found with the SWICS 2-hour data, wherein R_b is constrained to higher, narrower ranges in radial distance as mass increases. Despite having a similar number of data points. General slow wind exhibits a semblance of a trend, with the band of R_b increasing for each successive element while the range decreases (excluding alphas). When run on SNA wind, the PHZ

model is able to resolve more of the lower charge states of each element.

The trend in R_b vs. q/m seen in the 2-hour SWICS dataset is no longer present in Figs. 3.6d, 3.6e, and 3.6f . The PHZ model on SA wind does not produce enough viable R_b predictions for lower q/m ions, and the higher q/m ions have no clear dependencies. SNA wind has a shape similar to the 2-hour SWICS relation (note differences in plot range), but the R_b predictions are lower and the trend is not as strong. General slow wind has more viable R_b predictions than the other two categories. The addition of these ions does not improve upon the R_b vs q/m relationship.

The trend in R_b vs. q^2/m seen in the 2-hour SWICS dataset is no longer present in Figs. 3.6g, 3.6h, and 3.6i. The PHZ model on SA wind does not produce enough viable R_b predictions for mid- and lower q^2/m ions to see any clear dependencies on q^2/m. SNA R_b predictions decrease with q^2/m, similar to the 2-hour SWICS prediction. This relationship is not strong, and is further reduced in general slow wind.

The trend in ε_b vs. m_{ion} seen in Figs. 3.6j, 3.6k, and 3.6l is in good agreement with the Tracy 2016 (T16) relation, as well as the 2-hour relation. This is likely better attributed to the limited range in Fe, Si, and Mg charge states than to any true agreement in the observed ε_b. SNA wind, which has a broader range in charge states for the heavier, low-FIP ions, far exceeds the mass ratio dependence found in T16. The same is true for general slow wind from 1998-2002. All wind speeds from 1998-2011 in the SWICS 12-minute data produces much better agreement with T16, though slope is still slightly higher. The small difference may be due to the 12-minute data allowing more observed excess temperature bins to be formed at lower A_c than the 2-hour data. That the SNA wind appears to be more heated at the boundary than SA and general slow wind at the PHZ boundary is an unexpected result, and will be discussed further.

The trend in ε_b vs. q/m seen in Figs. 3.6m, 3.6n, and 3.6o is in good agreement with results from the SWICS 2-hour dataset. Though the full range of charge states is not present in the SA wind, it does still exhibit the mass stratification present in previous results and the other wind types shown here. Here it is easy to discern that the ε_b of He^{2+}, C, and O ions are in good agreement with each other while the heavier ions vary across all data types.

The following plots are not shown here, but a comment must be made on them for comparison: all wind speeds from 1998-2002, slow wind from 1998-2011, and all wind speeds from 1998-2011. These plots are not shown since the main purpose of this section is to compare SA and SNA wind, with general slow wind from 1998-2002 acting as a sort of control. However, the dependencies/lack of dependencies found in all of these categories may highlight the impact of binning statistics, solar cycle, the dataset, and the wind type itself.

The results shown and discussed above may largely be impacted by the limited amount of SA intervals. SNA wind was intentionally limited in an attempt to equalize the impact of low binning statistics. This impact may be seen when examining the 1998-2002 wind. The years covered in this comparison are also significant. Figures 3.5, 3.6, 3.7 and 3.8 are all limited to solar maximum of SC 23. In the following section, we will show how some model output varies with solar cycle. The SWICS 12-minute and 2-hour datasets should be nearly the same, considering the 2-hour ion velocity distribution functions are accumulations of 10 12-minute cycles. Error filtering has been employed in an attempt to reduce some of the uncertainty in the 12-minute dataset (see C). We have shown, however, that the model output is dependent on time cadence, and higher time resolution produces lower R_b values (see B).

Model results and R_b dependencies in the general slow wind from 1998-2011 using the 12-minute SWICS data match well with the 2-hour data over the same time interval, though the R_b tends to be shifted downward for all ions. The same is true for the 12-minute and 2-hour datasets over all solar wind speeds. Limiting the 12-minute dataset to solar max still results in good binning statistics, so the disorder in the R_b dependencies may be attributed to the solar cycle.

In Figure 3.7, SA boundary excess temperature is plotted against SNA, general slow, and all speeds wind. The black dashed line is representative of a 1:1 scaling between wind types. The magenta dashed line shows the linear fit between each pairing. The color bar indicates the mass of each plotted ion, and can be used to identify elements. From left to right, SA vs. SNA, SA vs. slow, and SA vs. all speeds are shown. It is evident that the greatest agreement is between SA and all speeds wind, which includes a significant population of fast wind. This pairing is in the panel furthest to the right,and has a slope of about 0.8, and correlation coefficient about 0.93. The slopes of SA vs. slow, and SA vs. SNA ε_b are about 0.60 and 0.64, respectively. Correlation coefficients of all the pairings are all high, but the lowest CC is for the SA vs. SNA pairing. Overall, the lower mass ions tend to stay in good agreement across pairings, while the heavier ions deviate the most from a 1:1 scaling.

In Figure 3.8, SA R_b prediction is plotted against SNA, general slow, and all speeds wind. The black dashed line is representative of a 1:1 scaling between wind types. The magenta dashed line shows the linear fit between each pairing. The color bar indicates the mass of each plotted ion, and can be used to identify elements. From left to right, SA vs. SNA, SA vs. slow, and SA vs. all speeds are shown. The greatest agreement is between SA and slow wind and lowest for SA vs. SNA. R_b predictions in SA wind, however, are much lower than any other wind type. The slope and correlation coefficients of all pairings

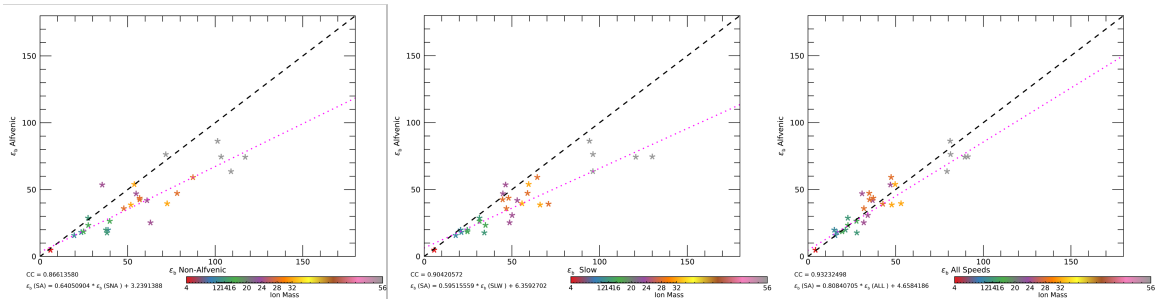

Figure 3.7 Direct comparisons of observed boundary excess temperature for SA wind vs. SNA, general slow, and all wind speeds.

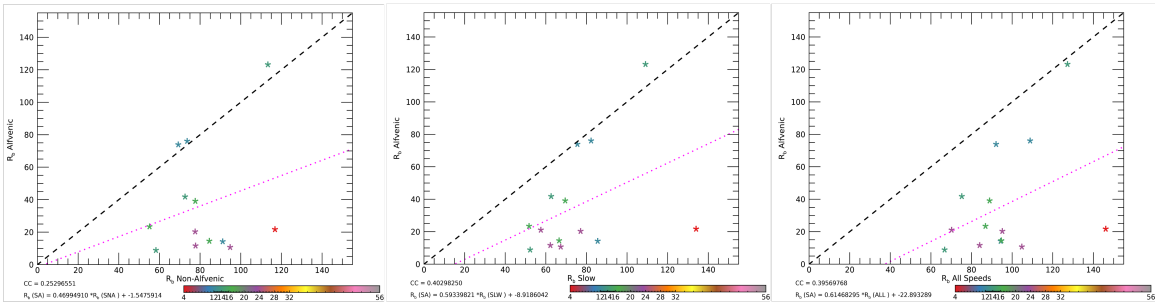

Figure 3.8 Direct comparisons of radial boundary prediction for SA wind vs. SNA, general slow, and all wind speeds.

are significantly lower than the ε_b metrics. The SA vs. all speeds pairing has a slope of 0.61 and correlation coefficient of 0.39. SA vs. slow has a slope of 0.59 and correlation coefficient of 0.40. SA vs. SNA has a slope of 0.47 and a correlation coefficient of 0.25. In the SA vs. SNA and SA vs. slow pairings, some of the more abundant ions, C^{5+}, C^{6+}, and O^{6+}, the R_b prediction remains close to the 1:1 scaling line.

Figures 3.7 and 3.8 demonstrate the distinctions between SA and SNA wind. A direct comparison between R_b and ε_b between SA and fast wind would give more information about the PHZ boundary. Due to its lack of collisionality, however, fast wind excess temperature cannot be traced via Coulomb collisions/A_c, and viable R_b predictions cannot be made. Boundary excess temperature also cannot be distinguished, as A_c remains low and there is no clear decay curve. Perhaps SA and SNA wind ε_b can be prepared to maximum ε in the fast wind, assuming ε_b in the slow wind types and ε_{max} in the fast wind correspond to where ions in both wind types experience the most preferential heating. This is not shown here, but the plots simply demonstrate that fast wind has higher excess temperature than all other wind types, and is confined to a low A_c, which is already well-known.

Because of SNA's tendency to have higher boundary excess temperature, it is actually best correlated with fast wind ε. This is not in agreement with the assumption that, like fast

wind, SA wind would be farther from thermodynamic equilibrium, and thus have consistently higher excess temperature than SNA wind. SA and SNA are both better correlated with general slow wind than with each other. The overall distribution of proton and ion temperatures for each solar wind type does reveal that, while SNA ions and protons peak at lower temperatures than SA, the overall SNA distribution still has a significant population of ion temperatures that overlap and exceed those of SA wind.

3.4.1 Direct σ_c Comparison

In an attempt to confirm, and perhaps explain the counterintuitive SNA results, using cross-helicity (σ_c) as the sole measure of Alfvénicity, we compare model output on high- and low-Alfvénicity wind. As discussed in the introduction, Alfvénic intervals are distinctive, sustained periods where the plasma and magnetic field exhibit a specific behavior. Normalized cross-helicity is not the only factor used to define or identify such wind. It is being used here as a threshold just to select data likely to have high Alfvénicity.

The direct comparison of slow Alfvénic intervals with slow non-Alfvénic intervals resulted in some surprising trends. R_b predictions are consistently significantly higher for SNA wind than for SA, and boundary excess temperature is slightly higher for SNA. Fast, Alfvénic wind experiences fewer Coulomb collisions and thus, has not been thermalized to the same extent as slow wind by the time it reaches 1 AU. We have shown that SA wind's collisional behavior is an intermediate between SNA and fast wind. Thermalization of the solar wind does not necessarily correspond to the heating it experiences within the PHZ, so the location of the radial boundary and the excess temperature might not be correlated. Further, the overall temperature distributions (see C) of the three solar wind types reveal that, although SA wind peaks at a higher temperature than SNA wind, there is a significant portion of SNA wind with comparable, and even higher temperatures than the SA wind.

As an additional check on the results from comparing the 42 Alfvénic intervals to SNA wind, normalized cross-helicity is used as the sole factor in determining Alfvénicity of the slow wind. The PHZ model is run on successively high thresholds of σ_c: 0.5, 0.7, and 0.8 for high-Alfvénicity wind, and successively low thresholds of σ_c: 0.5, 0.3, and 0.2 for low-Alfvénicity wind. Note that a specified number of points are selected from the entire dataset to meet this criteria to match the total number of data points, about 10,000, in the SA interval dataset in an attempt to keep statistics consistent. As a result, the amount of data does not increase as one lowers (raises) the threshold for SA (SNA) wind. In addition to the σ_c thresholds, limits of 200 and 500 km/s are placed on the velocity, and only years 1998-2003 are considered. As with all other parts of this study, ICMEs are removed.

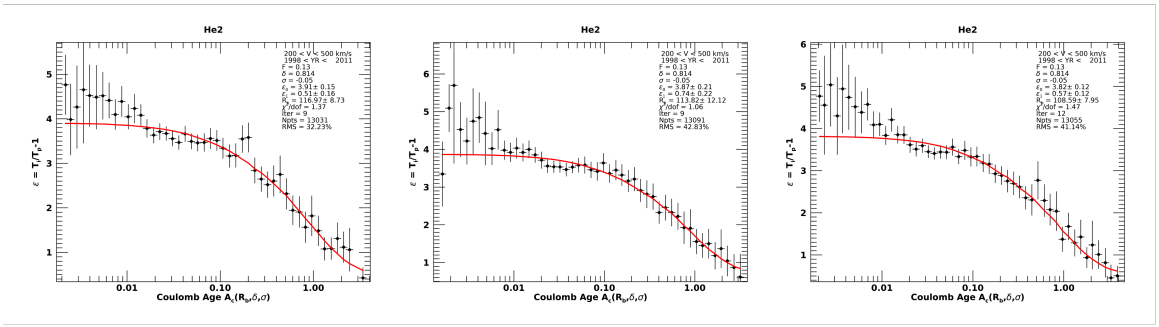

(a)

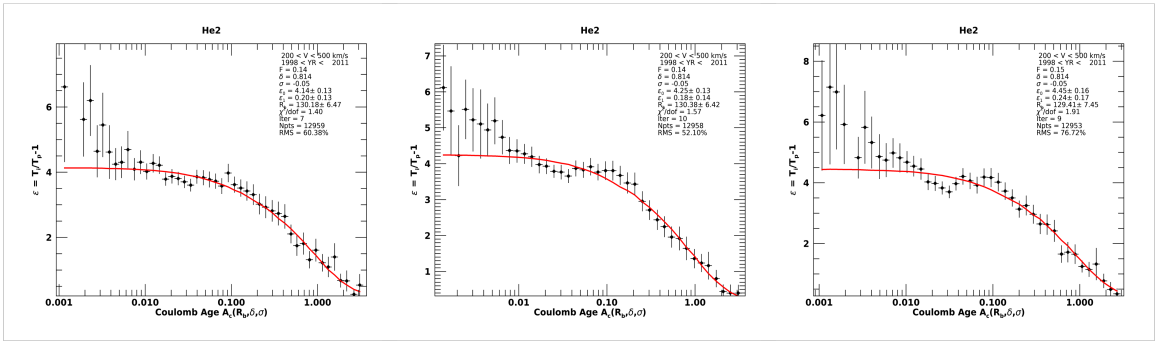

(b)

Figure 3.9 Top panels depict PHZ model results where $\sigma_c < 0.8, 0.7,$ and 0.5, left to right. Bottom panels depict PHZ model results where $\sigma_c > 0.5$, 0.3, and 0.2, left to right.

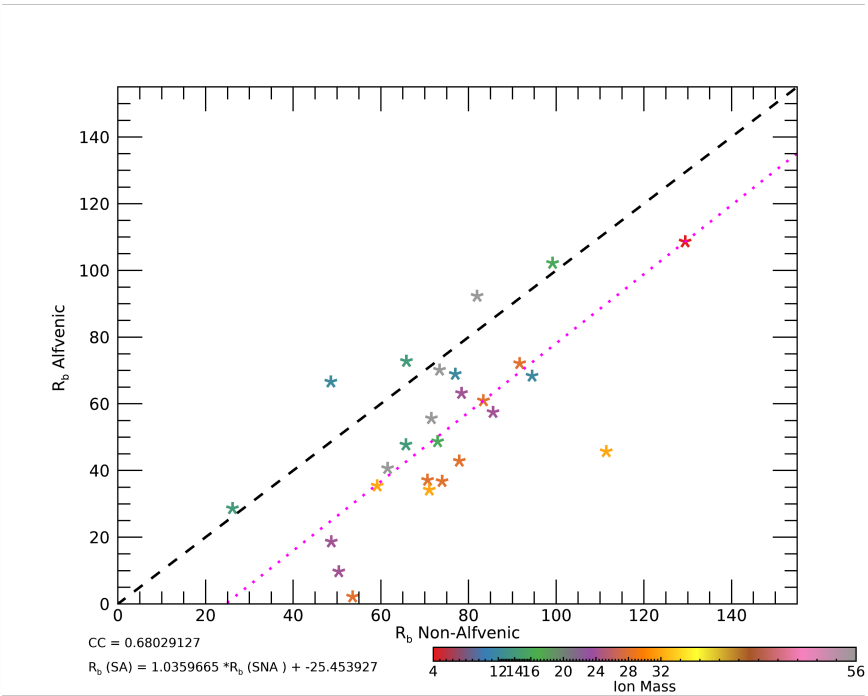

Figure 3.10 Direct comparison of predicted R_b between $\sigma_c > 0.8$ and $\sigma_c < 0.2$

The top three plots in 3.9 depict, from left to right, slow wind with $\sigma_c > 0.8$, 0.7, and 0.5. As the minimum σ_c decreases, the R_b prediction increases, along with a slight increase in boundary excess temperature. The bottom plots in 3.9 depict, from left to right, slow wind at $\sigma_c < 0.5$, 0.3, and 0.2. For both types, moving left to right, the σ_c values depict less mixed, or more "pure" wind types. Lower σ_c values do not produce any trend in R_b, though ε_b does increase slightly with decreasing sigma, as with the high σ_c trend in ε_b. Note that the high σ_c decay curves do not reach A_c as low as the low Ac A_c, though both types are comparable at high A_c. Overall, the low σ_c curves have less uncertainty in each bin, though there is quite a high level of uncertainty in the low-A_c bins. Finally, both the low and high σ_c subtypes exhibit heating in excess of that which is predicted by the model. This excess grows with decreasing Alfvénicity and low σ_c have higher ε than high σ_c. Mass density ratio decreases with increasing Alfvénicity. It can be seen in heavier ions that as σ_c decreases, the rate of increase in mass density ratio increases. We know that proton density is higher in non-Alfvénic wind, so this shows that heavy ion abundances are lower in Alfvénic slow wind, even considering the expected proton density drop.

In Figures 3.10 and 3.11, PHZ model results on high σ_c and low σ_c thresholds are directly compared. Figure 3.10 compares R_b for $\sigma_c > 0.8$ wind on the y-axis to $\sigma_c < 0.2$ on the x-axis. Some of the more abundant ions, including C^{5+} , O^{6+}, and Fe^{10+}, fall along the 1:1 ratio line. Other ions are shifted so that on average, low-Alfveénicity R_b predictions

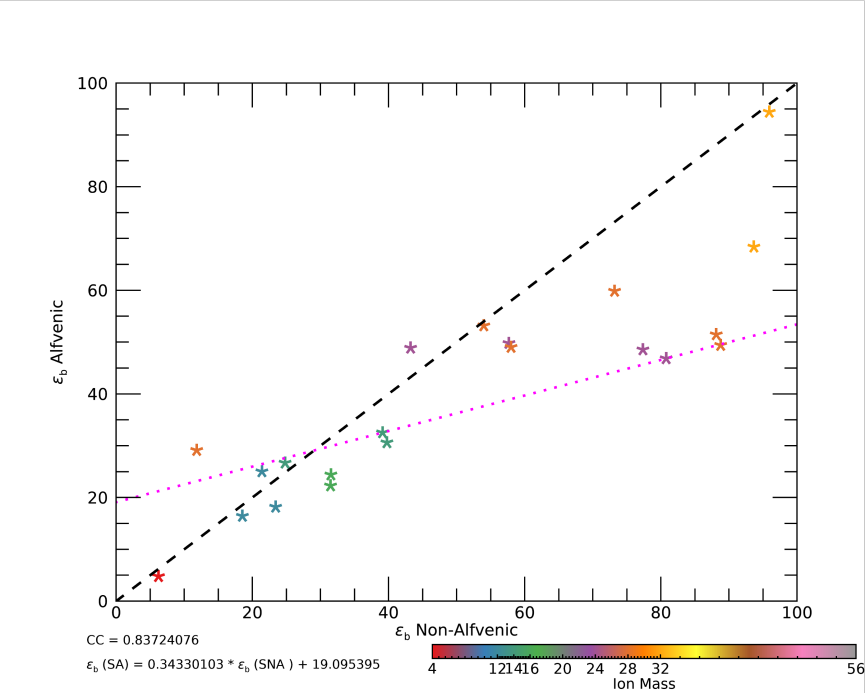

Figure 3.11 Direct comparison of observed ε_b between $\sigma_c > 0.8$ and $\sigma_c < 0.2$

are about 25 R_s higher than high-Alfvénicity. As the σ_c thresholds relax, the differences between the two subsets decrease (correlation coefficient increases and the radial boundary shift decreases).

Figure 3.11 compares ε_b for $\sigma_c > 0.8$ wind on the y-axis to $\sigma_c < 0.2$ on the x-axis. There is good agreement among the lower mass ions, including He^{2+}, C, N, and O. Beyond this, as mass increases, low-Alfvénicity wind exhibits more heating than high-Alfvénicity. Overall, ε_b tends to be higher in the low-Alf wind. Again, as the σ_c thresholds are relaxed, the correlation between high-Alfvénicity and low-Alfvénicity ε_b increases, and shifts in excess temperature decrease. Lower mass ions remain in good agreement across thresholds.

More Alfvénic wind results in a lower PHZ boundary prediction and boundary ε, and the difference between R_b for the two wind types grows as σ_c becomes more stratified. Though the plot is not shown here, the greatest agreement is achieved when < 0.5 is used as the low-σ_c threshold, and > 0.5 used as the high-σ_c threshold, as expected. These patterns are in agreement with results based on the selection of SA intervals, and demonstrate that the distinction between model results for the two wind types may be due to their Alfvénic nature.

3.5 Solar Cycle Variation

Figure 3.12 shows the variation in R_b predicted by the preferential heating zone model and boundary excess temperature in time. Monthly averaged sunspot number is overplotted as a proxy for solar cycle. R_b , ε_b, and ε_r come from model output run on a running window of 1.5 years of data at 0.1 year cadence. Such a broad time window was used because it was the lowest value that still retained reliable statistics in model output.

The top left plot in Figure 3.12 shows the overplotted timeseries of predicted R_b and averaged monthly SSN during the ACE mission from 1998-2011. The top right shows boundary excess temperature overplotted with SSN. The bottom two panels show the same as the top, but for O^{6+}. The R_b and ε_b timeseries were built from 1-year averages, taken at monthly intervals over the entire mission. The endpoints, naturally, will contain less data than the middle points between 1999 and midway through 2010.

The radial boundary prediction for He^{2+} is high during solar maximum, remains high during the initial descending phase, dips during descending minimum, then levels off at a lower distance during solar minimum. The O^{6+} radial boundary follows a similar, though less dramatic pattern, remaining low during solar minimum. Although excess temperature peaks just after solar max for both He^{2+} and O^{6+}, this peak does not sustain and is preceded and followed by values that do not overtly vary in accordance with SSN. Residual excess temperature exhibits a nearly identical pattern to boundary excess temperature (albeit at lower values), and is not shown here.

It is clear here that the radial boundary varies with the solar cycle, in agreement with Kasper and Klein, 2019, while the extent of preferential heating, expressed via excess temperature, does not. Here we seek to determine whether the trends in R_b with q/m or ion mass also have a solar cycle dependence. Figure 3.13 plots four different parameters against monthly averaged sunspot number: predicted PHZ boundary, boundary excess temperature,the correlation coefficient between R_b and q/m, and the slope of the linear fit between ion mass and excess temperature.

The top two panels show the relation for He^{2+}, C^{5+}, and O^{6+}. The top 3 panels each show a distinct shift in behavior at an average SSN of 60. Predicted R_b for the three ions shown here increases in step-like fashion at this point, while boundary excess temperature,which has no clear SSN dependence, becomes more scattered at higher SSN. We showed in the previous chapter that though there are some apparent relationships between PHZ location and ion parameters such as mass, q/m, and q^2/m, overall correlation coefficients tend to be low. Panel three of this figure, however, demonstrates two distinctive behaviors in the correlation coefficient between q/m and R_b: scattered correlations below SSN of about 60,

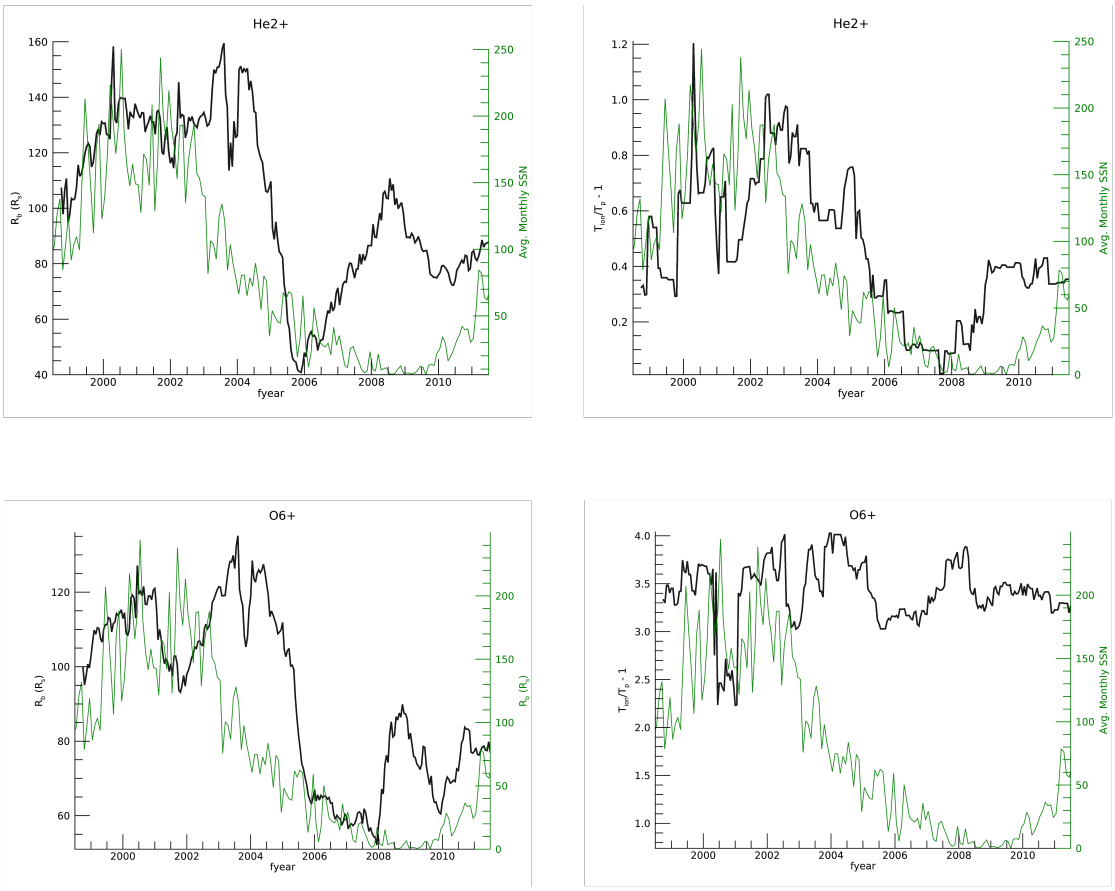

Figure 3.12 Each of these panels depicts a timeseries of an ion parameter overplotted with the monthly averaged SSN. Moving clockwise starting with the top left: He^{2+} R_b, He^{2+} ε_b, O^{6+} ε_b, O^{6+} R_b,

and a decreasingly negative linear relationship (if we were to look at absolute values, a negative dependency) beyond SSN $\sim$ 60. The bottom panel, depicting the slope of the excess temperature vs. ion mass relationship reveals no, or at most a weak, dependence on SSN.

Much of the behavior of these minor ions may be explained by the solar cycle, which is a factor in the overall ion abundances and charge states. During solar minimum, equatorial fast wind is more prevalent than during solar max due to the steady polar coronal holes. Solar max sees higher rates of transient, equatorial coronal holes. Though coronal hole-source wind is remarkably steady and consistent in composition, wind from polar vs. low- to mid-latitude coronal holes can impact the slow wind differently through stream interactions. Additionally, slow wind is highly variable throughout the solar cycle.

Stream interactions are more common during solar minimum and can significantly alter

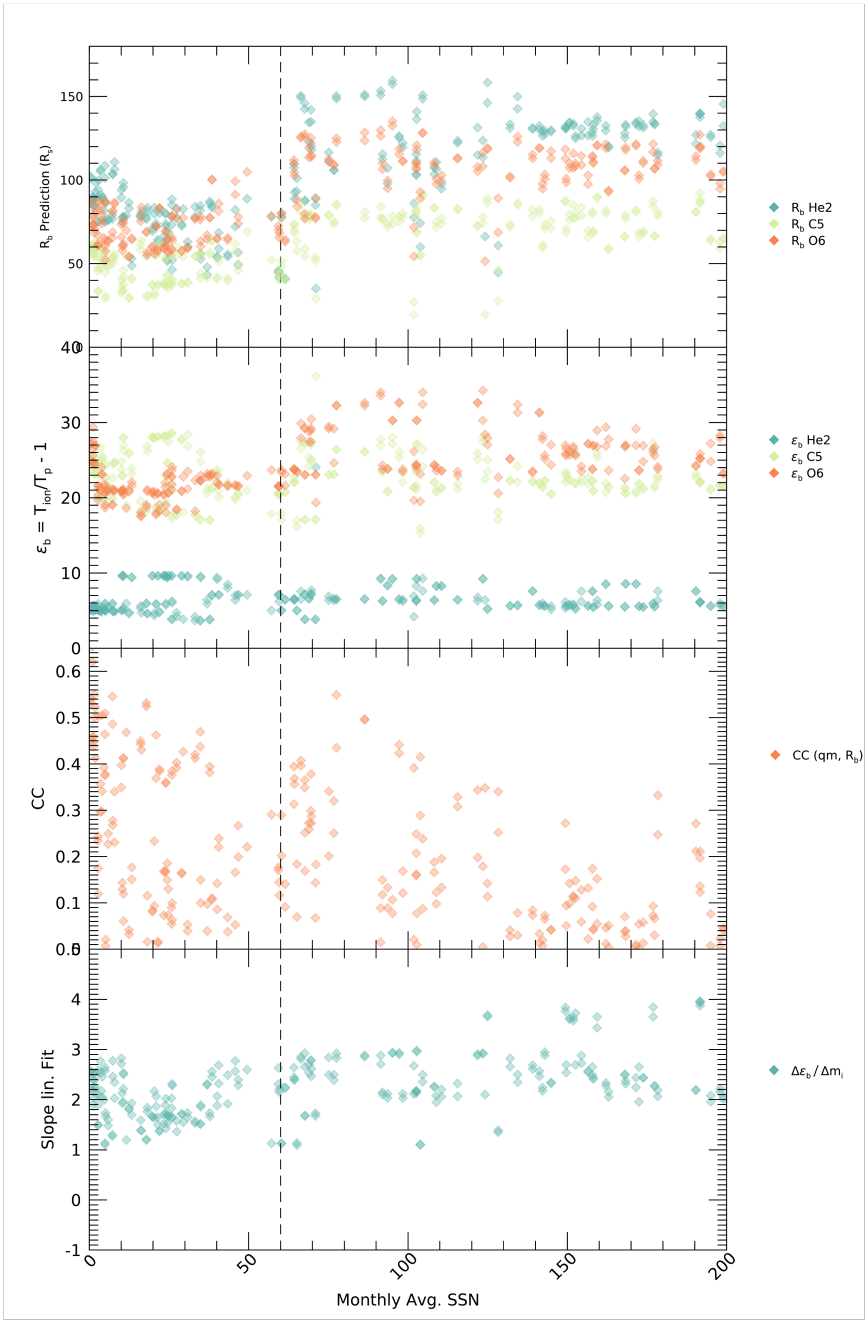

Figure 3.13 Each of these panels depicts an ion parameter plotted against the monthly averaged SSN. From top to bottom: predicted R_b for three abundant ions, ε_b for the same three ions, correlation coefficient of R_b and q/m calculated from model output from all ions, and slope of the linearization of ε_b and ion mass calculated from observed boundary excess temperature of all ions.

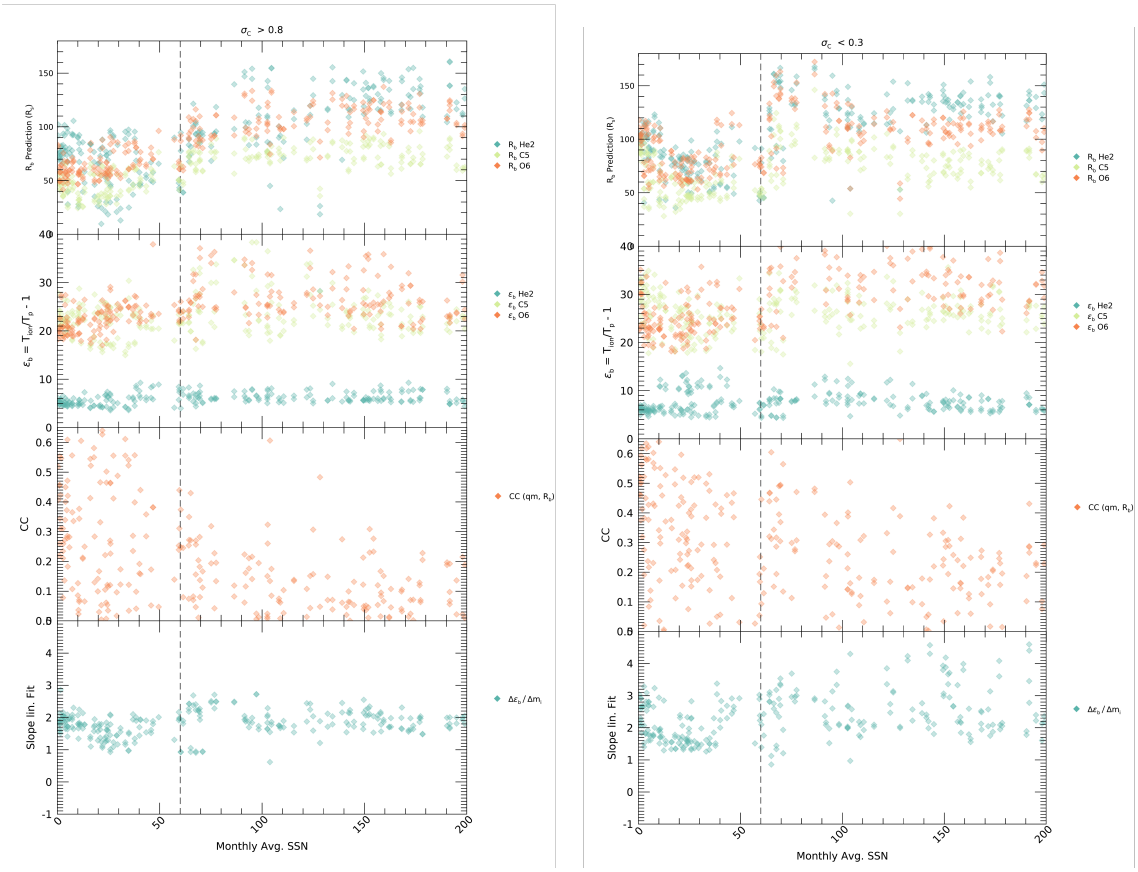

Figure 3.14 Same as above, but panel b shows high normalized cross-helicty wind, while panel c shows low cross-helicity.

the speed and temperature of the solar wind without affecting its composition as it travels out to 1 AU (and beyond). Slow wind ahead of the stream interface is accelerated and fast wind behind it is decelerated. Thus, during solar minimum, defining slow wind by v $<$ 500 km/s, rather than selecting distinct intervals of slow wind, could result in slow wind with kinetics that have been significantly altered by stream interactions. Doing the same during solar max could produce a higher proportion of "pure" slow wind. This could cause deviations from the expected minor ion composition at a given solar wind speed, as the impact of stream interactions increase by the time they reach 1 AU. Wind with streamer-like composition may be streaming faster than expected, while coronal hole-like wind may stream slower than expected.

Further, low-FIP ion abundances are higher and more variable in the slow wind during solar maximum, and lower and steadier during solar minimum. By extension, charge states follow the same pattern, favoring higher charge states and greater variation during solar max and lower, steadier charge states during solar min in the slow wind. The PHZ model results reflect this. When run on the years 2000-2002, encompassing solar maximum, it produced a viable thermalization curve for $Fe^{12\text{-}17+}$ while running the model on 2008-2010, corresponding to solar minimum of SC23, did not produce results for charge states beyond Fe^{11+}. Note that, due to the variation between solar cycles, it would be beneficial, if possible, to look at these relationships across multiple solar cycles.

R_b is driven by solar cycle for alphas and O^{6+} while ε_b is not. There appears to be a correlation of ε_r for alphas, but not O^{6+}. This is consistent for all slow wind, low σ_c, and high σ_c. According to Figure 3.14, high-σ_c wind is more strongly driven by solar cycle than low-σ_c wind. The direct relationship between R_b prediction and SSN, seen in the top panel of both figures, is stronger. The second panels depict ε_b variability, which is lower in , high-σ_c than SNA wind, , low-σ_c lowest when making no distinction based on cross helicity. In , high-σ_c wind, there is a distinct difference in the behavior of ε_b when using 60 SSN cutoff.

The absolute value of correlation coefficient between R_b and q/m (for all ions), shown in the third panel of Figure 3.14 has no dependence on SSN for SSN below 60. Above 60, the range of correlation coefficients diminishes and approaches zero This effect is stronger in , high-σ_c wind than , low-σ_c The linear fit of boundary excess temperature and ion mass (for all ions), shown in the bottom panel of figure 3.14, shows perhaps a gradual increase in slope as well as broadening of range at higher SSN for , low-σ_c wind, while high-σ_c wind remains fairly constant, concentrated around same value on both sides of the 60 SSN cutoff.

3.6 Discussion

3.6.1 Thermalization Curves

When binned in Ac, SNA extends to higher boundary excess temperature and lower residual excess temperature. SA wind clearly has lower bin populations in the high and low A_c range, which could does impact the model's R_b prediction. We have seen that the bulk of SA wind densities are in the same range as SNA wind, but high SA densities are depleted when compared to SNA. We've also shown that collisional age is more heavily influenced by the protons at the high and low end of the density distribution than at the peak. Thus, the lack of SA data at high A_c is consistent.

Model results on the full $\sim$13 years of data have been discussed for comparison. Clearly, limiting the dataset to 42 intervals during the ascending solar max phase (1998-2002) has impacted statistics. The trends seen in the full dataset are not apparent, due either to the inability of the model to resolve higher charge states and heavier ions, or some intrinsic quality of the wind types themselves. SNA does consistently predict higher R_b and slightly higher ε_b, despite being limited to a comparable amount of data.

The lower collisionality of SA wind coupled with reduced statistics are likely the cause of these results. Figure 3.4c shows that at high A_c, SA wind has no temperature ratios below 1 (it does, however, have distinct peaks at $T_i/T_p = 1$ in the lower A_c regimes).

Additionally, SA wind possesses composition similar to that of fast wind/wind originating from open field regions at the sun. In fast wind and open-field slow wind, low-FIP ion abundances are lower, and lower charge states overall are favored. In closed-loop, generally associated with non-Alfvénic wind, low-FIP ion abundances are enhanced, and higher average charge states are favored. Figures 3.6m and 3.6n clearly shows that, despite having a similar number of data points, and no significant difference in bin population, the PHZ model produces results for more of the lower charge states of heavier ions. The inclusion of more charge states in the SNA wind gives a greater sense of charge-dependent trends than in SA, though not as clearly as when the full dataset is analyzed.

The PHZ model predicts very low R_b for SA iron ions (this occurs again in the next chapter when running the model on HIS data), and does not resolve some of the higher charge states. Due to their large mass and broad range of q/m, the iron ions can have a disproportionate impact on trends in these two quantities. Running the PHZ model on the full SWICS dataset results in trends that are consistent with and without iron ions. Figure 3.6j demonstrates how the presence of only one iron charge state, one sulfur charge state, and one silicon charge state impacts the excess temperature scaling with mass. Low mass ions are in good agreement with each other across solar wind types, but higher mass ions

can dramatically increase this scaling.

Figures 3.6k, and 3.6l reflect the heating of SNA and general slow wind in excess of the modeled heating prediction at low A_c along the decay curve. SA exhibits the same behavior (see leftmost column of Figure 3.5), though it is far greater in the SNA wind. This disparity grows with increasing ion mass and charge, reaching very high values for Fe^{13+} and beyond. This has a few implications: 1) ongoing heating or thermalization processes in addition to Coulomb thermalization, and/or 2) not accounting for differential streaming in the collisional rate calculation.

This model does not make any assumptions about sources of heating within the PHZ boundary; however, there still may be sources of free energy beyond the boundary that act in opposition to the thermalization process. Interactions between ion VDF cores and non-thermal features of the VDF (double alpha peaks), heating of slow wind in the compression region of stream interactions. Wave particle interactions have not necessarily ceased, and even if confined to the corona/low heliosphere, could have ongoing effects that diminish gradually with distance [92].

Kasper et al., 2017 [1] point out that preferential heating can continue beyond the PHZ boundary; R_b just denotes the point at which Coulomb collisions become significant enough to thermalize the plasma. At low A_c, however, excess temperatures are reduced at higher rates than accounted for by Coulomb thermalization, especially if the ion-proton differential velocities are high. Collisional frequencies between species are reduced when those species stream at different speeds.

In this work, differential streaming is approximated rather than using the true value. Theoretically, using a slightly higher collisional frequency would result in either a shift to higher A_c or a steepening in the ε decay curve. We have compared model output with the approximate and true differential streaming, however, and R_b predictions, ε bins and dependencies on ion properties are not significantly impacted by using the approximation or the “true" value.

3.6.2 Ion Dependencies

In Chapter 2, slow wind and all speeds wind were compared in order to determine the impact of removing fast wind on the model's R_b prediction and boundary excess temperature. Since SA wind exhibits qualities of slow and fast wind, most notably a reduced collisional frequency, it was expected that SA wind would not be as thermalized at 1 AU as SNA wind, and that its thermalization curve might differ too greatly from the model for it to converge. The model did run for some of the SA ions, but the results did not align with expectation.

The SA R_b predictions are generally quite low as well as observed ε_b. We've already shown that, although SA wind ions peak at higher temperatures than SNA wind, much of the SNA temperature distribution achieves temperatures as high as or even higher than the SNA curve. Thus boundary excess temperature can be lower in the SA wind. It does not thermalize to the same degree as SNA wind, and if a "bump" is present for a particular ion, it is more pronounced in the SA wind than SNA.

Due to higher statistics, the 1998-2002 "all slow wind" curve contains most of the previously studied charge states. Note that 1998-2002 covers solar max, and the correlations with q/m and ion mass are not as strong here as they are over the entire dataset (1998-2011). Though not pictured here, the similar correlations are seen in the 2-hour data are also present in the full 12-minute dataset (albeit with lower R_b predictions, see Appendix B).

Ions with lower q/m had higher radial boundaries in the previous chapter. R_b also scaled directly, albeit weakly, with ion mass. The lack of clear scaling in the SA wind could either be due to poor statistics (an attempt was made to at least match the number of data points between SA and SNA wind), or due to qualities of the SA wind. SA composition is like the fast wind, thus it favors lower charge states and high-FIP ions. This is evident in the lack of results for many Fe, Si, and Mg charge states. Some of the missing ions are present in the SNA counterpart. Since these ions are missing, the high-mass and low-q/m portion of the correlation plots are not present for SA wind. That SNA appears to have a slight correlation in R_b with mass and none in q/m or q^2/m might be attributed to its non-Alfvénic nature, but enough data to overcome the low statistics of this data-set would be required to confirm this. If one were to assume that these results are reflective of actual conditions, it might be noted that the R_b predicted in SA wind ions are all in the vicinity of the range of distances associated with the Alfvén surface.

The ε_b vs. m_i fit in the SA wind is in agreement with the T16 curve only because of the absence of some of the heavier ions. SNA wind and general slow wind both are heated in excess of the T16 curve. This is likely due to solar cycle; Figure 3.14 demonstrates that while the mass dependence of excess temperature does not vary with SSN in the SA wind, it increases and broadens in range in the SNA wind. Since the plots in 3.6 are limited to solar maximum, the higher excess temperature values in SNA are to be expected.

Between SA and SNA, only the few iron charge states in SNA wind exhibit any ε_b vs q/m dependence. This result goes against initial expectations, as it may be attributed to lack of data points in some of the less abundant ions, and it is where distinctions between SA and SNA wind would have been most likely. The ε_b vs q/m only presented weakly in higher mass ions in the 2-hour data. Note, however, that in the general slow wind from

1998-2002, the q/m dependence is actually quite strong, indicating either a dependence on solar cycle, that the current SA and SNA results could be improved with more data, or a combination of both.

3.6.3 Solar Cycle and σ_c

Identifying high-Alfvénicity wind by σ_c only results in higher R_b predictions than the SA intervals, but 3.10 shows that SNA/low-Alfvénicity wind still has higher R_b and boundary excess temperature. Low σ_c wind is more collisional, causing it to thermalize more and achieve lower ε_r than high-σ_c wind, despite heavier ions having a higher starting ε_b.

Kasper et al., 2019 [2] showed that the zone of preferential heating varies with the Alfvén surface, which fluctuates in response to solar magnetic activity and thus has a natural variation with solar cycle. Since the PHZ zone is tied to solar activity, then a solar wind type from originating from a source that also fluctuates with solar activity would have heating and a PHZ boundary that reflects this activity, while a solar wind type with a dominant heating source that is independent of solar activity would not.

He^{2+} and O^{6+} ε_b do not exhibit any strong ties to the solar cycle in any of the wind types, but in low-σ_c wind, ε_b vs m_{ion} dependence does, as shown in 3.14. This is can likely be attributed to a combination of increased scatter at higher SSN as well as heavier ions (Mg, Si, Fe) being more sensitive to magnetic fluctuations. This may tie into an observation made in Chapter 2. A high radial boundary does not necessarily correspond to higher heating. An ongoing, localized preferential heating source would likely produce a distribution of boundary excess temperatures well correlated to the radial boundary height. The lack of correlation may imply a source of heating confined to the corona (or within a few solar radii), and the impacts of thermalization not becoming significant until tens of solar radii later.

General knowledge of the solar wind variations in accordance to the solar cycle are as follows: 1) fast wind dominates during solar minimum, slow and SA wind during solar max, 2) speeds and charge states are bimodal during solar minimum but cover a continuous range during solar max, 3) elemental abundance ratios are low and steady during solar minimum and higher and more variable during solar maximum. Observations according to figures 3.13 and 3.14 are as follows: High- σ_c wind exhibits 1) a stronger, better ordered correlation between R_b prediction and SSN, 2) steadier, less scattered ε_b, 3) a more pronounced difference in the reduction of correlation coefficients of R_b vs. q/m, and 4) less variation in the slope of ε_b vs. m_{ion}, though there is a distinct increase in variation at SSN $\sim$ 60, than low-σ_c wind. Why behavior seems to change at SSN $\sim$ 60 is not entirely

known. Looking at SWPC plots of monthly SSN during SC23, there is a jump from 50-80 between January and February 1998, which appears to be an uncharacteristically large monthly change for that period of the solar cycle. There are a few average SSN in the vicinity of 60 during the descending maximum phase, however.

Returning to the question of localized versus ongoing heating, the isolation of low-σ_c wind reveals both an increase and a broadening in range of the ε_b vs. m_{ion} dependence with SSN. This effect is absent in high-σ_c wind, which indicates that although highly Alfvénic and non-Alfvénic wind both experience mass-dependent heating within the PHZ, the dominant heating source for non-Alfvénic wind experiences fluctuations that correlate to the solar cycle while the highly Alfvénic wind's dominant heating source might remain steady regardless of solar cycle-associated activity. Alternatively, it is known that SA wind is the predominant slow wind during solar maximum while SNA wind is predominant during solar minimum. The perceived increase/broadening with sunspot number may be a result of reduced model performance due to lower statistics during solar maximum.

R_b vs. m_{ion}, q/m, and q^2/m has been shown not to be particularly strong. Note, however, that the absolute value of the correlation coefficient between R_b and q/m covers the full range between 0 and 0.6, but goes to zero as SSN increases for both solar wind types. This reduction to zero is far more dramatic in high-σ_c wind. Despite the correlation itself never being particularly high, the distinct behavior in wind types throughout the solar cycle may be significant. During solar max, any correlation between R_b and q/m goes away. This is in line with slow wind features being a continuum during solar max, but well ordered during solar minimum. The more pronounced reduction of the correlation coefficient in high-σ_c wind could be due to either lower population and thus reduced model performance during solar max. If this were the case, if low-σ_c wind is as sensitive to the solar cycle, it would exhibit the opposite trend, with higher correlations during solar max. Since R_b is tied to Coulomb collisions/collisional age, its location could be influenced by reduced/enhanced ion-proton mass density ratios for low-/high-FIP elements in high-σ_c wind during solar minimum. A broader range of thermal speeds during solar max could also cause more scatter in Coulomb collisional frequency, leading to more scatter in predicted R_b. This effect, however, would be stronger in low-σ_c than in high.

The overall steadiness of the features of high- σ_c wind throughout the full range of SSN is similar to the behavior of the fast wind throughout the solar cycle, while the low-σ_c wind increases in variability, forming more of a continuum during solar max.

3.7 Conclusions

The preferential heating of Alfvénic and non-Alfvénic slow wind were examined. First, intervals of SA wind during solar maximum of SC 23 were provided by Rafaella D'Amicis. In order to determine whether or not the slow wind is collisional *enough* to fall under the assumptions of the preferential heating zone model, the distributions of temperature ratios in low, low-mid, mid-high, and high regimes in collisional age were compared. This was done for SA, SNA, and, and Fast wind and it was shown that, in agreement with previous work, SA wind is more collisional than fast and less than SNA. Distinct collisional rates for heavy ions with protons for all three wind types were found.

To determine the extent to which collisionality depends on wind type as opposed to density and temperature (thermal spread), the thermalization of the three wind types in narrower bands of density and temperature are examined. We see that although there is a strong dependence of collisional frequency (and collisional age) on density, and to a lesser extent, temperature, the three wind types exhibit distinct behavior in these narrow bands. In general, SA wind often has a qualitative form similar to the fast wind, while it quantitatively it is closer to slow. From this analysis, we conclude that it will be possible to run the PHZ model on the slow-Alfvénic wind.

The results of the PHZ model on SA and SNA wind are not as expected. SNA is found to have higher predicted R_b and higher observed ε_b. It may be that the previous assumption that SA wind is collisional *enough* was wrong, and the model is tending to minimize for SA ions. Some theories are discussed assuming the results for SA wind are reliable, namely the lower abundance of heavier elements and higher charge state ions in SA wind as well as SA wind being predominantly heated at the corona while SNA wind's predominant heating may either extend farther away from the Sun or be local. The model output dependencies on ion properties do reveal the compositional differences between the two wind types. SA wind has lower abundances heavy ions in general, and in low charge states of most elemental species. This could impact the reliability of the SA model results.

Timeseries of predicted R_b, ε_b, and ε_r along with sunspot number are shown, revealing that although the radial boundary location is well correlated to the solar cycle, the actual heating that has occurred is not. We also show two distinctive behaviors in R_b and ε dependencies on q/m and mass.: fairly constrained correlations at low SSN, and more variable at high. This is in line with the fact that slow solar wind composition and parameters are typically well-ordered and bimodal at solar minimum, but highly variable during solar max.

To determine whether the SA/SNA results are reliable or due to poor statistics, we run the PHZ model on wind subtypes selected only via an Alfvénicity threshold. Doing so is

not as robust as the usual selection criteria, as slow-Alfvénic wind has distinct, identifiable features beyond normalized cross-helicity and can persist for periods of hours to days. The R_b prediction in the high-Alfvénicity wind is still higher than in the SA intervals, but overall R_b and ε_b are still consistently and distinctly higher in the low-Alfvénicity wind. Though these trends are not shown, through direct comparison of the high- and low- Alfvénic wind it is seen that as the minimum and maximum σ_c thresholds are relaxed, the two types become less distinct.

The solar cycle analysis was repeated for low- and high- Alfvénicity wind, finding that high- σ_c wind exhibits behavior similar to that of fast wind over the solar cycle, and that the two slow wind types show correlations (or lack thereof) that are telling of two distinct heating sources, one that fluctuates with the solar cycle, and one that does not.

This work could be improved if there were enough slow-Alfvénic intervals for a robust statistical analysis. This is not the case. Many studies of SA wind have tracked and analyzed specific intervals. Higher time resolution on the composition data would also result in more reliable calculations of differential streaming as well as σ_c, which are both known to occur on scales comparable to the 12-minute cadence of the SWICS data. Finally, directional temperatures/thermal speeds would be required to determine whether or not SNA $\varepsilon_b >$ SA ε_b is due to either higher mass or higher charge-to-mass ions having a higher perpendicular and lower parallel temperature.

To expand on this work, one could examine how the power spectra change with solar wind type and solar cycle. As SO/HIS encounters more SA wind during its mission, this analysis can be repeated on that data.

CHAPTER 4

Heavy Ion Kinetics from 0.28-1 AU

4.1 Introduction

The first two chapters of this work, in a way, deal with the radial evolution of the solar wind. Overall, collisional age increases with distance from the Sun, but at any given distance there still may be a broad distribution in observed collisional ages. The solar corona is marked by a rapid drop in density [45]. This increases the Coulomb collision time/decreases the frequency of ion-ion collisions, resulting in a nearly collisionless solar wind. This is compounded in the fast wind, which, due to its coronal hole origin, exhibits even lower density. Thermalization due to Coulomb collisions can only be achieved by the accumulation of encounters over long timescales, which is represented as collisional age. In low-speed solar wind, more collisions can accumulate due to the longer propagation time as well as the higher density, and the evolution toward thermal equilibrium happens more rapidly and over a smaller range in distance than in the fast-streaming wind. Therefor, likelihood of measuring collisionally young wind is certainly higher at 0.3 AU than at 1 AU, since far more collisional times have elapsed, and ions clearly undergo thermalization as radial distance increases [54].

The solar corona is marked by a rapid drop in density. This increases the Coulomb collision time/decreases the frequency of collisions between ions and electrons, resulting in a nearly collisionless solar wind. This is compounded in the fast wind, which, due to its coronal hole origin, exhibits even lower density . As such, thermalization due solely to Coulomb collisions can only be achieved by the accumulation of encounters over long timescales, which is represented as collisional age. In low-speed solar wind, more collisions can accumulate due to the longer propagation time as well as the higher density, and the evolution toward thermal equilibrium happens more rapidly and over a smaller range in distance than in the fast-streaming wind.

Helios [137], Ulysses [138], and ACE [110] have enabled in-situ plasma measurements

at varying distances. More recently, the addition of Parker Solar Probe [39] and Solar Orbiter have and will continue to provide a wealth of plasma kinetic data over a range of heliocentric distances. To date, HIS on SO has become the charge-resolving plasma mass spectrometer with the closest approach to the Sun [111].

Marsch et al., 1982 [53] demonstrated the radial evolution of non-thermal features of the solar wind, such as unequal temperatures between protons and alphas, streaming velocities, anisotropic velocity distributions where $T_{p\perp} > T_{p\parallel}$, and proton beams. They showed that non-thermal behavior diminishes between 0.3 and 1 AU in the slow wind, and to a lesser degree in the fast wind. They also found that $T_{\alpha\perp}/T_{\alpha\parallel}$ is not as enhanced as $T_{p\perp}/T_{p\parallel}$ ([53];[139]).

Also using Helios data, Hellinger et al., 2011 [85] (H11) and 2013 [86] (H13) calculated the radial scaling of proton densities, temperatures, and heat fluxes in the fast and slow wind. The density scaling was significantly lower than the expected $(r/r_0)^{-2}$ for spherical expansion. The temperature scaling in the fast wind was much slower than the double-adiabatic prediction ($T_\perp \propto r^{-2}$ and $T_\parallel \propto Constant$) in the perpendicular direction, and faster in the parallel. Slow wind temperatures also reduced slower than the expected $T \propto r^{-4/3}$ in adiabatic cooling. The rate of decrease is highest in the direction perpendicular to the magnetic field in the fast wind.

Similarly, Perrone et al., 2018 [87] calculated fits to the decrease in temperature, density, and magnetic field for sustained, pure, high speed streams as they traveled outward. A key difference between their work and previous, similar work with the Helios data is that they isolate the core of the proton VDF, whereas other studies have used the entire distribution, including proton beams. Their key findings were: 1) that the radial density scaling is actually quite close to -2, 2) a deviation in the magnetic field from the Parker spiral, 3) an increase in proton entropy, and 4) a decrease in proton-proton collisional frequency with radial distance. Their power law for proton temperature radial evolution differs from the H11 scaling, as do the $T_\parallel$ and $T_\perp$ scaling.

Temperature ratio evolution has been extensively discussed in the background of Chapter 1, so the radial and collisional evolution of differential streaming will be the focus here. Protons and alpha particles are known to differentially stream at some fraction of the Alfvén speed ([140];[59]), but this velocity difference is impacted by factors such as, bulk speed, distance from the Sun, stream interactions, ICMEs, the presence of Alfvén waves [141], etc.

Robbins et al., 1970 [88] first detected differential streaming when calculating alpha/proton density ratios. Differential streaming in the slow wind has a radial dependence at low collisional ages and radial distances, as demonstrated in Neugebauer et al., 1998

and Mostafavi et al., 2022 ([89];[90];[63]). Comparisons of PSP data [63] with observations from Helios and Wind reveals that instances of protons streaming faster than alphas increases with radial distance. They find a correlation between instances of $v_p > v_\alpha$ and radial distance, as well as a predominance of double peaks (positive and negative) in fast wind. Durovcova et al., 2017 also show in a comparison of WIND/SWE and Helios data, that these radial dependencies are not present in the fast wind. Johnson et al., 2024 [91] demonstrated that Coulomb collisional analysis can be used close to the sun to accurately predict differential streaming distributions at 1 AU.

Pre-SO, the Fast Imaging Plasma Spectrometer (FIPS) aboard MESSENGER had taken the closest solar wind composition measurements to the Sun [92]. Gershman et al., 2012 analyzed heavy ions up to 40 amu/e from March-December 2011, between 0.3 and 0.5 AU. They found that minor ion and proton velocities do not significantly differentiate until they reach speeds of about 450 km/s, above which differential streaming becomes significant. They also show alpha-to-proton temperature ratios of about 9. This is higher than temperature ratios shown in latter work (i.e., [65];[60];[58]; [1]), however FIPS took measurements much closer to the Sun, where temperature ratios could indeed be higher than those found when binning in collisional age from observations at 1 AU. They also show power law spectra spanning the inertial and dissipative ranges at different radial distances (ACE and MESSENGER locations), finding evidence of ion-cyclotron resonance at higher power for higher q/m ions. They show that magnetic power spectral density is higher at 0.37 AU than at 1 AU, demonstrating the dissipation in energy with radial distance. They also show that heavy ions, which typically have lower q/m (always lower than protons), interact with wave turbulence at lower frequencies/higher power, priming them to receive larger amounts of energy from MHD waves. Finally, they argue that the lack of jumps/discontinuities in the spectra at the ion gyrofrequencies may indicate that heating due to wave dissipation is non-local.

HIS allows a look not only at the composition of heavy ions, but also at their radial kinetic evolution. In this chapter, we examine the radial scaling of heavy ion temperatures and densities (see Section 4.2.2), determining whether or not these parameters decrease with a simple mass (temperature) and density ratio (density) proportionality. These curves are compared to H11, H13, and P18. We also directly plot the proton-ion thermalization curves with both collisional age and radial distance. Finally, we run the PHZ model on the HIS data to determine consistency with Chapters 1 and 2 and the impact of varying radial distance on the model output.

4.2 HIS Data (SWA-MAG)

PSP and SO, as well as earlier missions such as Ulysses and Helios I and II have each allowed a unique look at the Sun, solar atmosphere, and solar wind through the variation of radial distance and latitude. Like Ulysses, SO carries a mass spectrometer that allows for the characterization of the solar wind composition, as well as the measurement of the velocity distribution function of the heavy ion species. By measuring these heavy ion VDFs along SO's trajectory, which has orbited as close as 60 R_s, HIS data can give insight into the radial evolution of nonthermal properties of heavy ions due to preferential heating as well as the thermalization processes.

SO launched in 2020 and began science operations in 2021. In June, 2020 it achieved its first perihelion of about 112 solar radii. As of now, it has achieved its closest approach of about 60 solar radii. Throughout the mission its orbital inclination will rise to about 18 degrees and its extended mission will see a rise up to 30 degrees out of the ecliptic. This work uses data from January 2022 through March 2023. During this time, SO traversed distances between 1 AU and 60 R_s ([38];[111];[142]).

4.2.1 SWA

SWA-MAG consists of two suites of instruments. Solar Wind Analyzer (SWA), which includes the Proton and Alpha Sensor (PAS), which measures the proton and alpha velocity distribution functions, and HIS, the heavy ion sensor, which measures minor ion composition and kinetics. MAG, a fluxgate magnetometer, measures the magnetic field vector.

PAS and HIS were both in this work. Proton data are averaged down to the 10 minute HIS cadence. For much of this work, only validated He^{2+}, C^{5+}, O^{6+}, and Fe^{10+} are used, but more ions with acceptable statistics are included in order to examine trends in excess temperature and radial boundary. In all cases, quality flags are used as a first pass for all three data sources.

Originally, MAG was used to calculate the Alfvén speed for observations of normalized differential streaming. Either the 10-minute cadence of HIS or data gaps at different times in all three instruments rendered normalized differential streaming unable to be resolved. Instead, differential streaming presented later in this chapter is non-normalized.

4.2.2 HIS Densities

HIS heavy ion densities have yet to be fully calibrated. In order to work around this, the mean SWICS 2-hour Level 2 data n_i/n_p from July 1998 - October 1999 was used as a

standard. These dates were selected to correspond to a similar portion in solar cycle that SO/HIS sees between January 2022 and March 2023. Note that limiting the SWICS data used in the correction factor to the corresponding portion of SC 23, rather than using the entire dataset for the correction factor does not improve overall fits. This could be attributed to SC 25 being more active than SC 23 during the ascending maximum phase. Still, the July 1998 - October 1999 dates are used to keep this approximation as analogical as possible. The uncalibrated density values are each multiplied by a correction factor that would have them achieve the same mean n_i/n_α as SWICS during this period.

This assumption is likely to impact results in different ways. On one hand, due to differences in calibration, location, and the spatial variation of the solar wind, different instruments often measure different densities over the same time periods. The PHZ model is quite sensitive to these differences (see Appendix B). Future work to better calibrate HIS densities by comparing is SWA-PAS and historical values from WIND-SWE and ACE SWEPAM and SWICS could improve the interpretation of our work. Although SWICS densities have been cross-calibrated with WIND, differences in time series are still observed (See Figure 7, [19]). The previous statements stem from the assumption that mean SWICS density ratios serve as a valid standard for what HIS measures.

Additionally, using the mean SWICS n_i/n_p does not account for deviations from the expected -2 power law for spherical expansion. We have seen from [87] that in fast streams, the proton density power law is very close to -2, but this does not necessarily apply to minor ions traveling at lower speeds as processes may occur that impact the cores of the proton and minor ion VDFs differently. If different ions have different radial scaling laws, density ratios will shift with distance. This also has implications for a major assumption of the PHZ model, which assumes the same radial densities for all (both) species [1].

The following section shows the radial evolution of density and temperature for protons, He^{2+}, C^{5+}, O^{6+}, and Fe^{10+}, post correction factor for the densities. Though it was not done here, the results of this chapter could be improved by starting with the current “corrected" densities, setting SWICS densities as boundary condition at 1 AU. The radial power laws found here should still hold since the correction factor used for each ion was a constant. The new correction factor would be the leading coefficient to the power law, though there is still quite a lot of scatter around the current fit.

The use of unreleased versions of the data and employment of such approximations render this chapter unsuitable for publication. This work is an approximation, or demonstration of what we may see from the science level data later on, and provides a foundation for future study of this topic. Note that proton densities are taken from PAS public data, which has been calibrated, and have a far greater impact on ion-proton collisional fre-

quency calculations than ion densities. Calculations of excess temperature with collisional age, however, do depend on mass density ratio. All other base parameters (temperature, velocity, magnetic field) are calibrated. The current density correction will no longer be necessary, of course, once HIS heavy ion densities have been calibrated.

4.3 Thermalization of Solar wind with Radial Considerations

4.3.1 Radial Trends in Kinetic Moments

This section contains the radial evolution of heavy ion temperatures and (corrected) density. For sake of brevity, only protons, alphas, and O^{6+} are shown here, though comments on overall trends will include all ions. For $C^{5+}$and Fe^{10+}, see Appendix A. Figure 4.1 shows the radial trends in density and temperature for protons, divided into two solar wind types (not enough SA intervals have been identified to date for analysis. Keeping the simple slow/fast classification for this investigation, fast wind is in the top row, and slow speeds on the bottom. Figure 4.3 shows the same for alphas, and 4.4 shows the same for O^{6+}. Densities are in the left column, temperatures on the right. In all plots, the solid black line is the fit to HIS data, the green line is the fit to Helios fast wind proton data from [85] (H11), the blue line is the fit to Helios slow wind proton data from [86] (H13), and the magenta line is the fit to Helios "pure" core VDF fast wind data from [87] (P18).

Radially, fast and slow protons, exhibit very distinctive behaviors in this dataset. Density fit coefficients are shown in Table 4.1 and temperature coefficients in Table 4.2. Slow proton densities (Figure 4.1c) are about 30% lower than the H13 fit at 0.3 and 1 AU and fast wind proton densities (Figure 4.1a) are about 35% higher than H11 and P18. Note, however, that the H11 and P18 curve both pass well below the densities measured by PAS, and the power laws are in good agreement, particularly slow protons with H13 and fast with H11. Overall, fast densities here show little variability at 0.3 AU, likely due to fewer measurements at this distance, and scatter increases to about a full order of magnitude about the fit by 1 AU. H13 exhibits similar behavior, though variability at 0.3 AU is nearly two orders of magnitude and reduces to 1 by 1 AU. The variability in H11 is more consistent, with about 1 order of magnitude of variation about the fit throughout, whereas the scatter in the slow wind measured by PAS is somewhat larger. Disagreements may be explained by different criteria to select fast and slow wind. P18 identifies pure, flattop streams, H11 uses $v > 600$ km/s, and H13 uses $v < 400$ km/s, while here 500 km/s is used as the upper and lower limit for slow and fast wind, respectively. The 500 km/s speed cutoff was chosen

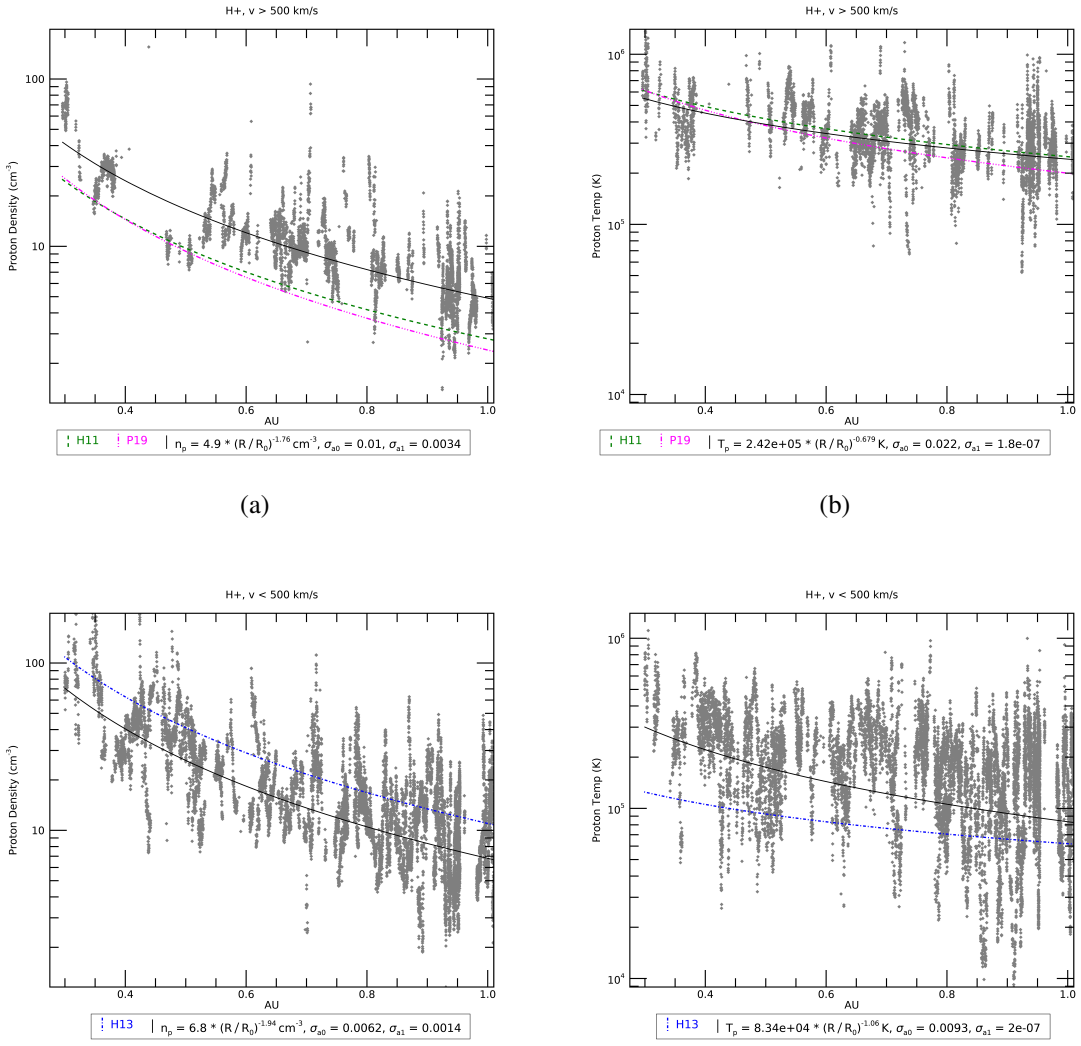

Figure 4.1 Radial evolution of solar wind density and temperature for protons. Fast densities are shown in panel (a), fast temperatures in panel (b), slow densities in panel (c), and slow temperatures in panel (d). Fit is overplotted in black. Previous observations by Hellinger et al., 2011 , 2013, and Perrone et al., 2018 are overplotted in green, blue, and magenta, respectively. The top row shows the trends in fast wind and slow wind in the bottom.

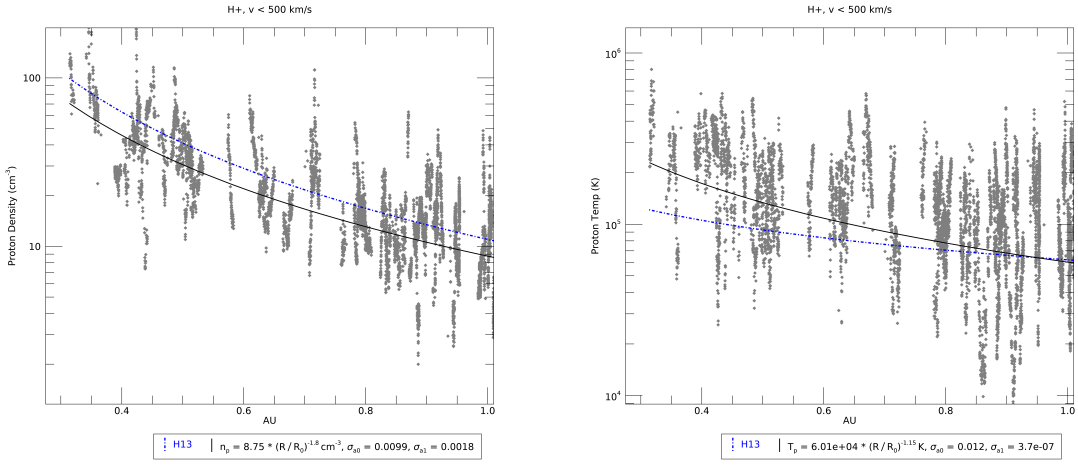

(a) (b)

Figure 4.2 Radial evolution of slow solar wind density and temperature for protons using 400 km/s as the upper limit.

to maintain consistency with the previous chapters. Using the 400 km/s cutoff in the slow wind improves agreement with the H13 fits for density and temperature, but using the 600 km/s does not improve agreement with previous fast wind fits. This is the case for protons and all minor ions considered here. Figure 4.2 shows this for protons. Flattop fast streams are not identified for this work. The use of a less strict limit can result in higher densities in the fast wind and lower densities in the slow, which is what we see here. Additionally, HIS data so far only covers the ascending phase of solar minimum, which could impact overall flux density in the ecliptic plane.

For fast wind protons (Figure 4.1b), the trend in temperature is in good agreement with P18 and H11, about 15% lower at 0.3 AU and passing between P18 and H11 at 1 AU. The radial scaling law is nearly the same as H11 (the P18 scaling is much closer to -2). Slow wind proton temperatures (Figure 4.1d), are twice that of the H13 curve at 0.3 AU, $\sim$25% higher at 1 AU, and have a power law scaling nearly twice that of H13. The same factors mentioned before contribute to differences between these fits and previous fits. Note, however, that the H13 curve does not capture the temperatures measured by PAS. Even the fit to the HIS data appears to pass below the bulk of the temperatures. It is known that slow wind has higher levels of variability than fast wind. Here and in H11, the fast wind temperature varies by over an order of magnitude while the slow wind here and in H13 varies by nearly 2 orders of magnitude over all radial distances. Impacts that this could have on the radial trends will be addressed in the discussion. Qualitatively, the H11 fits for

fast wind density and temperature are similar to the PAS fits. The P18 fits also match well. The H13 fit and PAS fit are in good qualitative agreement for slow wind densities, but the slopes of the slow temperature fits are quite different. These patterns hold for minor ions measured with HIS.

H11, H13, and P18 calculated radial trends for protons. For the minor ions, ion-proton density ratios are used to simply scale down the leading coefficient of the H11, H13, and P18 power laws for each minor ion. To compare temperatures, the H11, H13, and P18 fits are multiplied by the $(4/3) * (m_i/m_p)$ from [65]. Direct HIS observations and their fits are compared to the manipulated H11, H13, and P18 radial dependence.

Fast wind alpha densities (Figure 4.3a), are about one-third that of the scaled H11 and P18 curves at 0.3 AU and in good agreement with both curves at 1 AU. The scaling law itself is about 75% lower than H11. Slow wind alpha densities (Figure 4.3c) are significantly lower than the H13 curve; the scaling law is also about 75% lower. Note that the estimated H13 curve for alphas seems to hit above the bulk of the alpha densities, while the actual fit seems to be lower than the bulk of the densities, and is possibly being pulled down by a few anomalously low densities.

Fast alpha temperatures (Figure 4.3b) are about 30% higher than the H11 and P18 curves at 0.3 AU and come into good agreement with P18 at 1 AU. The scaling law is about 50% steeper steeper than the scaled H11 and and 24% steeper P18. Similar to the fast wind, slow alpha temperatures (Figure 4.3d) start out twice as high as the H13 curve but come into agreement by 1 AU due to having a much higher power law coefficient.

Fast O^{6+} densities (Figure 4.4a) are in good agreement with P18 and H11 between 0.3 and 1 AU. The scaling law is well below the P18 and H11 laws, lower than the law for protons, and a bit higher than the law for alphas. Like alphas, slow O^{6+} densities (Figure 4.4c) are about 25 % of the H13 curve throughout the full range of distances. The scaling law is a bit above the alpha law and well below the H11 and protons.

The fast O^{6+} temperature fit (Figure 4.4b) is about 50 % higher than H11 and P18 at 0.3 AU and 50% lower than H11 at 1 AU. The scaling law is higher than H11, P18, protons, and alpha scaling laws. The slow O^{6+} temperature fit (Figure 4.4d) is 3 times higher than the scaled up H11 and P18 curves. and still passes below what appears to be the bulk of the temperature data. The fit is much steeper than H11 and P18, and only comes into agreement with P18 close to 1 AU. The current $4/3 * m_i/m_p$ mass scaling does not appear to be applicable within 0.9 AU for the alphas or O^{6+}.

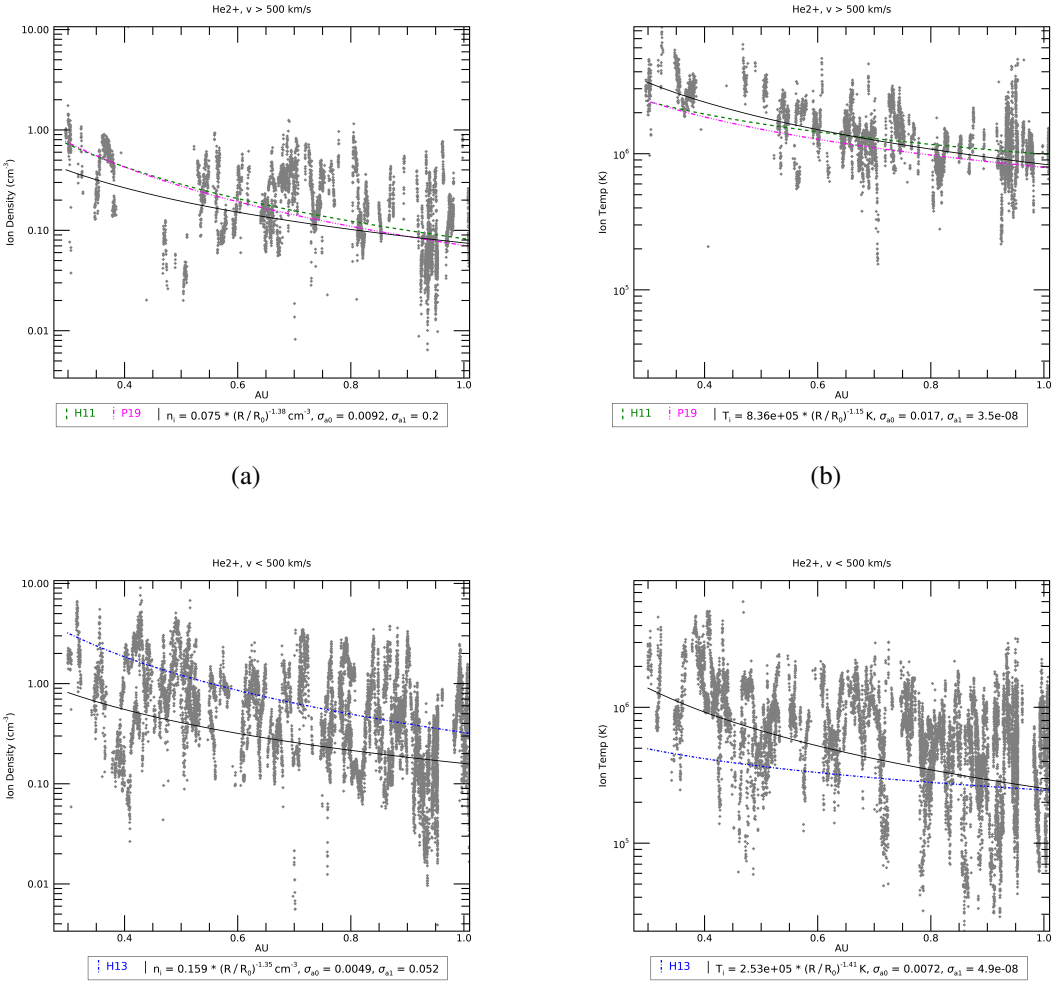

Figure 4.3 Radial evolution of solar wind temperature for He^{2+}. Fast densities are shown in panel (a), fast temperatures in panel (b), slow densities in panel (c), and slow temperatures in panel (d). Fit is overplotted in black. Previous observations by Hellinger et al., 2011, 2013, and Perrone et al., are overplotted in green, blue, and magenta, respectively. The top row shows the trends in fast wind and the bottom slow speeds.

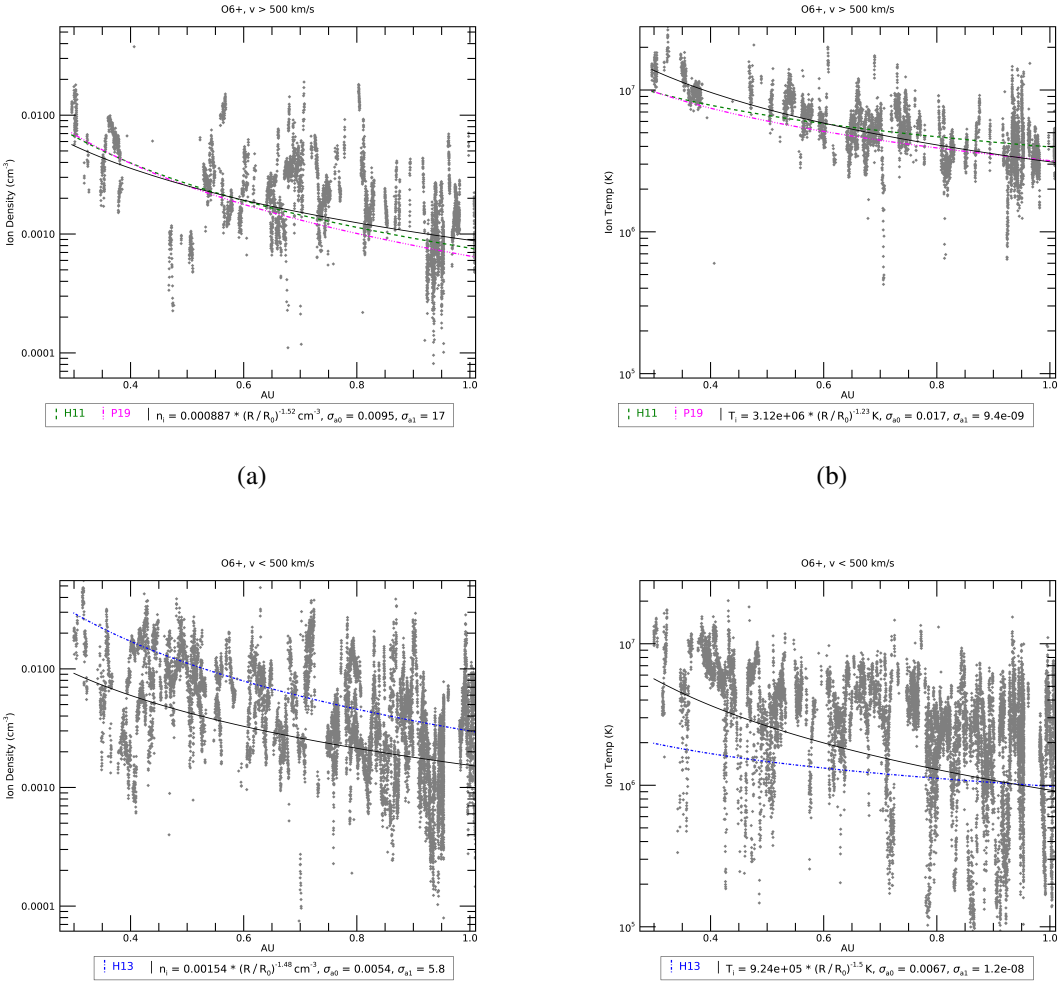

Figure 4.4 Radial evolution of solar wind density and temperature for O^{6+}. Fast densities are shown in panel (a), fast temperatures in panel (b), slow densities in panel (c), and slow temperatures in panel (d). Fit is overplotted in black. Previous observations by Hellinger et al., 2011, 2013, and Perrone et al., 2018 are overplotted in green, blue, and magenta, respectively. The top row shows the trends in fast wind and the bottom slow speeds.

	Protons	He^{2+}	O^{6+}	H13	H11	P18
a_0 (fast)	4.9	0.075	8.87e-4	-	2.8	2.4
a_1 (fast)	-1.76	-1.38	-1.52	-	-1.8	-1.96
a_0 (slow)	6.8	0.159	1.54e-3	11	-	-
a_1 (slow)	-1.94	-1.35	-1.48	-1.9	-	-

Table 4.1 Density fit coefficients. Fits are to the function: $n = a_0 * (R/R_0)^{a_1}\ cm^{-3}$

Table 4.1 compares the PAS/HIS density fit coefficients for protons, He^{2+}, and O^{6+} to previous fits derived from density observations from Helios.

	Protons	He^{2+}	O^{6+}	H13	H11	P18
a_0 (fast)	2.42e5	8.36e5	3.12e6	-	2.5e5	2.0e5
a_1 (fast)	-0.679	-1.15	-1.23	-	-0.74	-0.93
a_0 (slow)	8.34e4	2.53e5	9.24e5	6.2e4	-	-
a_1 (slow)	-1.06	-1.41	-1.50	-0.58	-	-

Table 4.2 Temperature fit coefficients. Fits are to the function: $T = a_0 * (R/R_0)^{a_1}\ K$

Table 4.2 compares the PAS/HIS temperature fit coefficients for protons, He^{2+}, and O^{6+} to previous fits derived from temperature observations from Helios.

4.3.2 Coulomb Thermalization

To determine the the radial evolution of Coulomb thermalization over distances achieved by SO, we have plotted ion-proton temperature ratios vs. collisional age and radial distance, color coded to show the median radial distance in the A_c bins and the mean A_c in the radial distance bins. The same has also been done with differential streaming vs. collisional age and radial distance. The four ions currently available via the Solar Orbiter Archive (L3) are He^{2+}, C^{5+}, O^{6+}, and Fe^{10+}, all of which are shown here. Note that none of these calculations rely on the minor ion densities, only protons. Figures 4.5 - 4.8 show the decay in temperature ratio with collisional age, as well as radial distance from the Sun. Wind speeds above 500 km/s are shown on the left, below 500 km/s on the right, and all speeds over the full range in A_c are on the bottom. The top row depicts temperature ratio vs. A_c, and the middle row depicts temperature ratio vs. radial distance. The color bar on the A_c plots shows the median radial distance associated with each bin. On the distance plots, it shows the median A_c in each bin.

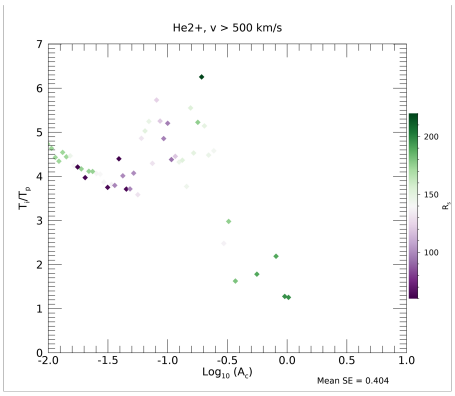

(a)

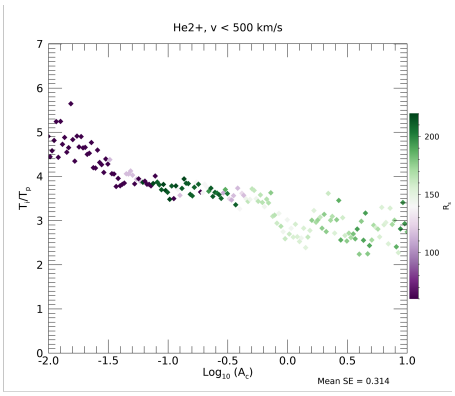

(b)

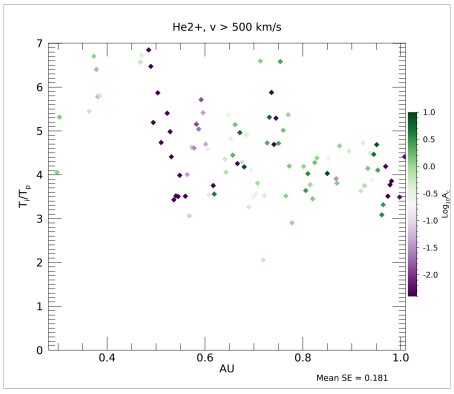

(c)

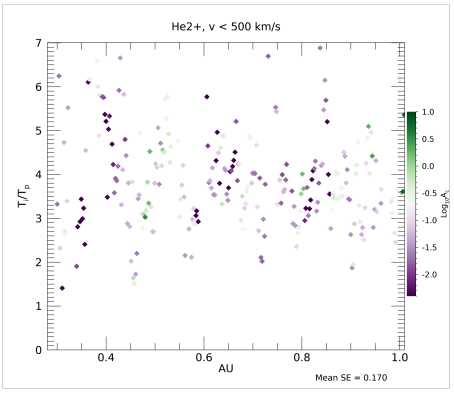

(d)

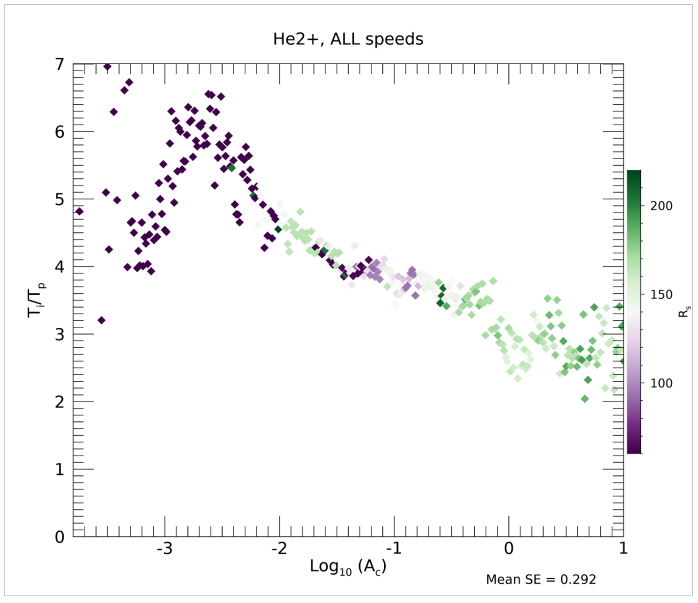

(e)

Figure 4.5 Alpha temperature ratios vs. collisional age in the top row and radial distance in the middle. Fast wind is plotted to the right, slow wind to the left, and the full range in A_c for all speeds is shown in the middle on the bottom.

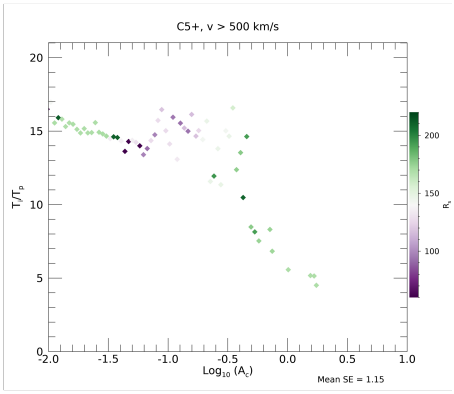

(a)

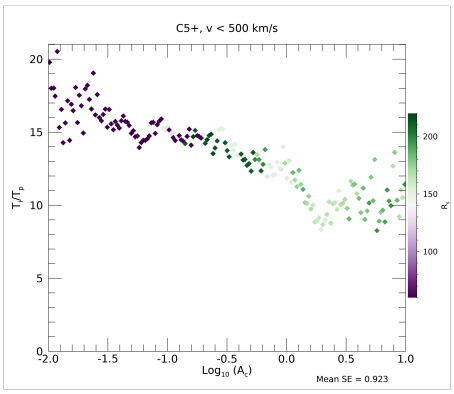

(b)

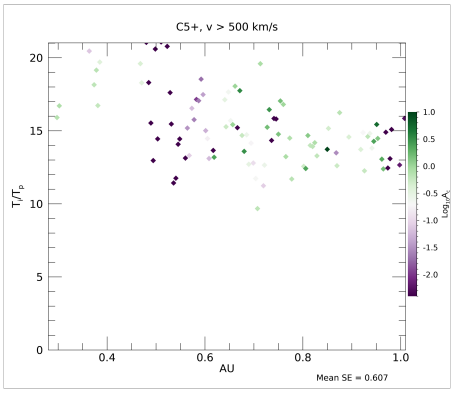

(c)

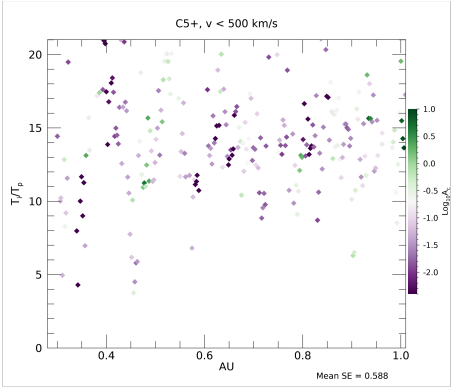

(d)

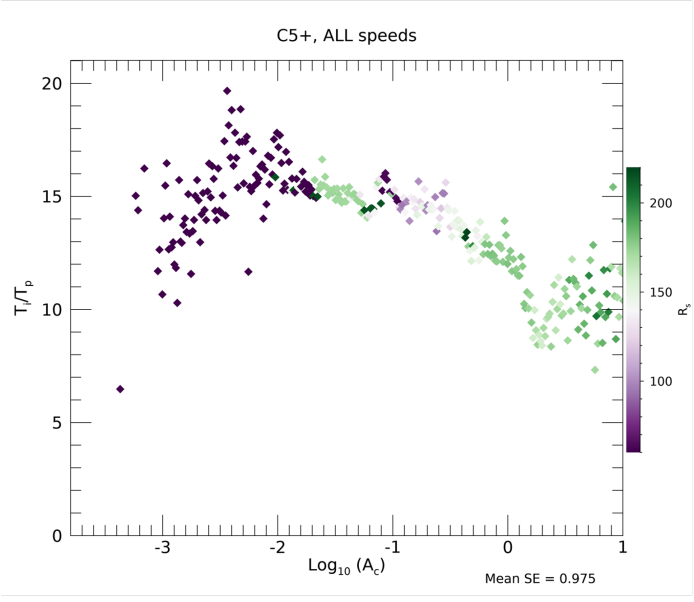

(e)

Figure 4.6 C^{5+} temperature ratios vs. collisional age in the top row and radial distance in the middle. Fast wind is plotted to the right, slow wind to the left, and the full range in A_c for all speeds is shown in the middle on the bottom.

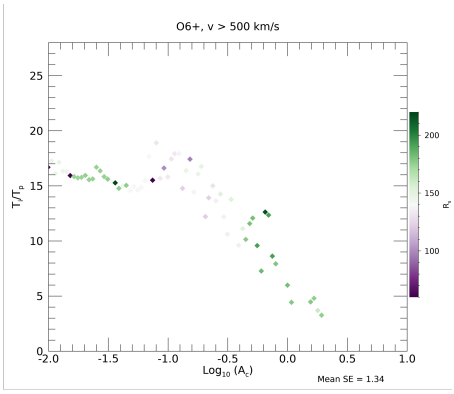

(a)

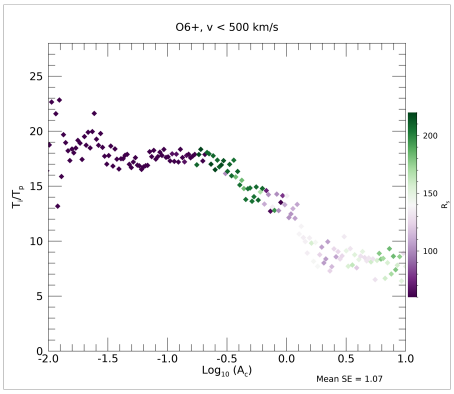

(b)

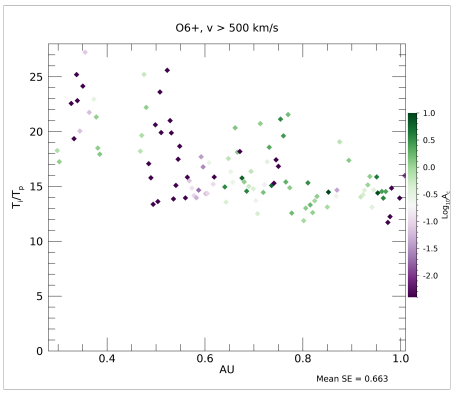

(c)

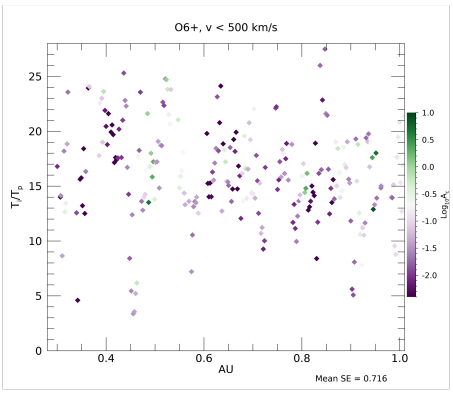

(d)

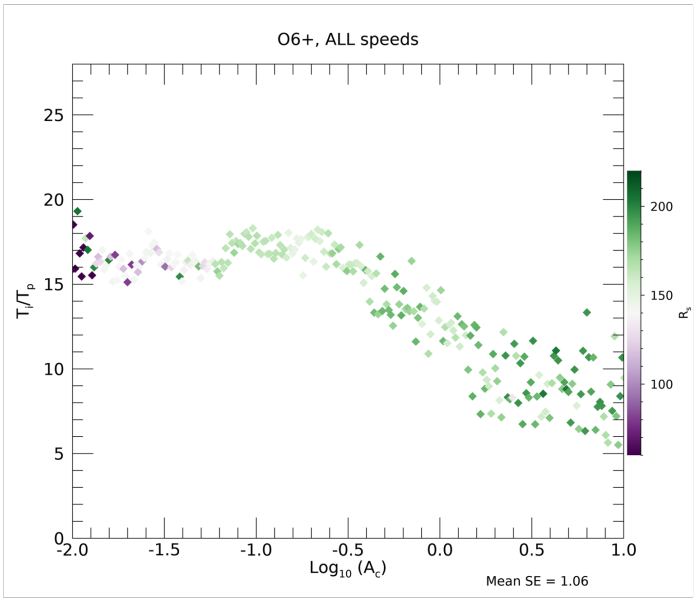

(e)

Figure 4.7 O^{6+} temperature ratios vs. collisional age in the top row and radial distance in the middle. Fast wind is plotted to the right, slow wind to the left, and the full range in A_c for all speeds is shown in the middle on the bottom.

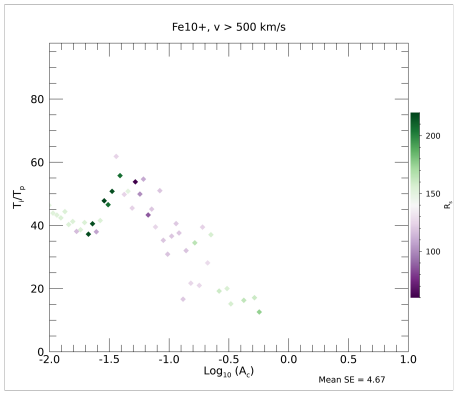

(a)

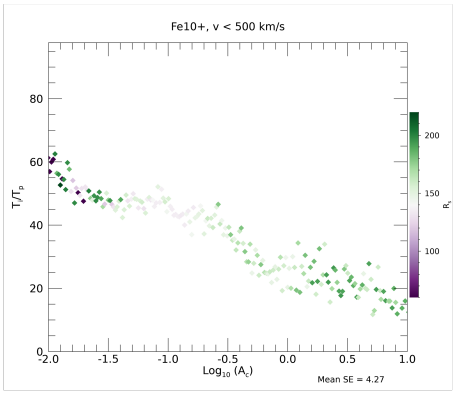

(b)

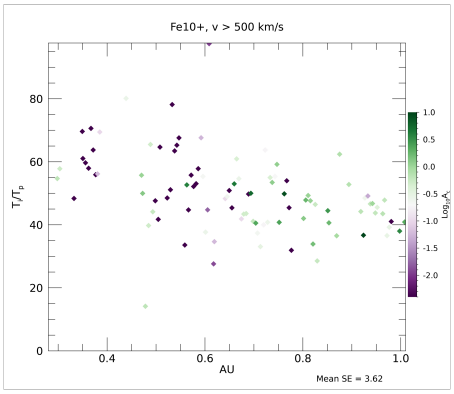

(c)

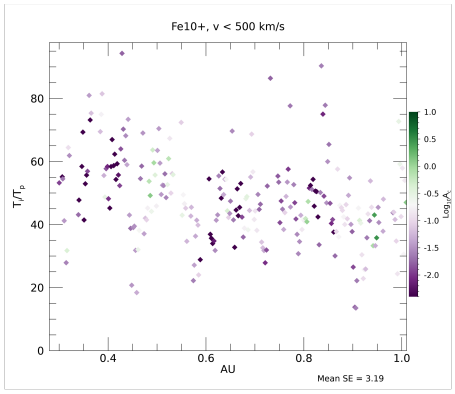

(d)

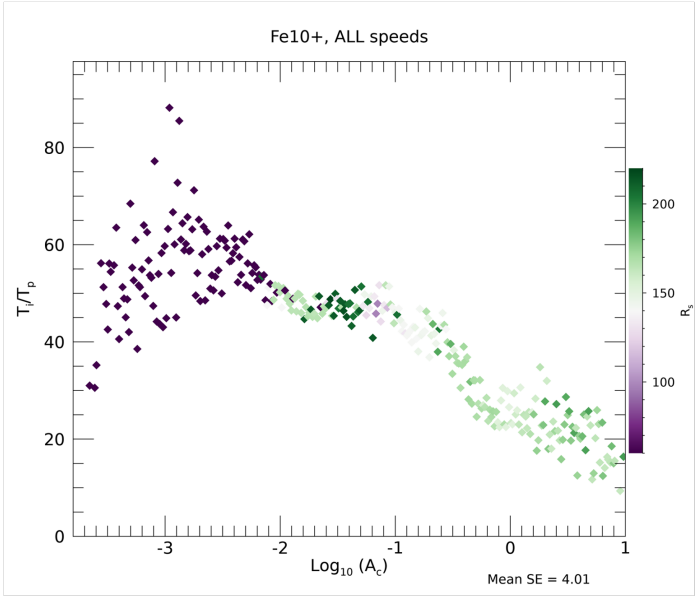

(e)

Figure 4.8 Fe^{10+} temperature ratios vs. collisional age in the top row and radial distance in the middle. Fast wind is plotted to the right, slow wind to the left, and the full range in A_c for all speeds is shown in the middle on the bottom.

Looking at Figures 4.5a, 4.6a, 4.7a, and 4.8a, T_i/T_p vs. Ac for fast wind cuts off between $10^{-0.5}$ and $10^{0.5}$. This cutoff is lowest for Fe^{10+} (Fig. 4.8a), and highest for O^{6+} (Fig. 4.7a). The T_i/T_p decays as expected with A_c in all wind types in the fast, slow, and all speeds ranges, though the "bump" is visible in O^{6+} and C^{5+} in the full curve. These plots point to $A_c \sim 1$ at $R_b \sim 170\ R_s$ for He^{2+}, but especially in the slow wind, a broad range of A_c are observed at 1 AU (Figs. 4.5d, 4.6d, 4.7d, 4.8d). This location shifts inward for each heavier ion, but is fairly consistent across solar wind types. The colors of each bin do not point to a direct correlation between radial distance and collisional age.

The slow wind curve (Figs. 4.5b, 4.6b, 4.7b, 4.8b) decay as expected, but do not achieve the residual values seen in the SWICS data. A_c does not achieve as high values, indicating that HIS may not have observed enough fully thermalized wind to meet the requirements to form a bin in this work. The slow curves do, however, depict the transition from low to high radial distances as A_c increases. This increase is not always monotonic, as a look at the corresponding fast (Figs. 4.5c, 4.6c, 4.7c, 4.8c) and slow Figs. 4.5d, 4.6d, 4.7d, 4.8d plots in radial distance show that one can observe a broad range in A_c at any given distances. T_i/T_p decay with radial distance is very weak in the fast wind, and apparent but highly scattered in the slow. In lower mass ions, He^{2+} and C^{5+}, there appears to be no dependence on radial distance. Note that for all four ions, the fast wind has a population of low A_c, high T_i/T_p associated with high radial distances. The only explanation for this is that all wind types have a distribution of temperature ratios, and in the nearly collisionless fast wind, observing fast wind that has undergone almost no thermalization is not unlikely.

The full curve (Figs. 4.5e, 4.6e, 4.7e, 4.8e) allows one to see that at very low A_c, there is actually an increase in temperature ratios with A_c. This could either be demonstrative of the ability of Coulomb collisions to drive differentially streaming species out of thermal equilibrium, or of ongoing preferential heating. Note the saturation of the color scheme in this range, indicating that the median radial distance in these very low A_c bins is $\leq 60\ R_s$, marking the transition from preferential heating to thermalization would be in agreement with [119].

Figures 4.9 - 4.12 depict differential streaming for the same four ions. Fast wind is plotted in the top row, slow wind in the middle, and the full range of velocity and A_c is on the bottom. Note here that we do not normalize the differential velocity between ions and protons to the Alfvén speed. The top plots plot Δv_{ip} vs. A_c and the middle plots are of Δv_{ip} vs. R. The color scheme and color bars hold the same meaning as before, corresponding to median radial distance in the A_c plots and median A_c in the radial distance plots.

The alpha-to-proton differential speed does not reduce with collisional age, as expected in the fast wind (Figure 4.9a). Bins beyond $A_c = 0$ are sparse, Δv_{ip} slightly increases with

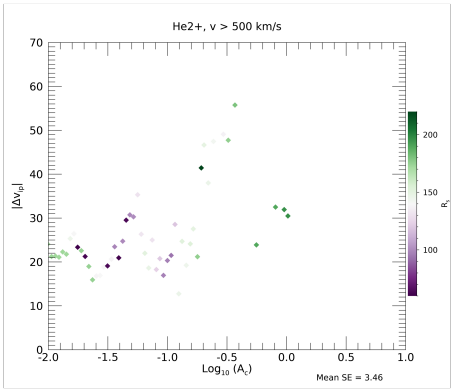

(a)

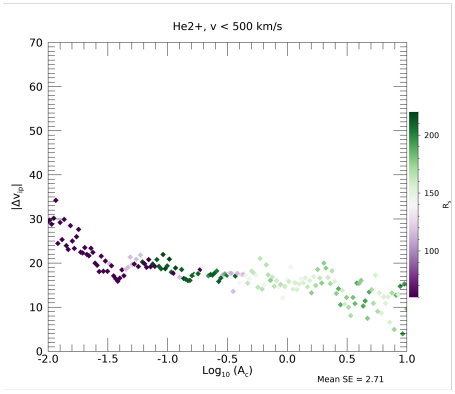

(b)

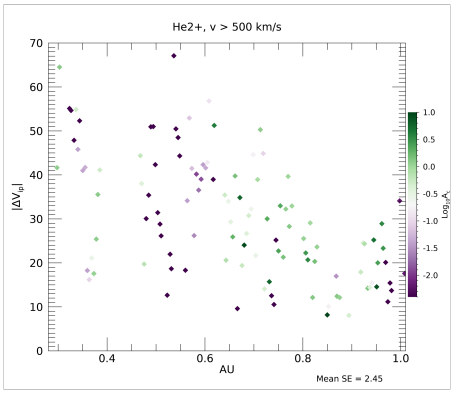

(c)

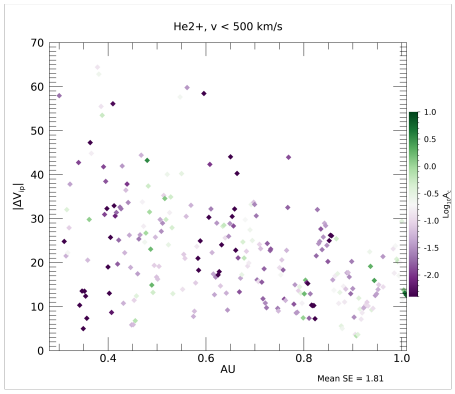

(d)

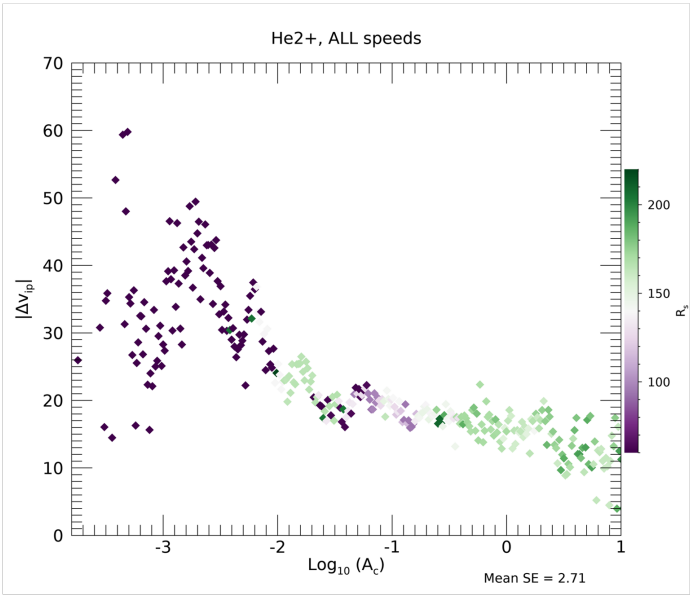

(e)

Figure 4.9 Alpha differential velocities vs. collisional age in the top row and radial distance in the middle. Fast wind is plotted to the right, slow wind to the left, and the full range in A_c for all speeds is shown in the middle on the bottom.

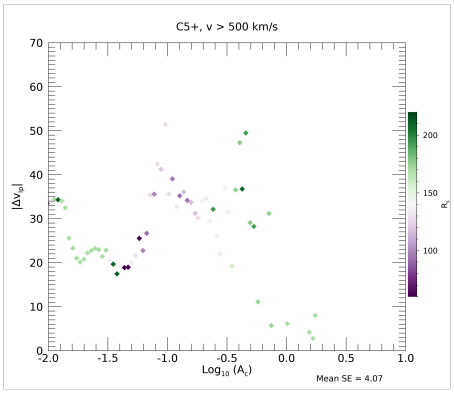

(a)

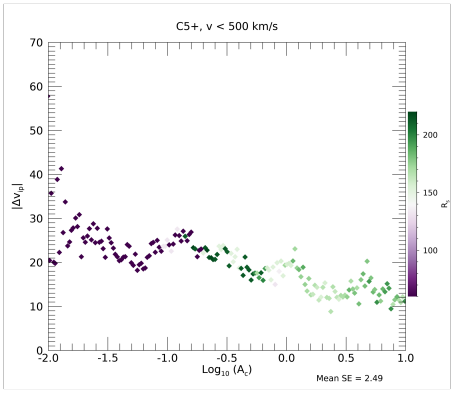

(b)

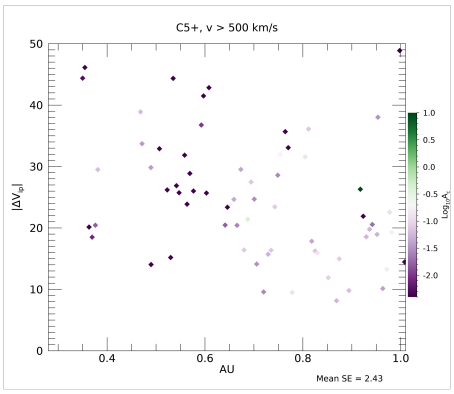

(c)

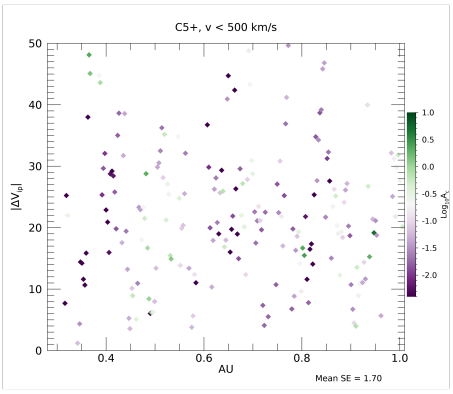

(d)

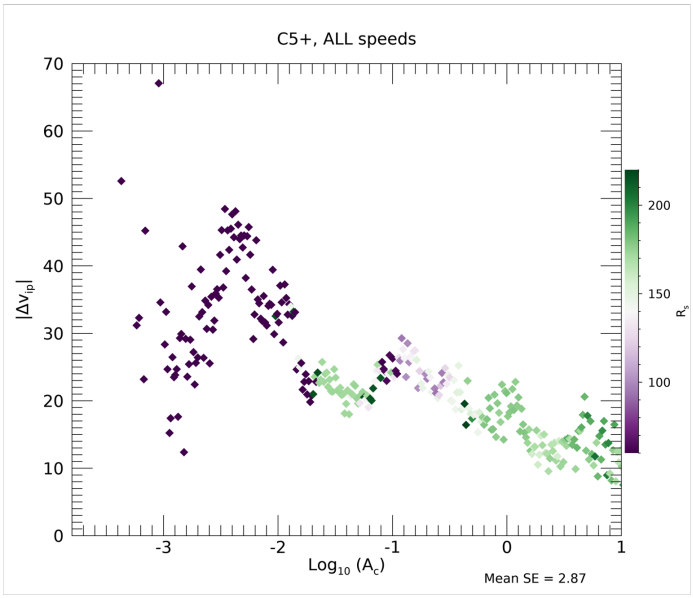

(e)

Figure 4.10 C^{5+} differential velocities vs. collisional age in the top row and radial distance in the middle. Fast wind is plotted to the right, slow wind to the left, and the full range in A_c for all speeds is shown in the middle on the bottom.

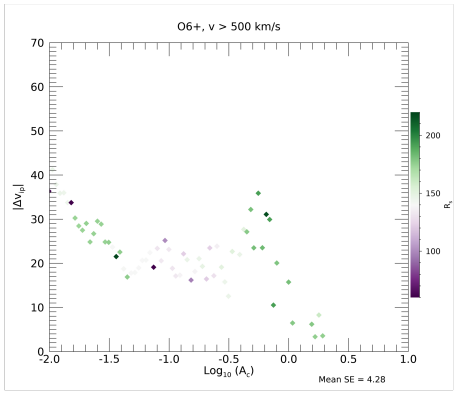

(a)

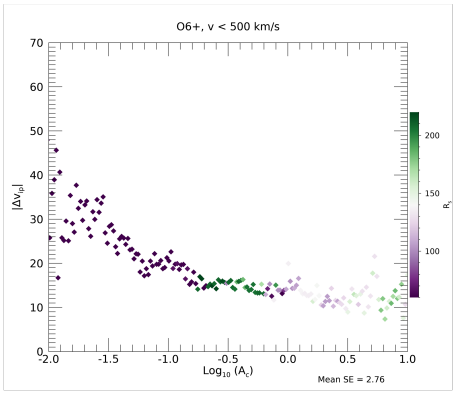

(b)

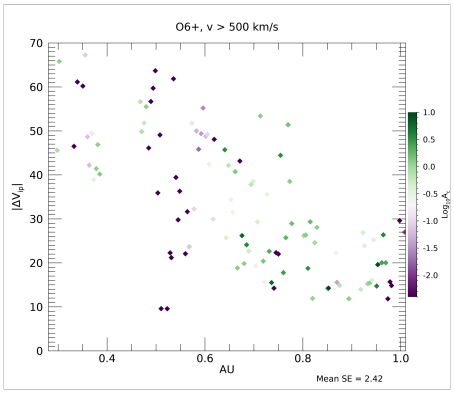

(c)

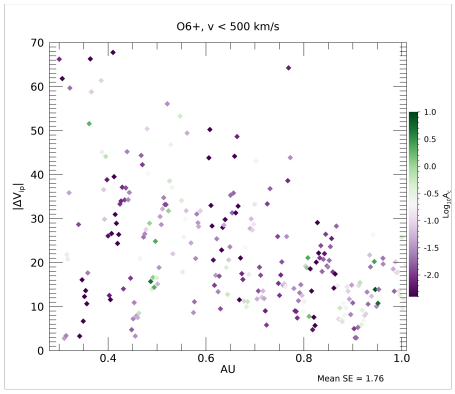

(d)

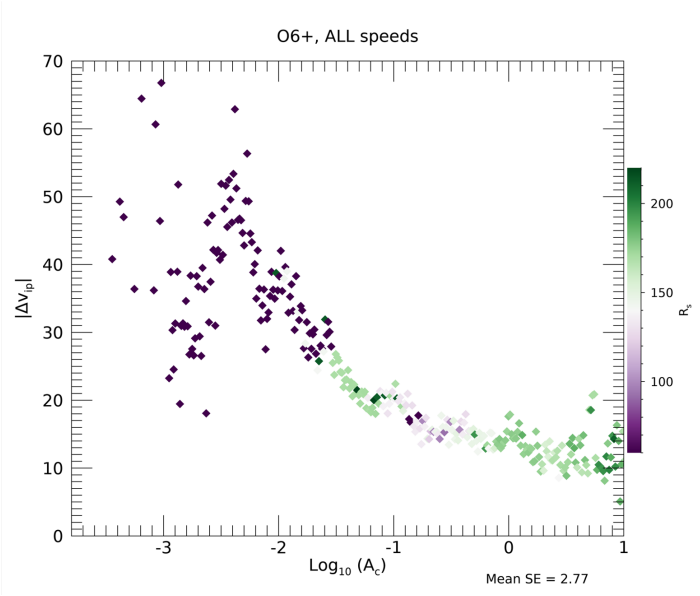

(e)

Figure 4.11 O^{6+} differential velocities vs. collisional age in the top row and radial distance in the middle. Fast wind is plotted to the right, slow wind to the left, and the full range in A_c for all speeds is shown in the middle on the bottom.

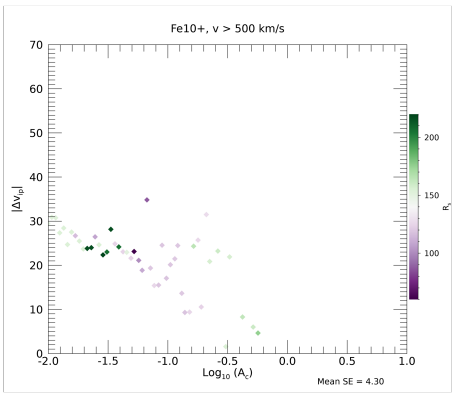

(a)

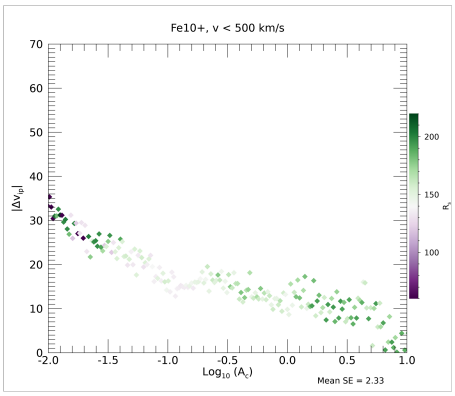

(b)

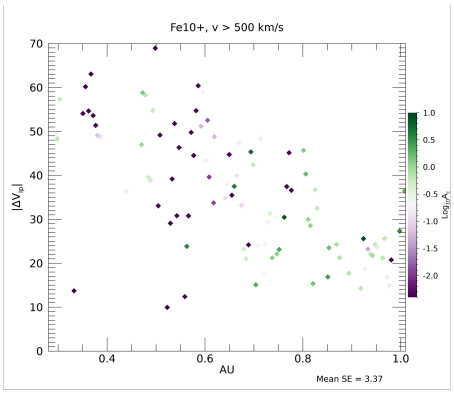

(c)

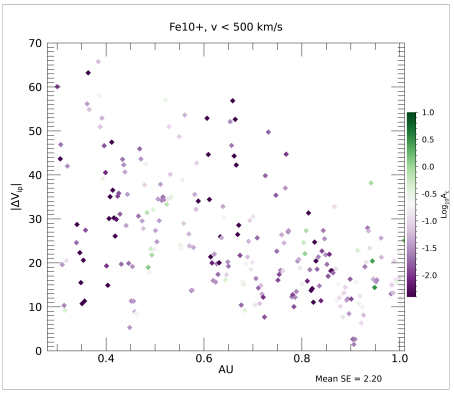

(d)

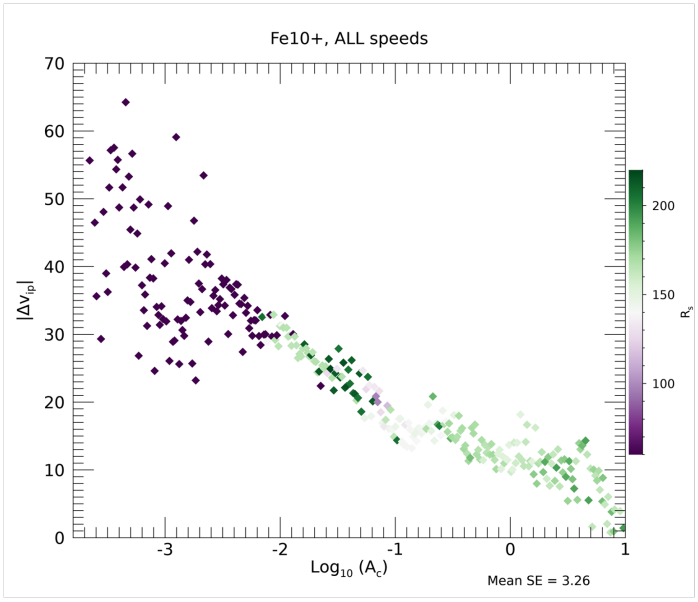

(e)

Figure 4.12 Fe^{10+} differential velocities vs. collisional age in the top row and radial distance in the middle. Fast wind is plotted to the right, slow wind to the left, and the full range in A_c for all speeds is shown in the middle on the bottom.

increasing A_c, and no apparent trend is visible with distance. Ions and alphas (Figs. 4.9a, 4.10a, 4.11a, and 4.12a) in the fast wind primarily stream between $10 - 60$ km/s. Slow wind alphas and protons (Figs. 4.9b, 4.10b, 4.11b, and 4.12b) have a differential speed of < 30 km/s. Between $10^{-2} < A_c < 10^{-0.5}$, corresponding to 100-150 R_s, Δv_{ip} dips before climbing to its peak. Though the increase with A_c is scattered, the increase with radial distance is less distinct. For all ions, the anticorrelation between Δv_{ip} and radial distance is stronger in the fast wind than in the slow. Combining both wind types for all speeds produces a very clear increase in Δv_{ip} with both radial distance and Ac, though the curve in R_b exhibits either a steady or gradually decreasing Δv_{ip} up to $\sim$150 R_s.

Differential streaming is better correlated to distance than T_i/T_p, especially in the fast wind (Figs. 4.9c, 4.10c, 4.11c, and 4.12c). T_i/T_p is better correlated to A_c than differential streaming. Fast wind Δv_{ip} does not decrease with A_c, except for in O^{6+}. For all other ions, Δv_{ip} is either level or decreases at very low A_c, then increases from $10^{-1.5} - 10^{1}$, then increases. It does not extend beyond 10^{0} - $10^{0.5}$. During this range in A_c, Δv_{ip} tends to start at about 30 km/s, decrease to about 10 km/s, then increase to over 50 km/s, beyond which statistics become too low to make more bins in A_c. Binning in radial distance reveals a full range of Δv_{ip} and a clear decrease toward 0 with increasing distance in the fast wind, though any given radial distance does see a broad range in Δv_{ip} . More bins with a high median A_c fall on the left side of the plots while more bins with a low median A_c have low radial distances. Bins in radial distance have high Δv_{ip} , predominantly at low radial distances, but the majority of bins have low Δv_{ip} .

The slow wind shows a clear, well-ordered decrease from $\sim 40 - 60$ km/s to < 10 km/s with A_c (Figs. 4.9b, 4.10b, 4.11b, and 4.12b). The descent is more gradual in alphas and steepens with each successively heavy ion. Binned in radial distance, slow wind Δv_{ip} is far more scattered (Figs. 4.9d, 4.10d, 4.11d, and 4.12d), ranges from $\Delta v_{ip} > 60$ km/s down to 0, and has a mix of bins with a low and high median A_c.

Plotting the full range in A_c for all solar wind speeds shows a similar climb to Δv_{ip} > 50 km/s followed by a drop at $A_c \sim 10^{-2}$. He^{2+} and C^{5+} both have a dip between 10^{-2} and 10^{-1}. O^{6+} and Fe^{10+} do not (Figs. 4.9e, 4.10e, 4.11e, and 4.12e). The bins in this dip have a median radial distance of > 200 R_s. There appear to be no ion-dependent (mass, charge-to-mass) trends in the magnitude or reduction of differential streaming.

4.4 Preferential Heating Zone Model Results

4.4.1 Excess Temperature Decay Profiles

These thermalization curves have some distinctions from those made with SWICS data at 1 AU. The hitherto limited duration of the mission disallows the PHZ model to be run on slow-Alfvénic and non-Alfvénic subsets, so here wind speeds below 500 km/s and all wind speeds are being compared. Figure 4.13 shows He^{2+} and C^{5+} slow and all speeds. Panel a is slow speed He^{2+}, panel b is all speeds. Panels c and d are slow and all speeds C^{5+}, respectively. In Figure 4.14 , O^{6+} slow and all speeds are in panels a and b, while Fe^{10+} are in panels c and d. The features of these plots are the same as in the previous two chapters.

Predictions of R_b are much lower, and observed excess temperature extends much higher, and a broader range in collisional age are also present. As a reminder, residual excess temperature, ε_r is to be found on the right side of the thermalization curve, at high A_c, while boundary excess temperature, ε_b, is to be found on the left at low A_c. The HIS instrument does not observe the residual excess temperature values seen by WIND, and produces ε_r even higher than that made with the SWICS data. Moreover, we see more departures from the clear collision-driven sigmoid decay function. The most notable of which is that at very low A_c, between 0.01 and 0.1, the curve steepens, indicating that at the PHZ boundary, the ions are heated in excess of the model prediction. This feature is present in nearly all ions and scales with each ion's range in excess temperature. It is higher in slow wind than all speeds wind. This is a bit surprising, given all speeds' disposition toward low A_c. While the plots made with SWICS data show a similar departure, the HIS deviation is much more apparent, and present in all speeds wind and v $<$ 500 km/s.

Multiple bumps are seen in some of the ions, most notably O^{6+} (Figs. 4.13b, 4.13c, 4.14b, 4.14c, and 4.14d). In O^{6+}, the bump is present in both all speeds and v $<$ 500 km/s wind, while in the SWICS data, it is absent in the slow wind. This feature occurs at $A_c \sim$ 0.1 At high A_c, He^{2+}, C^{5+}, and O^{6+} also display a slight rise in temperature ratio. There is greater uncertainty in each bin, due to lower statistics from only about 1.5 years of data all from solar minimum of SC 25. Eventually, this issue should resolve as more of the 10-minute HIS data is released.

Of the four ions shown here, He^{2+} is the only one in which the R_b prediction is higher in the slow wind than all speeds, as seen in text on Figures 4.13a and 4.14a. In general, R_b predictions are lower in the slow wind and ε_b is higher. In all speeds wind, χ^2/dof is never below 2, and in all but 2 cases is never higher than 7. In slow wind, χ^2/dof is always less than 5, and in most cases less than 3. Keep in mind, in both wind types, the χ^2/dof is moderated by the high uncertainty in excess temperature in each bin. The fact that χ^2/dof

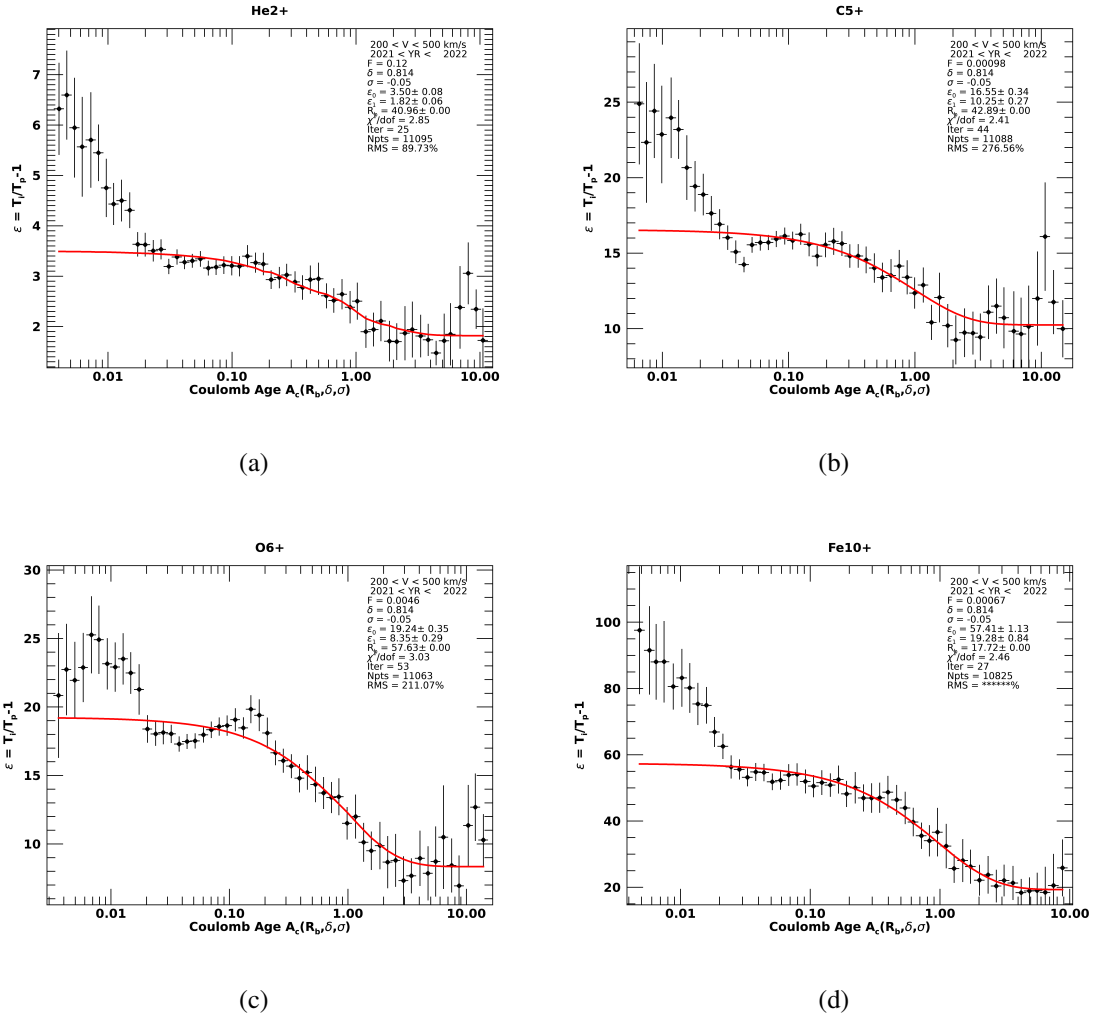

Figure 4.13 Decay in ε with A_c for He^{2+} and C^{5+}, O^{6+}, and Fe^{10+}. Speeds less than 500 km/s.

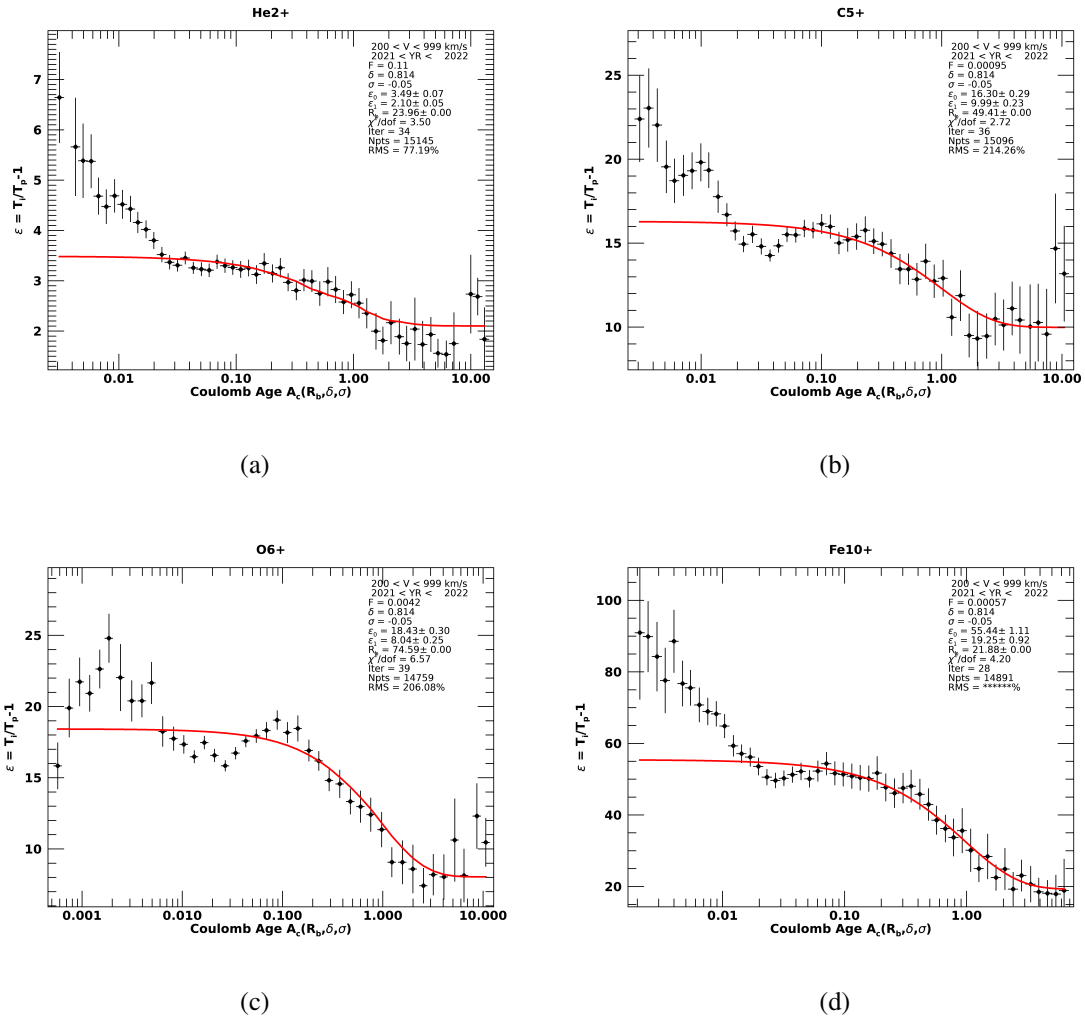

Figure 4.14 Decay in ε with A_c for He^{2+} and C^{5+}, O^{6+}, and Fe^{10+}.All wind speeds.

is generally lower in the slow wind, yet slow wind has greater deviation from the predicted decay curve (at low A_c) may be explained by higher binning statistics – all speeds wind has about 25-30 $\%$ more viable data points than slow wind – as well as stronger "bumps" along the decay curve in the all-speeds case.

This would also explain why the reduced χ^2 values here are comparable to those found in Chapter 2. The slow wind χ^2/dof in the HIS data is 2.9, and 3.9 with the 2-hour SWICS data. The fast wind χ^2/dof in the HIS data is 3.5, and 5.1 in the SWICS data. In general, reduced χ^2 in the SWICS data is almost never greater than 5, while here it is never greater than 7. In order to consistently show the relative uncertainty from the different datasets, weightings were not adjusted between chapters. As a result the χ^2/dof are comparable while the error bars/uncertainty is much higher for HIS, which as of now has half the data, all taken during ascending maximum of the solar cycle.

4.4.2 Dependence on Ion Properties

The HIS data exhibits some apparent trends in PHZ boundary predictions with ion characteristics, shown in Figures 4.15 and 4.16. High-FIP ions do not have a strong trend in charge state with radial boundary, while the boundary prediction for low-FIP ions is clearly higher for higher charge states, as seen in Figures 4.15a (v $<$ 500 km/s) and 4.15b (all wind speeds). The boundary predictions curve with q/m, rising from $q/m \sim 0.5$, peaking at about 0.35 amu before dropping steadily as charge to mass ratio decreases. In Figures 4.15c and 4.15d, Carbon and Oxygen both show a decrease in R_b prediction with increasing q/m, while heavier ions exhibit the opposite trend, with a few outlying charge states. There are no strong trends in q^2/m, as seen in Figures 4.15e and 4.15f. The trends in mass and q/m are qualitatively similar between v $<$ 500 km/s and all speeds wind, but stronger in the latter. This was also the case for ion dependencies in Chapter 2.

In Figures 4.16a and 4.16b, excess temperature is significantly higher than that seen in the Tracy et al., 2016 curve [60], as well as previous results with the SWICS 2-hour data. Slow wind boundary excess temperature actually tends to be higher in the v $<$ 500 km/s wind than in the all-speeds wind. This was also observed in the SNA wind in the previous chapter. When plotted against q/m, boundary excess temperature is better ordered, especially at lower q/m, in the slow wind than the all-speeds wind, which is shown in Figures 4.16c and 4.16d.

To determine the impact of some of the less well-resolved ions, all but the most abundant ions (He^{2+}, $C^{4\text{-}6+}$, $O^{6\text{-}8+}$, $Fe^{7\text{-}16+}$) are excluded. In Figure 4.17 it is apparent that the pattern seen in R_b vs. q/m is still present in all-speeds wind, and perhaps clearer in the

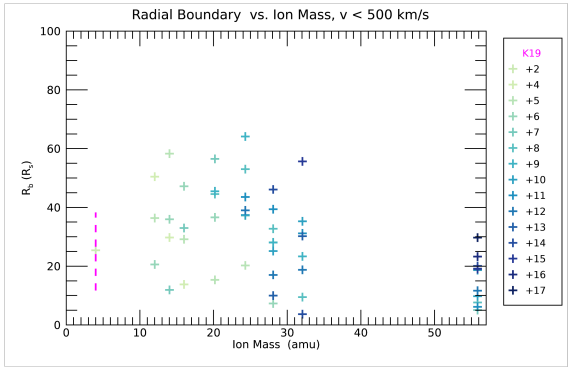

(a)

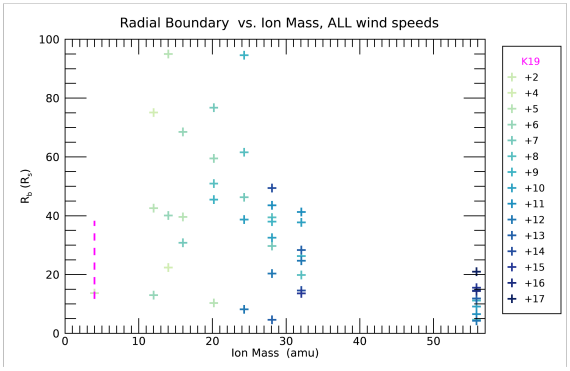

(b)

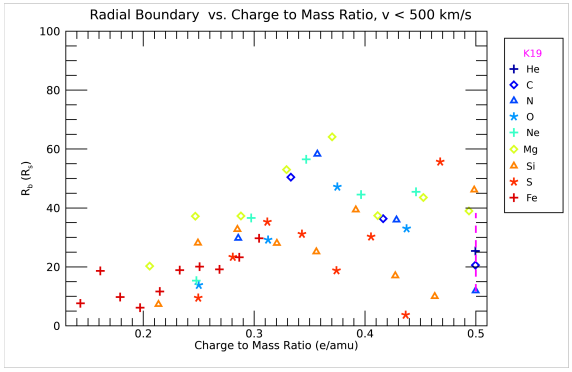

(c)

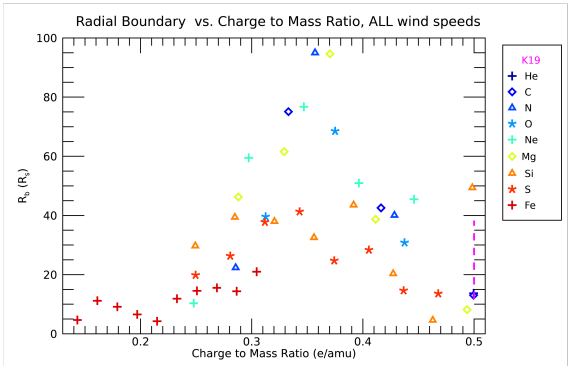

(d)

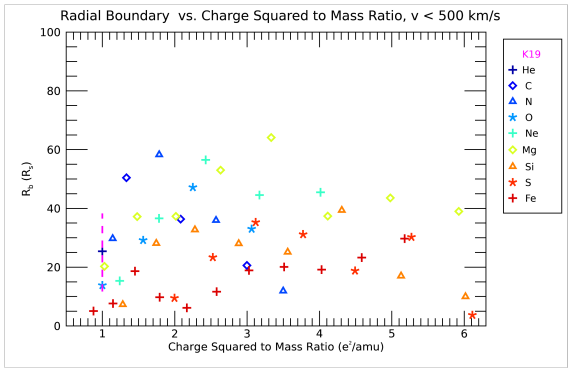

(e)

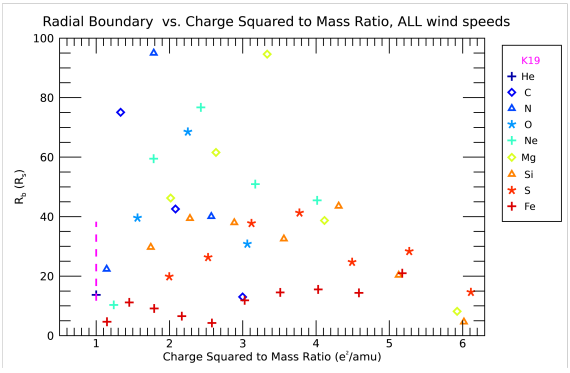

(f)

Figure 4.15 R_b scaling with ion (a) mass, (b) q/m, and (c) q^2/m. Slow speeds only are on the left side. All speeds are on the right.

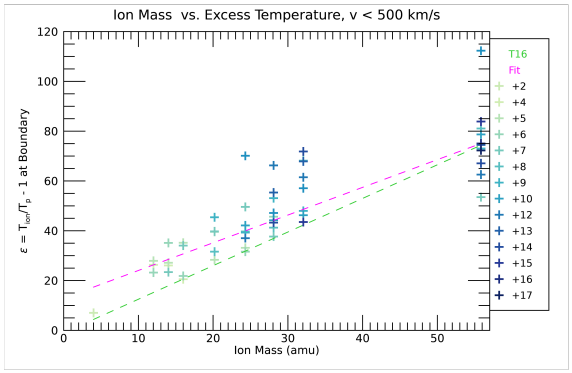

(e)

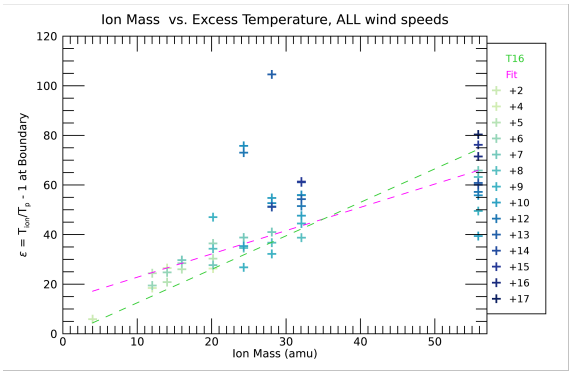

(f)

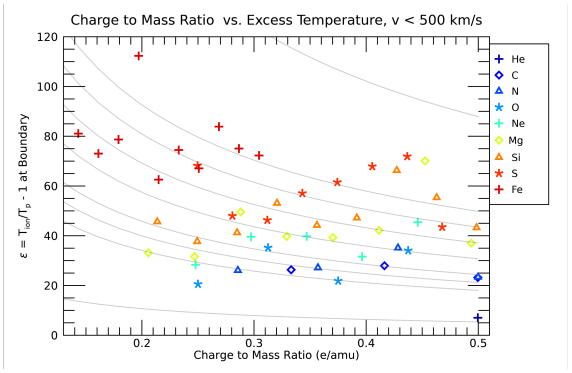

(e)

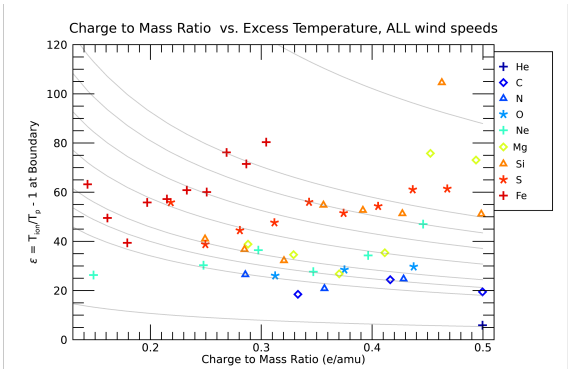

(f)

Figure 4.16 ε_b scaling with ion (a) mass and (b) q/m. Slow speeds only are depicted on the left, while all speeds are on the right.

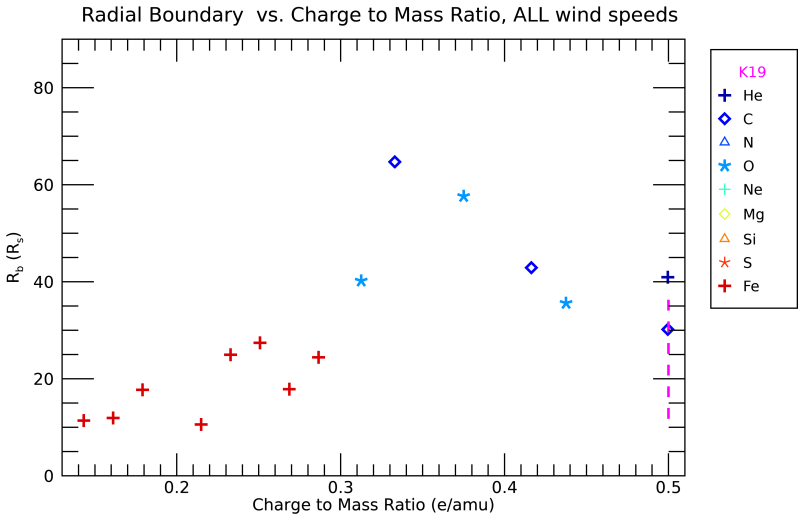

Figure 4.17 The R_b vs. q/m plot for the dataset when less abundant/reliable ions are excluded.

slow wind. The mass scaling of ε_r is driven higher when excluding the less reliable ions. As of now, for studies like this one, it may be more beneficial to work with the smaller subset of ions with the highest counting statistics since doing so does not heavily impact trends.

4.5 Preferential Heating Zone Model Predictions with Radial Considerations

The following plots, Figures 4.18, 4.19, 4.20, and 4.21 is of R_b predictions from various HIS distances. The x-axis denotes the HIS radial distance outer limit, while each color/symbol corresponds to an inner limit. As an example, the green triangle associated with a lower radial distance of 90 R_s includes data taken when the spacecraft is between 110 R_s, with each successive triangle corresponding to a greater distance from the Sun. Allowing data closer to the sun results in higher R_b predictions. Excluding data farther from the Sun results in higher PHZ predictions until one reaches a radial distance of about 160 R_s.

According to Figure 4.18, the location of Solar Orbiter can cause the PHZ boundary lo-

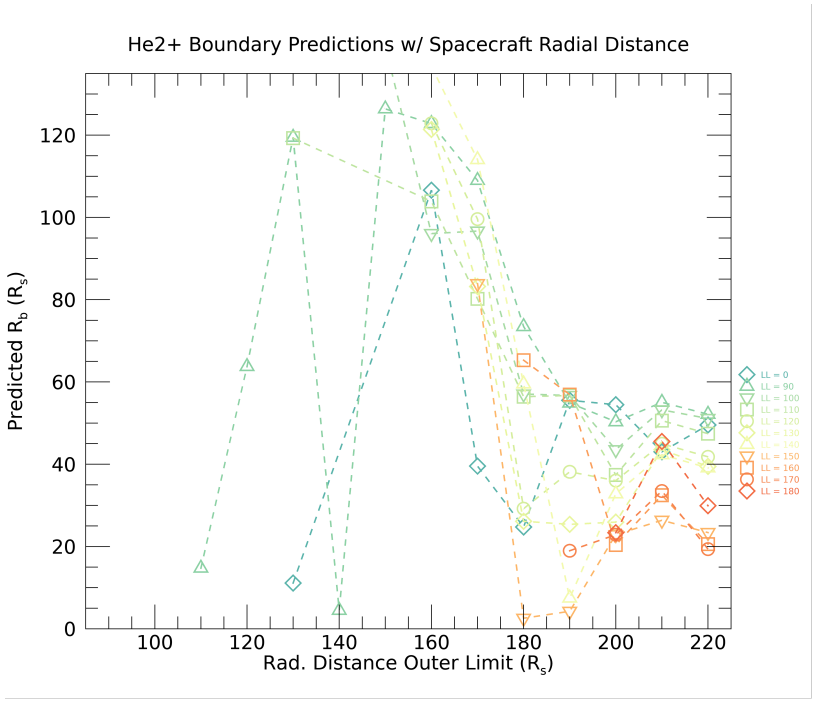

Figure 4.18 He^{2+} R_b prediction vs. maximum radial distance. Minimum radial distances are represented in the legend to the right of the plot.

cation prediction to vary as much as 100 R_s for He^{2+}. The aforementioned trend, however, could be a result of the evolving collisionality of the helium ions at these distances. The decrease in R_b prediction with outer limit is fairly well-ordered up to about 160 R_s. More measurements taken by the SWA suite at closer distances are needed to determine if the predictions within this distance are flattening, or if they are less ordered than those from beyond it. Minor ions may be examined to further clarify the He^{2+} observations.

For C^{5+}, shown in 4.19 the predictions follow stronger trends than the alpha particle. As the lower distance limit decreases, allowing data closer to the Sun, PHZ boundary predictions generally increase. The upper limit trend is less-straightforward. The R_b prediction follows a wave pattern as greater radial distances are allowed, starting out with relatively low predictions, increasing between 140-180 R_s, dipping at OL = 200 R_s, and increasing again beyond that point.

Figure 4.20 depicts O^{6+} . With some exceptions (LL = 0, OL = 180), predictions vary less than C^{5+} and O^{6+}. The LL trend is similar to that of C^{5+}, with higher LL generally being associated with lower R_b predictions. Aside from the dip at 200 R_s, the trend with the outer radial distance limit is quite steady. Unlike He^{2+} and C^{5+}, O^{6+} produced a result for LL=0, OL = 90, showing that the prediction tends to decrease closer to the Sun.

Fe^{10+} , shown in Figure 4.21, consistently predicts R_b below about 90 R_s. Consistent

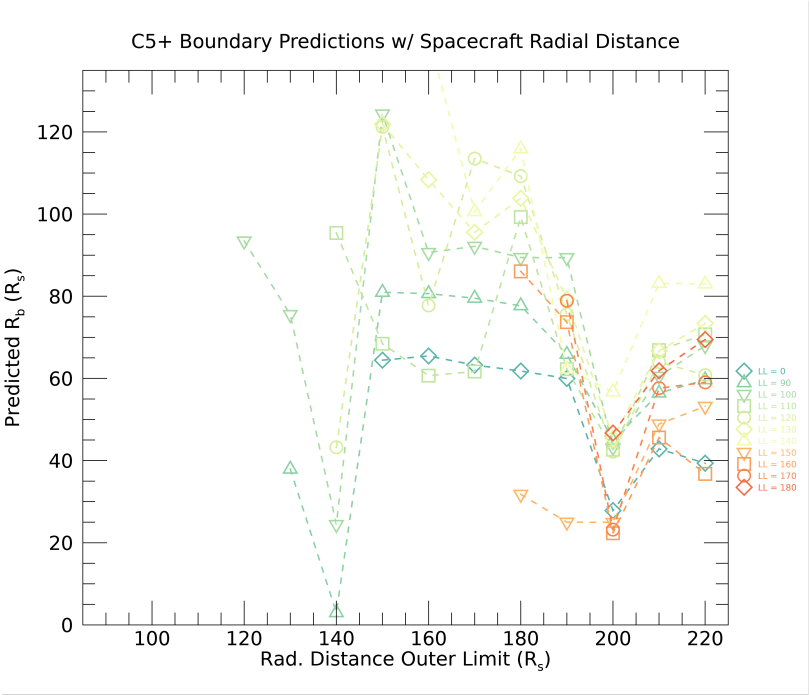

Figure 4.19 C^{5+} R_b prediction vs. maximum radial distance. Minimum radial distances are represented in the legend to the right of the plot.

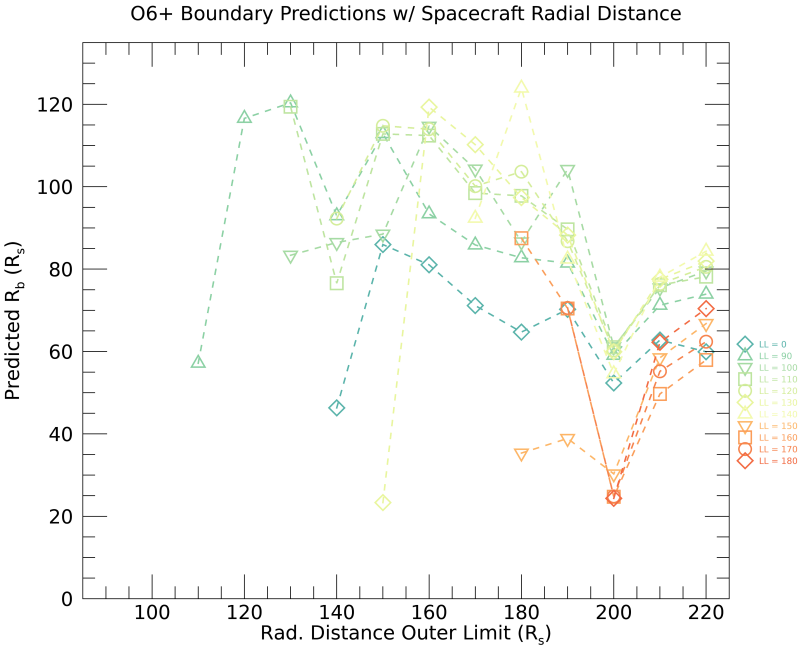

Figure 4.20 O^{6+} R_b prediction vs. maximum radial distance. Minimum radial distances are represented in the legend to the right of the plot.

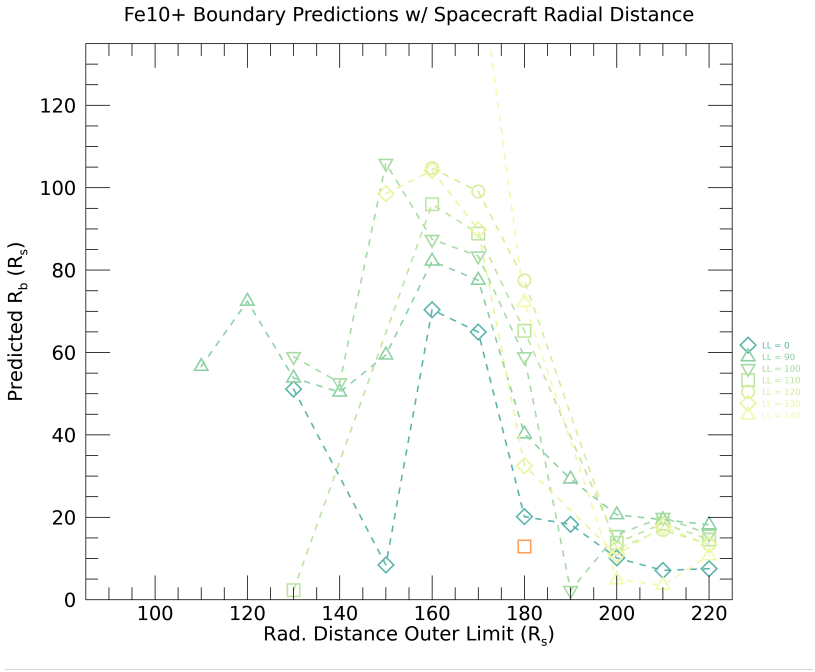

Figure 4.21 Fe^{10+} R_b prediction vs. maximum radial distance. Minimum radial distances are represented in the legend to the right of the plot.

with He^{2+}, the R_b prediction decreases as LL increases. Beyond about 150 R_s, the R_b prediction decreases as OL increases. The larger the distance of the spacecraft, the lower the prediction.

The PHZ model calculates collisional age with radial considerations (T, v evolution) to predict the distance at which Coulomb collisions become significant enough to override the effects of preferential heating. No consideration is made for any ongoing heating. Within the PHZ boundary, assumptions made by this model are no longer valid, and outside it, moving from a large distance toward the boundary, any ongoing heating would have an increasing effect. If the model is run on data with a significant enough subset inside the boundary, predictions may not be valid. Similarly, predictions from outside the boundary but closer to it would not have enough collisionally old wind to define a "thermalized" outer distance. Conversely, we have seen that in the slow wind, a mixture of A_c and T_i/T_p is observed at all radial distances. However, if the model assumes thermalization has occurred on this young subset of wind, where T_i/T_p is high but remains relatively steady, a larger radial distance might be predicted. Similarly, if one were to include very large radial distances, where the solar wind has been thermalized for a long time, the model would be run on wind with a large subset of collisionally old wind. It would likely see mostly very low, steady T_i/T_p (with distance). Therefore, it may also predict a lower R_b.

Higher charge state ions have higher collisional frequencies (with protons), and are more likely to be more thermalized by 1 AU. This may explain the consistently low predictions for Fe^{10+}, while the predictions for He^{2+}, C^{5+}, and O^{6+}, which have a greater mix of collisionally old and young wind, have broader range of predictions. Note that for most of the distance ranges (there are some exceptions, notably LL=0 line), the O^{6+} predictions vary less than helium and carbon.

4.6 Discussion and Conclusions

4.6.1 Radial Trends in Thermalization

Concerning the radial trends in density and temperature, for protons and minor ions, the best agreement with previous observations is seen in the fast temperatures. HIS fast proton temperatures agree well with previous work while slow wind densities are lower and fast wind densities higher than previous, despite better statistics in the slow wind. This may be due to a combination of the slow wind being more variable, and the inclusion of solar wind speeds between 400 and 600 km/s in both datasets. The removal of this range of speeds would help to control for solar wind that has undergone acceleration/deceleration due to stream interactions.

The plots are not shown here, but lowering the upper velocity limit from 500 to 400 km/s to better match the Hellinger criteria improves agreement between the HIS fit and H13 for slow wind densities. The scaled H13 fit does not capture slow wind minor ion temperatures well, and lowering the velocity threshold causes enough higher temperatures to be removed that the scaled H13 fit is in better agreement with the HIS data. The leading coefficient of the HIS fit reduces to achieve better agreement with H13. The scaling law, however, remains much higher than the H13 scaling. Raising the lower velocity limit did not significantly impact fits in the fast wind. Overall, the disagreements are mostly with scaling while the power laws are in good agreement, especially HIS with the H11 and H13 power laws. Minor ion deviations from power laws indicate that they are cooling at different rates from protons, which violates one of the assumptions of the PHZ model.

For all ions, including those not shown here, when stepping through the most abundant charge states of each element, the HIS observations increase relative to the scaled P18 and H11 curves with increasing charge state, demonstrating q/m-dependent heating in addition to the already accounted for mass-dependent excess heating. Slow wind exhibits a bit more complex behavior, rising above the scaled H11 curve at the lower charge states, peaking around $q/m \sim 0.36$ - 0.4, then decreasing. This occurs in addition to the fact that nearly all

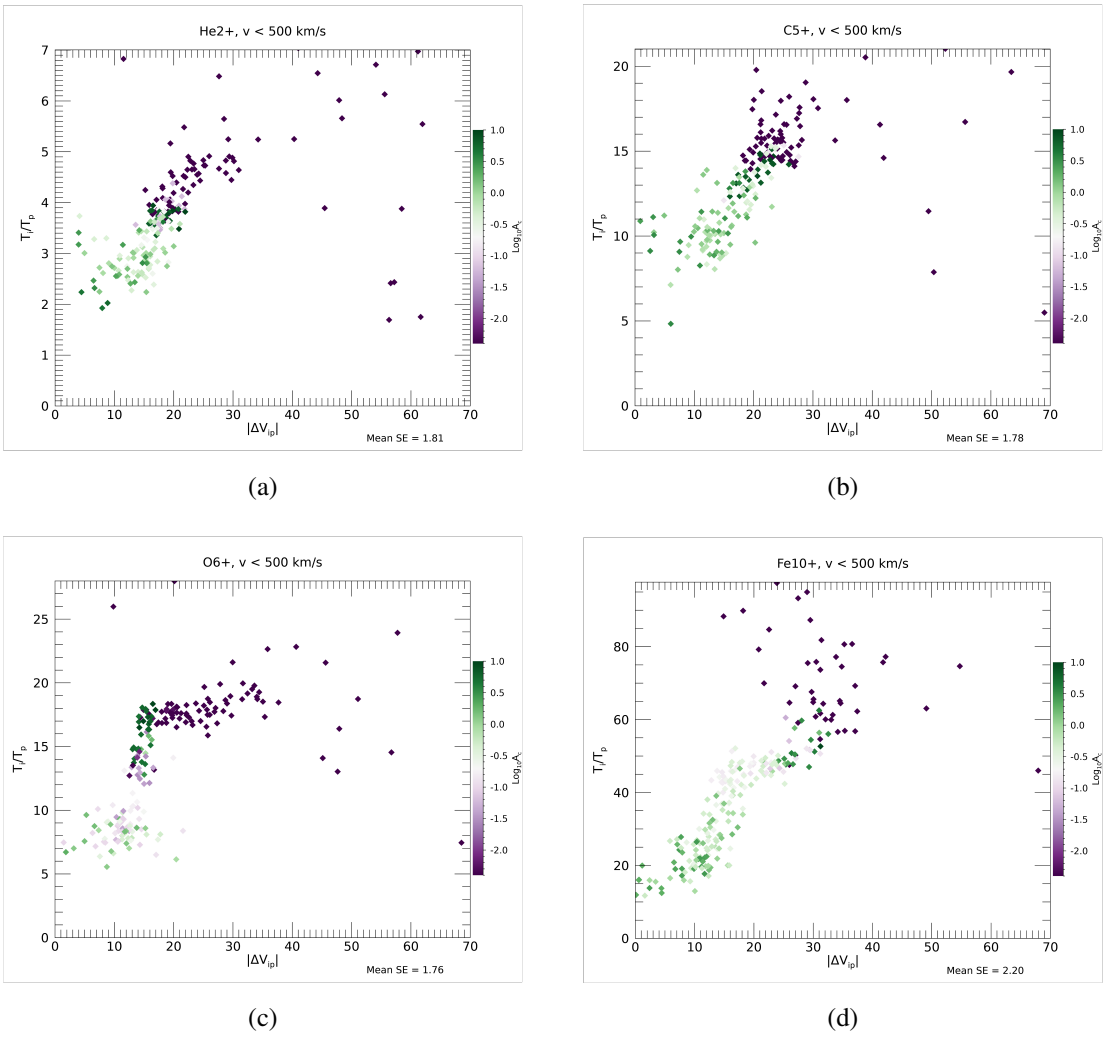

Figure 4.22 Differential velocities vs. temperature ratio over all speeds for (clockwise) He^{2+}, C^{5+}, O^{6+}, and Fe^{10+}

HIS slow wind observations have temperatures in excess of the scaled up H11 Helios fit.

The interplay between temperature ratio, differential streaming, and Coulomb collisions can be somewhat complex, especially at low collisional ages, so Δv_{ip} and T_i/T_p are plotted against each other in figure 4.22 .

All four ions are shown, with temperature ratio on the y-axis, and differential streaming on the left. The plots are shown for slow wind speeds, but note that for O^{6+} and Fe^{10+} plots of all wind speeds exhibit very similar behavior to what is shown here. These plots are not shown, however. He^{2+} and C^{5+} both have a direct linear relationship between T_i/T_p and Δv_{ip}, with a large amount of scatter at high values of both parameters, associated with low A_c. O^{6+} and Fe^{10+} behave a bit differently. Starting from high T_i/T_p and high Δv_{ip} (traveling downward and to the left), there is scatter beyond $\Delta v_{ip} > 30 - 40$ km/s. Within

this range, T_i/T_p reduces independently of Δv_{ip}. In step-like fashion, Δv_{ip} decreases, followed by a simultaneous reduction toward zero in both parameters at the lowest T_i/T_p and Δv_{ip}. The transition between Δv_{ip} being reduced and T_i/T_p is discontinuous in O^{6+}. Differentially streaming ions have a reduced likelihood of Coulomb collisions compared to species traveling at the same speed, resulting in an increased thermalization time. Coulomb drag can also increase the thermal speeds of the faster ion, actually causing an increase in temperature ratios as Δv_{ip} decreases [143]. This may be what is at play when thermalization appears to occur in stages (Δv_{ip} reduces to a certain threshold wherein the effects of Coulomb drag are small enough that collisions reduce relative temperatures).

4.6.2 Comparison to Previous Work

Predictions of the R_b location have some similarities and differences from previous work. In each use of the PHZ model in this thesis, different radial boundaries were predicted for minor ions. Each chapter is ruled by different parameters, however. Chapter 2 encompasses a broad range in time, but narrow range in radial distance. This chapter covers a broad range in distance, but narrow range in time. Chapter 3 focuses on the Alfvénicity of the slow solar wind. In Chapter 2 and the current one, the inclusion of all solar wind speeds results in a higher prediction for the PHZ boundary.

This is in agreement with Kasper 2017, which demonstrates (see Figure 5 of their work) a dependence of R_b prediction on speed window, at least up to 400 km/s. The caveat to this is that fast wind is essentially collisionless. Kasper et al., 2017 did not run the model on speeds greater than 500 km/s. It was only done in this work to assess how removal of the high speed subset impacted results in lieu of being able to run the model on narrow velocity ranges.

One might conclude that the fast wind, which intrinsically has higher Alfvénicity, is heated out to larger distances. In Chapter 2, however, SA/high Alfvénicity wind consistently predicts lower R_b than low Alfvénicity wind, despite allowing speeds up to 600 km/s in the SA wind, which should increase the R_b prediction based on previous findings.

Table 3.1 shows the collisional frequencies for all types, SA, fast, and SNA wind. From it we can see that the median collisional frequency for all wind speeds is lower than that of SNA wind, yet higher than that of SA wind. This places the SA wind in a more extreme category than that of simply allowing fast wind measurements along with slow (and seeing how the removal of fast wind changes model output). The speed dependence in the slow wind, and its assumed continuation into the fast wind (As seen in higher radial boundary predictions on the “all speeds" subset of wind in this chapter and Chapter 2) is superseded

by some aspect of the SA wind.

At first glance, the ion dependency plots shown here and in Chapter 2 are not in agreement, but they have some qualitative similarities that might be significant. The R_b vs. m_i has a similar distribution of R_b predictions, with lower charge states having higher R_b for low mass ions and higher charge states having higher R_b in high mass ions. the R_b vs. q/m curves both exhibit an increase in R_b with decreasing q/m (reading the plot right to left) up until $q/m \sim 0.3$. At this point, the iron ions become uncorrelated to q/m in the SWICS data, while in the HIS data, the trend reverses and R_b decreases with decreasing q/m.

The HIS ε_b vs. m_i is not in as good agreement with T16 as in the 2 hour SWICS data; this is to be expected as HIS is a different instrument making measurements at different locations. The fact that the HIS excess temperatures do not vary too much from SWICS demonstrates the success the technique of using A_c to predict conditions at the boundary. It also helps to reinforce that the significant excess temperatures seen in the SNA wind are actually due to differences in the wind type, since the 12-minute data over the full study has ε_b vs. m_i in agreement with the 2 hour data, as well as the HIS data and the Tracy et al., 2016 mass-dependence. Running the model on SNA wind throughout the entire SWICS dataset may help to distinguish how much of the additional excess temperature can be attributed to solar maximum, and how much can be attributed to the solar wind type. Note that Kasper et al., 2017 did not find a dependence in boundary excess temperature on solar wind speed. The stratification of ε_b with q/m is in qualitative agreement with the 2-hour SWICS data.

4.6.3 Conclusion/Future Work

In this chapter, the radial trends in temperature and density for some of the more abundant minor ions, as well as the averaged down protons (PAS data) were plotted and compared to fits to HELIOS observations. Decay curves for temperature ratio and normalized differential streaming with collisional age and radial distance were plotted, as well as the unique relationship between temperature ratio, differential streaming, and Coulomb thermalization. Observations of the transition from heating to thermalization may point to agreement with previous work by ([119];[91]) The PHZ model was run on the HIS data, and while full agreement was not found with the SWICS data, some important similarities were observed, namely in the behavior of the model when all wind speeds vs. slow speeds only are included as well as some aspects of the trend in R_b with q/m and m_i. Finally, we showed how model R_b predictions vary based on the radial distance of included observations. The most pertinent conclusion to draw from this chapter, however, is that more validated data

is required for any of these observations to be considered statistically sound.

CHAPTER 5

Conclusion

5.1 Summary

In this thesis, the preferential heating of heavy ions in the solar wind has been explored from three different angles. In Chapter 2, collisional age is used to model the thermalization of minor ion species, predicting the radial distance at which preferential heating becomes less significant than thermalization due to Coulomb collisions. The results were compared to those found for alpha particles using WIND data, as well as a model of mass-dependent heating. Though the predictions of the preferential heating zone boundary were higher than the range found in previous work, they did exhibit a clear relationship with mass. The fact that the bump in thermalization curves is reduced or vanishes when considering speeds below 500 km/s only indicates that it is likely a fast wind feature. The boundary ε vs. ion mass is slightly higher than in previous work, but within range of error estimates, and when plotted against q/m, boundary ε appears stratified, with only the higher mass ions exhibiting q/m dependence, and only at low q/m

In Chapter 3, slow-Alfvénic intervals from SC 23 solar maximum were selected, as well as fast and non-Alfvénic intervals. SWICS 12-minute data were used to analyze the collisionality of these wind types, with the overall goal of determining whether or not the SA intervals were collisional enough to be used in the PHZ boundary model. It was found that all three wind types exhibit collisionality, or non-collisionality independent of their density and temperature. The PHZ model was run on SA and SNA wind, finding that the model predicts a lower boundary for SA wind than for SNA. It was also found that R_b and ε_b vary with solar cycle and with normalized cross-helicity. The radial boundary is higher at solar max and lower at solar min. Excess temperature at the boundary does not have a clear SSN dependence, while excess temperature at 1 AU has a dependence in alphas, but not for O^{6+}. Subsets of slow solar wind with high cross-helicity predict a lower radial boundary than subsets with low cross-helicity, in agreement with the analysis run on

selected slow-Alfvénic intervals. Subsets of the slow solar wind with high cross-helicity exhibit less variability throughout the solar cycle, and a less scattered direct relationship between radial boundary and SSN than low cross-helicity subsets. These distinctions are indicative of differing heating mechanisms being dominant in the two wind types, one that exhibits a strong solar cycle dependence, and one that does not.

Chapter 4 applies the PHZ model to HIS observations, allowing for the direct input of varying distances from the Sun. Direct observations of the relaxation of T_i/T_p and $\Delta v_{i,p}/v_{alf}$ with radial distance and A_c are compared to each other, as well as modeled and observed trends in ion parameters. This is done for slow, fast, and combined wind. A distinct change in slope is seen at about 150 R_s for slow and, consequently, all wind for He^{2+}, C^{5+}, O^{6+}, and Fe^{10+}. PHZ model predictions in varying ranges of radial distance are compared, finding that when including data beyond about 150 R_s, model predictions become well-ordered, despite limitations on the inner radial distance limit.

5.2 Limitations of this Work

5.2.1 PHZ for Minor Ions

Some of the limitations of applying the PHZ model to the SWICS-2 hour dataset have previously been discussed in Chapter 2, and are further explored in the appendices. The major limitations here are the 2-hour cadence, which is likely causing high model R_b output, and the time resolution preventing its use in the slow Alfvénic wind study. The following is perhaps not a limitation, but something that could produce better results: SWICS data covers one full solar cycle, and SC 23, SC 24, and SC 25 all differ from each other in intensity. In-situ composition data that spans multiple solar cycles and covers various distances would be ideal for this work.

5.2.2 Minor Ions in the Slow Alfvénic Wind

Chapter 2 utilized SWICS 2-hour data. It was found that, due to the number and length of the SA intervals, the PHZ model could not be used on the 2-hour dataset. Instead, the 12-minute SWICS data, which has not been fully validated for L2, was used. Each timestep in the 2-hour data benefits from a 2 hour accumulation cycle, wherein 10 measurements are taken at the 12-minute cadence. The average of these 10 measurements, so long as they are of good quality, is used. The 12-minute data thus does not have the statistics and confidence for each measurement, especially for the less abundant ions. To counteract this,

an error threshold is used, requiring $\sigma_n/n < 0.4$.

The 42 slow-Alfvénic intervals used here all come from the maximum phase of SC 23, as SA wind becomes sparse during solar minimum. Due to the limited amount of data, it is difficult to confirm whether or not the results, which are quite different to those from the full 2-hour dataset, are the result of lower measuring statistics, or if they are reflective of actual features of the different wind types. SNA wind does consistently predict a higher radial boundary than SA wind, but this could be a result of SA wind having generally lower A_c. While the collisional age itself is a consequence of the wind type, the R_b prediction could be influenced simply by not having enough high A_c bins to see full thermal relaxation.

In order to improve upon and verify the work shown in Chapter 3, enough portions of the SWICS 12-minute dataset would need to be validated to cover as many SA intervals as possible, as well as a comparable amount of SNA and fast wind. In an ideal situation, composition data from multiple solar cycles would be available. Incorporation of SA intervals seen by PSP and SO would also help to verify.

This work could be improved if there were enough slow-Alfvénic intervals for a robust statistical analysis. This is not the case. Many studies of SA wind have tracked and analyzed specific intervals. Higher time resolution on the composition data would also result in more reliable calculations of differential streaming as well as σ_c, which are both known to occur on scales comparable to the 12-minute cadence of the SWICS data. Finally, directional temperatures/thermal speeds would be required to determine whether or not SNA $\varepsilon_b >$ SA ε_b is due to either higher mass or higher charge-to-mass ions having a higher perpendicular and lower parallel temperature.

5.2.3 Heavy Ion Sensor

As with the SWICS instrument, HIS has its own limitations, but does not benefit from over 25 years of validation and study. HIS does have a 10-minute cadence, which allows for convenient comparison with SWICS 12-minute data.

A potentially major setback for the work in Chapter 4 is the absolute density calibration. Heavy ion densities have not yet been calibrated, and each requires a unique correction factor. This work has used a workaround, assuming that mean HIS and SWICS n_i/n_p would be the same over the entire mission. Such an assumption could be misguided, as solar wind composition changes with the solar cycle. Alpha particle number density decreases during solar minimum and increases during solar max (with a lag).

Additionally, the prevalence of equatorial fast wind during solar min means that photospheric -like composition wind, which has a depletion of low-FIP ions and an enhancement

of higher charge states, would cause all heavy ions to experience shifts in their number density ratio. So far, the majority of available HIS measurements have been taken during the ascending/maximum phase of SC 25, so SW composition may be very different from an average over the ACE mission from 1998-2011. Average HIS n_i/n_p might be markedly lower than that of SWICS. Variations between solar cycles may also have an impact, as a weaker/stronger solar maximum is indicative of weaker magnetic activity, and may lead to lower Alfvénicity. There is no way of knowing without the actual HIS density measurements, which would eliminate the need for this approximation.

In this work, an attempt has been made to relate the collisional and radial evolution of nonthermal properties of solar wind heavy ions. At this point, there are still very few available measurements at 60 R_s. At the moment, there appear to be trends in R_b that abruptly change at about 150 R_s. More data within this point needs to be included to determine whether or not that radial distance holds any significant, and if the changes in trends are simply due to lower binning statistics, or any physical shifts. However, when binned in both radial distance and collisional age, excess temperature never shows a full relaxation to 1. Though the same issue is present in the SWICS 2-hour data, it may be for different reasons, as we do see an almost full relaxation in the SWICS 12-minute.

5.3 Future Work

Addressing some of the issues discussed in the previous section is the most obvious next step for future work. This thesis has been an attempt to draw broad conclusions: comparison of wind types, temporal, and radial evolution. It is in essence a statistical analysis and requires large amounts of data to be able to draw significant conclusions. Waiting for more HIS data to be available, further calibration of HIS densities, and the identification and incorporation of more SA intervals with SWICS (if possible, prevalent during solar max) and HIS (when available) will improve upon the results presented here. As an additional note, an in-depth study on how time resolution impacts this type of analysis may allow some upper limit to be placed on the time resolution required from a composition instrument for this type of analysis.

Minor ions are useful in two major ways: composition allows the relation of solar wind measurements to solar sources, and minor ion kinetics provide insight into how the solar wind is heated and thermalized. This provides two main paths for continuing this work.

Composition may be used to determine or select times when certain ions are depleted and enhanced, as this might impact any trends with ion properties. This is important in determining if any perceived fluctuations are due to actual changes in solar heating/magnetic

activity while controlling for the changes in composition that are associated with different wind types and the solar cycle.

As SO/HIS encounters more slow Alfvénic wind during the Solar Orbiter mission, the wind type/solar cycle analysis can be repeated on that data, and the radial evolution reexamined. Additionally, once enough HIS data are accumulated, it can be averaged down to SWICS' 2-hour cadence to compare PHZ R_b predictions. One could also examine how the power spectra change with solar wind type and solar cycle. Heating rates/heat flux calculations across heavy ion species could be calculated and related to heating estimates from more recent solar source observations/theory. The 3D VDFs from HIS are not currently available, but minor ion temperature anisotropies would help to give a more complete picture on the nonthermal features present in as the solar wind travels away from the Sun.

APPENDIX A

HIS Validation - Heavy Ion Kinetics (Temperature ratios, velocity ratios)

A.1 Heavy Ion Kinetics

Ion-Ion velocities and temperatures for each ion pairing across the entire dataset have been completed for each revision of the HIS Level 3 dataset. Pairings between the He^{2+}, C^{5+}, O^{6+}, and Fe^{10+} in the latest version are shown here. Velocity and temperature are provided in the “Level 3 Processed" internal file, which contains velocity and temperature calculated from the moments of the particle distribution function for each ion.

From Figure A.1, it can be seen that heavier ions stream the fastest, with Fe^{10+} having the highest velocity shift (among these four ions). The slope remains within +/- 7% for each pairing. These velocity shifts are in agreement with those found in [54], shown below. Note that different ions are shown here than in [54]. The magenta dashed line depicts a 1:1 ratio, while the magenta dotted line is the linear fit of the ion velocities.

The temperature pairings are also as expected, as shown in A.3. Three lines are over-plotted here: the dashed shows the mass scaling between the two ions, the dotted the linear fit, and the third, the dash/dotted line only visible in the C^{5+}/O^{6+} plot, shows the 1:1 temperature scaling. In all cases, the heavier ion is plotted on the y-axis, making the super-mass proportional temperature scaling quite evident. Because Log(T) is plotted, a temperature shift of 1 corresponds to an order of magnitude. As ion mass increases, the temperature peak increases, and a larger ratio of ion masses corresponds to a larger shift in the temperature relationship. Though some of the shifts here might seem dramatic in that light, it corresponds only to the low-temperature tail of the overall temperature distribution. The difference in peak temperatures for each pairing results in peak temperature ratios that are in agreement with mass proportionality. The slope of all pairings depicted here are within 9% of a 1:1 scaling. Figure A.4 shows similar plots from [54].

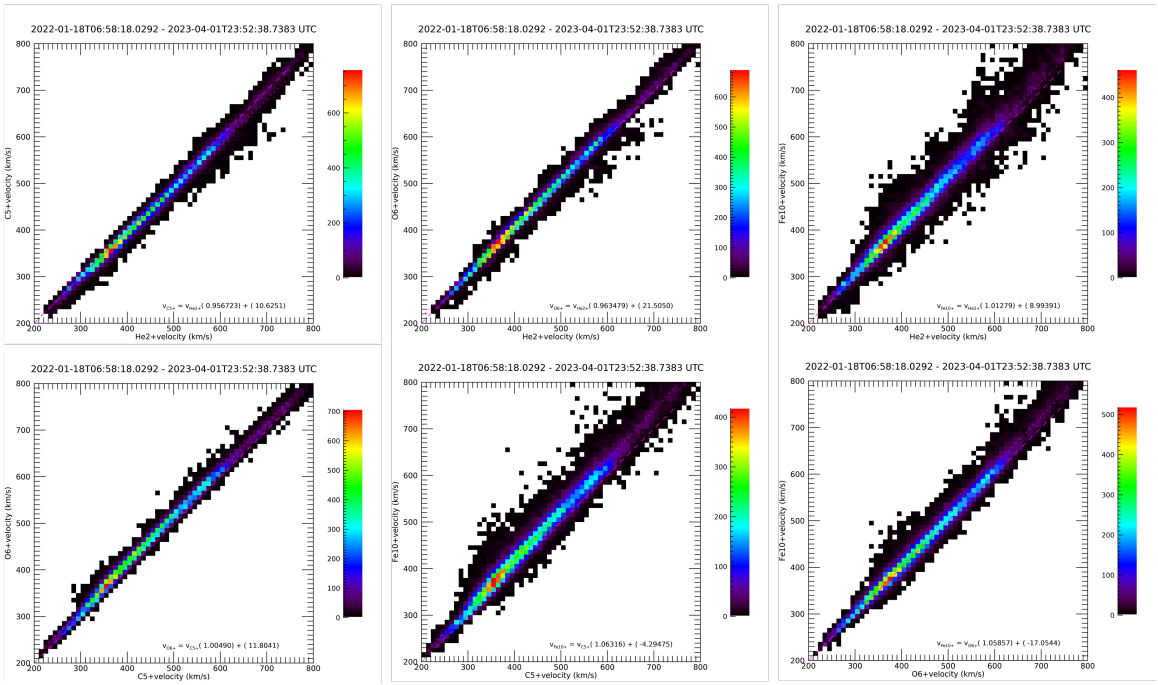

Figure A.1 Velocities and fits for all ion pairings between He^{2+}, C^{5+}, O^{6+}, and Fe^{10+}

The supra-mass proportional heating and differential velocities of the heavy ions are consistent with observations by other instruments. More data and further calibration may impact deviation in the slope of the linear velocity fit from 1:1.

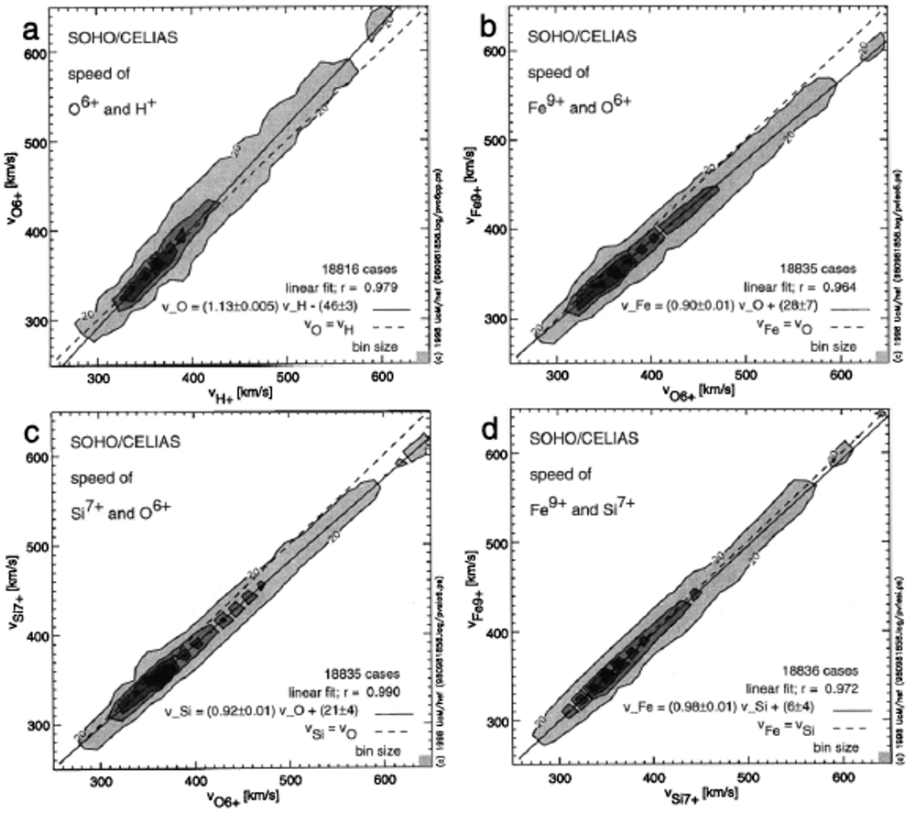

Figure 4. Comparison of the bulk speeds of protons O^{6+}, Si^{7+}, and Fe^{9+}. The dashed lines indicate equal bulk speeds of both ions species, while the solid lines show a linear fit to the data. The bulk speeds of all ions agree remarkably well, the correlation coefficient being 0.96 or higher. While O^{6+} tends to have a higher speed than protons, as expected from acceleration of minor ions by Alfvén waves, both silicon and iron tend to lag behind the protons. Ten-minute averages have been used for Figure 4. Note that because of the excellent count rates of the CTOF sensor, we have ~ 19.000 measurements, even for rare species like Fe^{9+}.

Figure A.2 From Hefti 1998

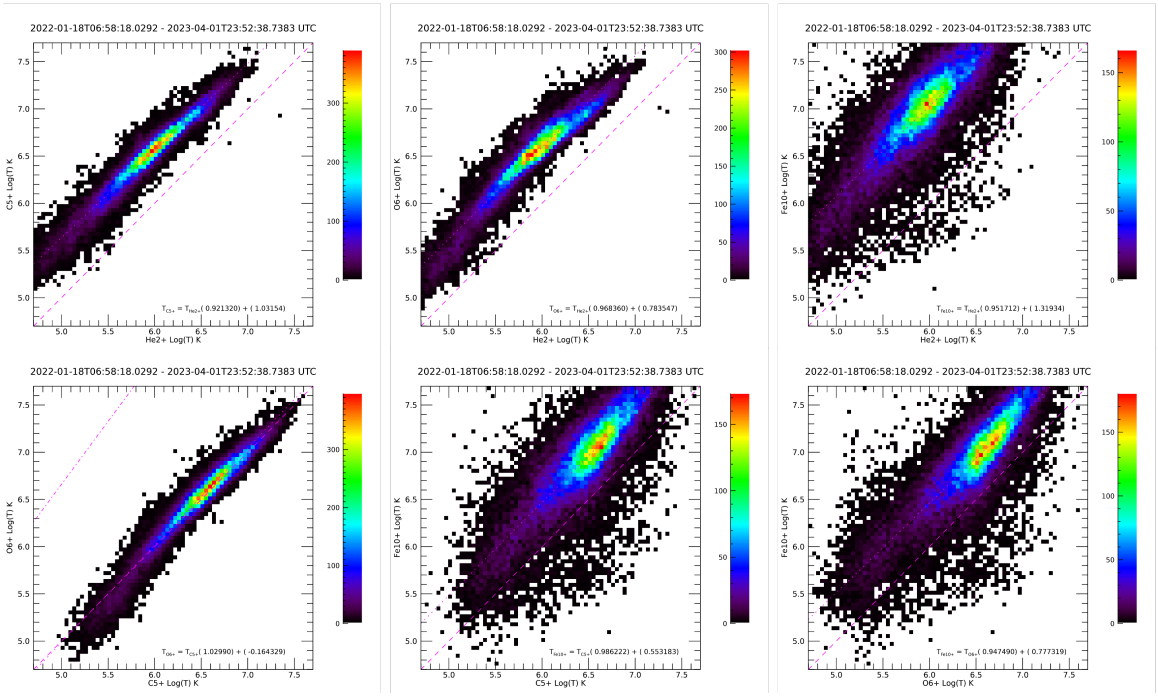

Figure A.3 Temperatures and fits for all ion pairings between He^{2+},Fe^{10+}, O^{6+}, and C^{5+}

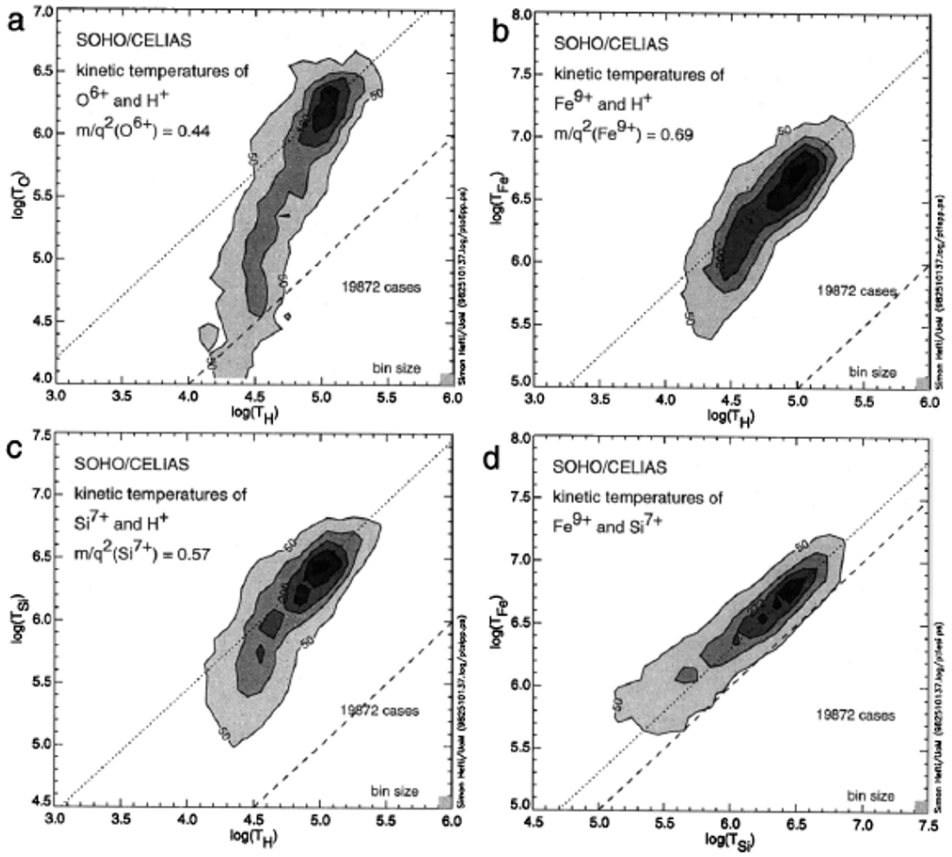

Figure 5. Comparison of the kinetic temperatures of protons O^{6+}, Si^{7+}, and Fe^{9+}. The dotted line indicates equal thermal speeds, or temperatures which scale with mass. The dashed lines show equal temperatures. Clearly, both cases with equal thermal speeds and cases with equal temperatures are observed. The trend toward equal temperatures diminishes with increasing m/q^2. Ten-minute averages have been used for Figure 5. Note that we have ~ 19.000 measurements for all ion species.

Figure A.4 From Hefti 1998

A.2 Radial Trends

In addition to the moment comparisons, radial trends in ion density and temperature are also plotted and compared to previous observations. This is a continuation of Chapter 4. The overall behavior of these two ions is in agreement with He^{2+} and O^{6+}. Note, however, that Fe^{10+}, which has a low q/m has fast wind temperatures that generally fall below the supra-mass-proportional scaling used on the P18 and H11 curves, while the other three ions fall above them. For all ions, including those not shown here, when stepping through the most abundant charge states of each element, the HIS observations increase relative to the scaled P18 and H11 curves with increasing charge state, demonstrating q/m-dependent heating in addition to the already accounted for mass-dependent excess heating.

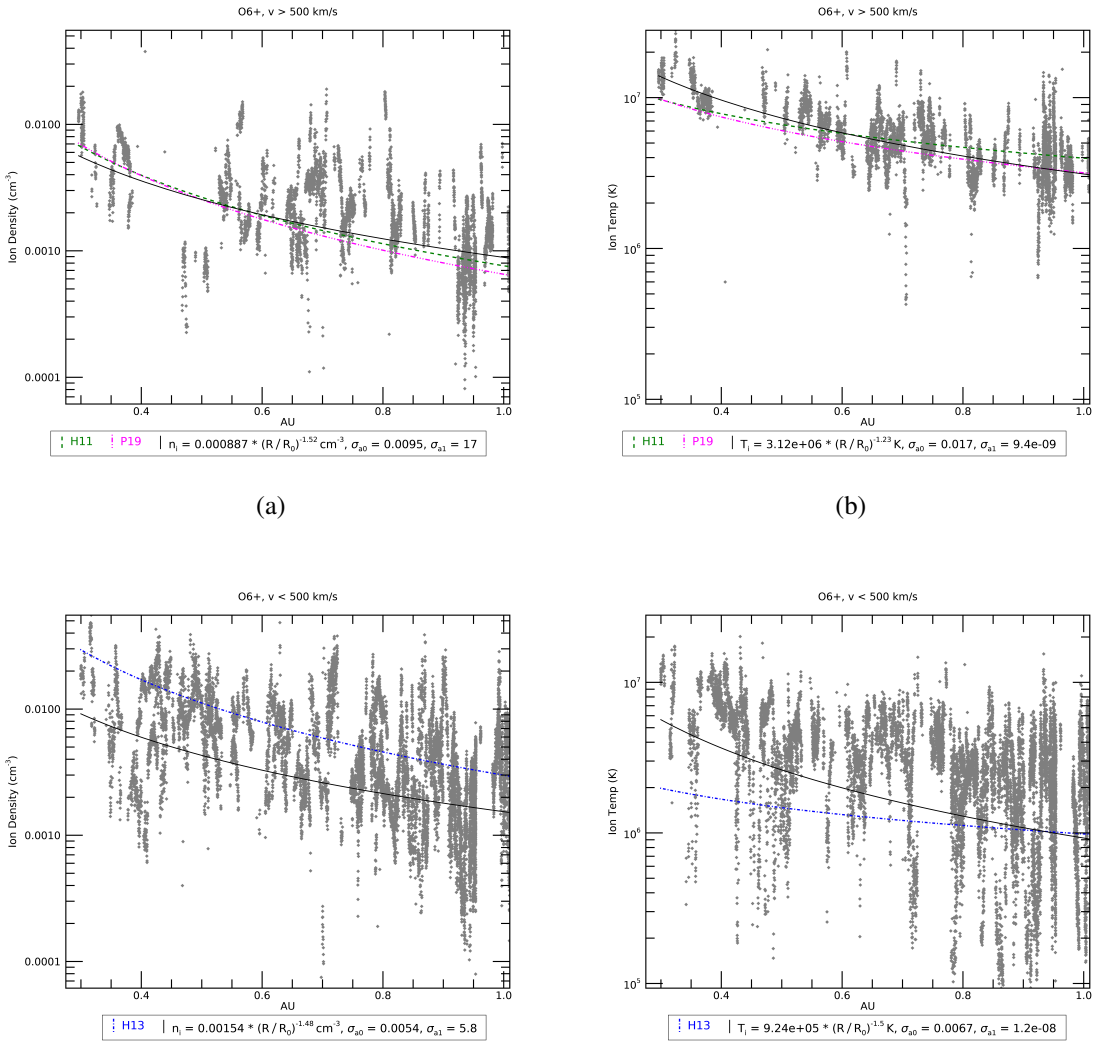

Figure A.5 Radial evolution of solar wind density and temperature for O^{6+}. Fit is overplotted in black. Previous observations by Hellinger et al., 2011, 2013, and Perrone et al., 2018 are overplotted in green, blue, and magenta, respectively. The top row shows the trends in fast wind, the middle slow wind, and the bottom all speeds.

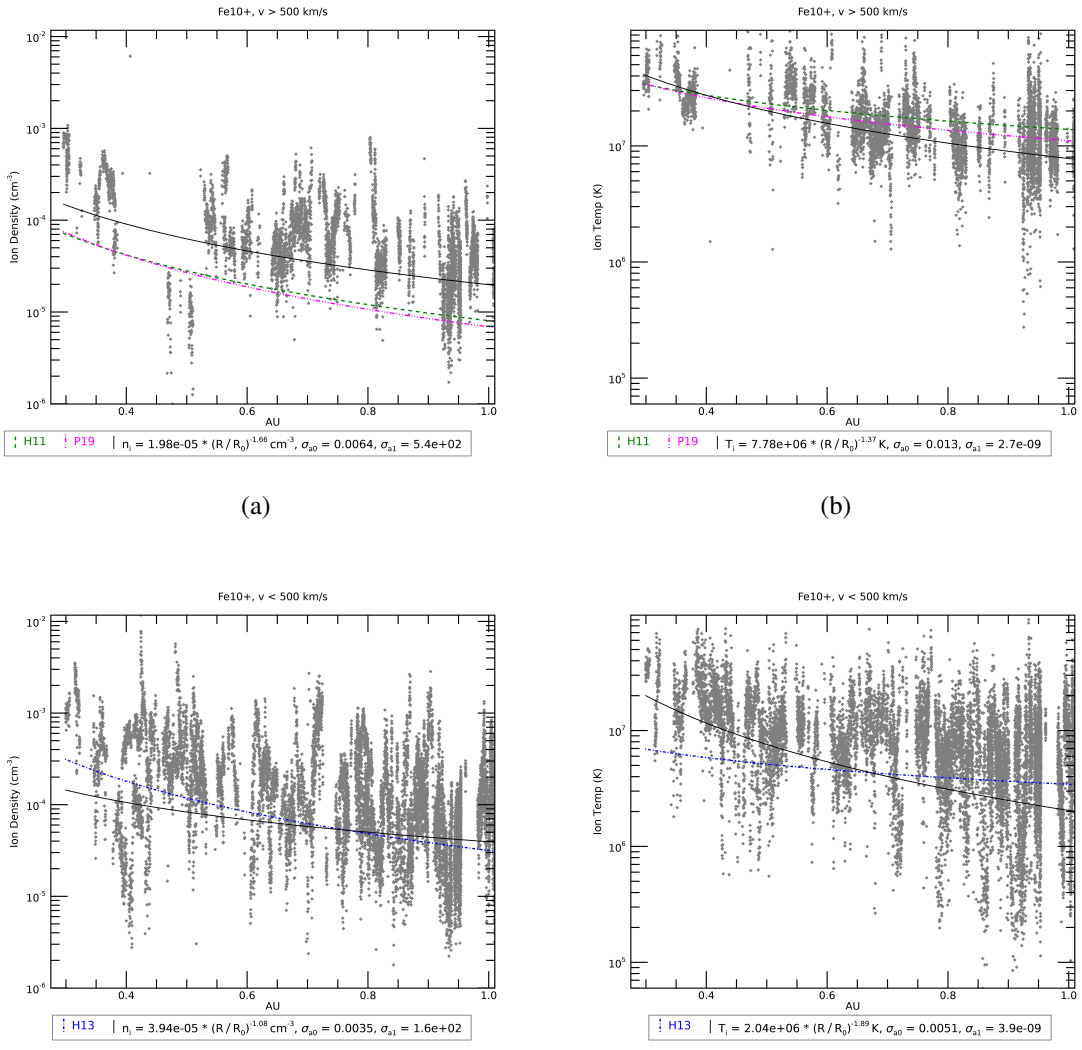

Figure A.6 Radial evolution of solar wind density and temperature for Fe^{10+}. Fit is overplotted in black. Previous observations by Hellinger et al., 2011, 2013, and Perrone et al., 2018 are overplotted in green, blue, and magenta, respectively. The top row shows the trends in fast wind, the middle slow wind, and the bottom all speeds.

APPENDIX B

PHZ Model Sensitivity

B.1 Absolute density calibration

Different instruments measure density in different ways and therefore may have discrepancies in their absolute calibrations (See [19] section 4.1.5 and Figure 7e). The effects of differences in densities on the R_b values are shown in Figure B.1 below, where the left side shows results of running the PHZ model on the unaltered WIND dataset, while the right shows the results when density is multiplied by a factor of two, which results in a 50 % increase in predicted R_b.

The calculation for R_b depends on the ratio of the heavy ion density to the proton density. The most accurate ratio of the heavy ion to proton densities are obtained using the same instrument to measure the densities, eliminating observational difference between instruments. SWEPAM and SWICS are known to measure slightly different proton densities, and both datasets are cross-calibrated to WIND/SWE, which is considered to provide the most accurate proton and alpha densities. A statement on this from the instrument team can be found in the release notes at the Ace Science Center data hub.

B.2 Data time resolution

The Kasper et al. [1] study uses 90-second resolution proton and alpha data. Our work uses the 2-hour SWICS dataset for heavy ions, and 12-minute proton data, averaged down to two hours. To determine the effects of time-resolution on the model output, we have averaged the WIND/SWE proton and alpha plasma parameters to 2-hour resolution, shown in the figure below. The time-averaging resulted in an almost 50 % increase in R_b prediction. As such, the results of our work, run on ACE/SWICS data can be interpreted as an upper limit on the PHZ boundary.

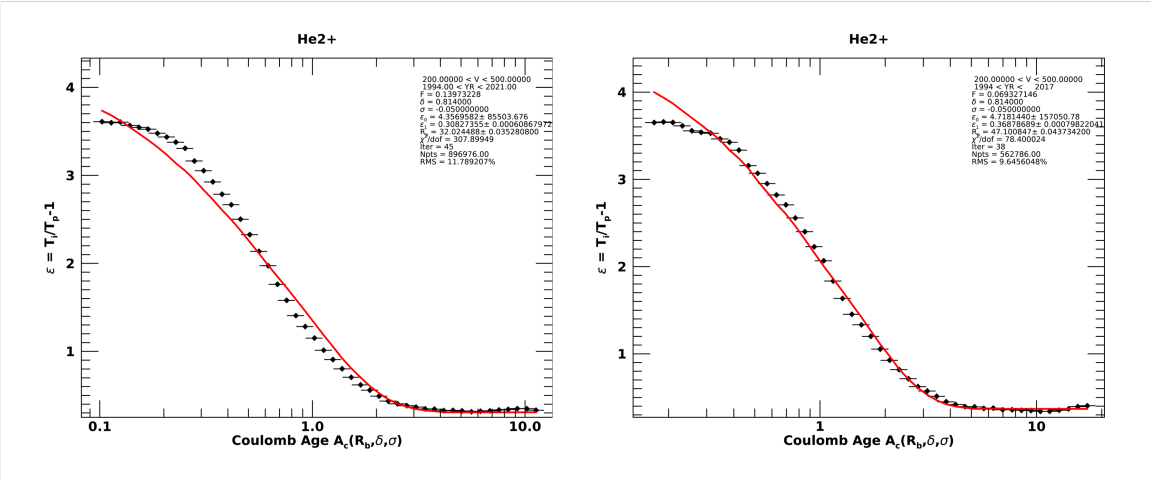

Figure B.1 The image on the left shows an unaltered dataset. The image on the right shows the results of multiplying proton density by two, which produces an R_b nearly 50 % larger than the unaltered dataset. WIND/SWE and ACE/SWICS are known to measure different densities during the same time periods, and the R_b produced by this model is heavily influenced by proton density. This would be a major contributing factor to the difference in results produced from the SWICS and SWE datasets.

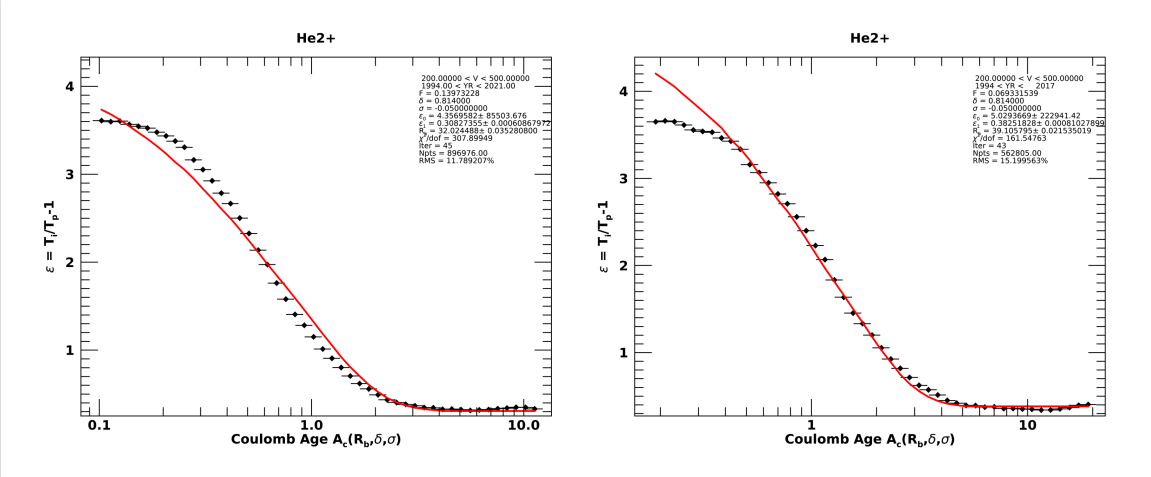

Figure B.2 The figure on the left shows the unaltered 90-second resolution WIND dataset. The figure on the right shows the dataset averaged down to two-hour resolution. Time averaging does result in an increased R_b value, in this case almost 50 % larger than the unaltered prediction. The results produced by the SWICS dataset at 2-hour place an upper limit on the radial PHZ boundary.

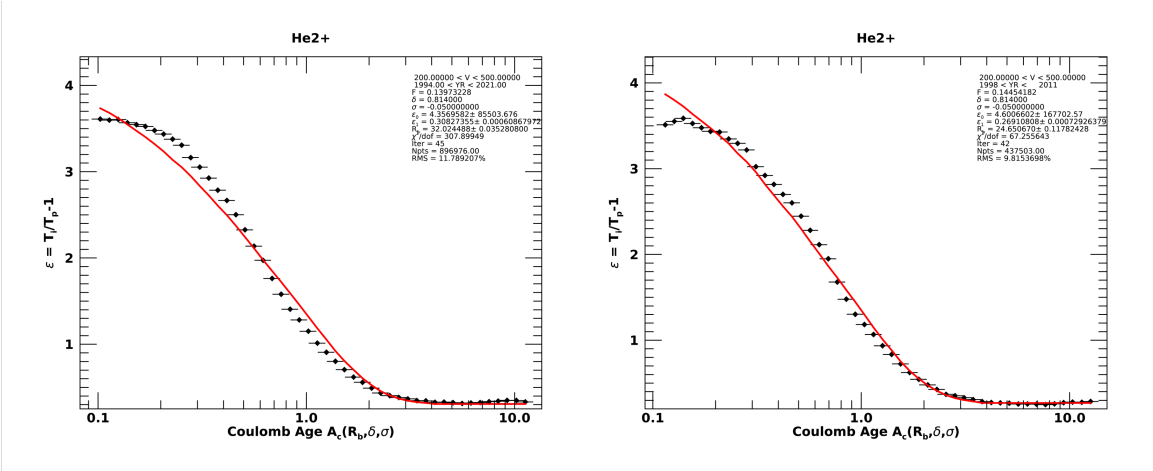

Figure B.3 The figure on the left shows the original 90-second WIND data set from 1994-2021. The figure on the right shows the WIND dataset when limited to the pre-anomaly ACE/SWICS years of operation, 1998-2011. The WIND dataset used in K17 covers the end of Solar Cycle 22 up to the beginning of SC 25, which includes SC 22 solar minimum, all of SC 23, and SC 24 solar and descending phase. The SWICS dataset spans (portions of) SC 23 and 24. Kasper 2019 showed a correlation between predicted R_b and sunspot number, so it would follow that the variation over a solar cycle and between different cycles would lead to R_b variation.

B.3 Solar cycle variations

The implications of the Sun's $\sim$ 11 year cycle extend to solar wind composition, type, and Alfvénic nature. In addition to variations within each solar cycle (SC), the Sun and solar wind also vary from cycle to cycle. Kasper et al. [2] demonstrates the effects of solar cycle variation on the model's R_b output. The WIND data used in Kasper 2017 covered 1994-2017, which includes the end of SC22 up to the beginning of SC25. Below, we show how model output changes when limiting the WIND/SWE dataset to 1998-2011, the years covered by SWICS (pre-anomaly). This spans portions of SC23 and SC24. Limiting the WIND dataset to 1998-2011 actually reduces the R_b prediction by about 25%.

APPENDIX C

Collisional Age, Density and Temperature in 3 Solar Wind Types

C.1 SWICS Dataset and Error Filtering

To determine an appropriate error threshold for this analysis, σ_n/n is stepped through, low to high. Three thresholds, 0.16, 0.40, and 0.58, are selected as representative of the overall trends. The lowest, strictest thresholds prohibit results on much of the higher mass ions. The top row of plots includes all ions that produced results in the PHZ model, and the bottom row limits to a subset of the more abundant ions. Ions included in the bottom row are He^{2+}, $C^{4\text{-}6+}$, $O^{5\text{-}8+}$, and $Fe^{7\text{-}16+}$. This is evident in the $<$0.16 column. Between 0.3 and 0.44, model output is quite consistent. Beyond about 0.44, some ions are allowed with very low R_b predictions, and overall R_b predictions drop. As such, errors close to 0.3 are taken as the lower limit of error filtering, and 0.44 is taken as the upper limit. Note that results for alpha particles remain consistent across nearly all error thresholds.

The trend in R_b with mass is evident to some extent in all error thresholds, though the 0.4 threshold is the cleanest. The trend is still evident in the truncated version, though the addition of some of the less abundant ions does support the correlation. The trend with q/m is actually stronger in the higher error thresholds, and for the 0.58 and no error threshold, the semblance of a trend is still apparent when only including the most abundant ions. Much of this trend is due to Fe and S (which is known to overlap with Si) in the top plots and Fe in the bottom row. The q^2/m plots exhibit a similar behavior to the R_b vs. q/m plots, with the higher/no error threshold having the strongest trends.

Excluding the 0.16 error threshold, there is no significant difference in χ^2/dof across different thresholds. χ^2/dof tends to be slightly higher $\sim$0.25 and RMS error slightly lower $\sim$1% at the 0.4 threshold. Values for 0.58 and no threshold are almost identical.

This helps to confirm that the trend ion mass with R_b is not likely to be due to measurement uncertainty; It is evident in every error threshold except the lowest. It does bring

to question whether or not some of the trends, driven by the heaviest ions, are a product of measurement error or some physical process. Fe, Si, and S all typically have higher abundance in the slow wind than the fast.

C.2 Density and Temperature

According to the equation for Coulomb collisions between ions of two different species, test particle density is of the major factors contributing to the collisional cross-section and thus the likelihood of the occurrence of a Coulomb collision. Other major contributing factors are species charge, mass, and thermal velocity, represented here as temperature.

The distribution of proton densities for the three wind types demonstrate the similarities between SA and fast wind. Qualitatively, SA wind behaves similarly to fast wind, but is shifted to higher density. SNA wind has a similar peak to SA wind, but drops off gradually, and has a significant present at high densities. Proton density is divided into three groups: low, mid, and high. In each density group, the distribution of temperature ratios in four different A_c regimes are observed, in the same manner as described for the full dataset. In Figure C.4, the rows correspond to A_c regimes, the columns to density groups, with the fourth row depicting the full dataset, for comparison. In the lowest density group, where fast wind would be largely depleted, the behavior of the different solar wind types is slightly different. Fast wind does not deplete as dramatically and SNA wind is more significantly present in the low Ac regime. In the medium density group, the differences between the solar wind types is vastly reduced. The high density regime bears the greatest similarity to the full dataset, though the depletion of fast wind in subsequently high regimes is slower.

These are just quick plots to visualize how Ac changes in smaller bands of temperature and density. Figure C.7 shows the derivative of collisional age with respect to proton density in all three solar wind types. As expected, the dependence is constant. This plot is shown to contrast with the temperature plot, shown in Figure C.8. Fast and SA wind exhibit similar behavior, though slow wind is shifted to low temperatures. SNA wind collisional age clearly decreases as temperature rises. That this temperature dependence is not present in the SA wind indicates that, although SA wind has a much higher collisional frequency than fast wind, its protons are not necessarily heated via collisions with minor ions. A corresponding plot for alphas was not done, but repeating Figure 3 C.8 for alphas to confirm the opposite trend (for SNA) wind might help to clarify this.

Overall, though the difference in behavior of the wind types is reduced when comparing similar densities, they are still distinguishable, especially in the low and high ends of the proton density distribution. This question may be further explored by looking at narrower

density windows.

The temperature distributions for each solar wind type are very different, with fast wind peaking at higher temperatures and having a double peak, SNA having more spread, and SA wind peaking between the other two wind types and having a significant skew. Temperature is divided in three groups and analyzed in the same manner as proton density. Low temperature exhibits a double peak, corresponding to equal proton and ion temperatures, which is not present in the higher temperature groups. At low temperatures, the behavior of the SW types across A_c regimes is nearly identical to the original plots. Like density, the types are far less distinguishable in the middle T group. At high T, the SW types are more distinct, with fast wind once again depleting less rapidly than in the original dataset. The proportion of SA wind in each Ac regime is actually consistent in all temperature groups.

C.3 Note on Correlations and Collisional frequencies

Correlations and median collisional frequencies were explored. Correlation coefficients were calculated for collisional age and density in the low, mid, and high groups, as well as over all densities. Fast, SA, and SNA wind types were each treated separately. The same was done for temperatures. Note that only three subgroups are used, so these windows are quite broad, and see a wide range of densities and temperatures. This analysis would likely be more effective on a spectrum of smaller subgroups, but the size of the bins is limited by data availability.

It is known in from the equation of collisional frequency that collisional frequency and thus, collisional age is directly dependent on the proton number density. The previously shown 2D histograms demonstrate that though this dependence is present, the correlation coefficient is not necessarily strong. There is a lack of correlation in the low and mid groups for fast and SA wind, followed by a stronger correlation in the high density group. SNA wind has stronger correlations in the low and high density subgroups. Correlations between temperature and A_c and density and A_c were low in individual subgroups, but pointed to a much stronger dependence on proton density than proton temperature, as expected.

Finally, collisional frequencies for the low, mid, and high density and temperature groups are calculated for each SW type. The collisional frequency of fast wind is significantly higher in the high density subgroup than its overall value in the low and mid density groups. This demonstrates that, generally, the collisionality of fast wind is determined by its low frequency and not by other factors (such as its Alfvénicity). Mid-temperature fast wind also has a higher collisional frequency. The results for fast wind could be due to the use of speed only as a cutoff for the fast wind. This analysis on pure fast wind streams

would likely result in a different outcome. SA collisional frequency is remarkably constant throughout these subgroups. SNA wind has reduced median collisional frequencies in all subgroups aside from high T, which is nearly identical to the overall medians.

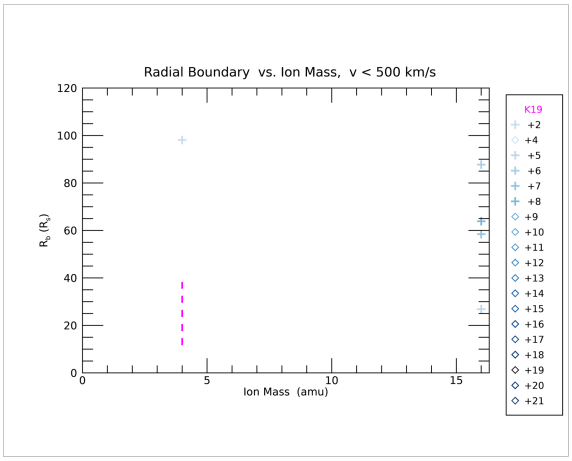

(a)

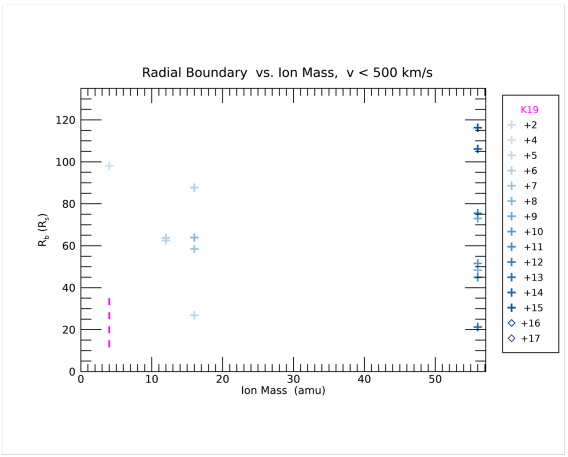

(b)

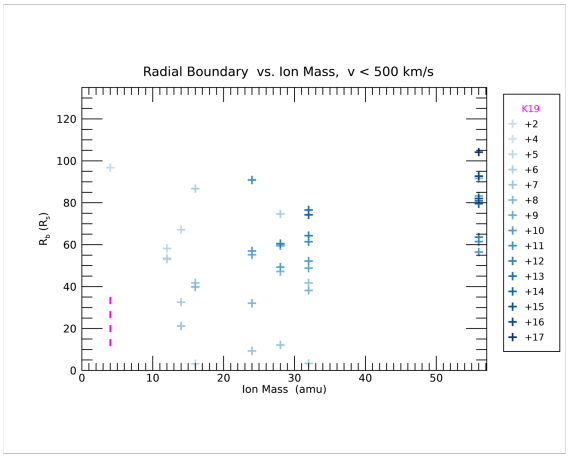

(c)

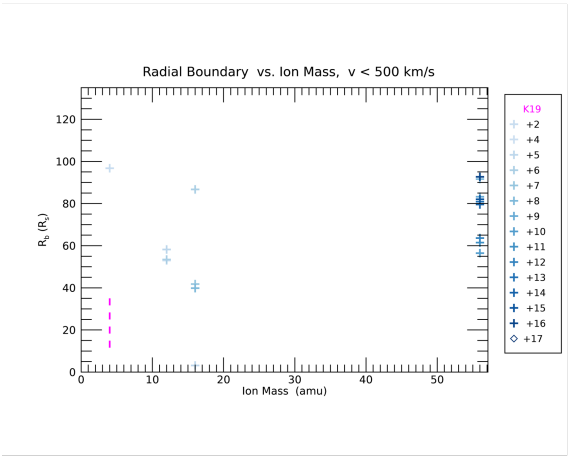

(d)

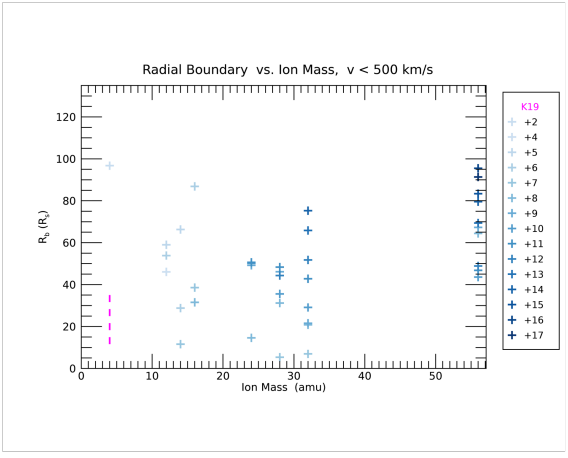

(e)

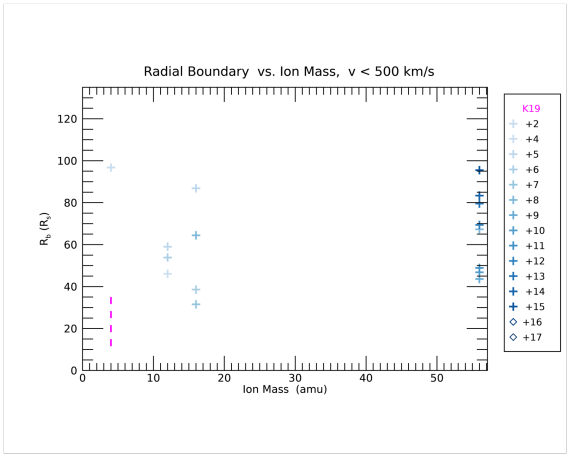

(f)

Figure C.1 Effects of varying error thresholds on the ion mass vs. R_b relationship. From top to bottom, $\sigma_n/n \leq 0.16$, $\sigma_n/n \leq 0.40$, and $\sigma_n/n \leq 0.58$. Full dataset is on the left, restricted to the most abundant ions is on the right.

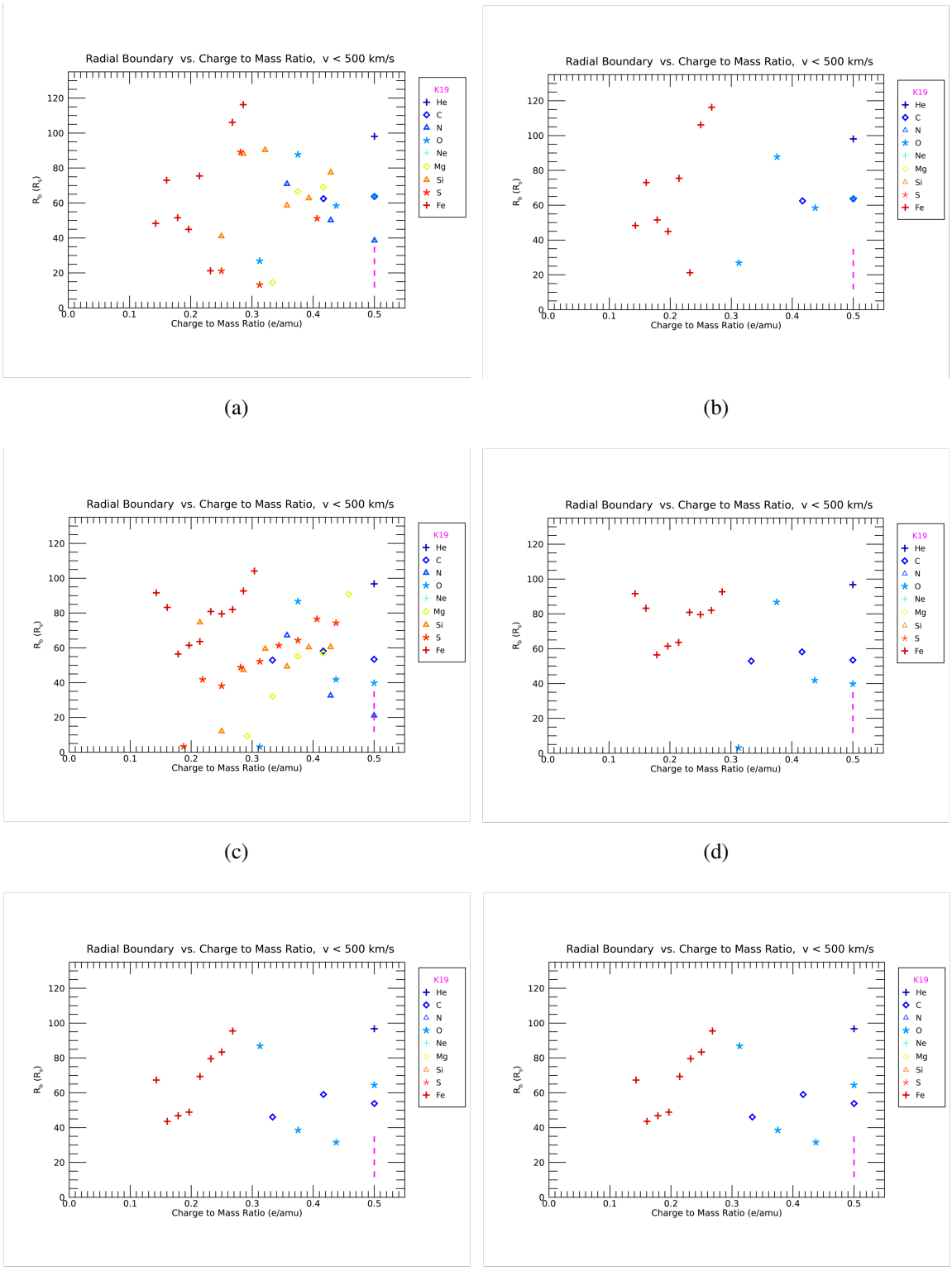

Figure C.2 Effects of varying error thresholds on the q/m vs. R_b relationship. From top to bottom, $\sigma_n/n \leq 0.16$, $\sigma_n/n \leq 0.40$, and $\sigma_n/n \leq 0.58$. Full dataset is on the left, restricted to the most abundant ions is on the right.

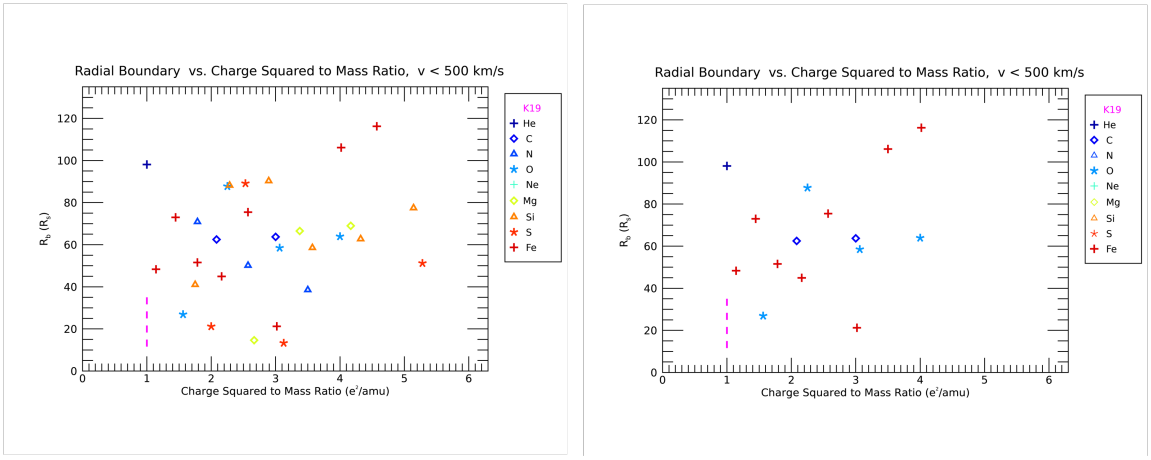

(a)

(b)

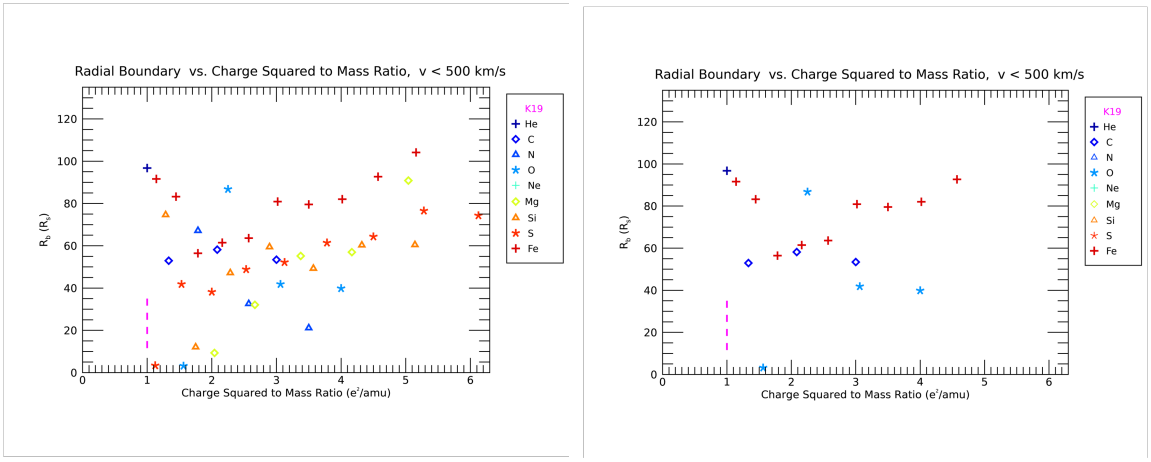

(c)

(d)

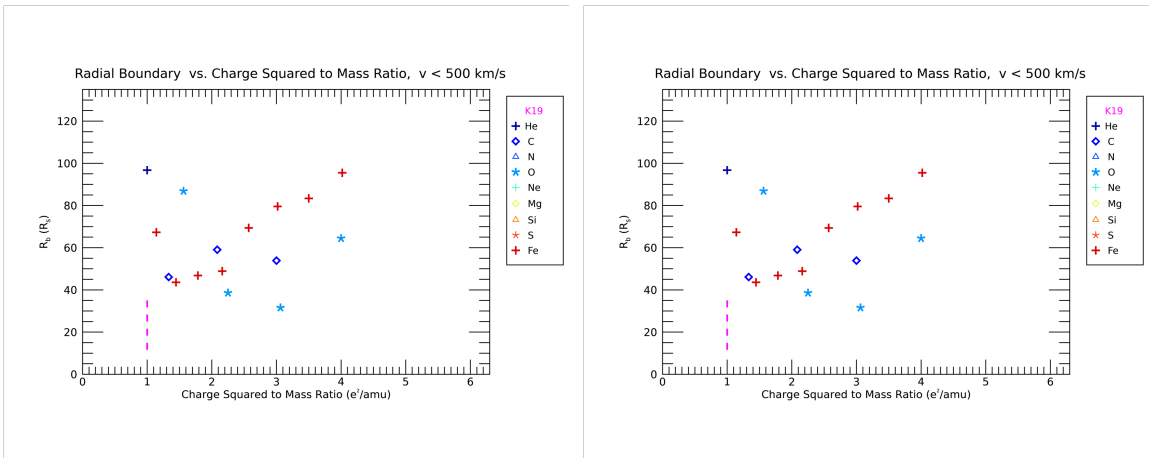

(e)

(f)

Figure C.3 Effects of varying error thresholds on the q^2/m vs. R_b relationship. From top to bottom, $\sigma_n/n \leq 0.16$, $\sigma_n/n \leq 0.40$, and $\sigma_n/n \leq 0.58$. Full dataset is on the left, restricted to the most abundant ions is on the right.

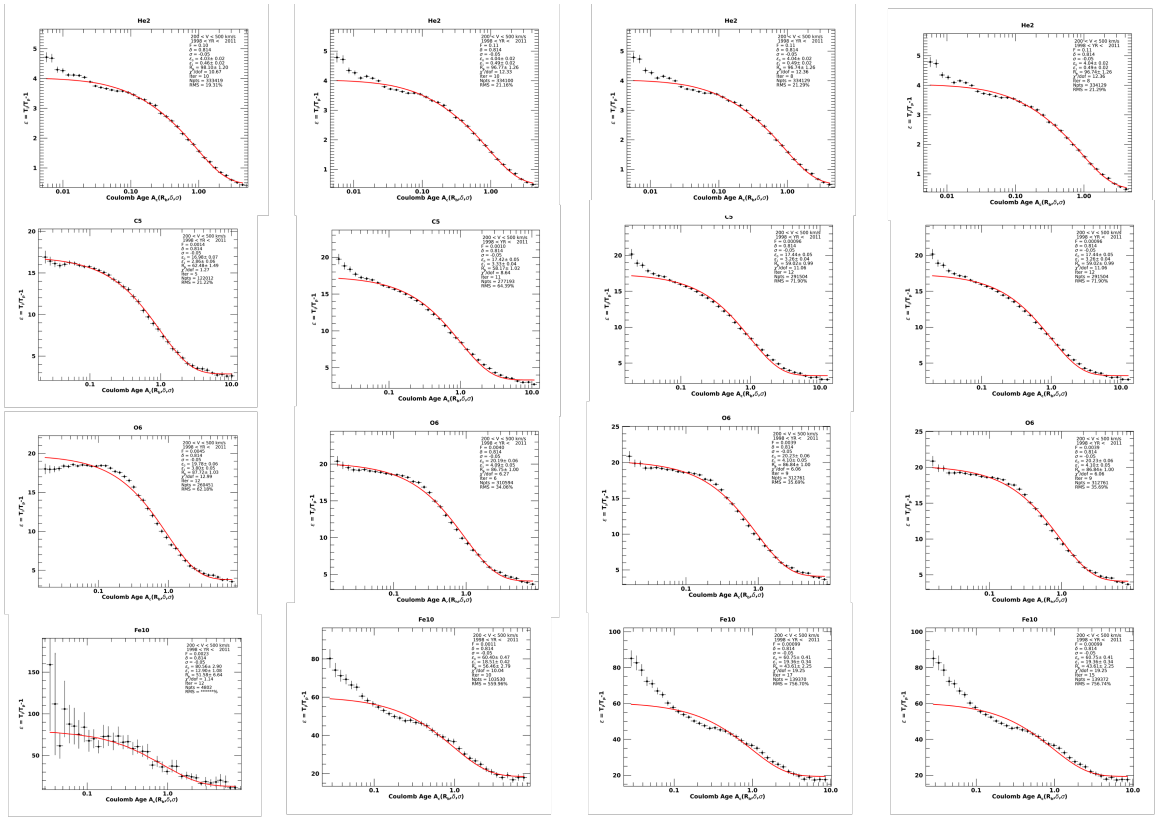

Figure C.4 Effects of varying error thresholds on the decay curves. From left to right, $\sigma_n/n \leq 0.16$, $\sigma_n/n \leq 0.40$, and $\sigma_n/n \leq 0.58$. Top row shows He^{2+}, followed by C^{5+}, O^{6+}, and Fe^{10+}.

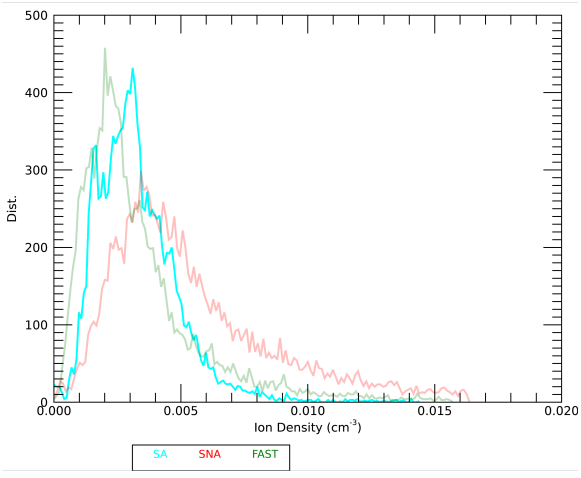

Figure C.5 Proton density distributions for SA, SNA, and Fast wind.

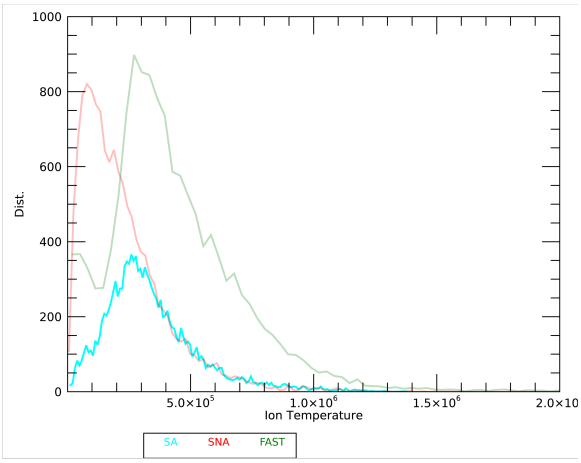

Figure C.6 Proton Temperature distributions for SA, SNA, and Fast wind. Note that SA wind has a slightly higher peak than SNA wind, but SNA wind has a high population overall of temperatures comparable to and higher than the SA peak.

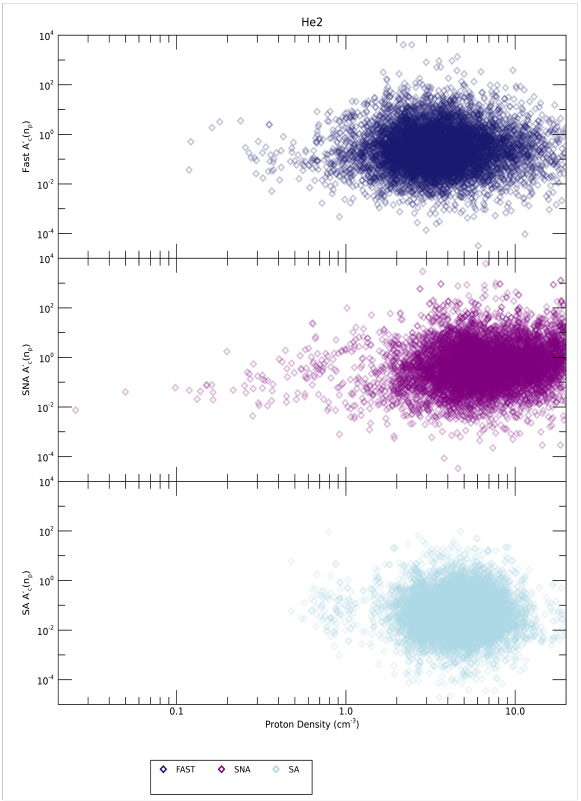

Figure C.7 Derivative of A_c w/r/to proton density.

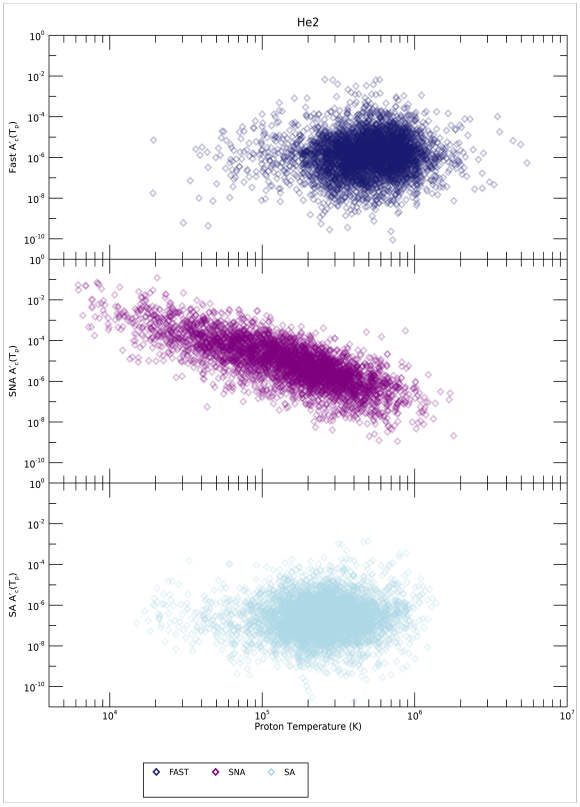

Figure C.8 Derivative of A_c w/r/to proton temperature.

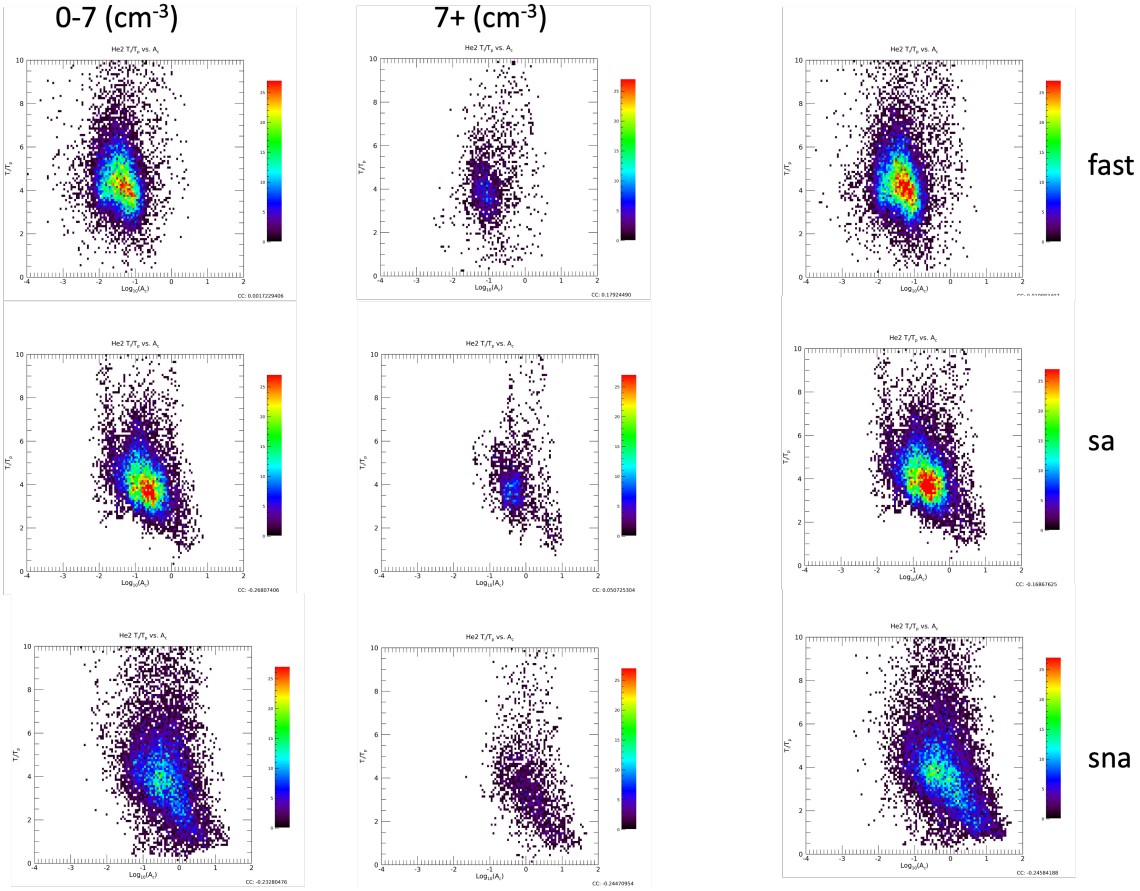

Figure C.9 Proton density distributions in 3 solar wind types in different density regimes. From top to bottom, fast, SA, and SNA wind. From left to right, low density regime, high density, and the full distribution of densities.

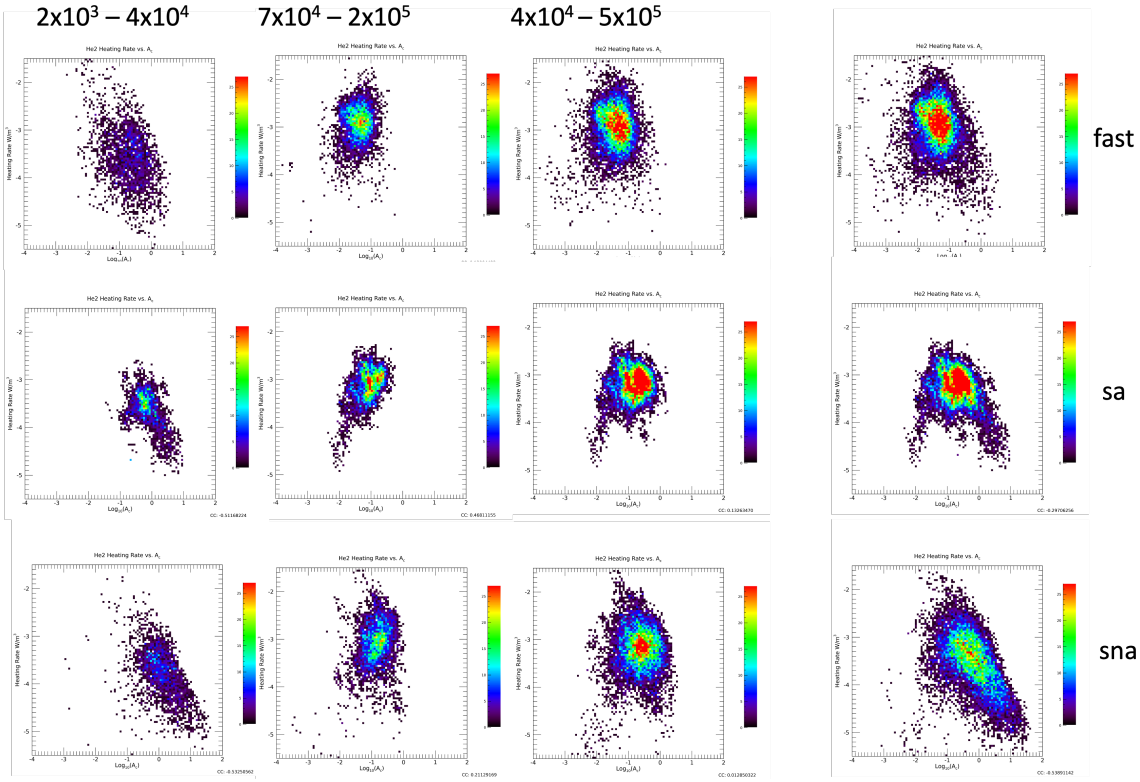

Figure C.10 Proton temperature in 3 solar wind types in different temperature regimes. From top to bottom: fast wind, SA wind, SNA wind. From left to right, low temperature, temperature covering SA peak T_p, high temperature, and the full distribution. Note that the second column overlaps with columns one and three.

BIBLIOGRAPHY

[1] Kasper, J. C., Klein, K. G., Weber, T., Maksimovic, M., Zaslavsky, A., Bale, S. D., Maruca, B. A., Stevens, M. L., and Case, A. W., "A Zone of Preferential Ion Heating Extends Tens of Solar Radii from the Sun," *Astrophys. J.*, Vol. 849, Nov. 2017, pp. 126.

[2] Kasper, J. C. and Klein, K. G., "Strong Preferential Ion Heating is Limited to within the Solar Alfvén Surface," *The Astrophysical Journal Letters*, Vol. 877, No. 2, jun 2019, pp. L35.

[3] Chandran, B. D. G., Verscharen, D., Quataert, E., Kasper, J. C., Isenberg, P. A., and Bourouaine, S., "STOCHASTIC HEATING, DIFFERENTIAL FLOW, AND THE ALPHA-TO-PROTON TEMPERATURE RATIO IN THE SOLAR WIND," *The Astrophysical Journal*, Vol. 776, No. 1, sep 2013, pp. 45.

[4] Verscharen, D., Klein, K. G., and Maruca, B. A., "The multi-scale nature of the solar wind," *Living Reviews in Solar Physics*, Vol. 16, No. 1, 2019, pp. 5.

[5] Geiss, J., "Processes affecting abundances in the solar wind." *Space Science Rev.*, Vol. 33, No. 1-2, March 1982, pp. 201–217.

[6] Landi, E., Gruesbeck, J. R., Lepri, S. T., Zurbuchen, T. H., and Fisk, L. A., "Charge State Evolution in the Solar Wind. II. Plasma Charge State Composition in the Inner Corona and Accelerating Fast Solar Wind," *Astrophys. J.*, Vol. 761, No. 1, Dec. 2012, pp. 48.

[7] Geiss, J., Gloeckler, G., and Von Steiger, R., "Origin of the solar wind from composition data," *Space Science Reviews*, Vol. 72, No. 1, 1995, pp. 49–60.

[8] von Steiger, R., Geiss, J., and Gloeckler, G., "Composition of the Solar Wind," *Cosmic Winds and the Heliosphere*, Jan. 1997, p. 581.

[9] von Steiger, R., Schwadron, N. A., Fisk, L. A., Geiss, J., Gloeckler, G., Hefti, S., Wilken, B., Wimmer-Schweingruber, R. R., and Zurbuchen, T. H., "Composition of quasi-stationary solar wind flows from Ulysses/Solar Wind Ion Composition Spectrometer," *Journal of Geophysical Research: Space Physics*, Vol. 105, No. A12, 2000, pp. 27217–27238.

[10] Zurbuchen, T. H., Fisk, L. A., Gloeckler, G., and von Steiger, R., "The solar wind composition throughout the solar cycle: A continuum of dynamic states," *Geophysical Research Letters*, Vol. 29, No. 9, 2002, pp. 66–1–66–4.

[11] Zhao, L., Zurbuchen, T. H., and Fisk, L. A., "Global distribution of the solar wind during solar cycle 23: ACE observations," *Geophysical Research Letters*, Vol. 36, No. 14, 2009.

[12] Geiss, J., Hirt, P., and Leutwyler, H., "On acceleration and motion of ions in corona and solar wind," *Solar Physics*, Vol. 12, 1970, pp. 458–483.

[13] Bodmer, R. and Bochsler, P., "Influence of Coulomb collisions on isotopic and elemental fractionation in the solar wind acceleration process," *Journal of Geophysical Research: Space Physics*, Vol. 105, No. A1, 2000, pp. 47–60.

[14] Zhao, L., Landi, E., Lepri, S. T., Gilbert, J. A., Zurbuchen, T. H., Fisk, L. A., and Raines, J. M., "On the Relation between the In Situ Properties and the Coronal Sources of the Solar Wind," *The Astrophysical Journal*, Vol. 846, No. 2, sep 2017, pp. 135.

[15] Cranmer, S. R. and Winebarger, A. R., "The Properties of the Solar Corona and Its Connection to the Solar Wind," *Annual Review of Astronomy and Astrophysics*, Vol. 57, No. 1, aug 2019, pp. 157–187.

[16] Stakhiv, M., Landi, E., Lepri, S. T., Oran, R., and Zurbuchen, T. H., "ON THE ORIGIN OF MID-LATITUDE FAST WIND: CHALLENGING THE TWO-STATE SOLAR WIND PARADIGM," *The Astrophysical Journal*, Vol. 801, No. 2, mar 2015, pp. 100.

[17] Stakhiv, M., Lepri, S. T., Landi, E., Tracy, P., and Zurbuchen, T. H., "ON SOLAR WIND ORIGIN AND ACCELERATION: MEASUREMENTS FROM ACE," *The Astrophysical Journal*, Vol. 829, No. 2, sep 2016, pp. 117.

[18] D'Amicis, R., Matteini, L., and Bruno, R., "On the slow solar wind with high Alfvénicity: from composition and microphysics to spectral properties," *Monthly Notices of the Royal Astronomical Society*, Vol. 483, No. 4, 12 2018, pp. 4665–4677.

[19] Borovsky, J. E., "The plasma structure of coronal hole solar wind: Origins and evolution," *Journal of Geophysical Research: Space Physics*, Vol. 121, No. 6, 2016, pp. 5055–5087.

[20] Feldman, W. C., Asbridge, J. R., Bame, S. J., and Gosling, J. T., "High-speed solar wind flow parameters at 1 AU," *Journal of Geophysical Research (1896-1977)*, Vol. 81, No. 28, 1976, pp. 5054–5060.

[21] Matteini, L., Hellinger, P., Landi, S., Trávníček, P. M., and Velli, M., "Ion Kinetics in the Solar Wind: Coupling Global Expansion to Local Microphysics," *Space Science Reviews*, Vol. 172, No. 1, 2012, pp. 373–396.

[22] Chew, G. F., Goldberger, M. L., Low, F. E., and Chandrasekhar, S., "The Boltzmann equation an d the one-fluid hydromagnetic equations in the absence of particle collisions," *Proceedings of the Royal Society of London. Series A. Mathematical and Physical Sciences*, Vol. 236, No. 1204, 1956, pp. 112–118.

[23] Hellinger, P., Velli, M., Trávníček, P., Gary, S. P., Goldstein, B. E., and Liewer, P. C., "Alfvén wave heating of heavy ions in the expanding solar wind: Hybrid simulations," *Journal of Geophysical Research: Space Physics*, Vol. 110, No. A12, 2005.

[24] Cranmer, S. R., "Ion Cyclotron Wave Dissipation in the Solar Corona: The Summed Effect of More than 2000 Ion Species," *The Astrophysical Journal*, Vol. 532, No. 2, apr 2000, pp. 1197.

[25] Feldman, W. C., Habbal, S. R., Hoogeveen, G., and Wang, Y.-M., "Experimental constraints on pulsed and steady state models of the solar wind near the Sun," *Journal of Geophysical Research: Space Physics*, Vol. 102, No. A12, 1997, pp. 26905–26918.

[26] Sakao, T., Kano, R., Narukage, N., Kotoku, J., Bando, T., Deluca, E., Lundquist, L., Tsuneta, S., Harra, L., Katsukawa, Y., Kubo, M., Hara, H., Matsuzaki, K., Shimojo, M., Bookbinder, J., Golub, L., Korreck, K., Su, Y., Shibasaki, K., and Nakatani, I., "Continuous Plasma Outflows from the Edge of a Solar Active Region as a Possible Source of Solar Wind," *Science (New York, N.Y.)*, Vol. 318, 01 2008, pp. 1585–8.

[27] Brooks, D., Ugarte-Urra, I., and Warren, H., "Full-Sun observations for identifying the source of the slow solar wind," *Nature communications*, Vol. 6, 01 2015, pp. 5947.

[28] Antonucci, E., Abbo, L., and Dodero, M. A., "Slow wind and magnetic topology in the solar minimum corona in 1996-1997," *asap*, Vol. 435, No. 2, 2005, pp. 699–711.

[29] Bavassano, B., Woo, R., and Bruno, R., "Heliospheric plasma sheet and coronal streamers," *Geophysical Research Letters*, Vol. 24, No. 13, 1997, pp. 1655–1658.

[30] Gosling, J. T., Borrini, G., Asbridge, J. R., Bame, S. J., Feldman, W. C., and Hansen, R. T., "Coronal streamers in the solar wind at 1 AU," *Journal of Geophysical Research: Space Physics*, Vol. 86, No. A7, 1981, pp. 5438–5448.

[31] Borrini, G., Gosling, J. T., Bame, S. J., Feldman, W. C., and Wilcox, J. M., "Solar wind helium and hydrogen structure near the heliospheric current sheet: A signal of coronal streamers at 1 AU," *Journal of Geophysical Research: Space Physics*, Vol. 86, No. A6, 1981, pp. 4565–4573.

[32] McComas, D. J., Ebert, R. W., Elliott, H. A., Goldstein, B. E., Gosling, J. T., Schwadron, N. A., and Skoug, R. M., "Weaker solar wind from the polar coronal holes and the whole Sun," *Geophysical Research Letters*, Vol. 35, No. 18, 2008.

[33] Alterman, B. L., Kasper, J. C., Stevens, M. L., and Koval, A., "A Comparison of Alpha Particle and Proton Beam Differential Flows in Collisionally Young Solar Wind," *The Astrophysical Journal*, Vol. 864, No. 2, sep 2018, pp. 112.

[34] Kasper, J. C., Stevens, M. L., Lazarus, A. J., Steinberg, J. T., and Ogilvie, K. W., "Solar Wind Helium Abundance as a Function of Speed and Heliographic Latitude: Variation through a Solar Cycle," *The Astrophysical Journal*, Vol. 660, No. 1, may 2007, pp. 901.

[35] Kasper, J. C., Stevens, M. L., Korreck, K. E., Maruca, B. A., Kiefer, K. K., Schwadron, N. A., and Lepri, S. T., "Evolution of the Relationships between Helium Abundance, Minor Ion Charge State, and Solar Wind Speed over the Solar Cycle," *Astrophys. J.*, Vol. 745, Feb. 2012, pp. 162.

[36] Lepri, S. T., Landi, E., and Zurbuchen, T. H., "Evolution of Solar Wind Heavy Ions over the Solar Cycle," *Outstanding Problems in Heliophysics: From Coronal Heating to the Edge of the Heliosphere*, edited by Q. Hu and G. P. Zank, Vol. 484 of *Astronomical Society of the Pacific Conference Series*, May 2014, p. 104.

[37] D'Amicis, R., Bruno, R., and Bavassano, B., "Response of the geomagnetic activity to solar wind turbulence during solar cycle 23," *Journal of Atmospheric and Solar-Terrestrial Physics*, Vol. 73, No. 5-6, April 2011, pp. 653–657.

[38] Müller, D., Marsden, R. G., St. Cyr, O. C., and Gilbert, H. R., "Solar Orbiter . Exploring the Sun-Heliosphere Connection," *Solar Physics*, Vol. 285, July 2013, pp. 25–70.

[39] Fox, N. J., Velli, M. C., Bale, S. D., Decker, R., Driesman, A., Howard, R. A., Kasper, J. C., Kinnison, J., Kusterer, M., Lario, D., Lockwood, M. K., McComas, D. J., Raouafi, N. E., and Szabo, A., "The Solar Probe Plus Mission: Humanity's First Visit to Our Star," *Space Science Reviews*, Vol. 204, No. 1, 2016, pp. 7–48.

[40] Kasper, J. C., Abiad, R., Austin, G., Balat-Pichelin, M., Bale, S. D., Belcher, J. W., Berg, P., Bergner, H., Berthomier, M., Bookbinder, J., Brodu, E., Caldwell, D., Case, A. W., Chand ran, B. D. G., Cheimets, P., Cirtain, J. W., Cranmer, S. R., Curtis, D. W., Daigneau, P., Dalton, G., Dasgupta, B., DeTomaso, D., Diaz-Aguado, M., Djordjevic, B., Donaskowski, B., Effinger, M., Florinski, V., Fox, N., Freeman, M., Gallagher, D., Gary, S. P., Gauron, T., Gates, R., Goldstein, M., Golub, L., Gordon, D. A., Gurnee, R., Guth, G., Halekas, J., Hatch, K., Heerikuisen, J., Ho, G., Hu, Q., Johnson, G., Jordan, S. P., Korreck, K. E., Larson, D., Lazarus, A. J., Li, G., Livi, R., Ludlam, M., Maksimovic, M., McFadden, J. P., Marchant, W., Maruca, B. A., McComas, D. J., Messina, L., Mercer, T., Park, S., Peddie, A. M., Pogorelov, N., Reinhart, M. J., Richardson, J. D., Robinson, M., Rosen, I., Skoug, R. M., Slagle, A., Steinberg, J. T., Stevens, M. L., Szabo, A., Taylor, E. R., Tiu, C., Turin, P., Velli, M., Webb, G., Whittlesey, P., Wright, K., Wu, S. T., and Zank, G., "Solar Wind Electrons Alphas and Protons (SWEAP) Investigation: Design of the Solar Wind and Coronal Plasma Instrument Suite for Solar Probe Plus," *Space Science Reviews*, Vol. 204, No. 1-4, Dec. 2016, pp. 131–186.

[41] Owen, C. J., Bruno, R., Livi, S., Louarn, P., Al Janabi, K., Allegrini, F., Amoros, C., Baruah, R., Barthe, A., Berthomier, M., Bordon, S., Brockley-Blatt, C., Brysbaert, C., Capuano, G., Collier, M., DeMarco, R., Fedorov, A., Ford, J., Fortunato, V., Fratter, I., Galvin, A. B., Hancock, B., Heirtzler, D., Kataria, D., Kistler, L., Lepri, S. T., Lewis, G., Loeffler, C., Marty, W., Mathon, R., Mayall, A., Mele, G., Ogasawara, K., Orlandi, M., Pacros, A., Penou, E., Persyn, S., Petiot, M., Phillips, M., Prech, L., Raines, J. M., Reden, M., Rouillard, A. P., Rousseau, A., Rubiella, J., Seran, H., Spencer, A., Thomas, J. W., Trevino, J., Verscharen, D., Wurz, P., Alapide, A., Amoruso, L., André, N., Anekallu, C., Arciuli, V., Arnett, K. L., Ascolese, R., Bancroft, C., Bland, P., Brysch, M., Calvanese, R., Castronuovo, M., Cermák, I., Chornay, D., Clemens, S., Coker, J., Collinson, G., D'Amicis, R., Dandouras, I., Darnley, R., Davies, D., Davison, G., De Los Santos, A., Devoto, P., Dirks, G., Edlund, E., Fazakerley, A., Ferris, M., Frost, C., Fruit, G., Garat, C., Génot, V., Gibson, W., Gilbert, J. A., de Giosa, V., Gradone, S., Hailey, M., Horbury, T. S., Hunt, T., Jacquey, C., Johnson, M., Lavraud, B., Lawrenson, A., Leblanc, F., Lockhart, W., Maksimovic, M., Malpus, A., Marcucci, F., Mazelle, C., Monti, F., Myers, S., Nguyen, T., Rodriguez-Pacheco, J., Phillips, I., Popecki, M., Rees, K., Rogacki, S. A., Ruane, K., Rust, D., Salatti, M., Sauvaud, J. A., Stakhiv, M. O., Stange, J., Stubbs, T., Taylor, T., Techer, J.-D., Terrier, G., Thibodeaux, R., Urdiales, C., Varsani, A., Walsh, A. P., Watson, G., Wheeler, P., Willis, G., Wimmer-Schweingruber, R. F., Winter, B., Yardley, J., and Zouganelis, I., "The Solar Orbiter Solar Wind Analyser (SWA) suite," *asap*, Vol. 642, 2020, pp. A16.

[42] Neugebauer, M., "The role of Coulomb collisions in limiting differential flow and temperature differences in the solar wind," *Journal of Geophysical Research (1896-1977)*, Vol. 81, No. 1, 1976, pp. 78–82.

[43] Ko, Y.-K., Fisk, L. A., Geiss, J., Gloeckler, G., and Guhathakurta, M., "AN EMPIRICAL STUDY OF THE ELECTRON TEMPERATURE AND HEAVY ION VELOCITIES IN THE SOUTH POLAR CORONAL HOLE," *Solar Physics*, Vol. 171, No. 2, 1997, pp. 345–361.

[44] von Steiger, R. and Zurbuchen, T. H., "Polar coronal holes during the past solar cycle: Ulysses observations," *Journal of Geophysical Research: Space Physics*, Vol. 116, No. A1, 2011.

[45] Landi, E. and Cranmer, S. R., "Ion Temperatures in the Low Solar Corona: Polar Coronal Holes at Solar Minimum," *Astrophys. J.*, Vol. 691, Jan. 2009, pp. 794–805.

[46] Hundhausen, A. J., Gilbert, H. E., and Bame, S. J., "Ionization state of the interplanetary plasma," *Journal of Geophysical Research (1896-1977)*, Vol. 73, No. 17, 1968, pp. 5485–5493.

[47] Hundhausen, A. J., "Nonthermal heating in the quiet solar wind," *Journal of Geophysical Research*, Vol. 74, No. 24, Jan. 1969, pp. 5810.

[48] Bochsler, P., "Minor ions in the solar wind," *The Astronomy and Astrophysics Review*, Vol. 14, 01 2007, pp. 1–40.

[49] Esser, R., Edgar, R. J., and Brickhouse, N. S., "High Minor Ion Outflow Speeds in the Inner Corona and Observed Ion Charge States in Interplanetary Space," *The Astrophysical Journal*, Vol. 498, No. 1, May 1998, pp. 448–457.

[50] Marsch, E. and Goldstein, H., "The effects of Coulomb collisions on solar wind ion velocity distributions," *Journal of Geophysical Research: Space Physics*, Vol. 88, No. A12, 1983, pp. 9933–9940.

[51] Marsch, E., "Kinetic Physics of the Solar Corona and Solar Wind," *Living Reviews in Solar Physics*, Vol. 3, No. 1, 2006, pp. 1.

[52] Marsch, E., Mühlhäuser, K.-H., Rosenbauer, H., Schwenn, R., and Neubauer, F. M., "Solar wind helium ions: Observations of the Helios solar probes between 0.3 and 1 AU," *Journal of Geophysical Research: Space Physics*, Vol. 87, No. A1, 1982, pp. 35–51.

[53] Marsch, E., Mühlhäuser, K.-H., Schwenn, R., Rosenbauer, H., Pilipp, W., and Neubauer, F. M., "Solar wind protons: Three-dimensional velocity distributions and derived plasma parameters measured between 0.3 and 1 AU," *Journal of Geophysical Research: Space Physics*, Vol. 87, No. A1, 1982, pp. 52–72.

[54] Hefti, S., Grünwaldt, H., Ipavich, F. M., Bochsler, P., Hovestadt, D., Aellig, M. R., Hilchenbach, M., Kallenbach, R., Galvin, A. B., Geiss, J., Gliem, F., Gloeckler, G., Klecker, B., Marsch, E., M/"obius, E., Neugebauer, M., and Wurz, P., "Kinetic properties of solar wind minor ions and protons measured with SOHO/CELIAS," *Journal of Geophysical Research: Space Physics*, Vol. 103, No. A12, 1998, pp. 29697–29704.

[55] Tu, C. Y., Marsch, E., Wilhelm, K., and Curdt, W., "Ion Temperatures in a Solar Polar Coronal Hole Observed by SUMER on SOHO," *The Astrophysical Journal*, Vol. 503, No. 1, Aug. 1998, pp. 475–482.

[56] Marsch, E., "Helios: Evolution of Distribution Functions 0.3–1 AU," *Space Science Reviews*, Vol. 172, No. 1, Nov 2012, pp. 23–39.

[57] Maruca, B. A., Bale, S. D., Sorriso-Valvo, L., Kasper, J. C., and Stevens, M. L., "Collisional Thermalization of Hydrogen and Helium in Solar-Wind Plasma," *Phys. Rev. Lett.*, Vol. 111, Dec 2013, pp. 241101.

[58] Kasper, J. C., Maruca, B. A., Stevens, M. L., and Zaslavsky, A., "Sensitive Test for Ion-Cyclotron Resonant Heating in the Solar Wind," *Physical Review Letters*, Vol. 110, No. 9, March 2013, pp. 091102.

[59] Kasper, J. C., Lazarus, A. J., and Gary, S. P., "Hot Solar-Wind Helium: Direct Evidence for Local Heating by Alfvén-Cyclotron Dissipation," *Phys. Rev. Lett.*, Vol. 101, Dec 2008, pp. 261103.

[60] Tracy, P. J., Kasper, J. C., Raines, J. M., Shearer, P., Gilbert, J. A., and Zurbuchen, T. H., "Constraining Solar Wind Heating Processes by Kinetic Properties of Heavy Ions," *Phys. Rev. Lett.*, Vol. 116, Jun 2016, pp. 255101.

[61] Wilson III, L. B., Stevens, M. L., Kasper, J. C., Klein, K. G., Maruca, B. A., Bale, S. D., Bowen, T. A., Pulupa, M. P., and Salem, C. S., "The Statistical Properties of Solar Wind Temperature Parameters Near 1 au," *The Astrophysical Journal Supplement Series*, Vol. 236, No. 2, jun 2018, pp. 41.

[62] Ďurovcová, T., Šafránková, J., and Nemecek, Z., "Proton Beam Abundance Variations and Their Relation to Alpha Particle Properties," *The Astrophysical Journal*, Vol. 923, 12 2021, pp. 170.

[63] Mostafavi, P., Allen, R. C., McManus, M. D., Ho, G. C., Raouafi, N. E., Larson, D. E., Kasper, J. C., and Bale, S. D., "Alpha–Proton Differential Flow of the Young Solar Wind: Parker Solar Probe Observations," *The Astrophysical Journal Letters*, Vol. 926, No. 2, feb 2022, pp. L38.

[64] Verscharen, D., Bourouaine, S., and Chandran, B. D. G., "INSTABILITIES DRIVEN BY THE DRIFT AND TEMPERATURE ANISOTROPY OF ALPHA PARTICLES IN THE SOLAR WIND," *The Astrophysical Journal*, Vol. 773, No. 2, aug 2013, pp. 163.

[65] Tracy, P. J., Kasper, J. C., Zurbuchen, T. H., Raines, J. M., Shearer, P., and Gilbert, J., "Thermalization of Heavy Ions in the Solar Wind," *The Astrophysical Journal*, Vol. 812, No. 2, Oct 2015, pp. 170.

[66] D'Amicis, R. and Bruno, R., "ON THE ORIGIN OF HIGHLY ALFVÉNIC SLOW SOLAR WIND," *The Astrophysical Journal*, Vol. 805, No. 1, may 2015, pp. 84.

[67] Marsch, E., Mühlhäuser, K.-H., Rosenbauer, H., Schwenn, R., and Denskat, K. U., "Pronounced proton core temperature anisotropy, ion differential speed, and simultaneous Alfvén wave activity in slow solar wind at 0.3 AU," *Journal of Geophysical Research: Space Physics*, Vol. 86, No. A11, 1981, pp. 9199–9203.

[68] Matthaeus, W. H. and Goldstein, M. L., "Measurement of the rugged invariants of magnetohydrodynamic turbulence in the solar wind," *Journal of Geophysical Research: Space Physics*, Vol. 87, No. A8, 1982, pp. 6011–6028.

[69] Tu, C. Y. and Marsch, E., "MHD structures, waves and turbulence in the solar wind: Observations and theories," *Space Science Reviews*, Vol. 73, No. 1, 1995, pp. 1–210.

[70] Marsch, E. and Tu, C.-Y., "Intermittency, non-Gaussian statistics and fractal scaling of MHD fluctuations in the solar wind," *Nonlinear Processes in Geophysics*, Vol. 4, No. 2, 1997, pp. 101–124.

[71] Bavassano, B., Pietropaolo, E., and Bruno, R., "Cross-helicity and residual energy in solar wind turbulence: Radial evolution and latitudinal dependence in the region

from 1 to 5 AU," *Journal of Geophysical Research: Space Physics*, Vol. 103, No. A4, 1998, pp. 6521–6529.

[72] Zank, G. P., Adhikari, L., Hunana, P., Shiota, D., Bruno, R., and Telloni, D., "Theory and Transport of Nearly Incompressible Magnetohydrodynamic Turbulence," *The Astrophysical Journal*, Vol. 835, No. 2, jan 2017, pp. 147.

[73] Zank, G. P. and Matthaeus, W. H., "Waves and turbulence in the solar wind," *Journal of Geophysical Research: Space Physics*, Vol. 97, No. A11, 1992, pp. 17189–17194.

[74] Bavassano, B. and Bruno, R., "Solar wind fluctuations at large scale: A comparison between low and high solar activity conditions," *Journal of Geophysical Research: Space Physics*, Vol. 96, No. A2, 1991, pp. 1737–1744.

[75] Borovsky, J. E., Denton, M. H., and Smith, C. W., "Some Properties of the Solar Wind Turbulence at 1 AU Statistically Examined in the Different Types of Solar Wind Plasma," *Journal of Geophysical Research: Space Physics*, Vol. 124, No. 4, 2019, pp. 2406–2424.

[76] Borovsky, J. E., "The Magnetic Structure of the Solar Wind: Ionic Composition and the Electron Strahl," *Geophysical Research Letters*, Vol. 47, No. 5, 2020, pp. e2019GL084586, e2019GL084586 2019GL084586.

[77] Bruno, R., Telloni, D., Sorriso-Valvo, L., Marino, R., De Marco, R., and D'Amicis, R., "The low-frequency break observed in the slow solar wind magnetic spectra," *asap*, Vol. 627, 2019, pp. A96.

[78] Matteini, L., Stansby, D., Horbury, T. S., and Chen, C. H. K., "On the 1/f Spectrum in the Solar Wind and Its Connection with Magnetic Compressibility," *The Astrophysical Journal Letters*, Vol. 869, No. 2, dec 2018, pp. L32.

[79] Belcher, J. W. and Davis Jr., L., "Large-amplitude Alfvén waves in the interplanetary medium, 2," *Journal of Geophysical Research (1896-1977)*, Vol. 76, No. 16, 1971, pp. 3534–3563.

[80] Richardson, I. G., "Solar wind stream interaction regions throughout the heliosphere," *Living Reviews in Solar Physics*, Vol. 15, No. 1, Jan. 2018, pp. 1.

[81] Allen, R. C., Ho, G. C., Jian, L. K., Vines, S. K., Bale, S. D., Case, A. W., Hill, M. E., Joyce, C. J., Kasper, J. C., Korreck, K. E., Malaspina, D. M., McComas, D. J., McNutt, R., Möstl, C., Odstrcil, D., Raouafi, N., Schwadron, N. A., and Stevens, M. L., "A living catalog of stream interaction regions in the Parker Solar Probe era," *asap*, Vol. 650, 2021, pp. A25.

[82] Jian, L., Russell, C., Luhmann, J., and Skoug, R., "Evolution of solar wind structures from 0.72 to 1AU," *Advances in Space Research*, Vol. 41, No. 2, 2008, pp. 259–266.

[83] Elliott, H. A., Henney, C. J., McComas, D. J., Smith, C. W., and Vasquez, B. J., "Temporal and radial variation of the solar wind temperature-speed relationship," *Journal of Geophysical Research: Space Physics*, Vol. 117, No. A9, 2012.

[84] Elliott, H. A., McComas, D. J., Matthaeus, W. H., and Henney, C. J., "Solar Wind Speed And Temperature Relationship," *AIP Conference Proceedings*, Vol. 1216, No. 1, 03 2010, pp. 98–101.

[85] Hellinger, P., Matteini, L., Štverák, v., Trávníček, P. M., and Marsch, E., "Heating and cooling of protons in the fast solar wind between 0.3 and 1 AU: Helios revisited," *Journal of Geophysical Research: Space Physics*, Vol. 116, No. A9, 2011.

[86] Hellinger, P., Trávníček, P. M., Štverák, v., Matteini, L., and Velli, M., "Proton thermal energetics in the solar wind: Helios reloaded," *Journal of Geophysical Research: Space Physics*, Vol. 118, No. 4, 2013, pp. 1351–1365.

[87] Perrone, D., Stansby, D., Horbury, T. S., and Matteini, L., "Radial evolution of the solar wind in pure high-speed streams: HELIOS revised observations," *Monthly Notices of the Royal Astronomical Society*, Vol. 483, No. 3, 12 2018, pp. 3730–3737.

[88] Robbins, D. E., Hundhausen, A. J., and Bame, S. J., "Helium in the solar wind," *Journal of Geophysical Research (1896-1977)*, Vol. 75, No. 7, 1970, pp. 1178–1187.

[89] Neugebauer, M., Goldstein, B. E., Bame, S. J., and Feldman, W. C., "Ulysses near-ecliptic observations of differential flow between protons and alphas in the solar wind," *Journal of Geophysical Research: Space Physics*, Vol. 99, No. A2, 1994, pp. 2505–2511.

[90] Ďurovcová, T., Šafránková, J., Němeček, Z., and Richardson, J. D., "Evolution of Proton and Alpha Particle Velocities through the Solar Cycle," *The Astrophysical Journal*, Vol. 850, No. 2, nov 2017, pp. 164.

[91] Johnson, E., Maruca, B. A., McManus, M., Stevens, M., Klein, K. G., and Mostafavi, P., "Application of collisional analysis to the differential velocity of solar wind ions," *Frontiers in Astronomy and Space Sciences*, Vol. 10, 2024.

[92] Gershman, D. J., Zurbuchen, T. H., Fisk, L. A., Gilbert, J. A., Raines, J. M., Anderson, B. J., Smith, C. W., Korth, H., and Solomon, S. C., "Solar wind alpha particles and heavy ions in the inner heliosphere observed with MESSENGER," *Journal of Geophysical Research: Space Physics*, Vol. 117, No. A12, 2012.

[93] Cranmer, S., "Coronal Holes," *Living Reviews in Solar Physics*, Vol. 6, sep 2009, pp. 1614–4961.

[94] Kasper, J. C., Lazarus, A. J., and Gary, S. P., "Wind/SWE observations of firehose constraint on solar wind proton temperature anisotropy," *Geophysical Research Letters*, Vol. 29, No. 17, 2002, pp. 20–1–20–4.

[95] Hellinger, P., Trávníček, P., Kasper, J. C., and Lazarus, A. J., "Solar wind proton temperature anisotropy: Linear theory and WIND/SWE observations," *Geophysical Research Letters*, Vol. 33, No. 9, 2006.

[96] Gary, S. P., Skoug, R. M., Steinberg, J. T., and Smith, C. W., "Proton temperature anisotropy constraint in the solar wind: ACE observations," *Geophysical Research Letters*, Vol. 28, No. 14, 2001, pp. 2759–2762.

[97] Kasper, J. C., Bale, S. D., Belcher, J. W., Berthomier, M., Case, A. W., Chandran, B. D. G., Curtis, D. W., Gallagher, D., Gary, S. P., Golub, L., Halekas, J. S., Ho, G. C., Horbury, T. S., Hu, Q., Huang, J., Klein, K. G., Korreck, K. E., Larson, D. E., Livi, R., Maruca, B., Lavraud, B., Louarn, P., Maksimovic, M., Martinovic, M., McGinnis, D., Pogorelov, N. V., Richardson, J. D., Skoug, R. M., Steinberg, J. T., Stevens, M. L., Szabo, A., Velli, M., Whittlesey, P. L., Wright, K. H., Zank, G. P., MacDowall, R. J., McComas, D. J., McNutt, R. L., Pulupa, M., Raouafi, N. E., and Schwadron, N. A., "Alfvénic velocity spikes and rotational flows in the near-Sun solar wind," *nat*, Vol. 576, No. 7786, Dec. 2019, pp. 228–231.

[98] Hollweg, J. V. and Isenberg, P. A., "Generation of the fast solar wind: A review with emphasis on the resonant cyclotron interaction," *Journal of Geophysical Research: Space Physics*, Vol. 107, No. A7, 2002, pp. SSH 12–1–SSH 12–37.

[99] Isenberg, P. A. and Vasquez, B. J., "Preferential Perpendicular Heating of Coronal Hole Minor Ions by the Fermi Mechanism," *The Astrophysical Journal*, Vol. 668, No. 1, oct 2007, pp. 546–556.

[100] Cranmer, S. R. and van Ballegooijen, A. A., "Alfvenic Turbulence in the Extended Solar Corona: Kinetic Effects and Proton Heating," *The Astrophysical Journal*, Vol. 594, No. 1, sep 2003, pp. 573–591.

[101] Klein, K. G., Alterman, B. L., Stevens, M. L., Vech, D., and Kasper, J. C., "Majority of Solar Wind Intervals Support Ion-Driven Instabilities," *Phys. Rev. Lett.*, Vol. 120, No. 20, May 2018, pp. 205102.

[102] Chandran, B. D. G. and Hollweg, J. V., "Alfvén Wave Reflection and Turbulent Heating in the Solar Wind from 1 Solar Radius to 1 AU: An Analytical Treatment," *The Astrophysical Journal*, Vol. 707, No. 2, Dec. 2009, pp. 1659–1667.

[103] Velli, M., Pucci, F., Rappazzo, F., and Tenerani, A., "Models of coronal heating, turbulence and fast reconnection," *Philosophical Transactions of the Royal Society of London Series A*, Vol. 373, No. 2042, April 2015, pp. 20140262–20140262.

[104] Fisk, L. A., "Motion of the footpoints of heliospheric magnetic field lines at the Sun: Implications for recurrent energetic particle events at high heliographic latitudes," *Journal of Geophysical Research: Space Physics*, Vol. 101, No. A7, 1996, pp. 15547–15553.

[105] Fisk, L. A., Schwadron, N. A., and Zurbuchen, T. H., "Acceleration of the fast solar wind by the emergence of new magnetic flux," *Journal of Geophysical Research: Space Physics*, Vol. 104, No. A9, 1999, pp. 19765–19772.

[106] Bale, S. D., Badman, S. T., Bonnell, J. W., Bowen, T. A., Burgess, D., Case, A. W., Cattell, C. A., Chandran, B. D. G., Chaston, C. C., Chen, C. H. K., Drake, J. F., de Wit, T. D., Eastwood, J. P., Ergun, R. E., Farrell, W. M., Fong, C., Goetz, K., Goldstein, M., Goodrich, K. A., Harvey, P. R., Horbury, T. S., Howes, G. G., Kasper, J. C., Kellogg, P. J., Klimchuk, J. A., Korreck, K. E., Krasnoselskikh, V. V., Krucker, S., Laker, R., Larson, D. E., MacDowall, R. J., Maksimovic, M., Malaspina, D. M., Martinez-Oliveros, J., McComas, D. J., Meyer-Vernet, N., Moncuquet, M., Mozer, F. S., Phan, T. D., Pulupa, M., Raouafi, N. E., Salem, C., Stansby, D., Stevens, M., Szabo, A., Velli, M., Woolley, T., and Wygant, J. R., "Highly structured slow solar wind emerging from an equatorial coronal hole," *nat*, Vol. 576, No. 7786, Dec. 2019, pp. 237–242.

[107] Raouafi, N. E., Stenborg, G., Seaton, D. B., Wang, H., Wang, J., DeForest, C. E., Bale, S. D., Drake, J. F., Uritsky, V. M., Karpen, J. T., DeVore, C. R., Sterling, A. C., Horbury, T. S., Harra, L. K., Bourouaine, S., Kasper, J. C., Kumar, P., Phan, T. D., and Velli, M., "Magnetic Reconnection as the Driver of the Solar Wind," *The Astrophysical Journal*, Vol. 945, No. 1, mar 2023, pp. 28.

[108] McComas, D. J., Bame, S. J., Barker, P., Feldman, W. C., Phillips, J. L., Riley, P., and Griffee, J. W., "Solar Wind Electron Proton Alpha Monitor (SWEPAM) for the Advanced Composition Explorer," *Space Science Reviews*, Vol. 86, July 1998, pp. 563–612.

[109] Gloeckler, G., Cain, J., Ipavich, F., Tums, E., Bedini, P., Fisk, L., Zurbuchen, T., Bochsler, P., Fischer, J., Wimmer-Schweingruber, R., Geiss, J., and Kallenbach, R., "Investigation of the composition of solar and interstellar matter using solar wind and pickup ion measurements with SWICS and SWIMS on the ACE spacecraft," *Space Science Reviews*, Vol. 86, No. 1, Jul 1998, pp. 497–539.

[110] Stone, E. C., Frandsen, A. M., Mewaldt, R. A., Christian, E. R., Margolies, D., Ormes, J. F., and Snow, F., "The Advanced Composition Explorer," *Space Science Reviews*, Vol. 86, No. 1, 1998, pp. 1–22.

[111] Müller, D., St. Cyr, O. C., Zouganelis, I., Gilbert, H. R., Marsden, R., Nieves-Chinchilla, T., Antonucci, E., Auchère, F., Berghmans, D., Horbury, T. S., Howard, R. A., Krucker, S., Maksimovic, M., Owen, C. J., Rochus, P., Rodriguez-Pacheco, J., Romoli, M., Solanki, S. K., Bruno, R., Carlsson, M., Fludra, A., Harra, L., Hassler, D. M., Livi, S., Louarn, P., Peter, H., Schühle, U., Teriaca, L., del Toro Iniesta, J. C., Wimmer-Schweingruber, R. F., Marsch, E., Velli, M., De Groof, A., Walsh, A., and Williams, D., "The Solar Orbiter mission - Science overview," *asap*, Vol. 642, 2020, pp. A1.

[112] Shearer, P., von Steiger, R., Raines, J. M., Lepri, S. T., Thomas, J. W., Gilbert, J. A., Landi, E., and Zurbuchen, T. H., "The Solar Wind Neon Abundance Observed with ACE/SWICS and Ulysses/SWICS," *The Astrophysical Journal*, Vol. 789, No. 1, July 2014, pp. 60.

[113] Gloeckler, G., Geiss, J., Balsiger, H., Bedini, P., Cain, J. C., Fischer, J., Fisk, L. A., Galvin, A. B., Gliem, F., Hamilton, D. C., Hollweg, J. V., Ipavich, F. M., Joos, R., Livi, S., Lundgren, R. A., Mall, U., McKenzie, J. F., Ogilvie, K. W., Ottens, F., Rieck, W., Tums, E. O., von Steiger, R., Weiss, W., and Wilken, B., "The Solar Wind Ion Composition Spectrometer," *asap*, Vol. 92, No. 2, Jan. 1992, pp. 267–289.

[114] Smith, C., L'Heureux, J., Ness, N., Acuña, M., Burlaga, L., and Scheifele, J., "The Ace Magnetic Fields Experiment," *Space Science Reviews*, Vol. 86, 07 1998, pp. 613–632.

[115] Horbury, T. S., O'Brien, H., Carrasco Blazquez, I., Bendyk, M., Brown, P., Hudson, R., Evans, V., Oddy, T. M., Carr, C. M., Beek, T. J., Cupido, E., Bhattacharya, S., Dominguez, J.-A., Matthews, L., Myklebust, V. R., Whiteside, B., Bale, S. D., Baumjohann, W., Burgess, D., Carbone, V., Cargill, P., Eastwood, J., Erdös, G., Fletcher, L., Forsyth, R., Giacalone, J., Glassmeier, K.-H., Goldstein, M. L., Hoeksema, T., Lockwood, M., Magnes, W., Maksimovic, M., Marsch, E., Matthaeus, W. H., Murphy, N., Nakariakov, V. M., Owen, C. J., Owens, M., Rodriguez-Pacheco, J., Richter, I., Riley, P., Russell, C. T., Schwartz, S., Vainio, R., Velli, M., Vennerstrom, S., Walsh, R., Wimmer-Schweingruber, R. F., Zank, G., Müller, D., Zouganelis, I., and Walsh, A. P., "The Solar Orbiter magnetometer," *asap*, Vol. 642, 2020, pp. A9.

[116] Holmes, J., Kasper, J., Klein, K. G., Lepri, S. T., and Raines, J. M., "Zone of Preferential Heating for Minor Ions in the Solar Wind," *apj*, Vol. 964, No. 1, March 2024, pp. 19.

[117] Hernández, R., Livi, S., and Marsch, E., "On the He2+ to H+ temperature ratio in slow solar wind," *Journal of Geophysical Research: Space Physics*, Vol. 92, No. A7, 1987, pp. 7723–7727.

[118] Chandran, B. D. G., "ALFVÉN-WAVE TURBULENCE AND PERPENDICULAR ION TEMPERATURES IN CORONAL HOLES," *The Astrophysical Journal*, Vol. 720, No. 1, aug 2010, pp. 548–554.

[119] Johnson, E., Maruca, B. A., McManus, M., Klein, K. G., Lichko, E. R., Verniero, J., Paulson, K. W., DeWeese, H., Dieguez, I., Qudsi, R. A., Kasper, J., Stevens, M., Alterman, B. L., III, L. B. W., Livi, R., Rahmati, A., and Larson, D., "Anterograde Collisional Analysis of Solar Wind Ions," *The Astrophysical Journal*, Vol. 950, No. 1, jun 2023, pp. 51.

[120] Stansby, D., Horbury, T. S., and Matteini, L., "Diagnosing solar wind origins using in situ measurements in the inner heliosphere," *Monthly Notices of the Royal Astronomical Society*, Vol. 482, No. 2, 10 2018, pp. 1706–1714.

[121] Abbo, L., Ofman, L., Antiochos, S. K., Hansteen, V. H., Harra, L., Ko, Y. K., Lapenta, G., Li, B., Riley, P., Strachan, L., von Steiger, R., and Wang, Y. M., "Slow Solar Wind: Observations and Modeling," *ssr*, Vol. 201, No. 1-4, Nov. 2016, pp. 55–108.

[122] Feldman, U., Landi, E., and Schwadron, N. A., "On the sources of fast and slow solar wind," *Journal of Geophysical Research: Space Physics*, Vol. 110, No. A7, 2005.

[123] Fu, H., Madjarska, M. S., Xia, L., Li, B., Huang, Z., and Wangguan, Z., "Charge States and FIP Bias of the Solar Wind from Coronal Holes, Active Regions, and Quiet Sun," *The Astrophysical Journal*, Vol. 836, No. 2, feb 2017, pp. 169.

[124] Altschuler, M. D. and Newkirk, G., "Magnetic Fields and the Structure of the Solar Corona. I: Methods of Calculating Coronal Fields," *Solar Physics*, Vol. 9, No. 1, Sept. 1969, pp. 131–149.

[125] Wang, Y. M. and Sheeley, N. R., J., "On Potential Field Models of the Solar Corona," *apj*, Vol. 392, June 1992, pp. 310.

[126] Neugebauer, M., Liewer, P. C., Smith, E. J., Skoug, R. M., and Zurbuchen, T. H., "Sources of the solar wind at solar activity maximum," *Journal of Geophysical Research: Space Physics*, Vol. 107, No. A12, 2002, pp. SSH 13–1–SSH 13–15.

[127] Fu, H., Li, B., Li, X., Huang, Z., Mou, C., Jiao, F., and Xia, L., "Coronal Sources and In Situ Properties of the Solar Winds Sampled by ACE During 1999–2008," *Solar Physics*, Vol. 290, No. 5, May 2015, pp. 1399–1415.

[128] Badman, S. T., Bale, S. D., Oliveros, J. C. M., Panasenco, O., Velli, M., Stansby, D., Buitrago-Casas, J. C., Réville, V., Bonnell, J. W., Case, A. W., de Wit, T. D., Goetz, K., Harvey, P. R., Kasper, J. C., Korreck, K. E., Larson, D. E., Livi, R., MacDowall, R. J., Malaspina, D. M., Pulupa, M., Stevens, M. L., and Whittlesey, P. L., "Magnetic Connectivity of the Ecliptic Plane within 0.5 au: Potential Field Source Surface Modeling of the First Parker Solar Probe Encounter," *The Astrophysical Journal Supplement Series*, Vol. 246, No. 2, feb 2020, pp. 23.

[129] Panasenco, O., Velli, M., D'Amicis, R., Shi, C., Réville, V., Bale, S. D., Badman, S. T., Kasper, J., Korreck, K., Bonnell, J. W., de Wit, T. D., Goetz, K., Harvey, P. R., MacDowall, R. J., Malaspina, D. M., Pulupa, M., Case, A. W., Larson, D., Livi, R., Stevens, M., and Whittlesey, P., "Exploring Solar Wind Origins and Connecting Plasma Flows from the Parker Solar Probe to 1 au: Nonspherical Source Surface and Alfvénic Fluctuations," *The Astrophysical Journal Supplement Series*, Vol. 246, No. 2, feb 2020, pp. 54.

[130] D'Amicis, R., Bruno, R., Panasenco, O., Telloni, D., Perrone, D., Marcucci, M. F., Woodham, L., Velli, M., De Marco, R., Jagarlamudi, V., Coco, I., Owen, C., Louarn, P., Livi, S., Horbury, T., André, N., Angelini, V., Evans, V., Fedorov, A., Genot, V., Lavraud, B., Matteini, L., Müller, D., O'Brien, H., Pezzi, O., Rouillard,

A. P., Sorriso-Valvo, L., Tenerani, A., Verscharen, D., and Zouganelis, I., "First Solar Orbiter observation of the Alfvénic slow wind and identification of its solar source," *asap*, Vol. 656, 2021, pp. A21.

[131] Bruno, R. and Bavassano, B., "Origin of low cross-helicity regions in the inner solar wind," *Journal of Geophysical Research: Space Physics*, Vol. 96, No. A5, 1991, pp. 7841–7851.

[132] Stansby, D., Matteini, L., Horbury, T. S., Perrone, D., D'Amicis, R., and Berčič, L., "The origin of slow Alfvénic solar wind at solar minimum," *Monthly Notices of the Royal Astronomical Society*, Vol. 492, No. 1, 12 2019, pp. 39–44.

[133] Livi, S., Marsch, E., and Rosenbauer, H., "Coulomb collisional domains in the solar wind," *Journal of Geophysical Research: Space Physics*, Vol. 91, No. A7, 1986, pp. 8045–8050.

[134] Bavassano, B., Pietropaolo, E., and Bruno, R., "Alfvénic turbulence in the polar wind: A statistical study on cross helicity and residual energy variations," *Journal of Geophysical Research: Space Physics*, Vol. 105, No. A6, 2000, pp. 12697–12704.

[135] Marsch, E. and Mangeney, A., "Ideal MHD equations in terms of compressive Elsässer variables," *Journal of Geophysical Research: Space Physics*, Vol. 92, No. A7, 1987, pp. 7363–7367.

[136] Tu, C.-Y., Marsch, E., and Thieme, K. M., "Basic properties of solar wind MHD turbulence near 0.3 AU analyzed by means of Elsässer variables," *Journal of Geophysical Research: Space Physics*, Vol. 94, No. A9, 1989, pp. 11739–11759.

[137] Rosenbauer, H., Schwenn, R., Marsch, E., Meyer, B., Miggenrieder, H., Montgomery, M. D., Muehlhaeuser, K. H., Pilipp, W., Voges, W., and Zink, S. M., "A survey on initial results of the HELIOS plasma experiment," *Journal of Geophysics Zeitschrift Geophysik*, Vol. 42, No. 6, Jan. 1977, pp. 561–580.

[138] Wenzel, K. P., Marsden, R. G., Page, D. E., and Smith, E. J., "The ULYSSES Mission," *asap*, Vol. 92, Jan. 1992, pp. 207.

[139] Stansby, D., Perrone, D., Matteini, L., Horbury, T. S., and Salem, C. S., "Alpha particle thermodynamics in the inner heliosphere fast solar wind," *asap*, Vol. 623, 2019, pp. L2.

[140] Gary, S. P., Yin, L., Winske, D., and Reisenfeld, D. B., "Alpha/proton magnetosonic instability in the solar wind," *Journal of Geophysical Research: Space Physics*, Vol. 105, No. A9, 2000, pp. 20989–20996.

[141] Berger, L., Wimmer-Schweingruber, R. F., and Gloeckler, G., "Systematic Measurements of Ion-Proton Differential Streaming in the Solar Wind," *Phys. Rev. Lett.*, Vol. 106, Apr 2011, pp. 151103.

[142] Livi, S., Lepri, S. T., Raines, J. M., Dewey, R. M., Galvin, A. B., Louarn, P., Collier, M R., Allegrini, F., Alterman, B. L., Bert, C. M., Bruno, R., Chornay, D. J., D'Amicis, R., Eddy, T. J., Ellis, L., Fauchon-Jones, E., Fedorov, A., Gershkovich, I., Holmes, J., Horbury, T. S., Kistler, L. M., Kucharek, H., Lugaz, N., Nieves-Chinchilla, T., O'Brien, H., Ogasawara, K., Owen, C. J., Phillips, M., Ploof, K., Rivera, Y. J., Spitzer, S. A., Stubbs, T. J., and Wurz, P., "First results from the Solar Orbiter Heavy Ion Sensor," *asap*, Vol. 676, 2023, pp. A36.

[143] Hernandez, R. and Marsch, E., "Collisional time scales for temperature and velocity exchange between drifting Maxwellians," *Journal of Geophysical Research: Space Physics*, Vol. 90, No. A11, 1985, pp. 11062–11066.